Dissertation

submitted to the
Combined Faculties of the Natural Sciences
and Mathematics

of the
Ruperto-Carola-University of Heidelberg,
Germany

for the degree of
Doctor of Natural Sciences

Put forward by

Jens Kröger

born in Lübbecke

Oral Examination: October 13th, 2021

Characterisation of a High-Voltage Monolithic Active Pixel Sensor Prototype for Future Collider Detectors

Referees:

Prof. Dr. André Schöning

Prof. Dr. Norbert Herrmann

To the four most important people in my life
for their endless support

Abstract

The physics goals and operating conditions at existing and proposed high-energy colliders, such as the Compact Linear Collider (CLIC), pose challenging demands on the performance of their detector systems. Precise hit-time tagging, excellent spatial resolution, and low mass are required for the vertex and tracking detectors. To meet these requirements, an all-silicon vertex and tracking detector system is foreseen for CLIC.

The ATLASpix high-voltage monolithic active pixel sensor (HV-MAPS) prototype was designed to demonstrate the suitability of the technology for the ATLAS Inner Tracker Upgrade and the CLIC tracking detector. It is manufactured in the AMS aH18 process with a pixel pitch of $130 \times 40\,\mu m^2$ and an active area of $3.25 \times 16.0\,mm^2$.

In this thesis, the performance of the ATLASpix_Simple prototype is characterised in laboratory and test-beam measurements and evaluated with respect to the requirements for the CLIC tracking detector. Samples with different substrate resistivities are compared.

The breakdown behaviour is determined, and a charge calibration of the threshold and the time-over-threshold charge is performed. A threshold dispersion of $\sim 100\,e^-$, a pixel noise of $\sim 120\,e^-$, and a signal-to-noise ratio of ≥ 12 are measured using an Fe-55 signal source. The power consumption of the sensor amounts to $\sim 190\,mW$ with the used settings.

The spatial resolution is close to the binary resolution limited by the pixel pitch, and the time resolution is found to depend significantly on the substrate resistivity. For a $200\,\Omega cm$ sample, a time resolution of 6.8 ns after offline corrections is measured at a detection threshold of $\sim 590\,e^-$. High efficiencies well above 99.9 % are reached at low noise rates below 1 Hz on the full chip with a $200\,\Omega cm$ sample at a bias voltage of $-75\,V$ and a threshold of $\sim 670\,e^-$. Lower substrate resistivities show a significantly worse timing performance and a smaller efficient operating window.

For a substrate resistivity of $200\,\Omega cm$, an active depth of 55-61 µm is estimated at a bias voltage of $-90\,V$.

The ATLASpix_Simple fulfils most of the requirements of the CLIC tracker. Moreover, its successful operation has lead to the development of further HV-MAPS prototypes, which are expected to meet all requirements and are currently investigated.

Zusammenfassung

Die Sensitivitätsanforderungen physikalischer Messungen sowie die Betriebsbedingungen an existierenden und zukünftigen Hochenergie-Teilchenbeschleunigern, wie dem Kompakten Linearbeschleuniger (CLIC), stellen strikte Anforderungen an die Leistungsfähigkeit ihrer Detektorsysteme. Vertex- und Spurdetektoren benötigen präzise Treffer-Zeitstempel, eine exzellente räumliche Auflösung und eine geringe Strahlungslänge. Um diese Anforderungen zu erfüllen, ist für CLIC ein ausschließlich auf Siliziumdetektoren basierendes Vertex- und Spurdetektorsystem vorgesehen.

Der ATLASpix_Simple ist ein hochspannungsbetriebener monolithischer aktiver Pixelsensor (HV-MAPS), der entwickelt wurde, um die Tauglichkeit der Technologie für den Einsatz in den Spurdetektoren des ATLAS Experiments und des CLIC Detektors demonstrieren. Er wurde von AMS im aH18-Prozess produziert, hat eine Pixelgröße von $130 \times 40\,\mu m^2$ und eine aktive Fläche von $3.25 \times 16.0\,mm^2$.

In der vorliegenden Arbeit wird die Leistungsfähigkeit des ATLASpix_Simple mithilfe von Labor- und Teststrahlmessungen bestimmt und im Hinblick auf die Anforderungen des CLIC Spurdetektors evaluiert. Zusätzlich wird der Einfluss der Substratresistivitäten systematisch analysiert.

Im Labor wurde u.a. die Durchbruchspannung bestimmt, eine Ladungskalibration des Schwellwertes und eine Messung des Signal-Rausch-Verhältnisses basierend auf Messungen mit einer Röntgenquelle durchgeführt. Eine Schwellwertdispersion von $\sim 100\,e^-$, ein Pixelrauschen von $\sim 120\,e^-$ und ein Signal-zu-Rausch-Verhältnis ≥ 12 wurden mit einer Fe-55 Quelle gemessen. Die Leistungsaufnahme bei den verwendeten Einstellungen ist $\sim 190\,mW$.

In mehreren Teststrahlkampagnen wurde die räumliche Auflösung bestimmt, die nahe an der binären Auflösung und limitiert durch die Pixelgröße ist. Die Zeitauflösung hängt signifikant von der Substratresistivität ab. Mit einem $200\,\Omega cm$-Sensor wird eine Zeitaufösung von $6.8\,ns$ nach Korrekturen bei einem Schwellwert von $\sim 590\,e^-$ gemessen. Hohe Teilchennachweiseffizienzen von über 99.9 % werden bei geringen Rauschraten unter 1 Hz auf dem gesamten Sensor für ein $200\,\Omega cm$-Exemplar bei einer Sperrspannung von $-75\,V$ und einem Schwellwert von $\sim 670\,e^-$ erreicht. Geringere Substratresistivitäten zeigen signifikant langsamere Zeitauflösungen und ein kleineres Schwellenbetriebsfenster mit hohen Effizienzen.

Für eine Substratresistivität von $200\,\Omega cm$ wurde eine aktive Dicke von 55-61 µm bei einer Sperrspannung von $-90\,V$ ermittelt.

Der ATLASpix_Simple erfüllt fast alle Anforderungen des CLIC Spurdetektors. Sein erfolgreicher Betrieb hat zu der Entwicklung weiterer HV-MAPS Prototypen geführt, die alle Anforderungen erfüllen dürften und aktuell vermessen werden.

Contributions From The Author

The following contributions to larger projects have been made while working on this thesis. *Publications are listed separately in the appendix.*

Caribou Readout System

The Caribou Readout System was originally developed in a collaborative effort within the CLICdp and ATLAS ITk Upgrade Collaborations. The author implemented a fast GTX Transceiver in the readout firmware in order to use the full potential of the readout speed for the ATLASpix. In addition, he made adjustments to the DAQ software to allow for an automated data taking in laboratory measurement campaigns including noise studies and calibration measurements with an X-ray machine.

Corryvreckan Reconstruction and Analysis Framework

The author was involved in the Corryvreckan software project as one of the main developers and maintainers. In close collaboration with other group members, he implemented many new features including an improved offline event building scheme required for data recorded using the EUDAQ2 DAQ framework during test-beam campaigns at DESY. He restructured internal coordinate transformations and contributed significantly to the writing of the user manual. Furthermore, he adjusted the analysis code to allow for a detailed timing performance analysis of the ATLASpix. In addition, the author reviewed and tested code contributions from other developers and users, and represented the framework in several public talks and tutorials at workshops and conferences.

ATLASpix and Data Acquisition

All laboratory measurements presented in this thesis were planned and conducted by the author. The test-beam campaigns leading to the results presented in this thesis were carried out in a collaborative effort with colleagues from the CLICdp collaboration as well as colleagues from DESY. All data analysed within the scope of this thesis was recorded with the involvement of the author, who participated in two test-beam campaigns at the CERN SPS and six campaigns at DESY. An exception is the SPS data from 2015 analysed as a cross-check of the Timepix3 timing performance presented in Section 9.2.2. The analysis of all data presented in this thesis was performed by the author.

Contents

Part I

Introduction

Chapter 1

Introduction

"New directions in science are launched by new tools much more often than by new concepts. The effect of a concept-driven revolution is to explain old things in new ways. The effect of a tool-driven revolution is to discover new things that have to be explained."

The great physicist Freeman J. Dyson (1923 – 2020) wrote these words in his book *Imagined Worlds* from 1997 [1]. At the time, the Large Electron-Positron Collider (LEP) [2] was still in operation at CERN, the European Organization for Nuclear Research, located near Geneva (Switzerland). While the experiments performed at LEP provided a successful empirical basis for the Standard Model of Particle Physics (SM), today, more than 20 years later, his words are more relevant than ever.

The SM summarises our current understanding of the fundamental particles and the interactions between them. With the discovery of the Higgs boson in 2012 by the ATLAS [3] and the CMS [4] collaborations at the Large Hadron Collider (LHC) [5], the successor of LEP at CERN, physicists celebrated a great success as the last missing piece in the collection of fundamental particles predicted by the SM was found. This result was awarded with the Noble Prize to François Englert and Peter Higgs in 2013 [6]. However, this scientific milestone does by far not imply the completion of particle physics. On the contrary, it marked the starting point for a new gold rush in the search for unknown particles and Physics Beyond the Standard Model (BSM) because the SM is known to be incomplete. Among other shortcomings, it does not include gravitation and cannot provide an explanation for the observed matter-antimatter asymmetry observed in our universe.

Numerous models are proposed as extensions of the SM and these often predict new particles heavier than the Higgs. This motivates further collider-based experiments with increasing centre-of-mass energies. And even if new particles might be too heavy for a direct production and detection, they may still be discovered through small deviations of the measurements from the SM predictions. In order to observe small anomalies, large quantities of data are needed such that the colliders are required to yield high luminosities.

The analysis of collision events relies on the reconstruction of the outgoing particles from the collisions. This requires highly specialised detector systems, which often consist of many sub-detectors to measure different observables. While calorimeters are used for a determination of particle energies, vertex and tracking detectors provide precise spatial measurements of outgoing charged particles that allow for a reconstruction of their trajectories by combining multiple measurement points into a track, and to determine their charge and momenta from the curvature of the trajectory in a magnetic field. With increasing event rates, also hit time measurements become relevant to suppress pile-up and reduce combinatorics in the reconstruction.

Today, silicon pixel detectors are often employed in vertexing and tracking applications due to their high granularity combined with a high rate capability, hit detection efficiency and radiation tolerance. While the use of hybrid pixel sensors is well established within particle physics, monolithic pixel detectors, which combine both the sensor and the readout electronics on one chip, become more attractive due to the advances of the CMOS imaging industry. Compared to hybrid technologies, they combine a cost-efficient production with a lower material budget.

The planned High-Luminosity LHC [7] and the proposed Compact Linear Collider (CLIC) [8] are two examples of future high-energy physics collider. Their experimental conditions pose challenging requirements on the performance of the detector systems to meet the foreseen physics goals. The ATLASpix is a high-voltage monolithic active pixel sensor (HV-MAPS), which was designed as a prototype to demonstrate the suitability of the technology for the ATLAS ITk Phase II Upgrade [9] and the CLIC tracking detector [10].

This thesis contains a comprehensive characterisation of the ATLASpix high-voltage monolithic active pixel sensor prototype, and an evaluation of its performance with respect to the requirements of the CLIC tracking detector.

Thesis Outline

The thesis is structured as follows:

The first part provides an introduction, which starts with an overview of the Standard Model of Particle Physics as well as a discussion of its limitations and the need for Physics Beyond the Standard Model. Possible future accelerator projects are presented with a focus on the ATLAS Upgrade for the High-Luminosity Large Hadron Collider (HL-LHC) and the Compact Linear Collider (CLIC) (Chapter 2). In Chapter 3, an introduction to the fundamentals of semiconductor physics as well as the interaction of particles with matter are discussed. In Chapter 4, the basic operation principle of silicon pixel detectors is introduced. Chapter 5 contains a detailed description of the high-voltage monolithic active pixel sensor (HV-MAPS) technology and the *ATLASpix* technology demonstrator chip, which is the main subject of investigation of this thesis.

The second part of the thesis is dedicated to the experimental methods. In Chapters 6 and 7, the experimental setups used for laboratory and test-beam measurements are presented, and in Chapter 8 the reconstruction and analysis strategy is discussed. Chapter 9 contains an evaluation of the precision of the reference telescopes used for the test-beam characterisation of the ATLASpix.

The third part represents the core part of the thesis. In Chapter 10, the basic performance parameters of the ATLASpix are derived from laboratory measurements. These comprise the current-voltage characteristics, a determination of the breakdown voltage as well as measurements of the power consumption and the noise rate. In addition, energy calibration measurements with monoenergetic X-rays are presented and the signal-to-noise rate is determined. Chapter 11 contains a detailed performance evaluation of the ATLASpix based on test-beam measurements comprising the investigation of the cluster formation, hit detection efficiency, and spatial and time resolution. The performance is compared for samples with different substrate resistivities. Finally, the active depth is determined with the help of inclined tracks and compared to the theoretical expectation for a pn-junction.

A summary is presented in Chapter 12, in which the performance of the ATLASpix is evaluated with respect to the detector requirements of the CLIC tracking detector. Limitations and possible improvements are discussed and an outlook on further developments of the HV-MAPS technology is presented.

Chapter 2

The Future of High-Energy Physics

This chapter provides an introduction, starting with an overview of the Standard Model of Particle Physics as well as a discussion of its limitations and the need for Physics Beyond the Standard Model. The Compact Linear Collider (CLIC) is presented as a possible future accelerator project.

2.1 The Standard Model of Particle Physics

The Standard Model of Particle Physics (SM) summarises our current understanding of the elementary particles and their interactions with an outstanding precision [11].

Figure 2.1 shows an overview of the 17 elementary particles of the SM. The six quarks and six leptons plus their respective anti-particles are classified as fermions. They are characterised by a spin of $1/2$ and thus obey the Pauli exclusion principle. They form three generations with increasing masses. Each generation comprises two quarks with fractional elementary charges of $+2/3$ and $-1/3$, respectively, as well as a lepton with an elementary charge of -1 and the corresponding neutrino, which is electrically neutral. For each fermion, an antiparticle exists with opposite quantum numbers.

While the particles of the first generation are stable and constitute all visible matter around us (except for the electron neutrino), the charged members of the higher generations are unstable and decay into fermions of the first generation through various channels and with different lifetimes. Neutrinos are stable and massless within the SM.[1]

The SM describes the interactions between the above particles through three forces: the electromagnetic, the weak, and the strong force. These are mediated by the gauge bosons, which carry a spin of 1. While all fermions can interact via the weak force through the exchange of a W or a Z boson, the electromagnetic interaction via a photon exchange is restricted to those fermions carrying an electrical charge. Quarks can additionally interact via the strong force by exchanging gluons.

[1] In contradiction to the SM, lepton flavour violation (LFV) has been observed in the neutrino sector. Several experiments have shown that neutrinos can oscillate between the three flavour eigenstates when propagating through space [12, 13, 14]. Extensions of the SM, such as the so-called μMSM [15] have been developed and yield consistent predictions with measurements.

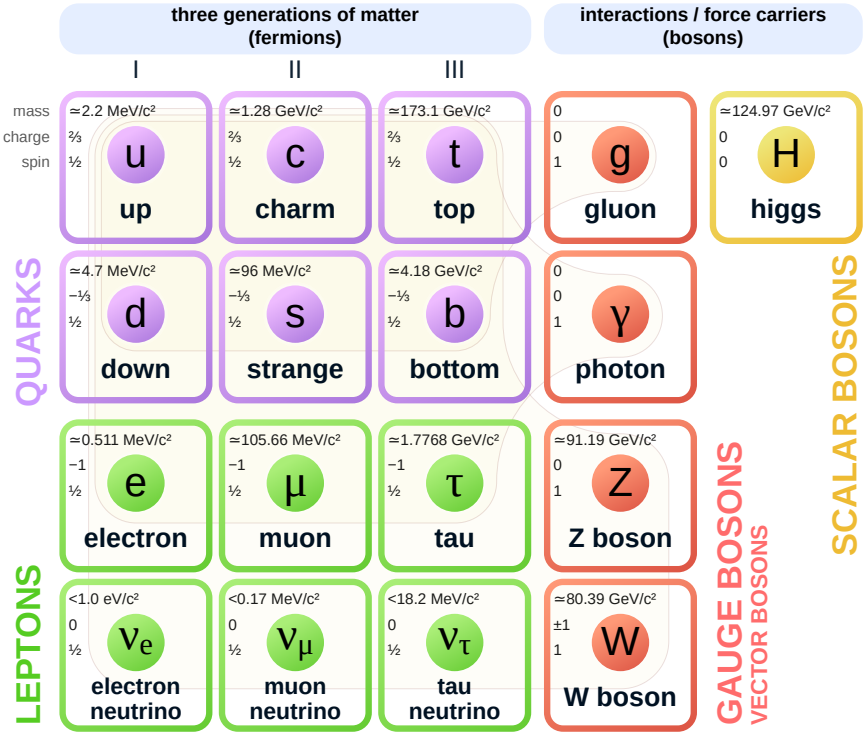

Figure 2.1: Overview of the elementary particles described by the SM of particle physics. From [16] (modified).

The Higgs boson is the only scalar particle (spin = 0) within the SM. It corresponds to the excitation of the Higgs field and provides the mechanism that gives rise to the masses of the W and the Z boson through the spontaneous symmetry breaking of the electroweak interaction.

2.2 Physics Beyond the Standard Model

The SM was developed over multiple decades along with numerous experimental tests and provides an accurate agreement with data up to a very high precision. And yet it is known to be incomplete. Several questions remain unanswered and there are strong indications for the need of new physics [11]:

- The matter-antimatter asymmetry observed in our Universe remains unexplained [17].
- The rotational behaviour of galaxies such as our Milky Way as well as the observation of gravitational lensing imply the presence of Dark Matter, which may only interact via the weak force and gravity but not through any of the other known elementary forces [18, 19].
- The accelerating expansion of our Universe suggests the presence of Dark Energy [20].
- Neutrino oscillations are observed in various experiments involving atmospheric and solar neutrinos as well as neutrinos produced in nuclear reactors

and accelerators, and require non-zero neutrino masses, which are not foreseen in the SM [12, 13, 14, 21].

- The SM provides no fundamental reason why there should be exactly three generations of elementary particle [22].
- While the SM describes three out of the four fundamental forces (the electromagnetic, the weak, and the strong force), gravity is not included [11].
- The masses of the elementary particles are not predicted by the SM. In contrast, they need to be determined experimentally. This is interpreted as an indication for a more fundamental theory [11].

Theories Beyond the Standard Model (BSM), such as supersymmetry (SUSY) or string theory, provide new theoretical approaches to address these open questions [23]. Often, they imply the existence of new (heavy) particles. However, to date none of them have lead to experimental discoveries of new physics phenomena. In the search for BSM physics, two different approaches can be followed:

- A theory can be developed to provide a prediction. This prediction can then be tested experimentally.
- Anomalies, i.e. small deviations, between the SM predictions and data can be searched. If a significant deviation is found, this is a clear indication for new physics, which motivates the development of new theories.

2.3 Experimental Tests of the Standard Model

In order to test the Standard Model experimentally to the highest precision, two approaches are used:

- A **direct search** for new heavy particles can be attempted. This requires the rest mass of a new particle to be smaller than the centre-of-mass energy of a collision, so that it can be produced and detected via its decay products. Current examples are new particle searches by the ATLAS [24] and CMS [25] experiments located at the LHC at CERN. These experiments also measure the properties of the SM. In order to probe higher energies, the collision energy needs to be increased.
- New particles may also be found in **indirect searches** by small deviations of the measurements from SM predictions. They explore extremely rare interactions of possible new particles with conventional matter. For a maximal sensitivity, extremely large interaction volumes and/or high-precision measurements of the observables are required. An example is the Mu3e experiment [26] searching for the lepton flavour violating decay $\mu^+ \to e^+e^-e^+$. It also employs the HV-MAPS technology for its tracking detector.

Experiments at the high-energy frontier typically make use of particle accelerators. Today, the Large Hadron Collider (LHC) is the world's largest and most powerful particle accelerator [5]. In operation since 2008, it has provided a wealth of data, which is analysed in search for deviations from the predictions of the standard model. In order to exploit the full potential of the machine, the next major upgrade to the High-Luminosity Large Hadron Collider (HL-LHC) is foreseen for 2024-2027, providing collisions until 2038 [7].

Beyond 2038, the future of accelerator-based high-energy physics is not yet decided at the time of writing. Several projects are proposed [27].

2.4 The Compact Linear Collider

The Compact Linear Collider (CLIC) is a proposed high-energy high-luminosity electron-positron collider [8]. As illustrated in Figure 2.2, it is proposed to be built at CERN in three consecutive stages with centre-of-mass energies between 380 GeV and 3 TeV, and start operation after the end of the lifetime of the HL-LHC around the year 2038.

2.4.1 Physics Case

As an electron-positron collider, CLIC is suitable for high-precision measurements because of the well-defined initial states of the colliding particles and low levels of background arising from quantum chromodynamics (QCD) processes compared to hadron colliders. On the other hand, at CLIC a background of photons arises from so-called beamstrahlung, i.e. synchrotron radiation emitted by the particles of one beam through the interaction with the electromagnetic field of the opposite beam [29]. This leads to a production of e^+e^- pairs and hadrons in $\gamma\gamma \to e^+e^-$ and

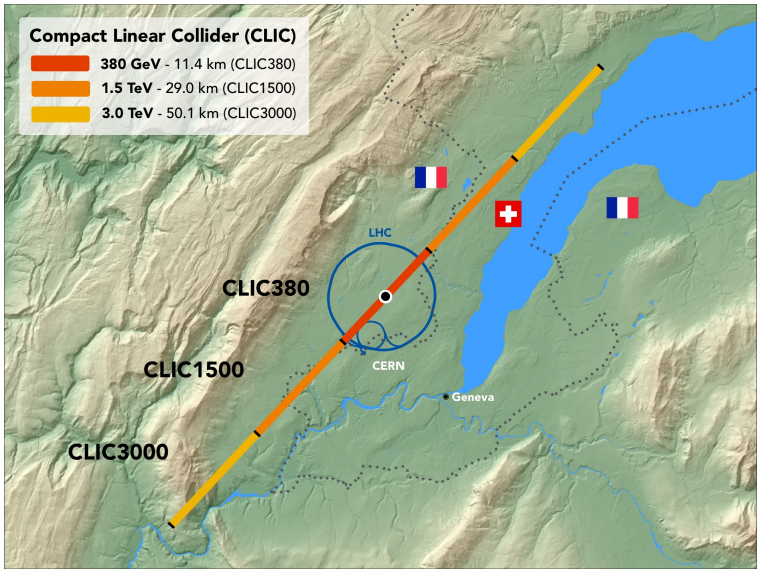

Figure 2.2: Illustration of the location and size of the CLIC accelerator complex at CERN for the three proposed energy stages. From [28].

$\gamma\gamma \rightarrow$ hadron events [30]. CLIC is proposed to be built in three energy stages with a unique physics potential in each stage [31]:

- In the first energy stage with a centre-of-mass energy of up to 380 GeV, precise Higgs boson measurements can be performed through the Higgs-strahlung and WW-fusion processes, which provide accurate and model-independent measurements of the Higgs couplings to fermions and bosons [32]. In addition, a threshold scan of the top pair production around 350 GeV is foreseen offering an accurate and well-defined measurement of the top quark mass. Until today, the top quark was only accessible in hadron collisions [33].
- The second stage at an energy of 1.5 TeV would enable to probe for new physics phenomena, but offers also additional top quark and Higgs measurements with an unprecedented precision, such as the top-Yukawa coupling, the Higgs self-coupling as well as rare Higgs branching ratios.
- The third stage with an energy of 3 TeV aims to provide a unique sensitivity for a large variety of new physics scenarios allowing the pair production of new particles with masses up to 1.5 GeV, in particular new electroweak particles or dark matter candidates. In addition, CLIC is sensitive to the Higgs self-coupling and rare Higgs decays at this energy.

2.4.2 Accelerator Design

A schematic illustration of the CLIC accelerator complex at an energy stage of 3 TeV is shown in Figure 2.3. It employs an innovative two-beam acceleration scheme [34] allowing for an operation of the accelerating structures at room temperature with accelerating gradients around 100 MV/m. So-called drive beams with a low energy and a high current are used to transfer their energy to the low-current high-energy main beams, which are brought to collision in the central detector.

To reach its design luminosity of $5.9 \times 10^{34}\,\mathrm{cm}^{-2}\mathrm{s}^{-1}$, very small bunch sizes of $40 \times 1\,\mathrm{nm}^2$ in the transversal plane and 44 µm along the beam axis are foreseen. Collisions would occur every 0.5 ns for a bunch train duration of 156 ns with a train repetition rate of 50 Hz. This results in a very low duty cycle of less than 0.001 % [28].

2.4.3 Detector Concept & Requirements

In order to exploit the full physics potential of CLIC, a detector design (called *CLICdet*) has been developed and optimised through simulations and extensive technology R&D [10, 36]. A three-dimensional schematic illustration in shown in Figures 2.4 and 2.5.

The detector requirements are derived from the physics objectives and the beam properties of the accelerator. The extremely low duty cycle of below 0.001 % allows for a triggerless readout of all detector systems in the 20 ms gaps between bunch

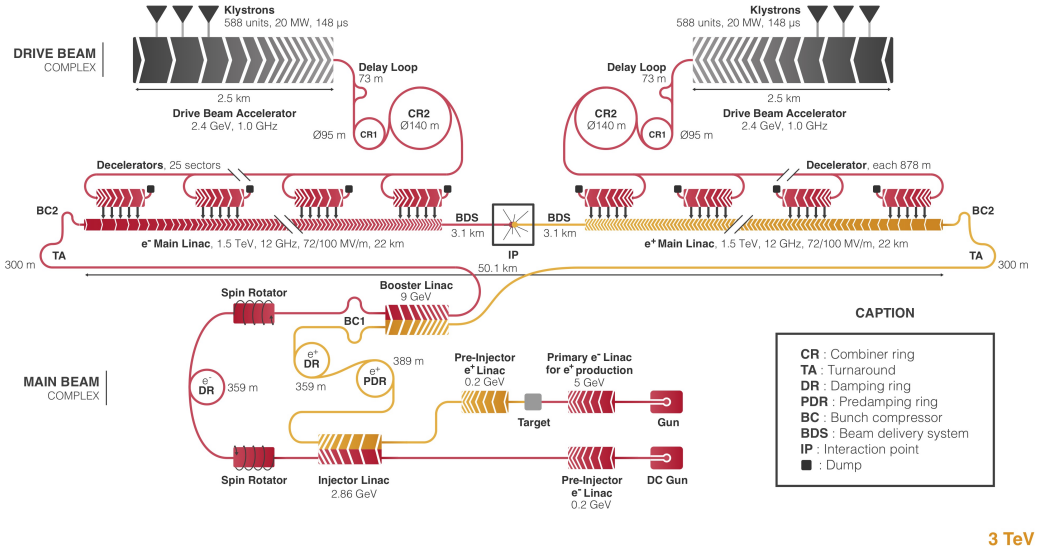

Figure 2.3: Illustration of the CLIC accelerator complex at the 3 TeV energy stage. From [35].

trains.[2] In addition, *power pulsing*, i.e. a periodic switching between normal operation (within the bunch train) and a low-power mode of sub-detector systems (between bunch trains), can be applied for a reduction of the average heat dissipation.

CLICdet is optimised for a reconstruction based on Particle Flow Analysis (PFA) [37]. PFA allows for the distinction of individual particles within jets by combining the measurements from the tracking system with the energy measurements of the calorimeters. The inner detector region consists of an all-silicon vertex and tracking detector combining a central barrel and two endcaps surrounding the beam pipe. A high-granularity silicon-tungsten electromagnetic calorimeter (ECAL) and a scintillator-steel hadronic sampling calorimeter (HCAL) are located around the tracking detector. A superconducting solenoid magnet provides a magnetic field of 4 T. Outside of the magnet, an iron return yoke is interleaved with muon identification detectors based on resistive plate chambers (RPCs). Additional electromagnetic sampling calorimeters, called LumiCal and BeamCal, are located close to the beam pipe in forward direction to provide luminosity measurements and to allow for electron tagging.

CLIC Tracking Detector

The requirements for the CLIC tracking detector with a total silicon area of around 137 m^2 are listed in Table 2.1. In order to achieve the required resolution on the transversal momentum of $\sigma_{p_T}/p_T^2 \leq 2 \times 10^{-5}\,\text{GeV}^{-1}$ in a 4 T magnetic field, the

[2] In this context, "triggerless" refers to the fact that no online event selection is needed. The readout of the detector systems is triggered with respect to the beam structure.

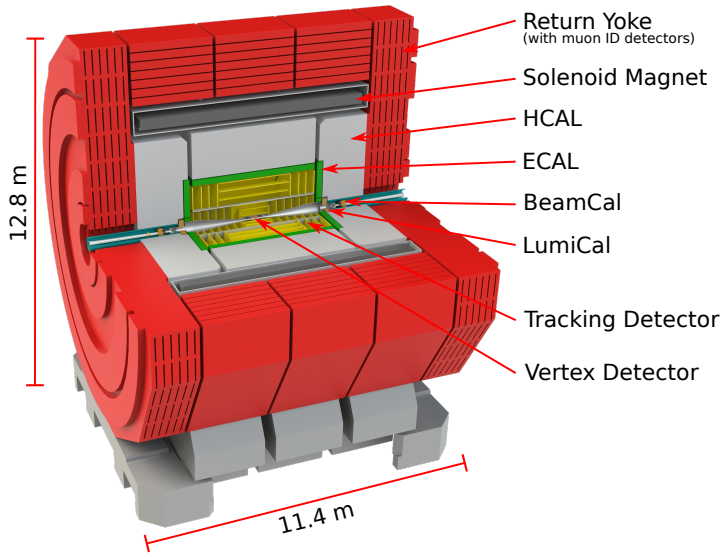

Figure 2.4: 3D illustration of the CLIC detector design. From [10] (modified).

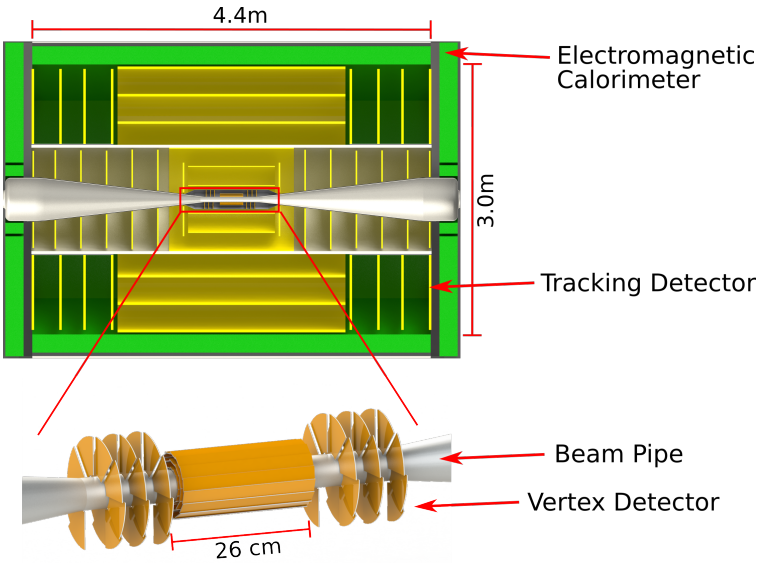

Figure 2.5: Schematic view of the inner detector region of the CLIC detector including the CLIC Tracker (yellow) and Vertex Detector (orange). From [10] (modified).

single-point resolution of the tracker has to be smaller than 7 µm. Assuming a binary detector resolution, this would correspond to a pixel pitch around 25 µm. In the longitudinal direction, the granularity is limited to 1-10 mm by the detector occupancy. To mitigate the impact of beam-induced background from beamstrahlung, a precise hit-time tagging with a resolution of $\sim$ 5 ns is required. The hit detection efficiency should exceed 99.7 % and the material budget is limited to $1-2$ % of a radiation length X_0 per layer to achieve the required transverse momentum resolution. A water-based cooling system is foreseen, which allows for an average power dissipation of $\sim$ 150 mW/cm^2. On the other hand, less stringent requirements are posed on the radiation tolerance due to the smaller QCD background compared to hadron colliders.

The vertex detector (see Figure 2.5) is located in the central detector region and surrounded by the tracker. Its requirements are much more stringent compared to the tracking detector. Further details can be found in [10].

Table 2.1: Summary of the requirements for CLIC Tracking Detector [10].

Parameter	**Value/Requirement**
Silicon area	$137\,\mathrm{m}^2$
Spatial resolution (transversal)	$7\,\mu\mathrm{m}$ if binary resolution: pitch = $25\,\mu\mathrm{m}$
Granularity (longitudinal)	$\leq$1-10 mm
Hit time resolution	$\sim 5\,\mathrm{ns}$
Hit detection efficiency	$99.7 - 99.9\,\%$
Material budget per layer	$1 - 2\,\%\mathrm{X}_0$
Power Consumption	$< 150\,\mathrm{mW/cm}^2$
NIEL	$<1 \times 10^{11}\,\mathrm{n_{eq}/cm^2/year}$
TID	$<300\,\mathrm{Gy/year}$

Chapter 3

Fundamentals of Particle Detection

Pixel detectors are solid state particle detectors, which are widely used in particle physics and beyond. Prominent examples from high-energy physics comprise the large experiments at the LHC: ATLAS [24], CMS [25], ALICE [38], and LHCb [39]. In addition, pixel detectors are developed for and employed in smaller-scale experiments like Mu3e [40] as well as in medical imaging applications like the Heidelberg Ion Beam Therapy Centre (HIT) [41].

The design of a pixel sensor is highly specific to its intended application. In particular in high-energy physics, it is common to choose the most suitable technology in each detector subsystem, as these underlie different constraints.

Pixel sensors make use of the properties and characteristics of semiconductors. To interpret the behaviour of a pixel sensor in laboratory and test-beam measurements, it is important to have an understanding of the fundamental principles of the underlying physics. More detailed introductions into the topic can be found in [11], [42] and [43].

3.1 Interaction of Particles with Matter

Within the scope of this thesis both, X-rays and charged particles were used for the signal generation in the ATLASpix. To understand the behaviour of the device, it is important to realise that photons and charged particles interact in different ways with matter and thus with the detector material.

3.1.1 Photons

Photons interact with matter in three different ways: the photoelectric effect, Compton scattering and pair production. Depending on their energy and the charge number Z of the absorber material, each of these effects occurs with a different probability as shown in Figure 3.1:

- **Photoelectric effect:** The photon transfers its total energy onto an atom, which emits an electron from a shell. This results in a vacancy, which is filled with a higher-shell electron. The difference in binding energy is released in the form of an additionally emitted lower-energy photon. An initial photon energy larger than the binding energy of the electron is required.

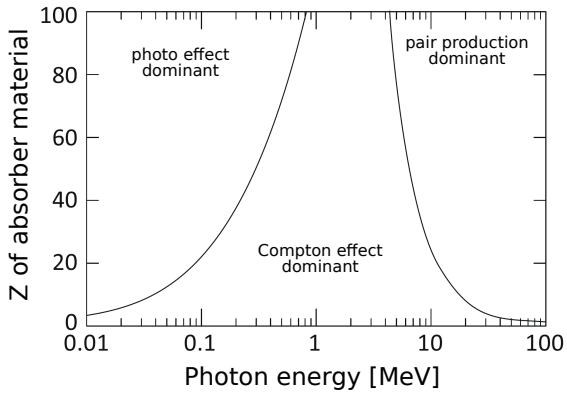

Figure 3.1: Dominant photon interaction processes in dependence of the photon energy and charge number of the absorber material. From [43] (modified).

- **Compton scattering:** The photon scatters elastically on a shell electron. It looses a fraction of its energy, which depends on the scattering angle ϕ. The energy of the scattered photon E'_γ after the interaction is given by [44]

$$E'_\gamma(\phi) = \frac{E_\gamma}{1 + \frac{E_\gamma}{m_e c^2}(1 - \cos(\phi))}. \tag{3.1}$$

  Hereby, E_γ denotes the initial photon energy, m_e is the electron mass, and c the speed of light in vacuum.

- **Pair production:** A photon is converted into an electron-positron pair in the electric field of a nucleus. The total energy of the photon is transferred into the rest mass and kinetic energy of the final state particles. Accordingly, a minimun energy of $E_{\gamma,\,\mathrm{min}} = 2m_e c^2 \sim 1.022\,\mathrm{MeV}$ is required. For the X-ray energy ranges used within the scope of this thesis, pair production does not play a role.

3.1.2 Charged Particles

The energy loss of charged particles mainly occurs through ionisation. In gaseous media this corresponds to the creation of free electrons and charged ions. In semiconductors it refers to the creation of electron-hole pairs. The mean energy loss along an infinitesimal distance of the trajectory is given by the Bethe-Bloch equation [45]:

$$-\left\langle \frac{\mathrm{d}E}{\mathrm{d}x} \right\rangle = 4\pi N_A r_e^2 m_e^2 z^2 \frac{Z}{A}\frac{1}{\beta}\left[\frac{2m_e c^2 \beta^2 \gamma^2 T_{max}}{I^2} - \beta^2 \; - \frac{\delta(\beta\gamma)}{2}\right] \tag{3.2}$$

where E is the energy of the particle, N_A the Avogadro constant, r_e the electron radius, m_e the electron mass, z the charge of the traversing particle, $\beta\gamma$ the velocity of the particle, and c the speed of light in vacuum. Z/A is the ratio of protons over the number of nucleons of the traversed matter, and I its mean excitation energy. T_{max} describes the maximal energy transfer in a single collision and $\delta(\beta\gamma)$ represents a

relativistic correction. Particles around the global minimum of $\beta\gamma \sim 3$ are called *minimum ionising particles (MIPs)*.

Energy Loss Spectrum

The Bethe-Bloch equation describes the average energy loss. However, ionisation is subject to large statistical fluctuations, which can be described by a probability density function called *straggling function* [46]. It is characterised by a most probable energy loss Δ_p, which is significantly smaller than the average energy loss, and the full-width-at-half-maximum w. Figure 3.2 depicts the straggling function for 500 MeV pions in silicon. If a particle is not stopped within the material, its energy deposition varies around the peak of the distribution and shows a large tail to high energy losses.

Delta electrons, also called delta-rays or δ-rays, are created in a central collision of an incident particle with a shell electron in the traversed medium. They are characterised by a kinetic energy sufficiently large to cause secondary ionisation and contribute to the tail of the energy loss spectrum. They can traverse a significant distance within the detector material and thus lead to outliers both in the measured energy spectrum as well as the spatial position measurement of the incident particle.

The energy loss spectrum can be approximated by a Landau-Vavilov distribution [47, 48], which has a Gaussian core and a long tail towards large energy depositions accounting for delta electrons.

For thin detector layers, the phenomenological parametrisation provided by Bichsel [49] results in a better agreement with data. Between a silicon thickness t of 13 µm and 110 µm, the most probable value (MPV) of the energy deposition for charged

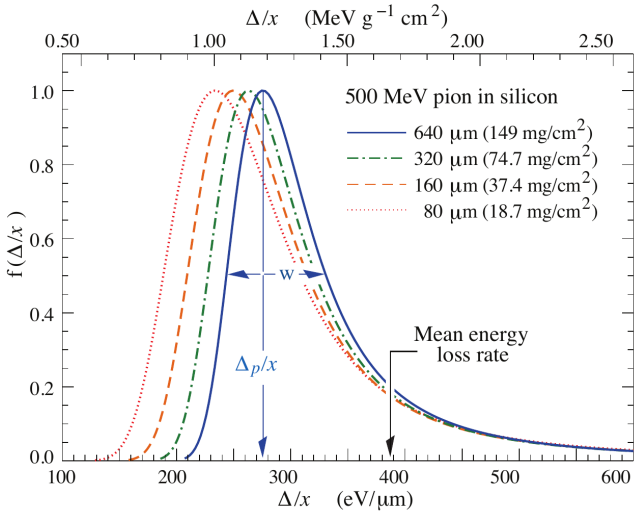

Figure 3.2: Straggling function for 500 MeV pions in silicon, normalised to 1 at the most probable energy loss Δ_p/x. From [46].

particles with $\beta\gamma > 500$ is given by the empirical formula [49]

$$\Delta_p[\mathrm{eV}] = t \cdot \left[100.6 + 35.35 \cdot \ln\left(\frac{t}{1\,\mu\mathrm{m}}\right)\right] \cdot \frac{\mathrm{eV}}{\mu\mathrm{m}} \tag{3.3}$$

with an uncertainty of about 1 %.

Bremsstrahlung & Radiation Length

Highly-relativistic charged particles can also loose part of their energy by the emission of photons. This effect is called *bremsstrahlung* and occurs with a probability

$$P_{\mathrm{brems}} \sim Z^2 \frac{E}{m^2}, \tag{3.4}$$

depending on the particle energy E, its mass m and the charge number Z of the absorber medium.

It predominantly occurs for electrons and positrons due to their low mass compared to all other charged particles, and leads to an exponential decrease of the particle energy according to

$$-\frac{\mathrm{d}E}{\mathrm{d}x} = \frac{E}{X_0}. \tag{3.5}$$

The radiation length X_0 is a characteristic property of the absorber material, which is defined as the average length over which a high-energy electron looses $1/e$ of its energy due to bremsstrahlung. It also quantifies 7/9 of the mean free path of a high-energy photon before it undergoes e^+e^- pair production and can be approximated by the empirical formula [50]

$$X_0 = 716.4\,\mathrm{g/cm^2} \frac{A}{Z(Z+1)\ln\left(\frac{287}{\sqrt{Z}}\right)}. \tag{3.6}$$

For a mixture or compound of different materials the radiation length can be calculated as [50]

$$\frac{1}{X_0} = \sum_i \frac{w_i}{X_i}, \tag{3.7}$$

where w_i and X_i are the mass fraction and the radiation length of the i-th element.

3.1.3 Multiple Coulomb Scattering

When a charge particle traverses a medium, it looses energy due to electromagnetic interactions with the nuclei within the material. Hereby, it is deflected in a large number of small-angle scatters as illustrated in Figure 3.3. This results in a net scattering angle and offset. For thin scatterers, the offset is negligible. The *root mean square (RMS)* of the central 98 % of the scattering distribution is described by the

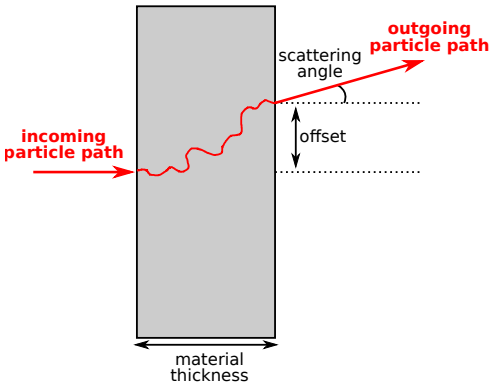

Figure 3.3: Illustration of a particle traversing material and undergoing multiple Coulomb scattering resulting in a change of direction as well as an offset.

Highland formula [46]:

$$\theta_0 = \frac{13.6\,\text{MeV}}{\beta c_0 p} z \sqrt{\frac{x}{X_0}} \left[1 + 0.0038 \ln\left(\frac{xz^2}{X_0 \beta^2}\right)\right] \tag{3.8}$$

where p, βc and z are the momentum, velocity and charge number of the incident particle, x is the thickness of the traversed layer, and X_0 the radiation length of the material.

3.2 Semiconductor Physics

The properties of a semiconductor are dictated by quantum mechanics, which governs the movement of charge carriers in a crystal lattice. The periodic structure of crystalline materials leads to the formation of well-defined energy bands within the solid. The electrons within the solid are confined to one of the energy bands, which are separated by the *band gap* of forbidden energies. Electrons in the *valence band* are bound to specific sites within the lattice. In contrast, electrons in the *conduction band* can move freely within the solid and thus contribute to the electrical conductivity of the solid. Depending on the size of the band gap energy E_g, materials are classified as insulators, semiconductors or conductors as illustrated in Figure 3.4.

The Fermi level E_F describes the energy up to which all energy states are filled with electrons at zero temperature. For non-zero temperatures T, this step function is smeared due to thermal excitations, which allow higher energy states E to be occupied with a probability $P(E)$ according to the Fermi-Dirac statistics [42]

$$P(E) = \frac{1}{\exp\left(\frac{E-E_F}{k_B T}\right) + 1}, \tag{3.9}$$

where k_B denotes the Boltzmann constant.

In conductors, the Fermi level lies within the conduction band such that electrons can move freely at any temperature resulting in a high electrical conductivity of the material.

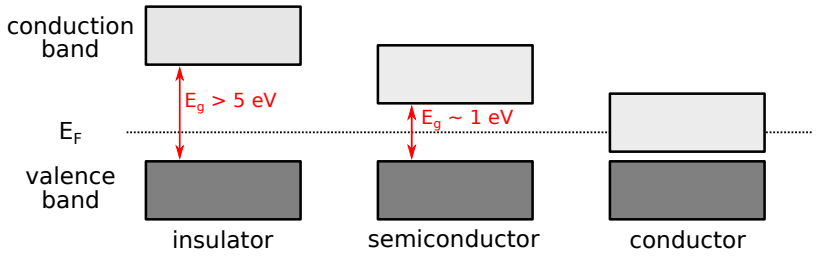

Figure 3.4: Illustration of the band gap structures comparing insulators, semiconductors and conductors. E_F is the Fermi level and E_g the band gap.

For insulators and semiconductors, the valence band is filled completely and the conduction band remains empty at zero temperature, such that they remain non-conductive. Only in the presence of thermal excitations, individual electrons can be lifted into the band gap. A semiconductor is distinguished from an insulator by a small band gap ($\sim$1 eV for semiconductors as compared to $>$5 eV for insulators). If an electron is lifted from the valence band into the conduction band, it leaves a vacancy (hole) in the valence band. Through the collective motion of the surrounding electrons in the valence band, the hole can be treated effectively as a positive charge carrier, which can move and contribute to the conductivity of the solid.

The band gap of silicon is 1.12 eV. However, a higher energy of $\sim$3.65 eV is needed for the creation of an electron-hole pair [42]. The energy difference arises from the fact that silicon is an indirect semiconductor, in which additional energy is needed for the excitation of a phonon, i.e. a lattice excitation of the silicon to allow for the transition of the electron into the conduction band.

Silicon is the most common material for pixel detectors because it allows for an operation at room temperature and benefits from the advanced manufacturing technologies of the semiconductor industry. Furthermore, the related readout electronics is based on silicon technologies. Other typical detector materials are germanium (Ge), gallium arsenide (GaAs), and cadmium telluride (CaTd). GaAs and CaTd have high atomic numbers, which makes them suitable for the detection of X-rays due to their high absorption coefficient (see also Section 3.1). Ge has a band gap of 0.7 eV and a high charge-carrier mobility, which leads to a higher achievable energy resolution of a detector compared to silicon because more electron-hole pairs are created for a given energy deposition. For the same reason, Ge detectors need to be cooled for operation as more electron-hole pairs are created from thermal excitations leading to higher noise rates.

3.2.1 Doping

Doping of a semiconductor describes the controlled introduction of impurities into the crystal structure. In this way, the conductivity can be manipulated by creating an excess of electrons or holes, which are called *majority charge carriers* and lead to the electrical conductivity.

An *n-type* semiconductor is created by replacing an atom in the lattice by an atom with more valence electrons than the material itself. This so-called *donor* releases an additional electron into the conduction band. Conversely, a *p-type* semiconductor is obtained by the use of an atom with less valence electrons than the base material. This so-called *acceptor* captures one of the valence electrons from the lattice, by which a hole is created.

In case of silicon, which has four valence electrons, typical dopants are boron (a group 3 element) for p-type doping and phosphorous (a group 5 element) for n-type doping.

3.2.2 pn-junctions

A pn-junction, as illustrated in Figure 3.5, is created when n-type and p-type semiconductors are brought into contact. As a consequence, the majority charge carriers from either side diffuse across the junction. There they recombine and a depletion region, also called space charge region, is formed, in which no free charge carriers exist. Within the depletion region, an electric field is built up, which is directed opposite to the diffusion, until an equilibrium is reached. This results in the so-called *built-in voltage* [42]

$$V_{bi} = \frac{k_B T}{e} \ln\left(\frac{N_a N_d}{n_i^2}\right), \tag{3.10}$$

where N_a and N_d are the respective concentrations of acceptors and donors, and $n_i \approx 1.45 \times 10^{10}\,\mathrm{cm}^{-3}$ the intrinsic charge carrier density at 300 K in silicon. Further, k_B is the Boltzmann constant, T the temperature, and e the elementary charge.

In equilibrium, the width of the depletion region W is given by [42]

$$W = \sqrt{\frac{2\epsilon_0\epsilon}{e}\left(\frac{1}{N_a} + \frac{1}{N_d}\right) \cdot V_{bi}}. \tag{3.11}$$

External Bias Voltage

When an external voltage V_{ext} is applied, the width of the depletion region changes depending on the polarity of the applied voltage according to [52]

$$W(V_{\mathrm{ext}}) = \sqrt{\frac{2\epsilon_0\epsilon}{e}\left(\frac{1}{N_a} + \frac{1}{N_d}\right) \cdot (V_{bi} - V_{\mathrm{ext}})}, \tag{3.12}$$

whereby ϵ_0 represents the vacuum permittivity and ϵ the dielectric constant of the semiconductor ($\epsilon = 11.9$ for silicon) [43]. For the case that $V_{bi} \ll |V_{\mathrm{ext}}|$ and a highly asymmetric doping, i.e. $N_a \ll N_d$ or $N_d \ll N_a$, the depletion region mostly extends into the weakly doped side and Equation 3.12 can be simplified to [52]

$$W(V_{\mathrm{ext}}) \approx \sqrt{\frac{2\epsilon_0\epsilon}{e}\frac{1}{N_{\mathrm{sub}}} \cdot |V_{\mathrm{ext}}|}, \tag{3.13}$$

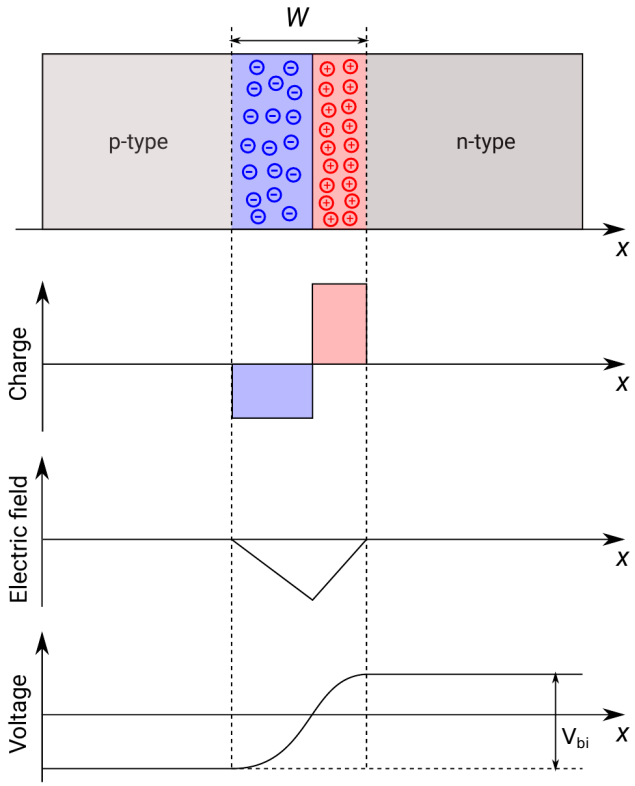

Figure 3.5: Schematic drawing of the build-up of the depletion region at the pn-junction and the resulting electric field and potential difference. The asymmetric extent of the depletion region into the p-type and n-type regions reflects different doping concentrations $N_d > N_a$. From [51] (modified).

where N_{sub} is the doping concentration of the weakly doped side, usually the substrate. The doping concentration is related to the resistivity ρ via [42]:

$$\rho = \frac{1}{e\mu N_{\text{sub}}}, \tag{3.14}$$

with μ denoting the majority charge carrier mobility. In intrinsic silicon, the electron and hole mobilities at room temperature are $\mu_e \sim 1450\,\text{cm}^2/(\text{Vs})$ and $\mu_h \sim 500\,\text{cm}^2/(\text{Vs})$, respectively [43]. The charge carrier mobility decreases with larger doping concentrations [53].

This allows to express Equation 3.13 as

$$W(V_{\text{ext}}) \approx \sqrt{2\epsilon_0\epsilon\mu\rho \cdot |V_{\text{ext}}|}. \tag{3.15}$$

Electrical Properties

The maximum electric field in the located at the junction and is given by [43]

$$E_{\text{max}} = \sqrt{\frac{2}{\epsilon_0\epsilon\mu\rho} \cdot |V_{\text{ext}}|} \tag{3.16}$$

and the capacitance of the pn-junction can be approximated by a parallel plate capacitor [52]:

$$C(V_{\text{ext}}) = \frac{\epsilon_0 \epsilon}{W(V_{\text{ext}})} \cdot A \approx \sqrt{\frac{\epsilon_0 \epsilon}{2\mu\rho V_{\text{ext}}}} \cdot A, \tag{3.17}$$

where A describes the area of the pn-junction.

In forward bias, $V_{\text{ext}} > 0$, the width of the depletion region is reduced as shown in Figure 3.6a. The pn-junction is conductive in this direction. In reverse bias, $V_{\text{ext}} < 0$, the width of the depletion region grows as shown in Figure 3.6b. In this direction, the pn-junction has a large resistance and is non-conductive apart from a small leakage current.

The current-voltage characteristics is described by the Shockley equation [54]:

$$I_{\text{diode}} \approx I_S \cdot \left(e^{\frac{eV_{\text{ext}}}{k_B T}} - 1 \right), \tag{3.18}$$

where I_S is the reverse bias saturation current. It is illustrated in Figure 3.7.

The reverse bias saturation current I_S has two contributions. Firstly, minority charge carriers can diffuse from the neutral regions into the depletion zone. In addition, electron-hole pairs can be created through thermal excitations within the depletion region, where they are separated due to the presence of the electric field. Accordingly, their contribution is proportional to the volume of the depletion region and shows a temperature dependence given by [52]

$$I_{vol} \propto T^2 \cdot e^{-E_g/(2k_B T)} \tag{3.19}$$

where E_g is the direct band gap, which is 3.65 eV for silicon at a temperature of 300 K [55]. The volume contribution to the leakage current doubles approximately every 8 K [52].

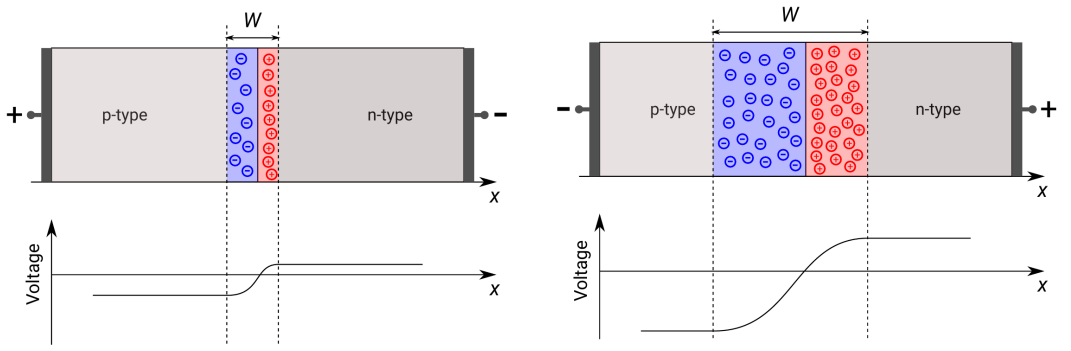

(a) In forward bias, the diode is conductive and the width of the depletion region decreases.

(b) In reverse bias, the diode is non-conductive apart from a small leakage current. The depletion region grows.

Figure 3.6: Illustration of the changing width of the depletion region and the potential difference across the pn-junction for different polarities of the applied external voltage. From [51].

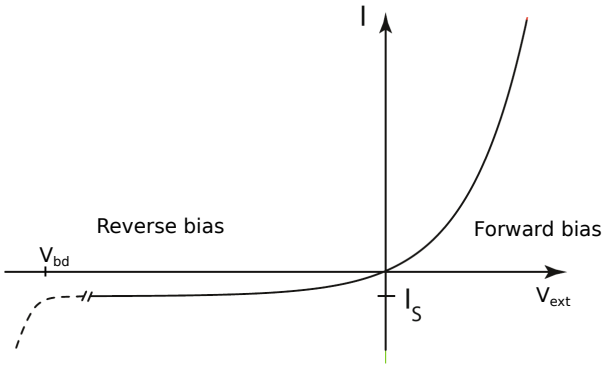

Figure 3.7: Current-voltage characteristics of an ideal diode as described by Equation 3.18. The dotted line represents the breakdown occurring at reverse bias voltage higher than the breakdown voltage V_{bd}. It is not described by the Shockley equation. From [43] (modified).

At reverse bias voltages higher than the breakdown voltage $|V_{bd}|$, a breakdown occurs. It is characterised by a large current and can be caused by two independent mechanisms: The Zener effect occurs when electrons tunnel from the valence band into the conduction band. An avalanche breakdown occurs if the electric field in the pn-junction is large enough such that electrons are accelerated sufficiently to create new electron-hole pairs by secondary ionisation.

A breakdown can lead to a thermal run-away: In a self-accelerating way, a large current heats up the diode such that more electron-hole pairs are generated, which increase the current even further. If the current is not limited externally, this can lead to non-reversible damage to the diode structure through overheating.

3.2.3 MOSFETs

Metal oxide semiconductor field-effect transistors (MOSFETs) are the fundamental building blocks of modern electronics. Like pn-junctions (see Section 3.2.2) they are created by a combination of n-type and p-type doping. As shown in Figure 3.8, two complementary types exists, which are called n-channel MOSFET (NMOS) and p-channel (PMOS) MOSFET. Complementary MOS (CMOS) technology makes use of a combination of both types on a common substrate [43].

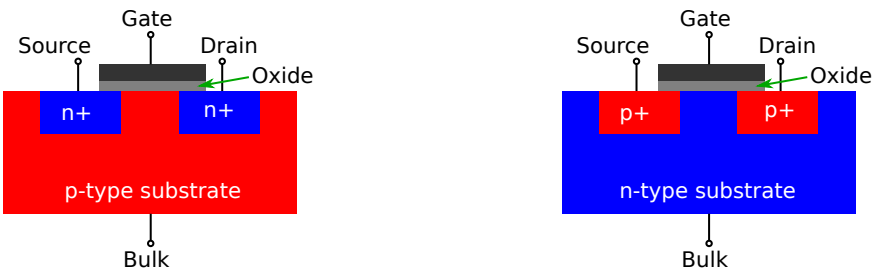

(a) n-channel MOSFET. **(b)** p-channel MOSFET.

Figure 3.8: Schematic drawing of n-channel and p-channel MOSFETs. $p+$ and $n+$ indicate high doping levels.

An NMOS (PMOS) transistor is created by implementing two strongly doped $n+$ ($p+$) regions called *source* and *drain* in a lightly doped *substrate*. Between source and drain, a *gate* electrode is placed on the surface, separated from the silicon by a thin isolating layer, typically made of SiO_2. Source and drain form pn-junctions with the substrate. The gate and the substrate act as a parallel plate capacitor. The operating principle is based on a change of the charge carrier concentration underneath the gate: If a positive (negative) voltage is applied to the gate, negative (positive) charge is accumulated in the substrate below the insulator by repulsing holes (attracting electrons). If the applied voltage is large enough, this leads to the formation of an inversion layer (also called channel) between source and drain, by which the current between source and drain I_D can be controlled. As illustrated in Figure 3.9, three modes of operation are distinguished [42]:

- **Cut-off mode:** The transistor is switched off when the voltage between gate and source V_{GS} is smaller than the intrinsic threshold voltage V_{TH} of the device. While the $I_D = 0$ in an ideal model, a small leakage current occurs in a real device.
- **Ohmic mode (linear region):** The transistor is turned on when $V_{GS} > V_{TH}$ and the voltage between drain and source V_{DS} remains below $V_{GS} - V_{TH}$. A current can flow through the channel (also called inversion layer) between drain and source. I_D can be controlled by varying V_{GS}.
- **Saturation mode:** For $V_{GS} > V_{TH}$ and $V_{DS} > V_{GS} - V_{TH}$, the channel does not fully extend to the drain ("pinch-off"). Nonetheless, a current can flow due to the large electric field between drain and source and I_D depends only weakly on V_{GS}.

The resulting current-voltage characteristic of a MOSFET is shown in Figure 3.10.

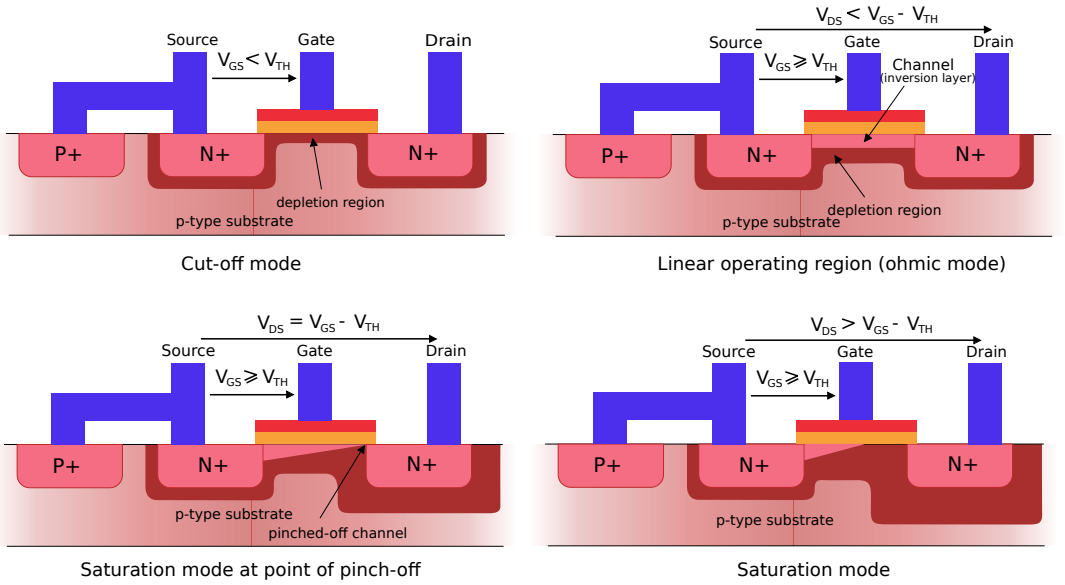

Figure 3.9: Schematic drawing of the different operating modes of an NMOS transistor. From [56] (modified).

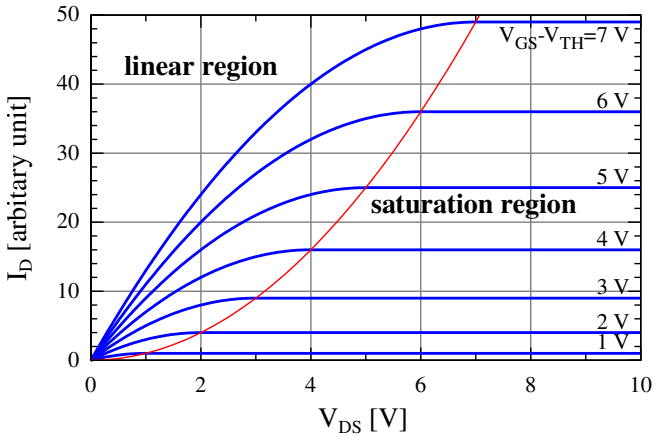

Figure 3.10: Current-voltage characterisitics of a MOSFET. The boundary between the linear and the saturation region is indicated by the red line. From [57] (modified).

Chapter 4

Silicon Pixel Detectors

Silicon pixel detectors, are based on a 2-dimensional array of pn-junctions operated in reverse bias. When a charged particle traverses through the silicon, electron-hole pairs are created along the trajectory of the particle due to ionisation as illustrated in Figure 4.1.

4.1 Signal Formation

Depending on the operating conditions, not necessarily the entire silicon is depleted. The electron-hole pairs created outside of the depleted volume of the diode diffuse in a random direction because no electric field is present. They may either recombine after a certain time or diffuse into the depletion region. Inside the depletion zone, the electron-hole pairs are separated by the electric field and drift towards the electrodes of the diode, the so-called collection electrodes. According to the *Shockley Ramo theorem* [58, 59], these drifting charges induce a signal on the collection electrodes.

As illustrated in Figure 4.2, the induced signal is typically fed into an amplifier to make the signals large enough to be processed further. The amplified signal is then fed into a comparator. If the signal is larger than a (user-configurable) threshold of the comparator, the traversing particle is detected as a hit. In many modern silicon pixel detectors, not only the 2-dimensional pixel address (column and row number

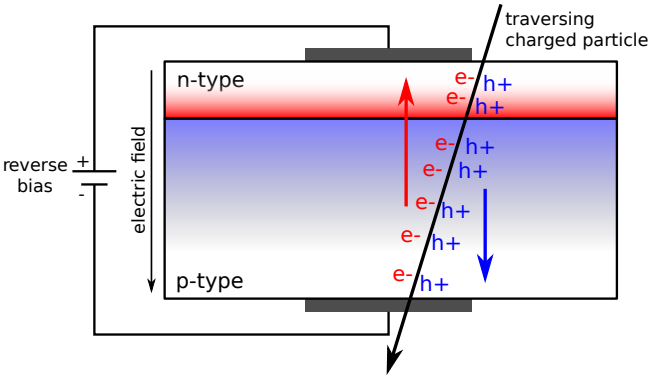

Figure 4.1: Schematic drawing of a pn-junction with a reverse bias voltage. The depleted region is indicated by the coloured gradient. A traversing ionising particle creates electron-hole pairs, which are separated in the electric field and drift towards the electrodes.

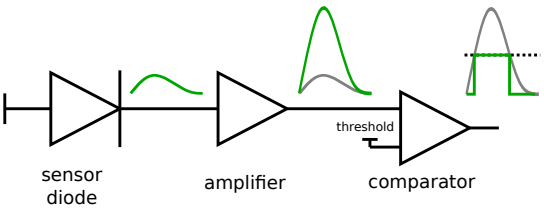

Figure 4.2: Illustration of the signal amplification and discrimination by the pixel front-end electronics.

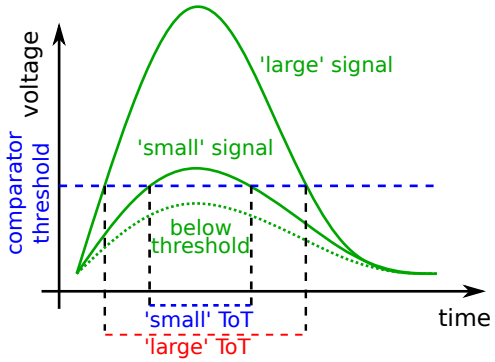

Figure 4.3: Illustration of the detection threshold and the time-over-threshold (ToT) measurement for different pulse heights.

of the hit) are recorded, but in addition a hit timestamp or time-of-arrival (ToA) and the amount of charge (i.e. the size of the signal) are detected. The concept of a charge measurement as the time-over-threshold (ToT) is illustrated in Figure 4.3.

The ToT value can be translated into deposited charge by means of a charge calibration, whereby a large ToT value corresponds to a large induced signal in the pixel and a small ToT value to a small signal. Therefore, the ToT spectrum can be related to the spectrum of the energy deposited by the ionising particles passing through the sensor.

The readout electronics of the pixel detector contains logic to generate a digital data stream, which is read out by the data acquisition system and stored for offline analysis.

4.1.1 Charge Sharing

Depending on the sensor and the integration time of the front-end, charge diffusing into the depleted region can contribute significantly to the total amount of collected charge. In addition, charge created by one traversing ionising particle may be collected in two or more adjacent pixels. This effect is called *charge sharing*. It can occur by lateral diffusion of the charge carriers within the sensor plane, when a particle penetrates the sensor under an angle, or when the sensor is located in a magnetic field as discussed in the following.

According to Fick's law of diffusion [43], the development of the width of a charge cloud in time starting from a point-like distribution can be described by a Gaussian with a standard deviation of

$$\sigma_{\text{diffusion}} = \sqrt{2Dt}, \tag{4.1}$$

where D is the diffusion coefficient and t the diffusion time. The Einstein relation [43] allows to derive the diffusion coefficient from the electron/hole mobility $\mu_{e/h}$:

$$D = \frac{\mu_{e/h} k_B T}{e}, \tag{4.2}$$

where k_B is the Boltzmann constant, T the temperature, and e the elementary charge. At room temperature ($T = 300\,\mathrm{K}$) and for an electron mobility of $1450\,\mathrm{cm}^2/(\mathrm{V}\cdot\mathrm{s})$ and a hole mobility of $500\,\mathrm{cm}^2/(\mathrm{V}\cdot\mathrm{s})$ [43] for undoped crystalline silicon one obtains a diffusion coefficient of $D_e = 37.5\,\mathrm{cm}^2/\mathrm{s}$ and $D_h = 11.6\,\mathrm{cm}^2/\mathrm{s}$. Equation 4.1 is plotted in Figure 4.4 for these value of D.

As illustrated in Figure 4.5a, the drift motion of the charge carriers in the electric field is superimposed with an isotropic diffusion. This way, the cloud of charge carriers expands within the sensor plane while drifting towards the collection electrodes. Consequently, the amount of charge sharing is strongly dependent on the strength and configuration of the electric field in the sensor. If the charge is collected in a short time due to a fast drift in a strong electric field, the amount of lateral diffusion is suppressed compared to a long drift time in a weak electric field allowing the charge cloud to expand further in the lateral dimension. E.g. a charge collection time of 1 ns leads to a diffusive expansion of ∼2.7 µm, a charge collection time of 10 ns to ∼8.7 µm for electrons according to Equation 4.1. A particle incidence point closer to the pixel edges or corners increases the amount of charge sharing. Charge deposited in the non-depleted region also expands diffusively before recombining or entering the depletion zone. Hence, it has more time to expand compared to drifting charge and can thus reach a larger lateral extent.

If a particle penetrates the sensor material under an angle, charge sharing occurs from geometrical considerations as illustrated in Figure 4.5b. For strongly inclined

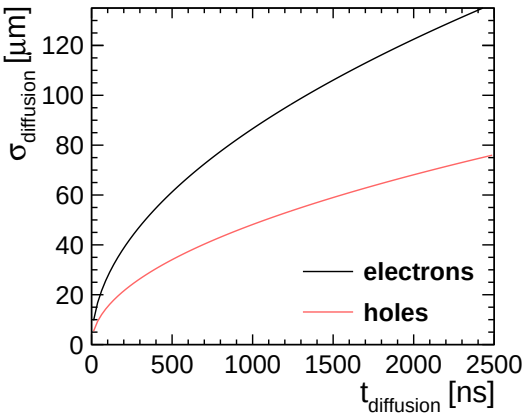

Figure 4.4: Time dependence of the expansion of a charge cloud by diffusion as calculated using Fick's law (see Equation 4.1) with diffusion coefficients of $D_e = 37.5\,\mathrm{cm}^2/\mathrm{s}$ and $D_h = 11.6\,\mathrm{cm}^2/\mathrm{s}$.

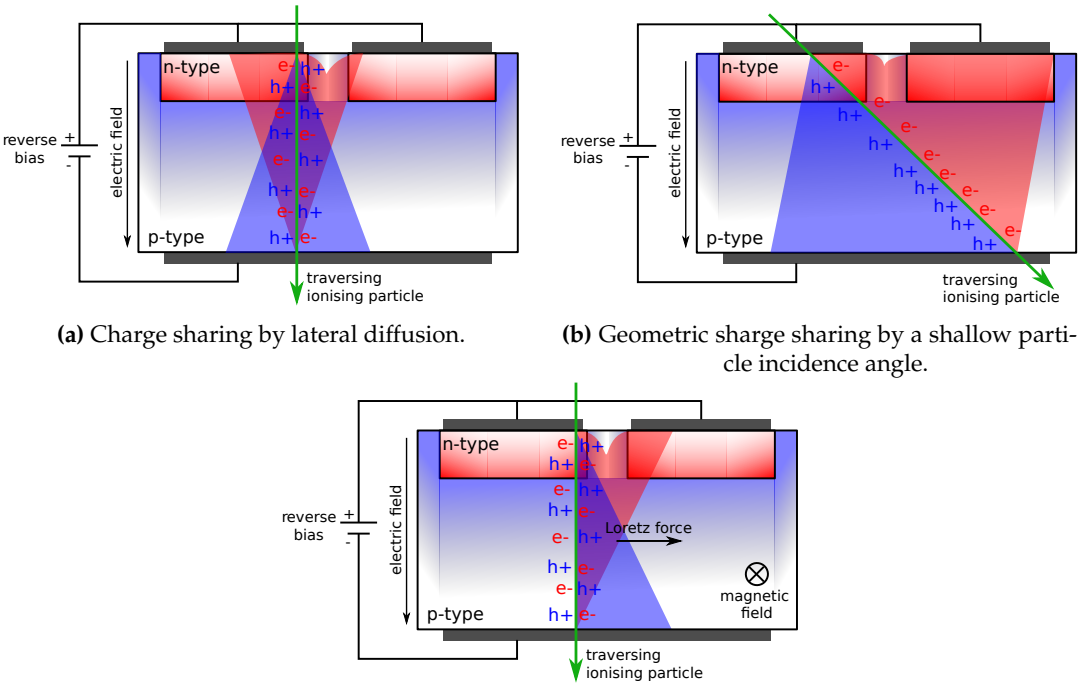

(a) Charge sharing by lateral diffusion.

(b) Geometric sharge sharing by a shallow particle incidence angle.

(c) Charge sharing in a magnetic field.

Figure 4.5: Illustration of difference charge sharing mechanisms through which charge is collected by more than one pixel.

tracks, i.e. shallow incidence angles, this can lead to large clusters comprising many pixels depending on the depth of the active volume of the sensor.

Vertex and tracking detectors of collider experiments, such as CLIC, are often located in a magnetic field $\vec{B}$. In this case, the moving charge carriers experience a Lorentz force $\vec{F}_L$ while drifting towards the collection electrodes with the velocity $\vec{v}$ [43]:

$$\vec{F}_L = q\left(\vec{v} \times \vec{B}\right), \tag{4.3}$$

which also leads to charge sharing as illustrated in Figure 4.5c.

4.1.2 Clustering

As a consequence of charge sharing, a clustering algorithm is needed to group pixels related to one particle into a cluster. If a pixel hit timestamp (ToA) is available, adjacent pixel hits can be combined into a cluster if they coincide within a certain time window. If no time information is available, the clustering is performed solely based on the hit positions.

If the energy deposition is measured by means of the time-over-threshold (ToT), the cluster ToT corresponds to the sum of all pixel ToTs. The pixel with the largest ToT within the cluster is referred to as the *seed pixel*. All others are called *secondary pixels*.

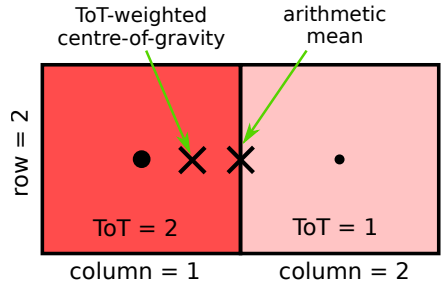

Figure 4.6: Illustration of the determination of the cluster position for an exemplary two-pixel cluster comparing the arithmetic mean and the ToT-weighted centre-of-gravity.

Charge sharing can be beneficial for the spatial resolution of a detector: If multiple pixel hits are recorded and a ToT-weighted mean of the cluster positions can be calculated as illustrated in Figure 4.6. This approach yields the best results assuming that the charge sharing between two pixels shows a linear behaviour with respect to the track incident point between both pixel centres [60]. A so-called η-correction can be applied to correct for non-linear charge sharing [61]. If the occurrence of multi-pixel clusters is restricted to a small region close to the pixel edges of a sensor and the charge sharing is highly non-linear, the simple arithmetic mean yields a better estimation for the track incidence point as will be discussed in Section 11.4.

Charge sharing reduces the amount of charge collected per pixel. For large thresholds or a small deposited charge, this can lead to a decrease of the measured cluster size or a loss in hit detection efficiency if the signals of one or multiple pixels remain below the threshold.

Additional reason for cluster formation can be cross-talk and the occurrence of δ-electrons as discussed in Section 3.1. Since these can travel a significant distance within the lateral dimension of the sensor and deposit energy along their trajectory, they can cause large clusters to occur. δ-electrons deposit most of their energy at the end of their trajectory due to the Bragg peak. Hence, they lead to a deterioration of the spatial resolution because neither the arithmetic mean nor the ToT-weighted centre-of-gravity yield a good measurement of the incidence point of the traversing ionising particle.

4.2 Noise Sources

Several sources of noise exist, which can limit the detector performance. They are related to fluctuations of the signal generation as well as the front-end electronics.

Fano Noise

Fano noise describes the fluctuations of the electric charge that is obtained in a detector even if the deposited energy is identical [62]. It is a result of the fact that the

energy loss in a collision is not purely statistical. The number of ways in which an atom can be ionised is limited due to the discrete energies of its shell electrons. Hence, the charge carriers created during the ionisation are not independent.

The relative resolution of the signal is quantified as [63]

$$R' = \sqrt{\frac{Fw}{E}}, \tag{4.4}$$

whereby w denotes the required energy to create an electron-hole pair and E the deposited energy. F is the so-called Fano factor, which is material dependent, e.g. $F = 0.115$ for silicon [64]. Fano noise represents a physical limit on the achievable energy resolution of a detector.

Electronic Noise

Also the pixel front-end electronics (see Figure 4.2) is affected by noise. Mainly three types of noise are distinguished [43]:

- **Thermal noise**, also called Johnson or Nyquist noise, occurs due to the Brownian motion of charge carriers. Hence, it is increases with temperature.
- **Shot noise** arises from the discrete nature of the charge, which results in statistical fluctuations of the number of charge carriers overcoming a potential barrier. In pixel detectors, its main contribution is the leakage current originating from the thermal generation of electron/hole pairs, which is a discrete process.
- **1/f noise**, also called flicker noise. In MOSFETs, it is mainly caused by trapping of charge carriers in the transistor channel by crystal defects with a delayed release.

In a pixel sensor with a front-end as shown in Figure 4.2, it can be shown that shot noise rises linearly with the leakage current of the sensor diode, while thermal noise and 1/f noise affect the input transistor of the amplifier and increase quadratically with the sensor capacitance [43, 65].

The noise sources described above lead to fluctuations of the amplifier output signal. In addition, the threshold and the baseline of the comparator underlie fluctuations. Consequently, a pixel hit cannot only originate from the energy deposition of a traversing ionising particle. If the noise fluctuations are large enough to cause an accidental crossing of the threshold, this leads to the detection of a *noise hit* or *fake hit*. Generally, a low noise rate is desired to reduce the occupancy of the readout system and avoid increased combinatorics in tracking applications.

4.3 Radiaton Damage

Pixel detectors are often employed close to the interaction point of particle physics experiments, where they are exposed to high levels of radiation. Over time, this can lead to a degradation of the detector performance. Two different types of damage are distinguished [43]:

- **Ionising energy loss (IEL)** leads to a damage of the sensor surface and the Si-SiO_2 boundaries and affects the performance of the electronics if charge is accumulated in the SiO_2 under the gate of a transistor. It is quantified as the total ionising dose (TID).
- **Non-ionising energy loss (NIEL)** causes a volume damage to the silicon bulk by displacing atoms and altering the lattice structure. This can lead to trapping centres for the charge carriers and reduced the amount of collected charge. It is usually quantified as the equivalent damage caused by a neutron flux with an energy of 1 MeV.

4.4 Hybrid Pixel Detectors

The "classical" design of solid state pixel detectors are *hybrid pixel detectors*. As depicted in Figure 4.7, they consist of two layers. The sensor layer acts as the active detection region. Usually, it is connected to a readout chip via small solder joints, called bump-bonds. The readout chip contains the electronics such as amplifiers, discriminators, etc. and processes the signal induced on the collection electrode to form data packages, which can be sent out to the data acquisition system.

It is an advantage of hybrid sensors that the development of the sensor and the readout electronics is decoupled. In consequence, a readout chip can be reused for multiple applications by combining it with different sensor materials optimised for each use-case. Furthermore, low noise levels can be reached as the high electric field in the sensor material is well separated from the sensitive electronics of the readout chip.

On the other hand, the bump bonding process is expensive. In addition, it limits the achievable minimal pixel pitch. For small pitches, the bump bonding yield, i.e. the reliability of the electric connection, is reduced.

Alternative bonding techniques are explored to overcome the limitations of the bump bonding. Examples are wafer-to-wafer bonding [66], a capacitive coupling between sensor and readout chip [67], or the usage of anisotropic conductive films [68].

The Timepix3 chips, which are used in the reference telescope at the SPS (see Section 7.2) as well as the timing reference plane employed at DESY (see Section 7.4), are examples of hybrid sensors.

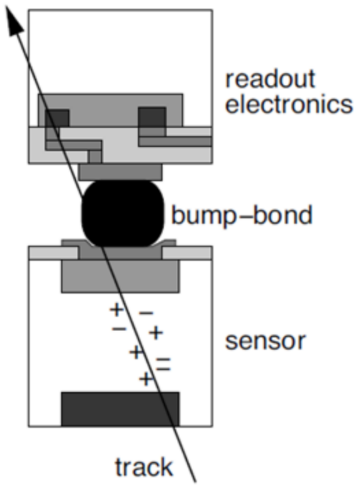

Figure 4.7: Schematic drawing of one pixel cell of a hybrid pixel sensor. The sensor layer is connected to the readout chip with a bump-bond. From [69].

4.5 Monolithic Pixel Detectors

In contrast to hybrid sensors, monolithic pixel sensors consist only of one single layer of silicon, in which the detection volume and the readout electronics are combined (see Figure 4.8). Monolithic sensors are often based on commercially available (imaging) CMOS manufacturing processes. Signal digitisation and data serialisation are usually implemented in a small dedicated area next to the active matrix of the chip, the so-called periphery. Since no bump bonding is required, the cost and manufacturing complexity are reduced, which makes them suitable for mass production for large-scale applications. Furthermore, the sensors can be thinned after production by removing bulk material from the backside, which leads to a very low achievable material budget. This is particularly important for many tracking applications, in which the material budget of the detector limits the achievable resolution due to multiple Coulomb scattering (see Section 3.1.3). On the other hand, a mutual influence between the electric field of the sensor and the circuitry needs to be considered in the design. This results in complex sensor layouts with complex electric field configurations. To study these and predict the behaviour of these sensors, detailed information about the process parameters is required. However, access to this proprietary information is often restricted by the manufacturers.

4.5.1 MAPS

In *monolithic active pixel sensors (MAPS)* [43], signal amplifiers are located in each pixel cell. This limits the applicable reverse bias voltage, resulting in a small depletion region. Hence, the majority of charge is collected via diffusion resulting in a slow and incomplete charge collection.

The Mimosa26 sensors, which are employed in the reference telescope used at DESY (see Section 7.4) are examples of MAPS.

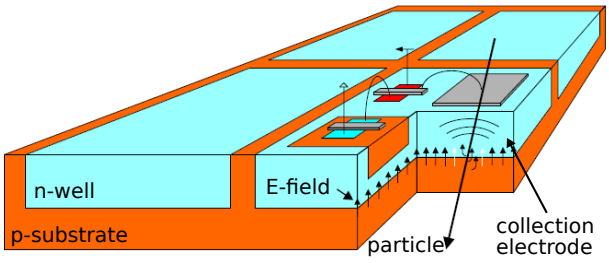

Figure 4.8: Schematic drawing of a four-pixel sub-matrix of a high-voltage monolithic sensor. The readout electronics is integrated in the n-wells, which form the sensor diodes. From [70] (modified).

4.5.2 HV-MAPS

In the *HV-MAPS* technology [70], the pixel design is based on a large collection electrode into which the signal processing circuitry is integrated. As depicted in Figure 4.8, a deep n-well is implemented in a p-substrate to form the sensor diode. A high reverse bias voltage of $\mathcal{O}(100\,\mathrm{V})$ is applied between the n-well and the p-substrate to create a large depletion region with a strong electric field leading to large signals and a fast charge collection via drift. In addition, charge diffusing into the depleted volume can contribute to the signal for larger sensor thicknesses.

The n-wells are large enough to house the entire in-pixel electronics and shield it from the high voltage.[1] They serve as the substrate for the implementation of PMOS transistors. Additional shallow p-wells inside the n-well allow for an implementation of NMOS transistors.

Due to the large collection diode, a uniform detector response is expected because of a uniform and less complex electric field configuration as compared to small collection diode designs. On the other hand, a large sensor capacitance potentially increases the noise rate as discussed in Section 4.2. The technology has shown to be intrinsically radiation tolerant [51].

The ATLASpix, which is the main device-under-test of this thesis, is an example of an HV-MAPS. It is introduced in detail in Chapter 5.

[1] Alternative monolithic sensor designs, such as the CLICTD [71, 72], are based on a small collection diode. In this design, the in-pixel electronics is placed in shallow n-wells next to the sensor diode.

Chapter 5

The ATLASpix_Simple Prototype

The main subject of investigation of this thesis is the *ATLASpix_Simple* [73] prototype. It is a high-voltage monolithic active pixel sensor (see Section 4.5), which was designed as a large-scale test chip for the ATLAS ITk upgrade [9] as well as the CLIC tracking detector [10]. It was produced on a common reticle together with two related sensors, the *ATLASpix_IsoSimple* and the *ATLASpix_M2*, and a similar sensor for a different application, the *MuPix8* [74].

A photograph of the three *ATLASpix* sensors is shown in Figure 5.1. The design of the *ATLASpix_IsoSimple* is identical to the *ATLASpix_Simple* except for the implementation of the in-pixel comparator. An additional deep P-well inside the N-well is used for a CMOS implementation of the comparator instead of NMOS in case of the *ATLASpix_Simple*. The *ATLASpix_IsoSimple* is not a subject of this thesis. Results can be found in [51] and [75].

The *ATLASpix_M2* features additional on-chip buffer cells, which allow the storage of hit information until the arrival of a trigger signal. Due to a different signal line routing, the pixel size is reduced to $60 \times 50\,\mu m^2$ compared to $130 \times 40\,\mu m^2$ for the ATLASpix. The implementation of the in-pixel amplifier and comparator are identical to the *ATLASpix_Simple*. Because a buffered readout is not foreseen for the CLIC Tracking Detector, this sensor was not investigated within the scope of this thesis. Results can be found in [76].

5.1 Sensor Fabrication

All three ATLASpix sensors are fabricated in the commercial aH180 HV-CMOS process by AMS [77, 78], which allows transistor gate lengths down to 180 nm. Six metal layers are available for power distribution and signal routing. The breakdown voltage is specified around 120 V. The sensors have been produced on wafers with different substrate resistivities between 20 Ωcm and 1 kΩcm. The comparison of the performance for different substrate resistivities is one aspect of this thesis.

After production, the sensors can be thinned by removing bulk material from the backside. In this work, samples with a thickness of 62-100 µm are investigated (see Section 5.4). Due to the relevance for this thesis, only the *ATLASpix_Simple* is described in the following. For simplicity, it is referred to as "*ATLASpix*" throughout the rest of this thesis.

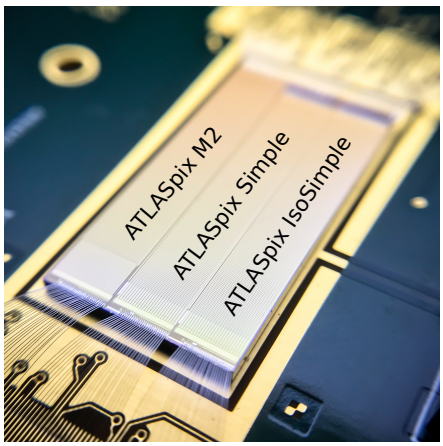

Figure 5.1: Photograph of the three ATLASpix matrices glued and wire-bonded to a printed circuit board.

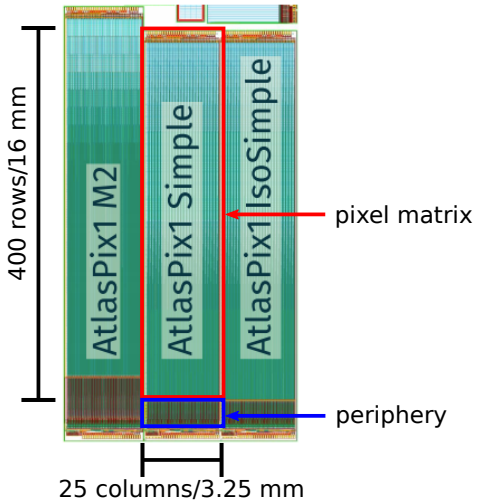

Figure 5.2: Micrograph of the *ATLASpix* sensors showing the geometric dimensions and the division into active matrix and digital periphery. From [73] (modified).

5.2 Sensor Architecture

The micrograph in Figure 5.2 illustrates the dimensions of the pixel matrix and the digital periphery of the ATLASpix. The sensor has an active matrix with a size of $3.25 \times 16.0\,\text{mm}^2$ consisting of 25 columns and 400 rows of pixels with a pitch of $130 \times 40\,\mu\text{m}^2$.

As depicted in Figure 5.3, a pixel consists of a sensor diode, which is connected to a charge-sensitive amplifier (CSA) and a comparator. It is possible to inject a test-pulse into the CSA. After the comparator, a line driver sends the discriminated signal to a readout cell in the digital periphery, which comprises a receiver and an edge detector. Here, the pixel address of a hit as well as two timestamps are assigned, which are used to reconstruct the time-of-arrival (ToA) and the time-over-threshold (ToT) of the signal. In addition, the digital periphery houses a state machine, which coordinates the readout of the entire pixel matrix and performs an 8b/10b encoding [79] before a serializer sends the data out from the chip via a low-voltage differential signal (LVDS) link of up to 1.6 Gb/s. For the results presented in this thesis, the link speed was set to 1.25 Gb/s. In addition, the digital periphery contains a voltage controlled oscillator (VCO) and a phase-locked loop (PLL) which locks to an external clock and from which all on-chip clocks are derived.

5.2.1 Pixel Readout Cells

Each pixel in the active matrix has a corresponding readout cell in the digital periphery of the chip to which it is connected by an individual signal line. The arrangement of the readout cells and the routing scheme of the signal lines connecting the pixels

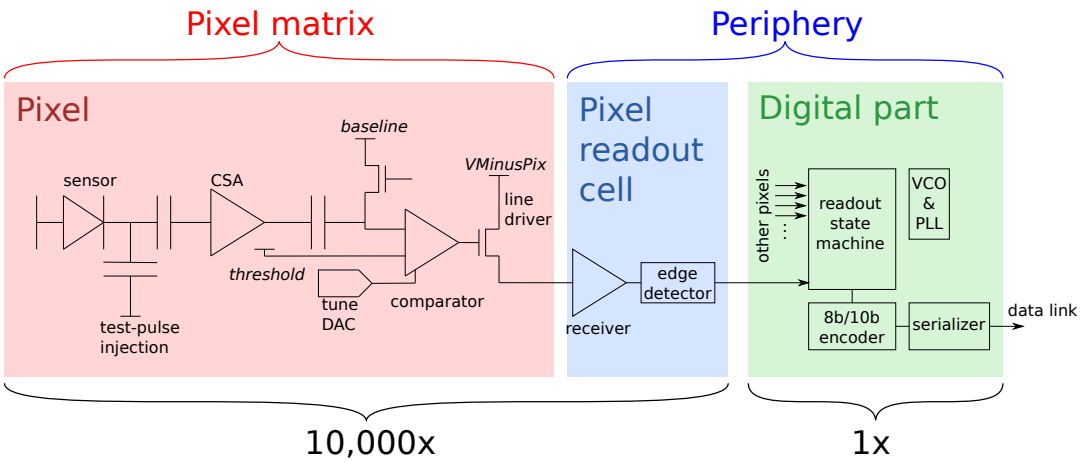

Figure 5.3: Schematic drawing of the signal chain of the ATLASpix including the in-pixel electronics and the digital periphery. From [75] (modified).

of the active matrix to the readout cells is shown in Figure 5.4. The readout cells have a size of $62.5 \times 4.2\,\mu m^2$ and are arranged in a double-column structure. They receive discriminated signals from the connected pixels in the active matrix. In these cells, the digital hit address is assigned together with two timestamps, which are used to reconstruct both the time-of-arrival (ToA) and the time-over-threshold (ToT) of the hit.

The first one is called $TS1$ and represents the time-of-arrival (ToA) as it is assigned when a rising edge is detected on the transmission line connecting the comparator with the readout cell. It has a range of 10 bit. At an input clock frequency of 125 MHz, it is recorded with a binning of $16\,\text{ns}/(1 + \texttt{ckdivend})$, where `ckdivend` is a configurable clock divider ranging from 0 to 15.

The second timestamp $TS2$ is set upon a falling edge on the transmission line. It has a range of 6 bit and a granularity of $8\,\text{ns}/(1 + \texttt{ckdivend2})$, with its clock divider `ckdivend2` also ranging from 0 to 15. The difference of the two timestamps $TS2 - TS1$ gives the time-over-threshold (ToT).

For the results presented in this thesis, `ckdivend` was set to zero to achieve the smallest possible granularity. `ckdivend2` was set to 7 or 15 leading to a binning of the ToT measurement of 64 ns or 128 ns.

5.2.2 Readout Scheme

The readout of pixel hits from the pixel cells in the periphery is data-driven, meaning that hits are sent out continuously and no external trigger signal is required. It is implemented in a column-drain scheme, which leads to a non-chronological readout order as illustrated in Figure 5.5. Below the matrix of readout cells the end-of-column (EoC) is depicted.

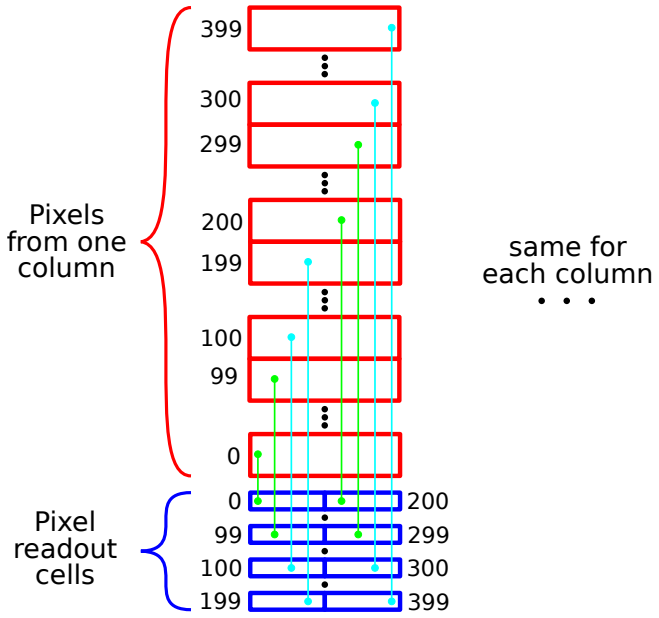

Figure 5.4: Illustration of the arrangement of the readout cells and the routing of the signal lines connecting the pixels in the active matrix to the readout cells in the digital periphery. The two colours of the signal lines indicate the routing on different metal layers. From [75] (modified).

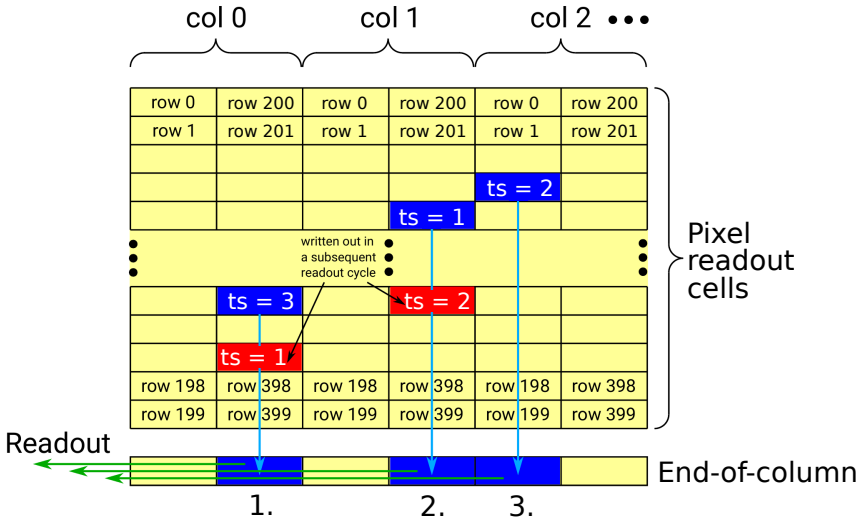

Figure 5.5: Illustration of the column-drain readout scheme of the ATLASpix. The *ts* indicate hits with exemplary timestamps. It can be seen that the chronological order of the hits is not conserved in the readout. From [51] (modified).

In one readout cycle, the hits with the lower-most row addresses from each column are "drained" into the EoC and then sent out consecutively. This procedure is repeated continuously.

It shows that the chronological order of the occurrence of the pixel hits is not conserved in the readout. However, it can be retained offline with the help of the ToA of each pixel. It also illustrates a limitation of this readout scheme: If a high occupancy leads to new hits with lower row addresses before the matrix was read out completely, pixels with higher row numbers can get stuck in the matrix.

5.3 Voltage Supply & Sensor Configuration

A total of six external supply voltages are required, which are listed in Table 5.1. In addition, the pixel baseline and the pixel threshold values can either be generated on-chip or applied externally. For this work, they have been applied externally. The P-substrate was contacted from the backside through conductive epoxy glue (*backside biasing*).[1] Backside biasing is expected to yield a better performance due to a more homogeneous development of the depletion region between pixels [80, 81].

The chip can be configured via linear shift registers connected to configurable logic elements and digital-to-analogue converters (DACs). However, these cannot be read back to confirm a successful configuration. The configuration used during this work are listed in Table A.1 in the Appendix. Detailed descriptions of the in-pixel electronics and all configuration values can be found in [51, 73, 75].

Table 5.1: Summary of the required external voltages for the ATLASpix.

Name	Voltage [V]	Function
VSSA	1.2	power of the in-pixel CSA
VDDA	1.85	power of the in-pixel logic
VDDD	1.85	power of the digital periphery
VDDHigh[2]	1.85	power of custom-design periphery blocks using differential current mode logic (DCL)
VMinusPix	0.65	ground level of line driver
VGatePix	2.2	gate level for in-pixel comparator
HV	−50-95	bias voltage for the sensor diode

Optimisation of Chip Settings

The optimisation of chip settings is an important part of the commissioning and characterisation of pixel sensor. It has a large impact on the chip performance such as the power consumption, the time resolution or the efficiency. Hence a careful study of all parameters is necessary. For the ATLASpix it has been covered by [51, 75, 82, 83, 84].

Threshold Equalisation and Pixel Masking

The pixels of the active matrix contain digital-to-analogue converters (DACs) for a tuning of the local comparator threshold in each pixel. This allows for an equalisation of the varying thresholds in the individual pixels across the matrix and reduce the threshold dispersion. In addition, noisy pixels can be masked ("switched off") to

[1] In contrast, the results shown in [51] and [75] were obtained with samples, where the frontside of the substrate was contacted with the HV (*frontside biasing*).

[2] In the setup used for the results shown in [51] and [75], the voltages VDDD and VDDHigh are combined and referred to as VDD.

reduce the readout occupancy. However, a pixel tuning or pixel masking was not performed within the scope of this thesis as it was found to cause issues including unresponsive pixels and a significant increase in the noise rate [84].

5.4 Overview of the Investigated ATLASpix Samples

The ATLASpix was produced in two batches: a preproduction batch called *batch 1* and a production batch called *batch 2* [85]. All samples investigated within the scope of this thesis stem from batch 2. An overview is shown in Table 5.2. They are labelled according to the following naming scheme: `w<wafer_number>s<sample_number>`. It should be noted that the sample number is arbitrary, meaning that two samples with subsequent numbers (e.g. w23s15 and w23s16) do not necessarily stem from neighbouring locations on the wafers. All samples are wire-bonded to custom chip-boards that are described in detail in Section 6.1 and backside-biased through the use of conductive epoxy glue.

The standard resistivity of the AMS aH180 technology is 20 Ωcm. The comparison of samples with different substrate resistivities aims to answer the question if it is beneficial to deviate from the nominal process to gain performance.

Sample w10s30 is the only sensor with a reduced thickness of 62 µm. This needs to be taken into account when comparing the sensor performance for samples with different substrate resistivities as presented in Section 11.6 of this thesis. It was used because samples with a thickness of 100 µm and a resistivity of 80 Ωcm were not available.

Table 5.2: Overview of the tested ATLASpix samples.

Sample	**Thickness** [µm]	**Substrate Resistivity** [Ωcm]		**Measurements**
		nominal	*expected range*	
w06s12	100	20 (standard)		lab + DESY
w06s14	100	20 (standard)		lab
w10s30	62	80 (non-standard)	50-100	lab + DESY
w23s11	100	200 (non-standard)	100-400	lab + DESY
w23s15	100	200 (non-standard)	100-400	SPS
w23s16	100	200 (non-standard)	100-400	lab
w23s22	100	200 (non-standard)	100-400	DESY

Part II

Experimental Setups & Methods

Chapter 6

Laboratory Setups

This section introduces the experimental setups used for laboratory measurements with the ATLASpix within the framework of this thesis. The results are shown and discussed in Chapter 10.

6.1 The Caribou Readout System

The *Caribou Readout System* [86, 87, 88, 89] has been used for powering, configuration and readout of the ATLASpix for all laboratory and test-beam measurements presented in this thesis. It has been developed as a flexible open-source readout system for fast and efficient prototype development, as it minimises the required effort for adapting it to new sensors. A photograph of the setup and a schematic of the architecture are shown in Figure 6.1 and Figure 6.2.

The system is based on a Xilinx Zynq System-on-Chip (SoC), which runs a full Yocto-based Linux distribution called *Poky* and the data acquisition software *Peary* as described in more detail below. It comprises the following hardware components:

- The **ZC706 evaluation kit** [90] provides a Zynq-7000 SoC, which combines a Kintex-7 Field Programmable Gate Array (FPGA) and a dual-core ARM Cortex-A9 processor. It is connected to the network via Ethernet. An SD card is used to provide both the firmware image for the FPGA as well as the operating system. The FPGA fabric of the SoC is used for the implementation of a hardware interface for the sensor prototype combining common firmware blocks with detector-specific modules. The ARM processor can access the FPGA registers via an Advanced eXtensible Interface (AXI) bus.

- The generic **Control and Readout (CaR) board** is connected to the Zynq board via an FPGA Mezzanine Card (FMC) Adapter Board. It is not chip-specific and provides peripherals commonly required to interface and operate a sensor. These comprise programmable power supplies with monitoring, analogue-to-digital converters (ADCs), an I^2C interface bus, and adjustable voltage and current references. Various single-ended general purpose inputs and outputs (GPIO) and low-voltage differential signal (LVDS) links and high-speed transceivers (GTx) are available. In addition, it hosts a programmable low-jitter

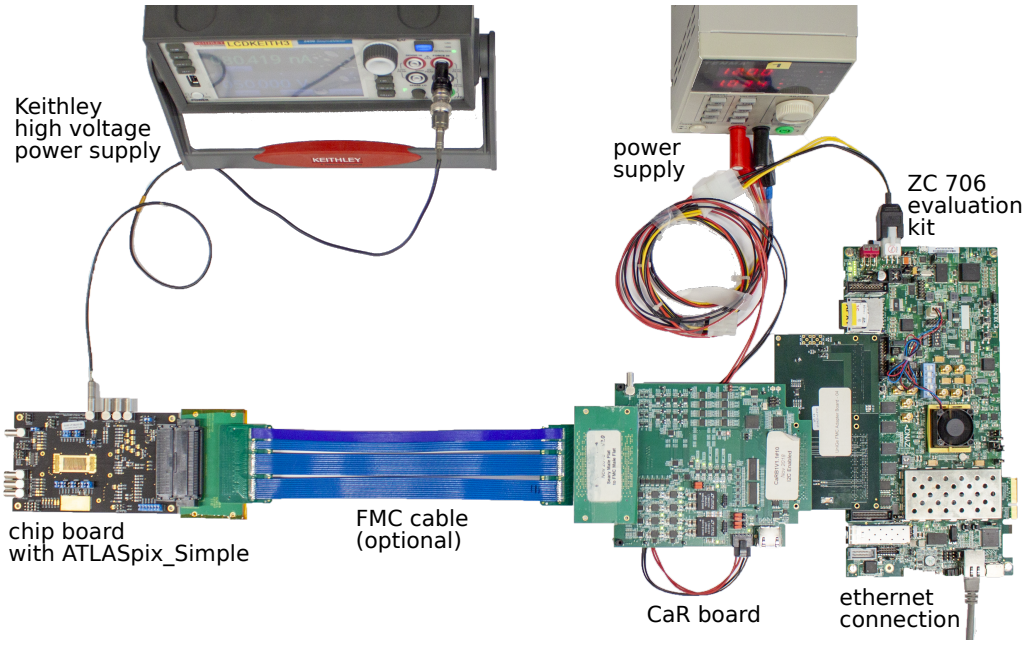

Figure 6.1: Photograph of the *Caribou Readout System* including Zynq board (ZC 706), CaR board and chip board.

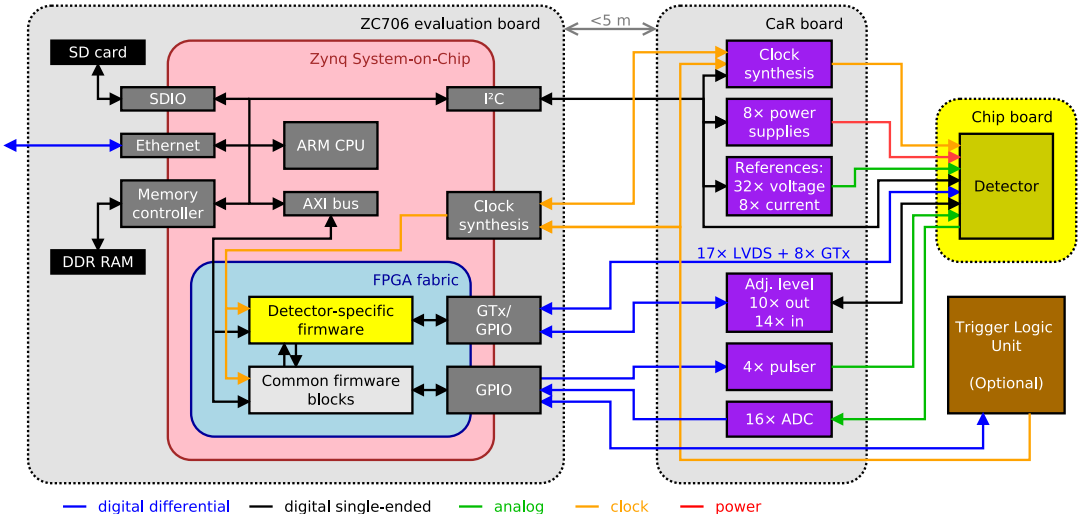

Figure 6.2: Schematic of the Caribou hardware architecture comprising a Zynq System-on-Chip, a Control-and-Readout board as well as a detector-specific chip board. From [10].

clock generator with external reference and interfaces for trigger and time references that can be used in test-beam operation for the synchronisation with other devices.

- The actual detector is glued and wire-bonded to a chip-specific **Carrier Board**, also called chip board, which only contains passive elements, such as resistors and capacitors (for filtering) and detector-specific circuits not available on the CaR board, such as LVDS buffers. It is interfaced with the CaR board via a 320-pin SEARAY connector [91].

- A **power supply** provides both the Zynq board as well as the CaR board with 12 V.
- A **Keithley 2450 SourceMeter** [92] provides the bias voltage and is configured with a current limit to protect the sensor. It can be connected to the network and controlled remotely via a web interface or by using Python scripts.

Optionally, an extension cable can be used between the Zynq board and the CaR board and/or the CaR board and the chip board. This allows for a more flexible mounting in case of mechanical constraints in a test-beam setup and to separate the SoC spatially from the sensor when operating in high radiation environments.

The ARM processor runs a full Linux-based operating system (OS) with a network connection. The user logs in via a secure shell (SSH) such that no additional PC is required, making the system more compact and portable.

The Linux system is based on the reference distribution called *Poky* provided by the Yocto Project [93] and is built using the OpenEmbedded [94] build system, which is an embedded system solution widely used in industry. A data acquisition (DAQ) software called *Peary* [95] runs on the OS. The software architecture is depicted in Figure 6.3. *Peary* adds a Hardware Abstration Layer (HAL), which functions as an interface between the physical hardware components and the software. It allows to handle the hardware peripherals, such as voltage regulators and ADCs, as C++ objects. In addition, detector-specific functions to configure and operate a sensor are implemented in the DAQ library.

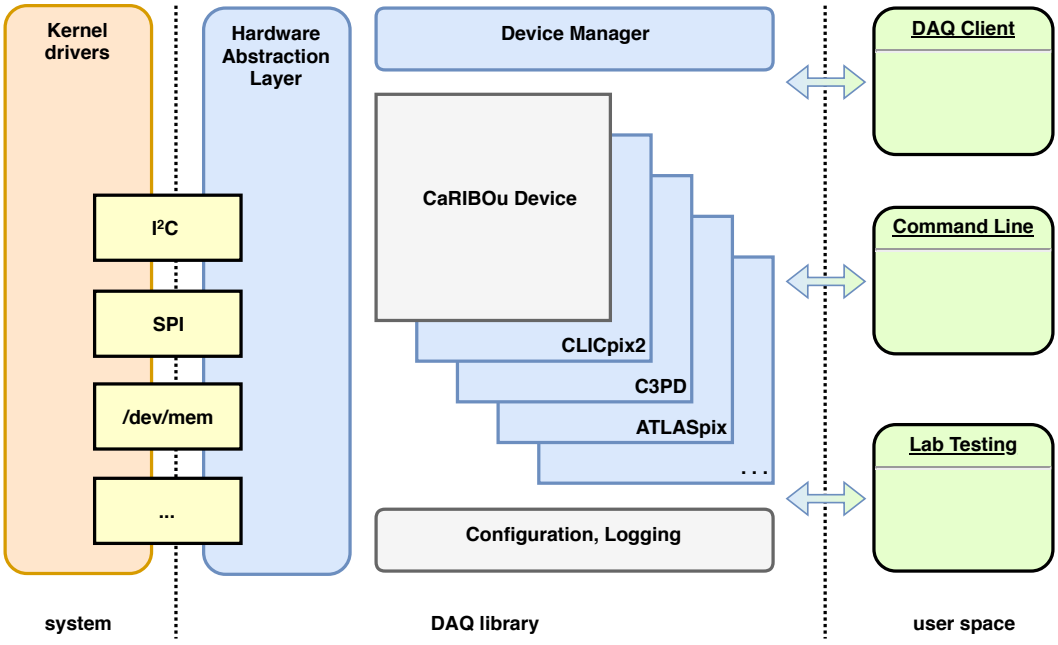

Figure 6.3: Schematic of the *Peary* software architecture. From [10].

The command line interface (CLI) is used for standalone use-cases like laboratory measurements. The application programming interface (API) is needed for an integration into a higher-level DAQ system as used in test-beam operation (see Section 7.2 and 7.4).

Currently, the *Caribou* system supports the following devices: CLICpix2 [96], C3PD [97], FE-I4 [98], H35Demo [99], CLICTD [71], FastPix [100], RD50-MPW2 [101], and all three ATLASpix submatrices (see Chapter 5).

6.2 The ATLASpix Chip Board Assembly

As described above, the ATLASpix is glued and wire-bonded to a chip board, which is interconnected to the CaR board with a SEARY connector [91]. The chip board can be used for all three ATLASpix submatrices. Jumpers are used to choose which submatrix is powered. In addition, the chip board is equipped with resistors and capacitors to filter the supply voltages. Test points and Lemo connectors are available for probing and debugging. In addition, the bias voltage is supplied via a Lemo connector. A clock distribution circuit [102] fans out the clock from the CaR board to all three submatrices. A photograph is shown in Figure 6.4.

Material Budget of the ATLASpix Chip Board Assembly

For a precise modelling of the amount of multiple scattering (see Section 3.1.3) that occurs when a particle traverses the detector material, the material budget (see Section 3.1.2) of the detector including the chip board needs to be taken into account.

The ATLASpix is thinned to a thickness of 62 µm or 100 µm depending on the sample. This corresponds to the full thickness of the chip including silicon substrate,

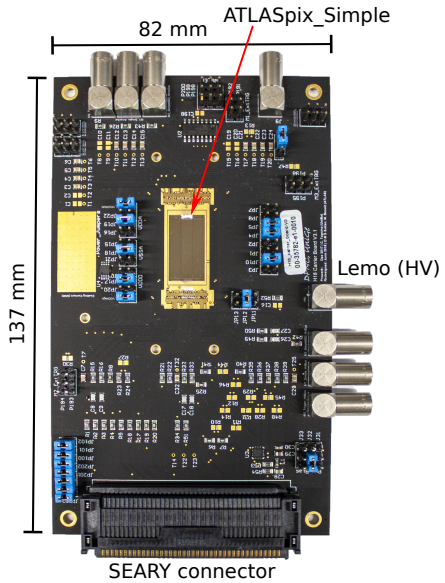

Figure 6.4: Photograph of the ATLASpix on a chip board.

metallisation and passivation. The metal layers sum up to $\sim$ 15 µm [77, 84, 82] and the passivation layer of a few 100 nm can be neglected.

The chip board consists of 5 substrate layers made of FR-4 with a total thickness of 1.1 mm and six copper layers with a total thickness of 90 µm. However, below the sensor, only the top metal layer with a thickness of 9 µm is present. Silk screen and solder mask are neglected. The sensor is fixed to the PCB with STAYSTIK 571 [103], a conductive epoxy glue containing silver (Ag) particles. It has a thickness of 3 mil = 0.0762 mm. Its exact composition is not revealed by the manufacturer, but similar conductive glues consist of 30 % vol. metal filler and 70 % vol. epoxy [104].

All relevant numbers are broken down in Table 6.1 and result in a total radiation length X/X_0 of 0.99 % and 1.03 % for samples with a thickness of 62 µm and 100 µm, respectively.

Table 6.1: Estimation of the material budget X/X_0 for the ATLASpix including the chip board, where X_0 is the radiation length and X the thickness of each material. Data for X_0 from [105, 106].

Component	Material	X_0[mm]	X[mm]	X/X_0[%]
ATLASpix Chip			62-100	**0.07 - 0.11**
Substrate	Si	93.70	0.047-0.085	0.05 - 0.09
Metal layers	Al	88.97	0.015	0.0169
Carrier PCB				**0.76**
Substrate	FR-4	159.3	1.1	0.691
Metal layers	Cu	14.36	0.009	0.063
Conductive epoxy glue			0.0762	**0.116**
Resin	Epoxy	42.6	0.0762 · 70 % vol.	0.125
Metal filler	Ag	85.43	0.0762 · 30 % vol.	0.027
Total				**0.99 - 1.03**

6.3 The Temperature Calibration Setup

To investigate the temperature dependence of the current-voltage characteristic or the noise rate of the ATLASpix (see Chapter 10), the temperature needs to be monitored during the operation of the sensor. Since the silicon surface of the monolithic sensor is very fragile, physical contact can cause damage to the chip. Thus, a contact-less measurement of the temperature using an infrared (IR) camera was chosen. However, the camera needs to be calibrated as the measured temperature depends on the reflectivity of the sensor surface, which consists of a combination of silicon and aluminium in case of the ATLASpix.

Figure 6.5 illustrates the setup used for the temperature calibration of the IR camera. An electrically damaged ATLASpix sample has been placed on a Peltier element [107]. Even though it is a broken sample, it has the same optical properties as a functional sensor. Thermal contact was ensured by the use of thermal

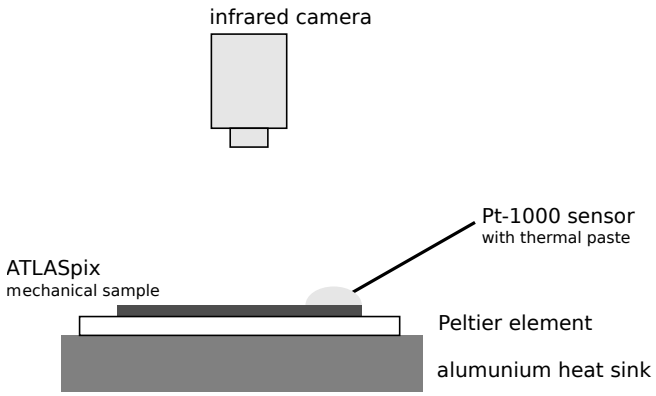

Figure 6.5: Illustration of the setup for the temperature calibration of the infrared camera.

paste. The Peltier element was placed on an aluminium heat sink. Furthermore, the surface of the ATLASpix sample was contacted with a PT1000 temperature sensor P1K0.308.7W.B.007 [108] using thermal paste while a clean area of the chip surface was focussed by a FLIR E75 infrared camera [109]. The resistance of the Pt1000 sensor was monitored using a FLUKE 45 Dual Display Multimeter [110].

Temperature Calibration of the Infrared Camera

The infrared camera needs to be calibrated because the reliability of the measurement depends significantly on the surface reflectivity/emissivity of the measured object.

The temperature was varied by applying different voltages to the Peltier element. For each step, the ohmic resistance of the Pt1000 sensor was recorded after a few minutes when the temperature stabilised. Simultaneously, the temperature was read off from the IR camera focussed on the chip surface. The FLIR provides calibration options for a variety of different common materials, such as steel or concrete. For the presented measurements, it was left at its default settings.

According to a European industry norm [111], the following calibration function is valid for a temperature range of 0-850 °C for platinum temperature sensors:

$$R_{\mathrm{T}} = R_0 \cdot (1 + AT + BT^2), \tag{6.1}$$

where R_T and $R_0 = 1000\,\Omega$ are the ohmic resistances of the sensor at a temperature T and at 0 °C, respectively. $A = 3.9083 \times 10^{-3}\,1/^{\circ}\mathrm{C}$ and $B = -5.775 \times 10^{-7}\,1/^{\circ}\mathrm{C}^2$ are calibration constants defined in the norm. Equation 6.1 can be inverted to obtain the temperature for a measured ohmic resistance:

$$T = \frac{-A + \sqrt{A^2 - 4B \cdot (1 - (R_T/R_0))}}{2B} \tag{6.2}$$

Figure 6.6 shows the temperatures obtained with the Pt1000 sensor applying Equation 6.2 and the values read off from the IR camera for different voltages applied to the Peltier element and thus different temperatures of the ATLASpix sensor

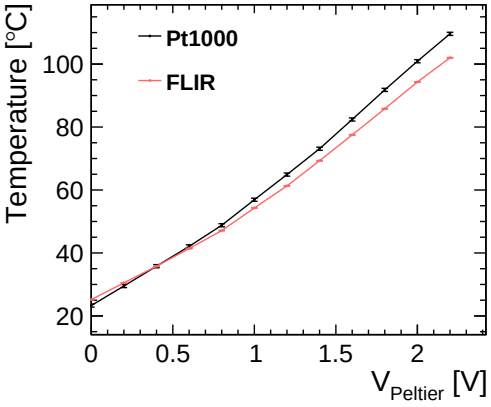

Figure 6.6: Temperatures measured with the Pt1000 sensor and the IR camera after stabilisation for different voltages applied to the Peltier element.

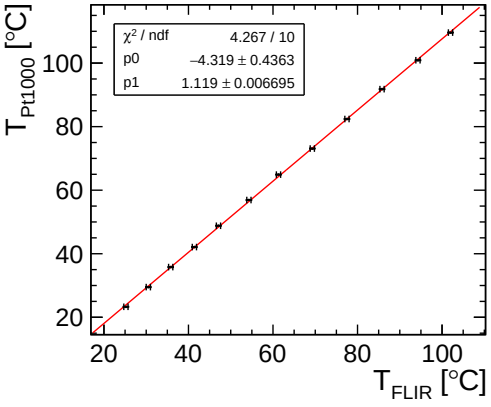

Figure 6.7: Temperature measured with the Pt1000 sensor plotted against the temperature read off from the IR camera. The linear fit to the data serves as a calibration function.

dummy. The uncertainty of the Pt1000 element is dominated by the read-off accuracy of the ohmmeter and results in 0.1 °C. For the FLIR, fluctuations of ±0.5 °C were observed during the measurement. As can be seen, the curves follow a similar trend where a larger applied voltage to the Peltier element results in a higher measured temperature. However, it can be seen that both curves differ with an increasing trend towards higher temperatures. Pt1000 sensors yield precise temperature measurements when in good thermal contact. This has been ensured by the use of thermal paste.

Consequently, the values obtained with the Pt1000 are assumed as accurate and can serve as a calibration reference for the FLIR. Both temperature measurements are plotted against each other in Figure 6.7. A first-order polynomial is fitted to the data. It yields a calibration formula that can be applied to obtain a reliable temperature from a value read off from the IR camera:

$$T_{\mathrm{Pt1000}} = p_0 + p_1 \cdot T_{\mathrm{FLIR}} \tag{6.3}$$

with $p_0 = (-4.32 \pm 0.44)\,1/°\mathrm{C}$ and $p_1 = (1.119 \pm 0.007)\,1/°\mathrm{C}^2$ as empirical calibration constants. According to Gaussian error propagation, the uncertainty on the temperature is given by

$$\Delta T_{\mathrm{Pt1000}} = \sqrt{(\Delta p_0)^2 + (T_{\mathrm{FLIR}} \cdot \Delta p_1)^2 + (p_1 \cdot \Delta T_{\mathrm{FLIR}})^2}. \tag{6.4}$$

The calibration shown in Figure 6.7 will be used in Chapter 10 to measure the temperature of the ATLASpix in-situ without touching the sensor surface.

6.4 The Laboratory Setup for Noise, IV, Power Consumption and Source Measurements

For noise and current-voltage (IV) measurements, a Caribou setup as described in Section 6.1 has been used. By default, it was operated at room temperature and without ambient light shielding. In order to investigate the temperature influence on the noise and IV characteristics of the sensors, the temperature was varied by a fan or a heat gun directed at the back of the chip board, while the temperature was monitored using an infrared camera as introduced in Section 6.3. An illustration is shown in Figure 6.8.

For the determination of the power consumption, the Fluke 45 Dual Display Multimeter [110] was connected in series with the respective voltage line by replacing the corresponding jumper on the carrier board of the ATLASpix. In order to perform automated IV measurements, the Keithley 2450 Source Meter [92] was controlled via the network using Python scripts.

For source measurements, a radioactive iron isotope, Fe-55, was placed close to the sensor surface as depicted in Figure 6.9. Fe-55 is a γ-source with a half-life of 2.737 years and is considered monoenergetic with an energy of 5.9 keV for the scope of this thesis [112, 113].

6.5 The X-ray Tube Setup

To perform an energy calibration of the detection threshold and the time-over-threshold, the ATLASpix samples were exposed to X-rays with well-defined energies. To this end, two experimental setups were utilised. Firstly, the laboratory setup as described in Section 6.4 was used with a Fe-55 source directed at the sensor.

To obtain further data points at different energies, an X-ray tube model PW3373/10 Ceramic Tube Cu LFF [114] was used in addition. It accelerates electrons to an energy of 25 keV that generate primary X-rays in a copper (Cu) target resulting in a bremsstrahlung spectrum superimposed with the characteristic K-lines of the Cu

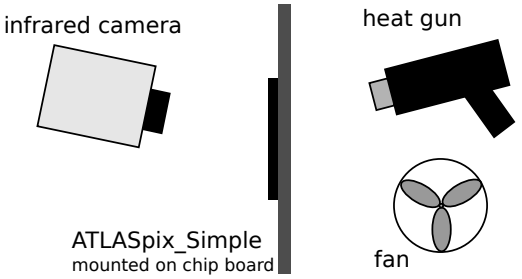

Figure 6.8: Illustration of the laboratory setup for noise, IV, power consumption and source measurements with IR camera and fan/heat gun pointed at the backside of the chip board.

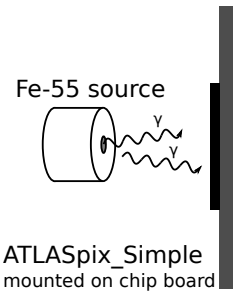

Figure 6.9: Illustration of the laboratory setup with an Fe-55 source pointed at the sensor.

target. These X-rays are subsequently used to excite a secondary target, which is placed in front of the X-ray tube. By choosing different target materials, sharp K_α peaks with well-defined energies are generated. The ATLASpix is then exposed to the X-rays and operated using the Caribou system as described above. The intensity of the X-ray tube is controlled by the cathode current. A schematic drawing of the setup is shown in Figure 6.10.

An energy of 3.7 eV per electron-hole pair can be approximated for the relevant energy range of X-rays used for the measurements presented in this thesis [115]. Thus, the number of electron-hole pairs created by an absorbed X-ray of a given energy can be calculated. A summary is shown in Table 6.2. The absorption depth in silicon, describing the distance after which a fraction of $1/e$ of the photons is absorbed, is illustrated in Figure 6.11.

It shows that for a silicon thickness below 85 µm as for the used ATLASpix samples[1] (see Table 6.1), a majority of the photons for the Ca, Ti, Fe and Cu target are absorbed in the sensor material. The absorption depth of Pb already exceeds the sensor thickness meaning that only a small fraction of photons interact in the sensor volume. For Zr and In, the absorption depth is even larger. This implies that the energy range of this measurement approach is limited. For larger X-ray energies, the number of absorbed photons reduces significantly, which requires longer data taking times to acquire a similar amount of statistics.

The line widths of the K_α peaks are in the order of electron volts [119], i.e. the relative widths are on the permille level and are therefore negligible within the precision of all measurements presented in this thesis. On the other hand, the X-rays

[1]This represents an upper limit given by the silicon thickness. The actual active volume is even thinner than this as discussed in Section 11.7.

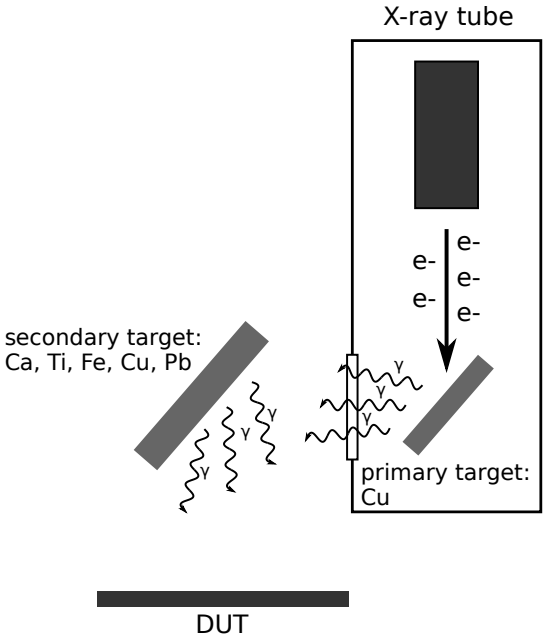

Figure 6.10: Illustration of the setup used for the energy calibration with X-rays.

Table 6.2: Target materials, energies of Kα X-ray fluorescence peaks, absorption depth, and deposited charge in silicon (* not available). Data from [116, 117, 118].

Target Material	Energy of Kα [keV]	Absorption depth [µm]	Deposited charge [e^-]
Ca	3.69	8	997
Ti	4.51	14	1219
Fe-55 (source)	5.9	29	1595
Fe	6.4	42	1730
Cu	8.09	66	2186
Pb (Lα)	10.5	155	2838
Zr*	15.77	430	4264
In*	24.14	1400	6534

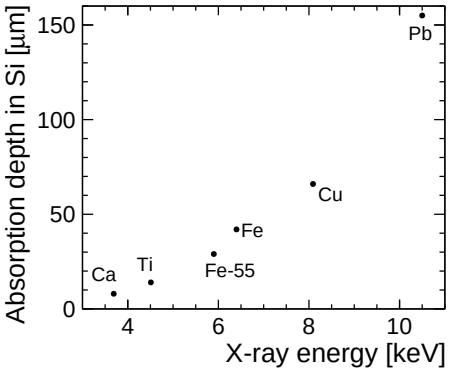

Figure 6.11: Absorption depth of X-rays in silicon for different energies. Data from Table 6.2

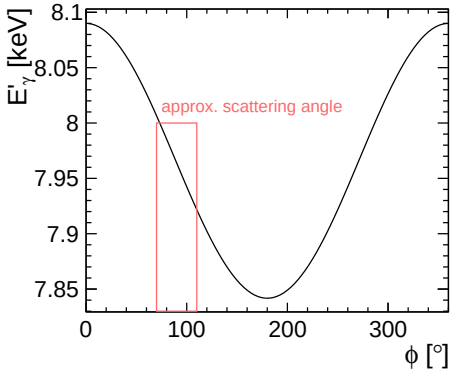

Figure 6.12: Energy of scattered K_α X-rays from the Cu target E'_γ for different scattering angles ϕ, calculated with Equation 6.5.

impinging on the sensor are not exclusively from the K_α peaks of the secondary target. They are superimposed with Compton-scattered primary X-rays from the Cu target inside the X-ray tube. The energy of an outgoing scattered photon E'_γ is given by [44]

$$E'_\gamma(\phi) = \frac{E_\gamma}{1 + \frac{E_\gamma}{m_e c^2}(1 - \cos(\phi))}. \tag{6.5}$$

It depends on the initial photon energy E_γ and the scattering angle ϕ. m_e is the electron mass and c denotes the speed of light in vacuum.

The scattering angle in the setup (see Figure 6.10) was not determined precisely but is estimated to be approximately 70-110°. Consequently, the spectrum incident on the DUT can contain photons in the energy range of 7.9-8.0 keV as indicated in Figure 6.12. In addition, photons from the bremsstrahlung spectrum of the primary target may be scattered and detected as well. Previous measurements show that these contaminant X-rays are present in the obtained spectrum but cannot easily be quantified [120, 121].

Chapter 7

Test-beam Facilities & Reference Telescopes

Within the scope of this thesis, test-beam campaigns have been conducted at CERN near Geneva (Switzerland) and at DESY in Hamburg (Germany). This chapter presents the test-beam facilities and the experimental setups used to acquire the data shown in this thesis. The results are shown in Chapter 11.

7.1 The Super-Proton Synchrotron at CERN

Part of the data recorded and analysed within the scope of this thesis has been recorded at the Super-Proton Synchrotron (SPS) at CERN. The SPS is not only used as a pre-accelerator to fill the Large Hadron Collider, but it also provides particles for a range of smaller experiments and it serves as a test-beam facility.

It has a circumference of around 7 km and accelerates protons to energies of up 450 GeV [122]. Part of the protons is extracted and directed onto a target in order to produce secondary particles. These are provided to multiple beamlines in the experimental hall at which independent measurements can be performed. The particle beam used for the measurements presented in this thesis consists of charged pions π^+ with a momentum of 120 GeV/c.

7.2 The Reference Telescope at the SPS

The data recorded and analysed for this work was acquired with the *Timepix3 reference telescope* of the CLICdp collaboration [10, 123]. It is based on the LHCb Timepix3 telescope [124] and located in the H6 beamline of the experimental hall in the North Area at CERN.

A photograph and a schematic of the telescope setup are shown in Figures 7.1 and 7.2. Its components are described in the following:

- The **Trigger Logic Unit (TLU)**[124] (shown in yellow) provides a global clock of 40 MHz as well as a time reset *T0* to all subsystems and thus allows for a time synchronisation between the individual subsystems.

- The **Timepix3 reference telescope** (shown in black) consists of seven planes of Timepix3 readout chips [125], which are bump-bonded to p-in-n silicon sensors with a thickness of 300 µm. Each Timepix3 consists of a matrix of 256×256 pixels with a pitch of 55×55 µm^2 resulting in an active area of 198 mm^2. The sensors were operated fully depleted at a bias voltage of 50 V. p-in-n type sensors were chosen for cost reasons and production capabilities [126]. This means that the signal is induced by the collection of holes, which is intrinsically slower than electrons (see Section 4.1).

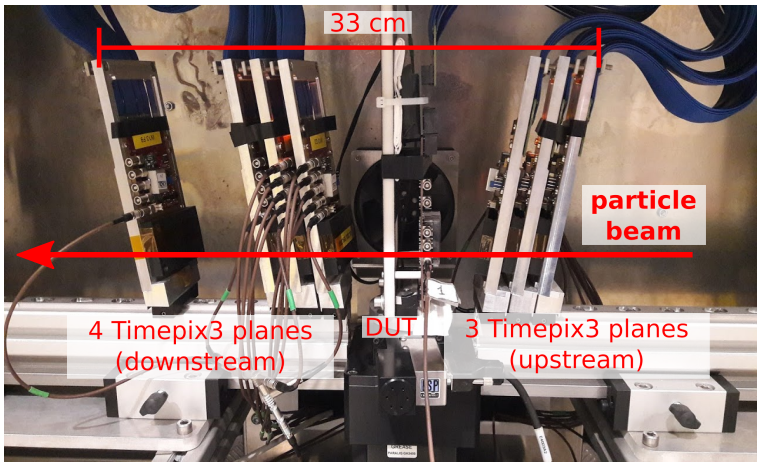

Figure 7.1: Photograph of the CLICdp Timepix3 telescope at the SPS, CERN.

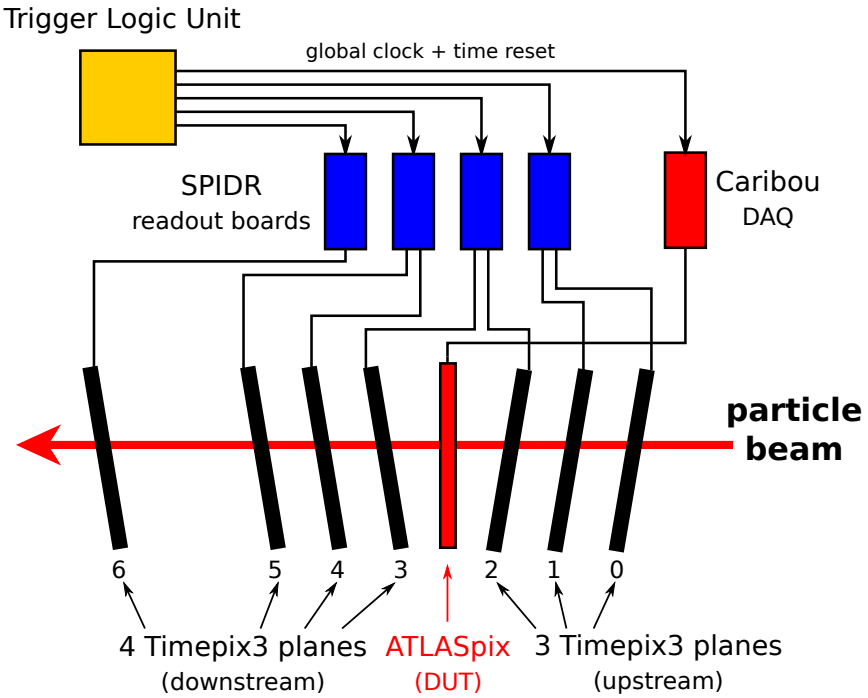

Figure 7.2: Schematic drawing of the CLICdp Timepix3 telescope setup used at the SPS (CERN).

In addition to the pixel address, the Timepix3 provides a time-of-arrival (ToA) with a binning of 1.5625 ns (640 MHz) and a time-over-threshold (ToT) measurement with a range of 10-bit (0-1023) for each hit. As can be seen in Figure 7.2, the telescope planes are rotated by $\pm 9^\circ$ around the x- and y-axes (the beam defines the z-axis) so that the signal induced by a traversing particle is detected by multiple pixels from geometrical considerations (see Section 4.1.1). This improves the achievable spatial resolution by increasing the amount of charge sharing [127]. The telescope is controlled and read out using the SPIDR DAQ system [128]. Hits from the telescope planes are combined into reference tracks as will be discussed in Section 8.2.4.

- As the **device-under-test (DUT)** different **ATLASpix_Simple** samples (shown in red) have been operated. These have been introduced in detail in Chapter 5.

The telescope is positioned such that the particle beam traverses the sensor planes approximately parallel to the telescope axis as indicated in Figure 7.2. It reaches a tracking resolution of $\sim$1.75 µm at the position of the DUT with a timing precision of $\sim$560 ns as will be shown in Section 9.1.

7.2.1 Telescope Coverage of the DUT

Figure 7.3 shows a true-to-scale schematic drawing of a Timepix3 telescope plane and the ATLASpix. The Timepix3 is much wider than the DUT in the horizontal direction. However, in the vertical direction, the ATLASpix protrudes from the telescope. As a consequence, not the entire ATLASpix chip can be characterised using one single alignment, but at least two complementary data sets need to be combined to cover the entire chip. In principle, a complete telescope coverage could be achieved by a rotation of the DUT around the beam axis by 45°. However, this was not possible due to mechanical constraints of the experimental setup.

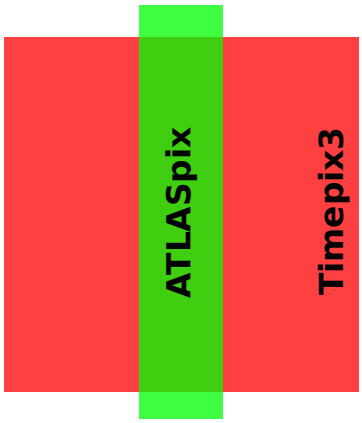

Figure 7.3: True-to-scale schematic drawing showing the telescope coverage of the DUT for the setup used at the SPS. The rotation of the telescope planes by $\pm 9^\circ$ in both x- and y-direction is taken into account in the projection.

Table 7.1 summarises the dimensions of the telescope and the DUT. Due to the rotation of the telescope planes by $\pm 9^\circ$ in both x- and y-direction, the telescope acceptance is slightly reduced by a factor of $\cos^2(9^\circ)$. Comparing the acceptance of the telescope with the area of the DUT, it can be seen that for a maximum of 23 % of all reconstructed tracks an associated hit may be found on the DUT. A misalignment of the telescope planes relative to each other may slightly reduce this number. Vice versa, the telescope covers a maximum of 88 % of the DUT area for an ideal alignment.

Table 7.1: Telescope and DUT dimension and coverage for the setup used at the SPS. The rotation of the telescope planes is taken into account by the $\cos^2()$-term.

	Width	**Height**
Timepix3	$256 \times 55\,\mu\text{m} = 14.08\,\text{mm}$	$256 \times 55\,\mu\text{m} = 14.08\,\text{mm}$
ATLASpix	$25 \times 130\,\mu\text{m} = 3.25\,\text{mm}$	$400 \times 40\,\mu\text{m} = 16.00\,\text{mm}$
Area for tracking	$198.2\,\text{mm}^2 \times \cos^2(9^\circ) = 193.3\,\text{mm}^2$	
DUT/telescope overlap	$45.8\,\text{mm}^2 \sim 23\,\%$	
DUT coverage	$\sim 88\,\%$	

7.3 The DESY II Test-beam Facility

Due to the Long Shutdown 2 of the accelerator complex at CERN during 2019-2021, part of the data recorded and analysed for this work has been acquired at the test-beam facility [129] at DESY (Deutsches Elektronen-Synchrotron) in Hamburg.

The DESY II synchrotron has a circumference of about 300 m and accelerates electrons or positrons to energies of up to 7 GeV. There are three independent test-beam areas called TB21, TB22 and TB24 as illustrated in Figure 7.4. For these, the test-beams are generated by a double-conversion: The DESY II beam hits a primary target along its orbit such that bremsstrahlung photons are generated. These impinge on a secondary target where electron/positron pairs are created. A dipole magnet is used to select the desired particle polarity and momentum between 1-6 GeV/c.

All data analysed within the scope of this thesis was recorded using electrons with a momentum of 5.4 GeV/c.

7.4 The Reference Telescopes at DESY

In each of the three areas, EUDET-type pixel sensor tracking telescopes [130] called *DATURA* (TB21), *DURANTA* (TB22) and *AZALEA* (TB24) are installed for users. They are used to reconstruct reference particle tracks and their performance is discussed in detail in Section 9.2. A schematic drawing is shown in Figure 7.5. The data acquisition (DAQ) was controlled via the EUDAQ2 software framework [131]. The components of the telescopes are described in the following:

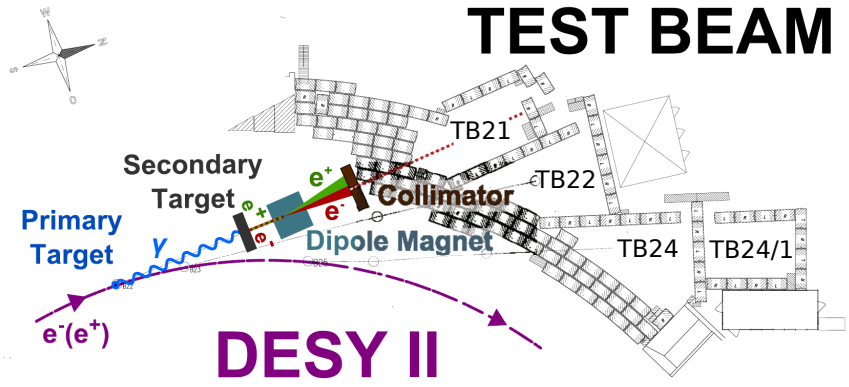

Figure 7.4: Schematic drawing of the DESY II test-beam area with the test-beam areas TB21, TB22 and TB24. From [129] (modified).

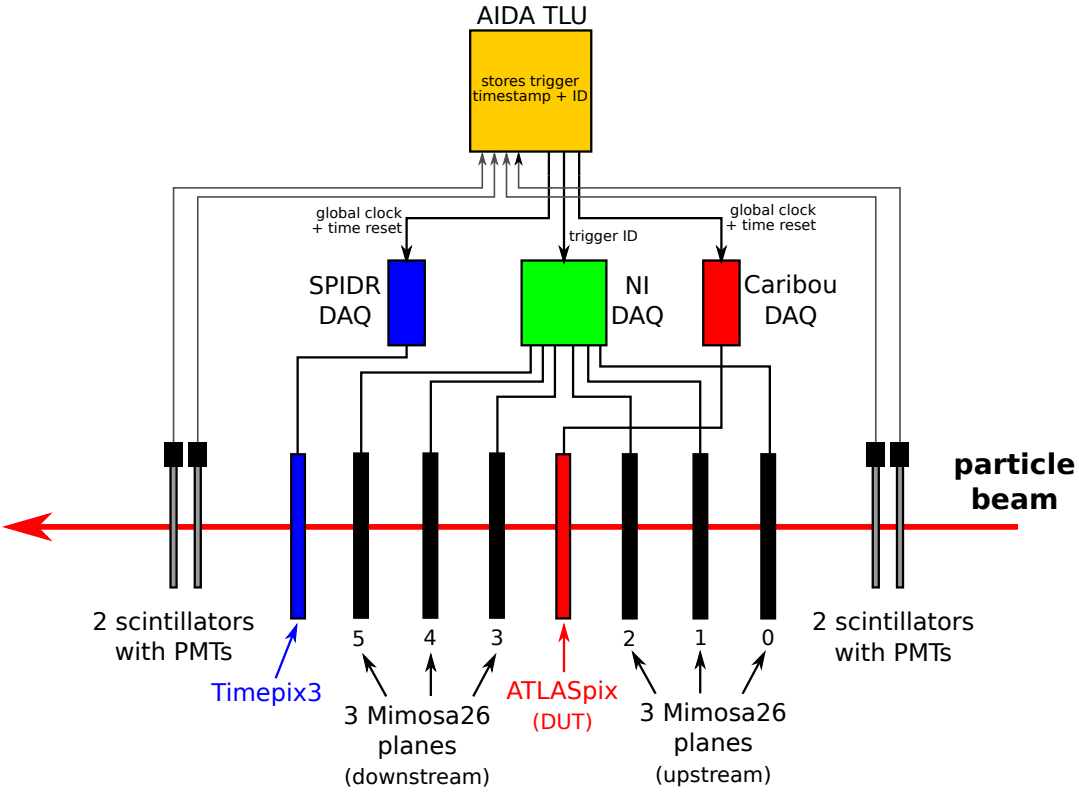

Figure 7.5: Schematic drawing of the EUDET-type telescopes with DUT used at DESY.

- The **AIDA Trigger Logic Unit (TLU)** [132] (shown in yellow) distributes a global clock and a global time reset, and receives input signals from two to four scintillators. For these, Hamamatsu PMT assemblies with scintillating tiles and lightguides with an acceptance of $20 \times 10\,\text{mm}^2$ are used [133]. When a coincidence is detected, it generates a trigger ID, records a trigger timestamp and ID, and sends out the trigger ID to the NI DAQ of the Mimosa26 planes (see below).

- The EUDET-type reference telescope [130] consists of six monolithic **Mimosa26** sensors (shown in black) [134, 135]. Each sensor has a thickness of 50 µm and

an active matrix of 1152×576 pixels with a pitch of 18.4×18.4 µm^2 resulting in an active area of 225 mm^2. They are read out by the NI DAQ system in a continuous rolling shutter mode with a periodicity of 115.2 µs. Only when a trigger signal is received, the data of the corresponding shutter period and one additional shutter period ($2 \times 115.2\,\mu m = 230.4\,\mu s$) are stored. The trigger is provided by the TLU and the associated trigger ID is recorded together with the data to allow for an offline synchronisation with the other detectors. Individual pixel timestamps are not available so that all pixels stemming from a possible time interval of 230.4 µs are associated to one trigger. Hits from Mimosa26 planes and the Timepix3 (see below) are combined into reference tracks as will be discussed in Section 8.3.3.

- A **Timepix3** hybrid silicon pixel detector assembly [125] (shown in blue) is operated as a timing reference plane. An n-in-p type sensor with a thickness of 100 µm is bump-bonded to the Timepix3 readout ASIC and biased −20 V. This leads to a signal generation by electron collection, which is intrinsically faster than hole collection (see Section 4.1). The recorded pixel timestamps with a binning of 1.5625 ns are used to assign unambiguous track timestamps as will be discussed in Section 8.3.3. As a data-driven device it is always active and sends its pixel hits off to the SPIDR DAQ system [128] directly after detection without the need of an external trigger signal. The sample properties and operating conditions of the used Timepix3 assembly are summarised in Table 7.2.

- As the **device-under-test (DUT)** different **ATLASpix_Simple** samples (shown in red) have been operated. These have been introduced in detail in Chapter 5.

As indicated in Figure 7.5, the telescope is aligned such that the particle beam traverses the sensor planes approximately parallel to the telescope axis. The track pointing resolution of the reference telescope is approximately 2.4-5.4 µm and depends significantly on the spacing of the telescope planes as well as the material budget of all detectors along the beam. It is discussed in more detail in Section 9.2.

Table 7.2: Summary of the sample properties and operation conditions of the used Timepix3 assembly. A detailed characterisation can be found in [136, 137].

Sample name	W5_E2
Sensor type	n-in-p
Sensor thickness	100 µm
Threshold	900 e^-
Bias voltage	−20 V
Calibration	timewalk + energy calibration based on laboratory data [136]

7.4.1 Telescope Coverage of the DUT

Figure 7.6 shows a true-to-scale illustration of the overlap of the Timepix3 with the Mimosa26, i.e. the area in which tracks can be reconstructed, as well as the overlap with the DUT. Due to the usage of the Timepix3 timing layer, the telescope acceptance for tracks is reduced as indicated by the yellow box. Furthermore, not the entire DUT can be covered similarly to the telescope used at the SPS. Table 7.3 summarises the dimensions of the detectors of the telescope and the DUT. For a larger coverage it is rotated by 90° around the beam axis compared to the setup used at the SPS, which was discussed in Section 7.2.1.

For a maximum of 30 % of all tracks, an associated hit on the DUT may be found. Misalignments between the telescope planes and the DUT can reduce this number slightly. Like for the Timepix3 telescope at the SPS, the telescope covers 88 % of the DUT area. For rotations of the DUT larger than 28° in column direction as it is done for part of the studies conducted at DESY, the coverage reaches 100 %.

Table 7.3: Telescope and DUT dimension and coverage for the setup used at DESY.

	Width	**Height**
Mimosa26	$1152 \times 18.4\,\mu m = 21.20\,mm$	$576 \times 18.6\,\mu m = 10.71\,mm$
Timepix3	$256 \times 55\,\mu m = 14.08\,mm$	$256 \times 55\,\mu m = 14.08\,mm$
ATLASpix	$25 \times 130\,\mu m = 3.25\,mm$	$400 \times 40\,\mu m = 16\,mm$
area for tracking	$149.2\,mm^2$	
DUT/telescope overlap	$45.8\,mm^2 \sim 30\,\%$	
DUT coverage	88 %	

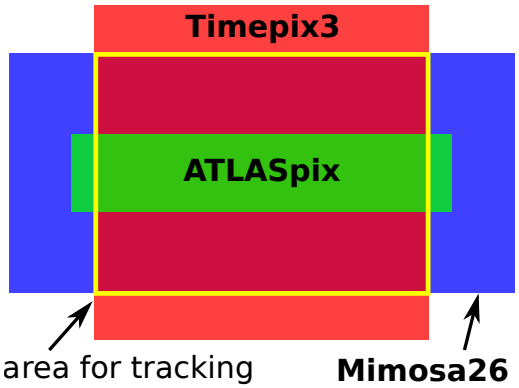

Figure 7.6: True-to-scale schematic drawing showing the telescope coverage of the DUT for the setup used at DESY. The ATLASpix is rotated by 90° with respect to the SPS setup (see Figure 7.3).

Chapter 8

Test-beam Reconstruction & Analysis

The reconstruction and analysis of the test-beam data recorded at the CERN SPS and DESY was performed using the *Corryvreckan* framework. In this chapter, the framework is introduced and all steps of the reconstruction chain are presented and discussed.

Some of the following passages have been published in [138] and parts of this section use the exact same wording.

8.1 Corryvreckan: The Reconstruction and Analysis Software

The *Corryvreckan* framework [139, 140, 141] is a modular and configurable software for the reconstruction and analysis of laboratory and test-beam data and was initially developed in the framework of the *CLIC Detector & Physics (CLICdp)* collaboration [142] at CERN.

The software is capable of performing all steps of a test-beam analysis. Each step of the reconstruction is performed by a dedicated module, which can be configured by the user. The individual reconstruction steps are discussed in detail in Section 8.2 for the data taken at the SPS and in Section 8.3 for test-beam studies conducted with data taken at DESY.

Within the scope of this thesis, major contributions were made to the development, maintenance and documentation of the *Corryvreckan* framework. More details about the framework can be found in the user manual [143, 144] and in [138, 139].

The software was verified through multiple independent groups, e.g. by comparing analysis results obtained with *Corryvreckan* and another widely used reconstruction and analysis framework, *EUTelescope* [133]. Relevant presentations and tutorials can be found on the project website [140].

8.2 Reconstruction of Data Recorded at the SPS

The setup used to acquire data at the SPS is presented in Section 7.2. The reconstruction chain is depicted in Figure 8.1. In the following, all steps of the analysis and the relevant selection cuts are presented and discussed. The corresponding *Corryvreckan* configuration files can be found in Appendix B.1.

8.2.1 Event Building

All sensor planes of the Timepix3 telescope at the SPS provide pixel hit addresses as well as pixel timestamps and are read out continuously. Consequently, the data stream of pixel hits is continuous and does not contain any intrinsic definition of an event as it would be the case e.g. for shutter-based devices such as the Mimosa26 sensors used at DESY (see Section 7.4).

Therefore, the data stream is divided into even time intervals with a fixed length using the *Corryvreckan* module `Metronome` as illustrated in Figure 8.2. The pixel hits of all Timepix3 planes as well as the ATLASpix are then added by the respective `EventLoader` modules based on their individual pixel timestamps and the entire analysis is performed for one event before proceeding to the next. The event length is set to 20 µs. It should be chosen small enough to avoid too large hit multiplicities within one frame leading to excessive combinatorics in the correlations. On the other hand, in the final analysis a time cut is applied to ensure that the analysis is not biased by effects close to the edges of the event (see Section 8.2.6). Hence, it should be chosen large enough to avoid that too many tracks are discarded when they have timestamps too close to the event edge.

Masking

At this stage, noisy pixels of the telescope planes are excluded from the analysis ("masked") based on previous studies [145]. No masking is applied to the DUT.

8.2.2 Clustering

As described in Section 4.1, charge created by one traversing ionising particle may be collected in two or more adjacent pixels. Particles impinging on the sensor under an angle lead to charge sharing from geometrical considerations.

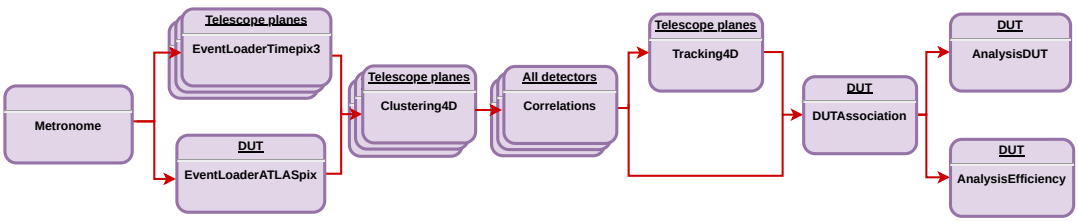

Figure 8.1: Flow chart of the full *Corryvreckan* reconstruction and analysis chain for the SPS analysis.

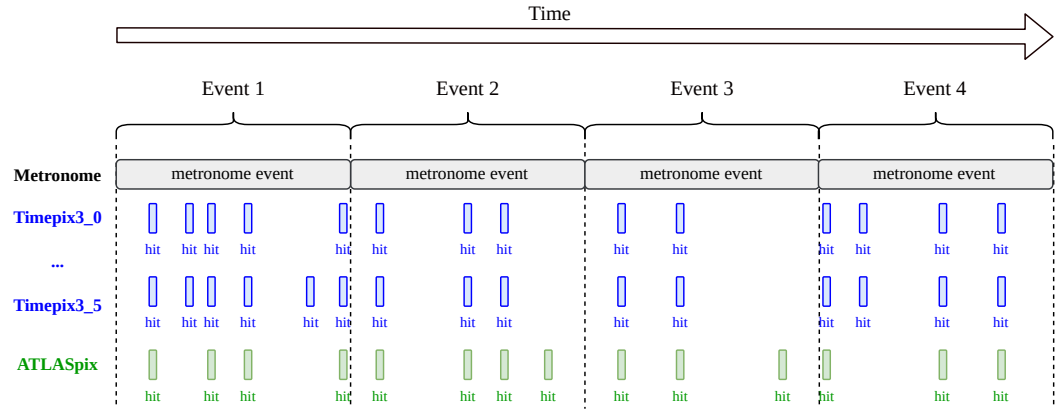

Figure 8.2: Schematic of the event building logic based on the `Metronome` for the Timepix3 telescope at the SPS. Pixel hits from the Timepix3 planes as well as the ATLASpix are added to an event based on their indiviual pixel timestamps.

Clustering is performed individually for each detector plane using the *Corryvreckan* module `Clustering4D`:

Timepix3 planes

For the Timepix3 planes, adjacent pixels (including pixel corners) are grouped into a cluster, if their timestamps lie within a time interval of 200 ns. This means that no split clusters are allowed. The time cut is motivated empirically by the in-cluster time distribution shown in Figure 8.3, in which the time difference between all secondary pixels within a cluster and the seed pixel, i.e. the pixel with the largest ToT within the cluster, is drawn versus the ToT of the secondary pixel. The effect of timewalk can be clearly observed as pixels with a smaller ToT show a larger ("later") timestamp with respect to the pixel with the largest ToT. Furthermore, a clear separation into two populations is observed in the distribution. Negative time differences $t_{\text{pixel}} - t_{\text{seed pixel}} < 0$ correspond to clusters for which seed pixel, i.e. the pixel with the largest ToT, is not the earliest pixel in the cluster.

This effect is explained as follows: As described in Section 7.2, the Timepix3 planes are rotated by $\pm 9^\circ$ around the x- and y-axis (the z-axis defines the beam direction). Due to the sensor thickness of 300 µm, which is fully depleted at 50 V, and a pixel pitch of $55 \times 55\,\mu\text{m}^2$, charge deposition in a single pixel is unlikely from geometrical considerations as illustrated in Figure 8.4. Because p-in-n type sensors are used, the signal is generated by holes collected on the frontside, which is intrinsically slower than electron collection due to the lower charge carrier mobility (see Section 3.2.2). If the charge deposition within a pixel is closer to the backside of the pixel, this results in a much larger drift time compared to a charge deposition close to the frontside.

The so-called *small pixel effect* occurs when the sensor thickness is significantly larger than the pixel pitch [146]. It describes the effect that most of the signal is

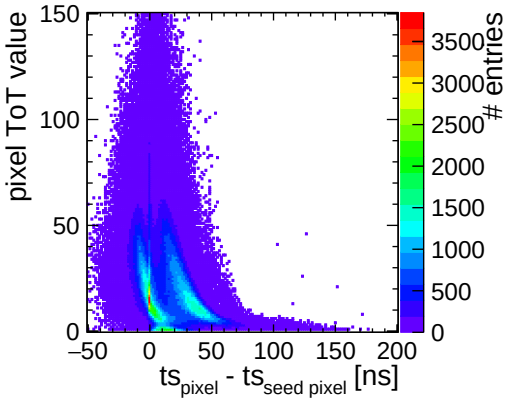

Figure 8.3: In-cluster time distribution distribution vs. the pixel ToT for the Timepix3_2. The distributions for all other planes look similar.

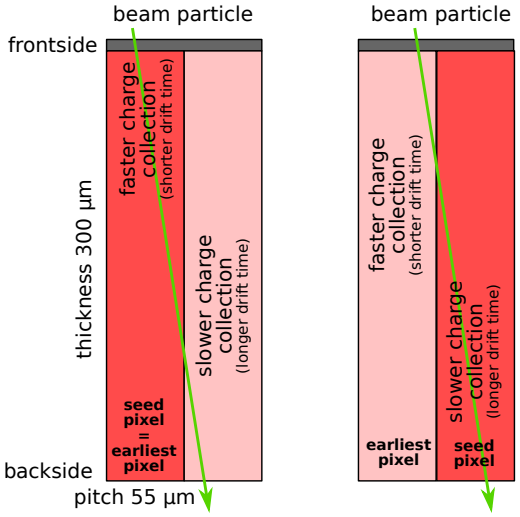

Figure 8.4: Illustration of the geometric effect that the pixel with the largest charge deposition does not always correspond to the earliest pixel in the cluster. Holes are collected on the frontside.

induced on the collection electrode only when the charge reaches a distance to the electrode, which is in the order of the pixel pitch.

This means that if the largest energy is deposited close to the frontside in one pixel and less energy in the neighbouring pixel, the pixel with the largest ToT corresponds to the earliest pixel in the cluster. Vice versa, if the largest charge is deposited closer to the backside of one pixel, and a smaller amount closer to the frontside of the neighbouring pixel, the pixel with the smaller signal can have an earlier timestamp than the seed pixel due to a shorter drift time of the holes. A more detailed analysis confirming this explanation is shown in Appendix C. The separation of the two populations by $\sim 20 - 25$ ns is related to the strength of the electric field due to the applied bias voltage. A larger bias voltage is expected to reduce the separation, while a smaller bias voltage would increase it [126, 147].

Figure 8.5 shows the cluster size distribution for the Timepix3_2 for different time cuts applied for the clustering. In agreement with the previous observation, the cluster size remains constant for time cuts larger than 150 ns and the number of single-pixel clusters starts to increase for smaller cuts as the "late" pixels in the right tail of the distribution in Figure 8.3 are separated. In consequence, a time cut of 200 ns is chosen and the cluster timestamp is defined as the earliest pixel timestamp within the cluster to mitigate the time spread from different drift times [124, 148]. The cluster position $\mathbf{x}_{\text{cluster}} = (x, y)_{\text{cluster}}$ is determined by calculating the ToT-weighted centre-of-gravity [124, 148]:

$$\mathbf{x}_{\text{cluster}} = \frac{\sum_{i=1}^{n} ToT_i \cdot \mathbf{x}_i}{\sum_{i=1}^{n} ToT_i} \tag{8.1}$$

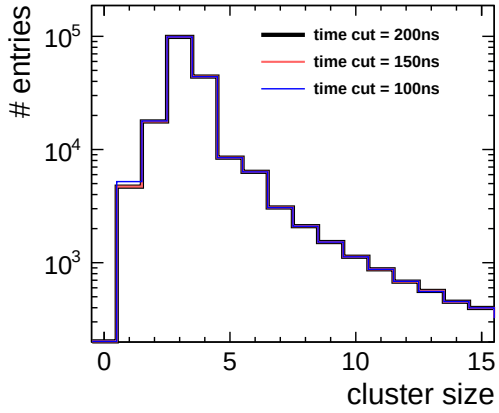

Figure 8.5: Cluster size distribution of Timepix3_2 for different time cuts.

for n pixels within the cluster. The cluster ToT corresponds to the sum of all pixel ToTs:

$$ToT_{\text{cluster}} = \sum_{i=1}^{n} ToT_i \tag{8.2}$$

ATLASpix

For the ATLASpix, nearest neighbour pixels (including pixel corners) are clustered if they coincide within a time interval of 300 ns. This number will be justified a posteriori in Section 11.3.6, where the cluster formation is investigated in detail. The cluster timestamp is defined by the earliest pixel within the cluster. Like for the Timepix3, the cluster ToT is calculated as the sum of all individual pixel ToTs according to Equation 8.2. However, the cluster centre is calculated as the arithmetic mean, which yields a better estimation for the track intercept compared to the ToT-weighted centre-of-gravity as will be discussed in the context of the spatial resolution in Section 11.4:

$$\mathbf{x}_{\text{cluster}} = \frac{1}{n} \sum_{i=1}^{n} \mathbf{x}_i \tag{8.3}$$

8.2.3 Correlations between Telescope Planes

The correlations in space and time between hits on the telescope planes are used to determine appropriate cuts for the track finding, which is discussed in the next step. Spatial correlations exist because the particle beam traverses the telescope approximately parallel to the telescope axis as described in Section 7.2. Correlations in time exist because a global clock is provided to all telescope planes by the TLU for time synchronisation (see Section 7.2).

Figure 8.6 shows exemplary spatial and time correlation plots between two planes of the reference telescope as obtained with the *Corryvreckan* module `Correlations`. The distributions for all other planes look similar. As can be seen, the vast majority

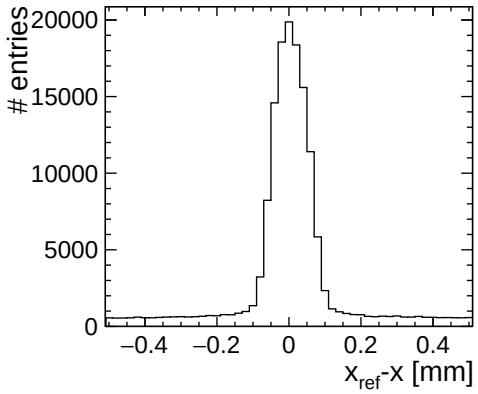

(a) Spatial correlation in x. The correlation in y looks similar.

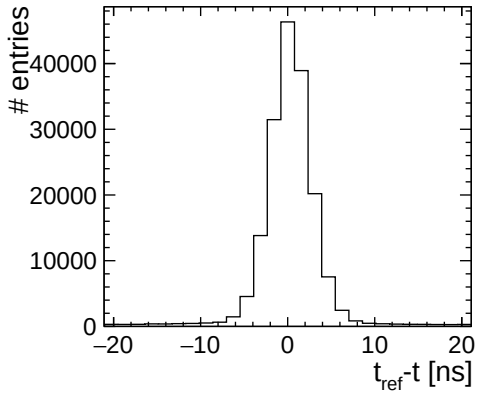

(b) Time correlation.

Figure 8.6: Correlations between all clusters on Timepix3_2 and Timepix3_3 (reference plane). The correlations between all other planes look similar.

of entries lies within a window of $\pm 200\,\mu m$ and $\pm 10\,ns$. The tails represent uncorrelated clusters stemming from independent tracks and noise hits.

8.2.4 Tracking & Track Quality

Tracking describes the reconstruction of a particle trajectory through the experimental setup. Tracks are be reconstructed based on the pixel hits on the detector planes of the reference telescope to study the properties of the DUT, which is excluded from the tracking to avoid a bias of the analysis. The track reconstruction consists of two consecutive steps: track finding and track fitting, which are performed by the *Corryvreckan* module `Tracking4D`.

Track Finding

During the track finding, clusters on the reference planes are combined into so-called track candidates as illustrated in Figure 8.7. For this, clusters on the first and second telescope plane are connected by a straight line, which is extrapolated onto the third telescope plane. If a cluster can be found within a defined spatial and time interval, it is added to the track candidate and the straight line is refitted. Iteratively, this process is repeated for all further telescope planes.

Track Fitting

For high beam momenta, such as at the SPS at CERN, a *straight-line track fit* is appropriate for an accurate fit of the particle trajectory through the telescope because the effect of multiple scattering is negligible. Each track candidate is fitted by a minimisation of the track χ^2:

$$\chi^2 = \sum_{i=0}^{n_{meas}} \left[\frac{(x_{\mathrm{t,i}} - x_{\mathrm{c,i}})^2}{\sigma_{x,i}^2} + \frac{(y_{\mathrm{t,i}} - y_{\mathrm{c,i}})^2}{\sigma_{y,i}^2} \right], \tag{8.4}$$

where $x/y_{t,i}$ denotes the track intercept on plane i and $x/y_{c,i}$ the position of the cluster that is part of the track. $\sigma_{x/y,i}$ correspond to the uncertainties of the cluster position, i.e. the single-plane resolution. The principle is depicted in Figure 8.8.

Selection Cuts & Track Quality

Track candidates are formed from clusters on all planes that coincide within a circular spatial cut of $\pm 200\,\mu m$ and a time window of $\pm 10\,ns$ derived from the width of the correlations (see Section 8.2.3). As shown in Figure 8.9, the distribution peaks at $\chi^2/ndof = 1.0$ and falls off for higher values of $\chi^2/ndof$. Hereby, $ndof$ denotes the number of degrees of freedom of the fit. It can also be seen that doubling the spatial and time cuts to 400 µm and 20 ns leads to a slight increase in the total number of reconstructed tracks. However, the majority of these additional tracks have a large $\chi^2/ndof$ and would thus be excluded from the further analysis for which only tracks with $\chi^2/ndof < 3.0$ are accepted. They are expected to arise from track candidates

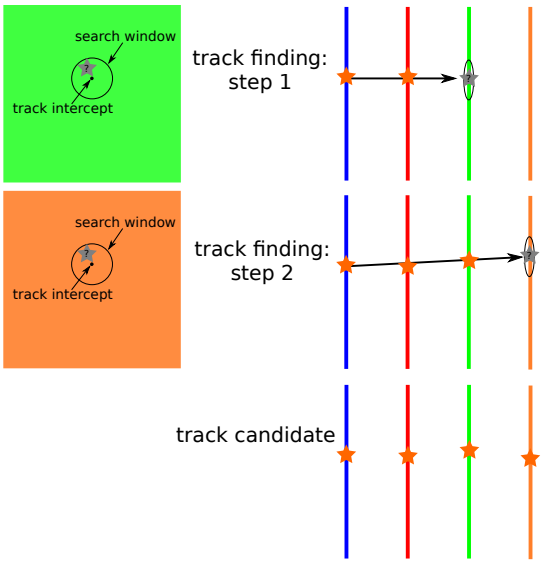

Figure 8.7: Schematic illustration of the iterative track finding.

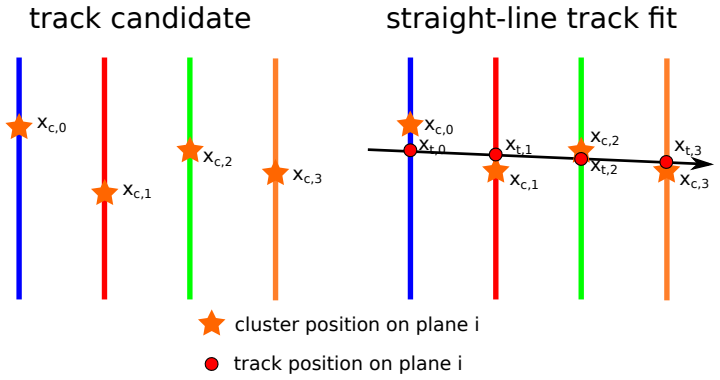

Figure 8.8: Schematic illustration of the track fitting using a straight-line fit. $x_{c,i}$ and $x_{t,i}$ mark the positions of the clusters and calculated track incidence points on each plane.

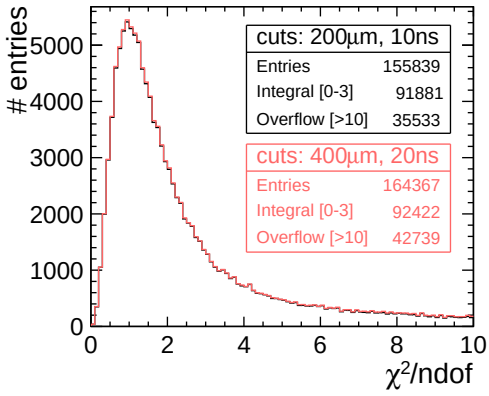

Figure 8.9: Comparison of the track $\chi^2/ndof$ distribution for a straight-line track fit using different spatial and time cuts for track finding.

formed from uncorrelated hits and/or fake hits, and particles undergoing a large amount of multiple scattering.

8.2.5 Track-based Telescope Alignment

In order to achieve the previously presented track $\chi^2/ndof$ distribution, a track-based telescope alignment is performed. For this, the *Corryvreckan* reconstruction chain is altered as shown in Figure 8.10.

In a first step, the module `Prealignment` is used to perform a translational pre-alignment. The positions of the telescope planes are shifted in x and y by subtracting the offsets from zero obtained from spatial correlations between all planes. One plane, marked as the reference plane, is not moved. This provides the starting point for a track-based alignment with the `AlignmentTrackChi2` module. The positions (x and y) and rotations (around the x-, y- and z-axes) of all telescope planes are varied iteratively with respect to the reference plane and tracks are re-fitted repeatedly with the aim of minimising the sum of all track χ^2 using Minuit2 [149]. The alignment procedure is repeated until it converges and no further improvement in the width of the biased residuals on each plane is seen, and the track $\chi^2/ndof$ peaks at 1.0.

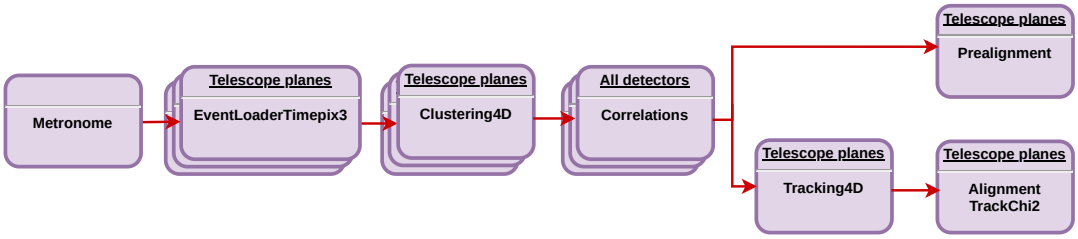

Figure 8.10: Flow chart of the *Corryvreckan* reconstruction chain for the SPS analysis used for the track-based alignment of the reference telescope.

8.2.6 Track-Hit Association for the DUT

Since the DUT is excluded from the tracking to avoid a bias on the analysis (see Section 8.2.4), its clusters need to be associated to the reference tracks in a separate step to be able to determine performance parameters such as the hit detection efficiency or the spatial and time resolution of the DUT as discussed below. For this, the track intercept with the DUT is calculated. Clusters within a defined spatial and time cut are associated to the track as illustrated in Figure 8.11. Since delta electrons can lead to larger clusters for which the cluster centre is shifted away from the track incidence point, the matching performed based on the clostest pixel within a cluster towards the track and not the cluster centre.

Association Cuts

Analogously to the track finding described in Sections 8.2.4, selection cuts are derived from the widths of the 1-dimensional correlation plots in space and time between all clusters on the ATLASpix and all reconstructed reference tracks. They are shown in black in Figure 8.12.

The vast majority of entries lies within an interval of $\pm 300\,\mu m$ in x and $\pm 150\,\mu m$ in y, and a time window of $\pm 200\,ns$. The different widths of the correlations in x and y reflect the elongated pixel geometry of $130 \times 40\,\mu m^2$. The tails arise from uncorrelated tracks and hits as well as noise hits. They are more prominent in the column

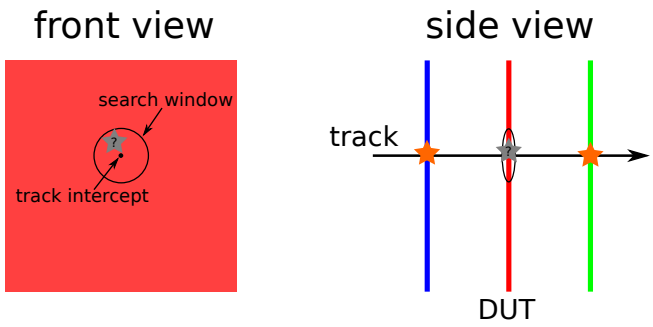

Figure 8.11: Illustration of the association of DUT clusters to a reference track.

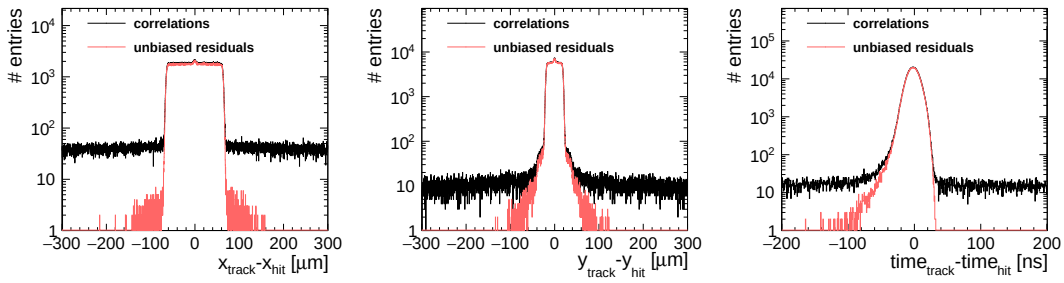

(a) Column direction. **(b)** Row direction. **(c)** Time.

Figure 8.12: Correlations and unbiased residuals between reference tracks and clusters on the ATLASpix at a bias voltage of $-75\,V$ and a threshold of $845\,mV \approx 716\,e^-$ after a track-based alignment (see Section 8.2.7).

direction because of the elongated chip geometry with 25×400 pixels, leading to more uncorrelated hits from different rows for a given column.

In red, the unbiased residuals are shown, meaning the distance in space and time between the extrapolated track intercept and the associated hit on the DUT (see Equation 8.11 in Section 8.4.2). As expected, the track association significantly reduces the number of entries in the tails, which arise from uncorrelated tracks and hits. On the other hand, the number of entries within the main peaks of the distributions are only slightly reduced as the peaks of the correlations may contain some hits which are uncorrelated in the other two dimensions. The residual distributions are investigated in detail in the context of the spatial resolution and the time resolution (see Section 8.4).

Time Cut at Event Edges

Due to the division of the continuous data stream into events with a constant length of 20 µs, it is possible that a track is reconstructed with a timestamp close to the edge of an event whereas the cluster on the DUT that physically corresponds to this track is reconstructed in a different event as illustrated in Figure 8.13. To avoid an influence on the analysis, e.g. a loss of the measured DUT hit detection efficiency, tracks with a time stamp too close to the event edge are discarded from the further analysis. A value of 200 ns is chosen as it should be greater or equal to the track-hit association cut in time. If more than one cluster on the DUT is found for one track within the spatial and time association cuts, the cluster closest in space to the track intercept point is used for the further analysis.

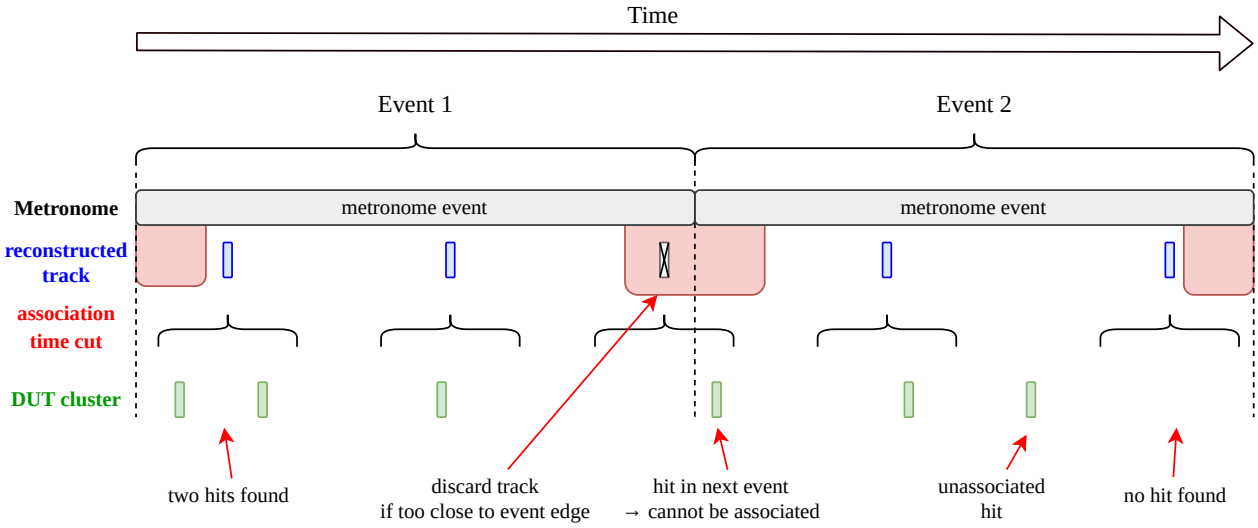

Figure 8.13: Schematic of the track-hit association in time. Tracks too close to the frame edges are discarded. Drawing is not to scale: the event length is 20 µs whereas the association time cut is 200 ns.

8.2.7 Track-Based Alignment of the DUT

In order to obtain the previously presented unbiased residuals, a track-based alignment of the DUT is performed in two steps. In a first step, the module `Prealignment` is used to perform a translational prealignment. The position of the DUT plane is shifted in x and y by subtracting the offsets from zero obtained from spatial correlations between DUT clusters and reference tracks. This provides a starting point for the track-based alignment using the module `AlignmentDUTResiduals`, which performs a minimisation of the widths of the spatial residuals on the DUT by iteratively varying the position and rotation of the DUT [150]. The alignment of the telescope and hence the reconstructed reference tracks is not changed. The procedure is repeated until it converges and no further change in the width of the unbiased spatial residuals is seen. The unbiased spatial residuals are discussed in Section 11.4 in the context of the spatial resolution.

8.2.8 Defining a Region-of-Interest

Regions-of-interest (ROIs) are defined depending on the particular goal of the different studies presented below. They are described and justified individually in each case. The ROI is applied to the track selection, i.e. only tracks penetrating the sensor within the ROI are used for the further analysis. This avoids a possible influence on the analysis results from edge effects and allows to focus on a particular area of the pixel matrix, e.g. to exclude regions with an increased cross-talk probability.

8.2.9 Influence of Noisy Pixels

The probability of matching a noise hit to a track ϵ_{noise} is given by Equation 8.9 (see Section 8.4.1). In Section 10.3, it was seen that the noise rate on the full chip remains below 3×10^5 Hz for all investigated samples and under all conditions. For association cuts of $\pm 300\,\mu\text{m}$ in x, $\pm 150\,\mu\text{m}$ in y, and $\pm 200\,\text{ns}$ in time as discussed in Section 8.2.6, this corresponds to probability below $1.62 \times 10^{-4} \approx 0.016\,\%$. Consequently, the accidental matching of a noise hit to a track is highly unlikely such that no offline masking during the analysis is required.

8.3 Reconstruction of Data Recorded at DESY

The setup used to acquire data at DESY is presented in Section 7.4. Due to the different readout scheme of the involved Mimosa26 planes of the EUDET telescope, the reconstruction chain is altered as depicted in Figure 8.14. Each step including the used selection cuts and configuration parameters is discussed in the following. The corresponding *Corryvreckan* configuration files can be found in Appendix B.2.

8.3.1 Event Building

The following description has been published in [138] and parts of this section use the exact same wording.

Event Definition

As the experimental setup consists of six triggered devices (Mimosa26) and two always-active data-driven detectors (Timepix3 and ATLASpix), a reasonable event definition should be based on the active time of the triggered devices. Outside of these active time windows, no hits are recorded on the Mimosa26 planes so that no reference tracks can be reconstructed.

Since the Mimosa26 data do not contain timestamps but only trigger IDs, their active time must be reconstructed using the AIDA TLU relating the trigger IDs to timestamps. Hence, the event building needs to start with the TLU defining an event with a trigger timestamp and a trigger ID, so that the Mimosa26 data can be matched by comparing the trigger ID. The event is then refined by spanning a time interval around the trigger timestamp covering the time in which the Mimosa26 hits may have been recorded.

According to the implementation of the rolling shutter readout scheme with a periodicity of 115.2 µs [134], this time span can cover a maximum of one cycle (115.2 µs)

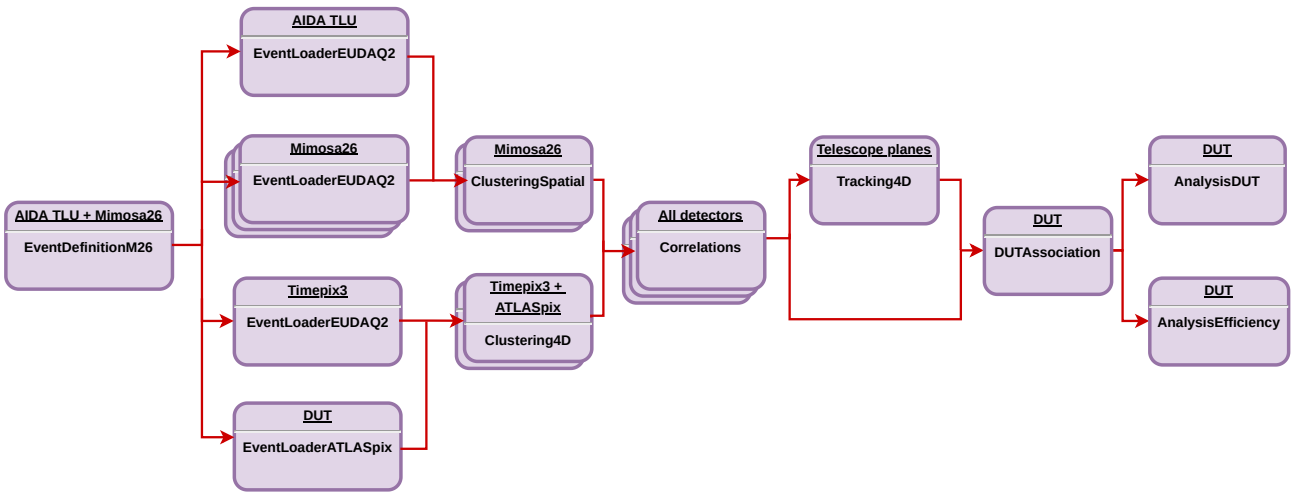

Figure 8.14: Flow chart of the full *Corryvreckan* reconstruction and analysis chain for the DESY analysis.

before and two cycles (230.4 µs) after the trigger time. The exact interval depends on the position of the rolling shutter at the moment when a trigger signal is received. The Mimosa26 data contains the information which pixel row the rolling shutter was passing when a trigger signal was received, the so-called *pivot pixel*. Using this information, the precise time interval with a duration of two readout cycles (230.4 µs) can be calculated relative to the trigger timestamp as illustrated in Figure 8.15. This event definition is performed using the *Corryvreckan* module `EventDefinitionM26`.

Adding Detector Data

Once the time extent of the event is defined, further detector data can be added. Based on the timestamp, additional TLU triggers (timestamp and ID) are added using the `EventLoaderEUDAQ2`. These may occur if the TLU detects further coincidences between the connected scintillators caused by additional traversing particles. The additional triggers within this event can be used for debugging purposes but are not relevant for the further analysis because they cannot issue a new readout cycle of the Mimosa26. During the event definition, only the pivot pixel information was extracted from the Mimosa26 data to obtain the correct time interval. Hence, the Mimosa26 pixel information is now added based on the trigger ID of the event using the `EventLoaderEUDAQ2`. Thereafter, hits from the data-driven detectors Timepix3 and ATLASpix are added to the event based on individual pixel timestamps, i.e. hits with timestamps earlier than the currently defined event are discarded, those with a later timestamp are kept for the next event, ensuring that a coherent block of data is used for the analysis. For the Timepix3, this is done using the `EventLoaderEUDAQ2` as it is fully integrated into the EUDAQ2 framework (see

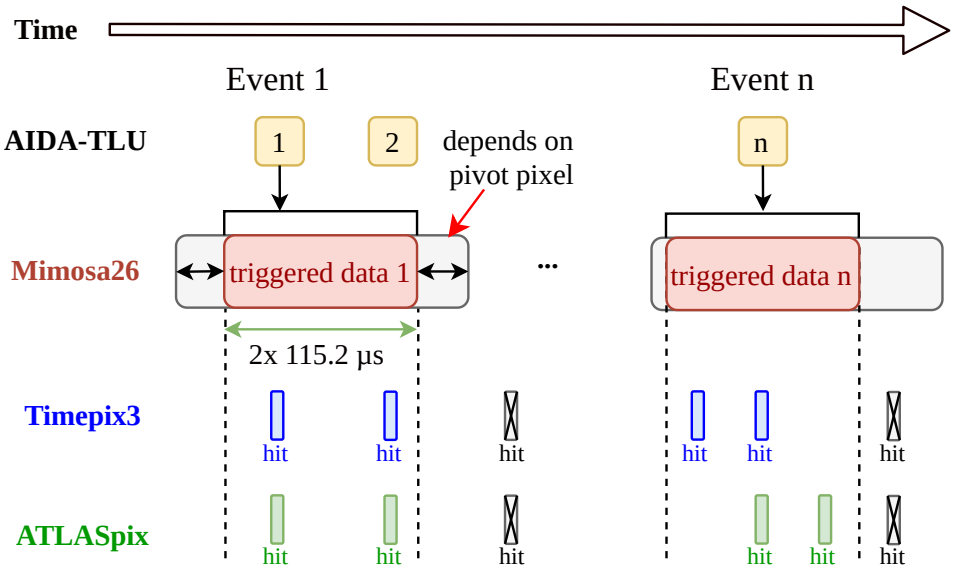

Figure 8.15: Schematic of the event building logic based on the triggers from *AIDA TLU* and the pivot pixel information from the Mimosa26 for the EUDET telescope at DESY. Subsequently, pixel hits from the Timepix3 planes as well as the ATLASpix are added to an event based on their indiviual pixel timestamps. From [138].

Section 7.4). The `EventLoaderATLASpix` is used for the ATLASpix, for which the data was recorded with the Caribou readout system (see Section 6.1).

Timepix3 Calibration

For the Timepix3 sample W5E2 used in this setup, calibration data for a timewalk correction of the pixel timestamps and a charge calibration of the pixel ToT based on laboratory measurements is available [136, 137]. It is applied directly to the raw pixel hits before any further reconstruction.

Masking

Noisy pixels of the telescope planes are excluded from the analysis ("masked") based on previous studies [145]. No masking is applied to the DUT.

8.3.2 Clustering

Clustering is performed for each detector plane individually:

Mimosa26

For the Mimosa26 planes, no individual pixel timestamps are available. For this reason, a time cut cannot be applied and the clustering is performed using spatial information only. The *Corryvreckan* module `ClusteringSpatial` is used to combine direct neighbours (including pixel corners) into a cluster. The cluster timestamp is defined as the trigger timestamp of the TLU corresponding to the trigger ID of the pixels within the cluster. The arithmetic mean of all pixels within the cluster is calculated as the cluster centre according to Equation 8.3, because no charge measurement is available. Figure 8.16 shows an exemplary cluster size distribution of the most upstream telescope plane Mimosa26_0. The distributions for the other telescope planes look comparable. A significant amount of charge is collected from the non-depleted region via diffusion [133]. This leads to a mean cluster size is significantly larger than one due to charge sharing. The shape of the distribution is in accordance with previous studies [145].

Timepix3

The clustering of the Timepix3 differs from the SPS reconstruction shown in Section 8.2.2. Using the *Corryvreckan* module `Clustering4D`, direct neighbours (including pixel corners) are combined if they lie within a time range of $\pm 100\,\text{ns}$. This search window is justified by the in-cluster time distribution shown in Figure 8.17. The sample operated at DESY shows a different timing behaviour with respect to the planes of the Timepix3 telescope used at the SPS (see Section 8.2.2) for the follow reasons: Firstly, the Timepix3 used at DESY is an n-in-p sample, meaning that the signal is generated by the collection of electrons. The planes of the Timepix3 telescope at the SPS are p-in-n type, such that hole collection is responsible for the

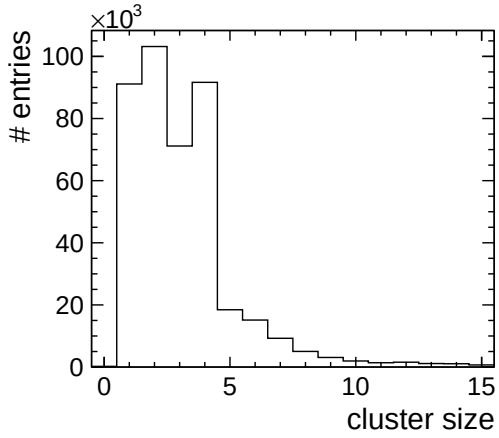

Figure 8.16: Cluster size distributions for Mimosa26_0. The cluster size distributions for the other Mimosa26 planes look similar.

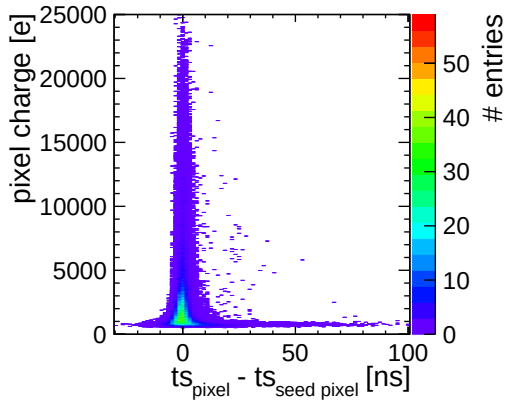

Figure 8.17: In-cluster time distribution vs. the pixel charge for Timepix3_0.

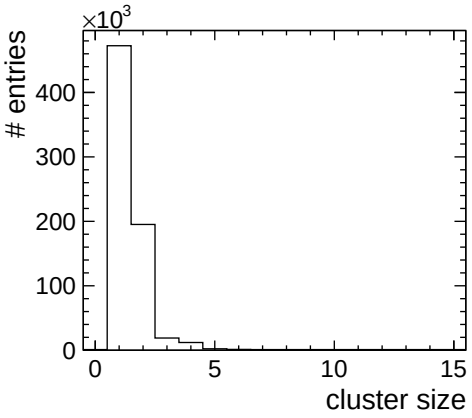

Figure 8.18: Cluster size distribution for Timepix3_0 used as the timing reference plane in the EUDET telescopes at DESY.

signal generation. The latter is intrinsically slower due to the smaller charge carrier mobility of holes compared to electrons. Secondly, a timewalk correction of each pixel timestamp is performed for the sample employed at DESY using a calibration from previous studies [136]. The cluster size distribution is shown in Figure 8.18. It is evident that the average cluster size is much smaller compared to the planes of the SPS telescope (see Figure 8.5). This has two reasons: Firstly, the telescope planes at the SPS are rotated by $\pm 9^\circ$ with respect to the beam axis to increase the cluster size and optimise the spatial resolution as discussed in Section 8.2.2. Secondly, the sensor thickness of 100 µm for the sample used at DESY does not allow for as much charge sharing as the samples of the SPS telescope with a thickness of 300 µm.

Because a charge calibration of the ToT is applied to this sample, the cluster centre is now determined as the charge-weighted centre-of-gravity and the cluster charge corresponds to the sum of all pixel charges. The cluster timestamp is determined by the pixel with the largest charge [136].

ATLASpix

The clustering of the ATLASpix is performed in the same way as for the SPS analysis as presented in Section 8.2.2, i.e. neighbouring pixels are clustered if they occur within a time range of $\pm 300\,\text{ns}$ and the earliest pixel is used to define the pixel timestamp. The cluster ToT corresponds to the sum of all pixel ToTs (Equation 8.2), and for the cluster centre, the arithmetic mean of all pixels is calculated (Equation 8.3).

8.3.3 Tracking & Track Quality

Multiple Coulomb scattering is a significant effect at DESY due to the lower beam momentum of 5.4 GeV compared to 120 GeV used at the SPS. Consequently, a *General Broken Lines* [151, 152] track fit is performed. It takes the single-plane resolution of each detector as well as uncertainties from multiple Coulomb scattering into account by allowing for a kink angle at each scatterer (detector plane or passive material) along the trajectory and performs a linear extrapolation between them. If a detector plane, such as the DUT, is excluded from the tracking, it is treated as a passive scatterer.

A two-dimensional offset $\mathbf{u} = (u_x, u_y)$ and kink angle $\mathbf{k} = (k_y, k_y)$ are defined at each scatterer. This allows to define the track χ^2 as the sum of the χ^2 for the measurement offsets χ^2_m and kink angles χ^2_k, which is minimised during the track fit [151]:

$$\chi^2 = \chi^2_m + \chi^2_k = \sum_{i=1}^{n_{meas}} \mathbf{r'}_i^T \mathbf{V}_{m,i}^{-1} \mathbf{r'}_i + \sum_{i=2}^{n_{scat}-1} \mathbf{k}_i^T \mathbf{V}_{k,i}^{-1} \mathbf{k}_i \tag{8.5}$$

Hereby, $\mathbf{r'}$ are the residuals in the curvilinear coordinate system, which is defined as the Cartesian coordinate system travelling along the particle trajectory such that the z-axis points in the direction of motion. $\mathbf{V}_m$ and $\mathbf{V}_k$ are the respective variance matrices. The principle is depicted in Figure 8.19.

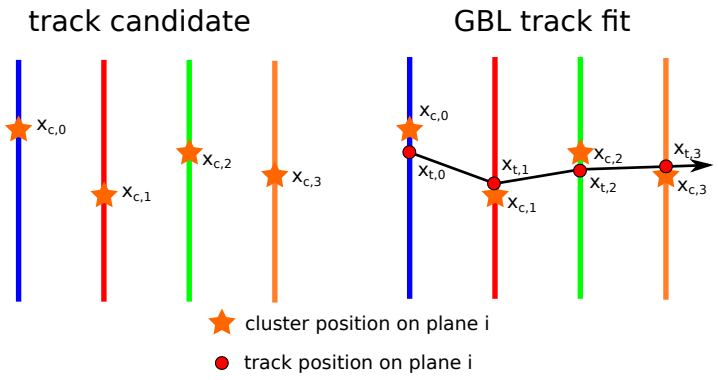

Figure 8.19: Schematic illustration of the track fitting using a GBL fit. $x_{c,i}$ and $x_{t,i}$ mark the positions of the clusters and the calculated track incidence points on each plane.

Selection Cuts & Track Quality

The track finding is performed in the same way as for the SPS analysis (see Section 8.2.4) by extrapolating a straight line through candidate clusters from two planes onto a third plane and then successively adding further planes. Hereby, it suffices to estimate the width of the correlations between adjacent planes due to the iterative procedure of the track finding. It can be seen in Figure 8.20, that the vast majority of entries lies within a window smaller than $\pm 200\,\mu m$ for the adjacent telescope planes Mimosa_2 and Mimosa_3 (reference). The consistency of this value was confirmed by successively assigning each of the telescope planes as the reference detector and repeating the analysis.

Consequently, track candidates are formed from clusters on all telescope planes that coincide within a circular spatial cut with a radius of 200 µm as derived from the correlations as shown in Figure 8.20. For the time cut, a value of $\pm 230.4\,\mu s$ is chosen in order to cover the extent of an entire event because Mimosa26 hits may stem from any time within the given event derived from the trigger timestamp and the pivot pixel as described above.

For the tracking, a hit on each telescope plane including the Timepix3 is required. No individual pixel timestamps are available for Mimosa26 hits and ambiguities arise from assigning one trigger timestamp to each of the Mimosa26 pixel hits. Each track candidate is fitted with a GBL track model and the timestamp of the Timepix3 hit is used to define a precise and unambiguous track timestamp. As shown in Figure 8.21, the $\chi^2/ndof$ peaks at 1.0 and falls off for larger values of $\chi^2/ndof$.

Doubling the spatial cuts for the track finding from $\pm 200\,\mu m$ to $\pm 400\,\mu m$ leads to an increase in the total number of reconstructed tracks. However, the number of tracks used for the further analysis (those with a $\chi^2/ndof < 3.0$) remains constant, whereas the number of tracks with a larger $\chi^2/ndof$ rises significantly, as seen in the

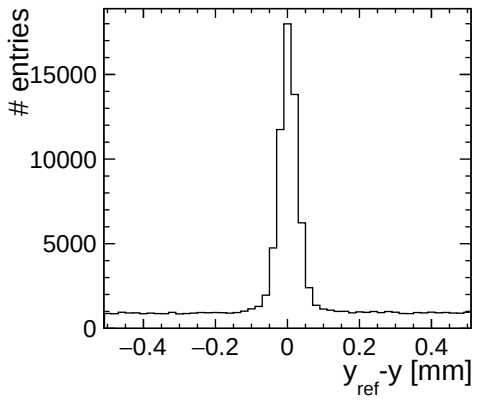

Figure 8.20: Spatial correlations in y between two consecutive Mimosa26 planes: Mimosa_2 and Mimosa_3 (reference). The correlations between all other consecutive planes look similar.

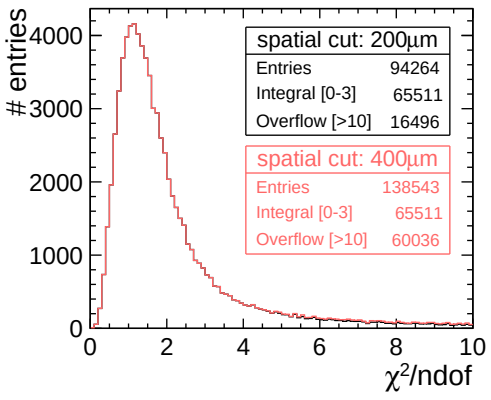

Figure 8.21: Comparison of the track $\chi^2/ndof$ distribution for a GBL track fit using different spatial association cuts for track finding.

right tail of the distribution and in particular in the overflow bin, which contains entries with a $\chi^2/ndof > 10$. The additional tracks stem from combinations of clusters from uncorrelated tracks or noise found through the larger search window.

8.3.4 Track-based Telescope Alignment

A track-based alignment was performed in order to achieve the previously shown track $\chi^2/ndof$ distribution. The alignment strategy is identical with the procedure performed for the SPS analysis (see Section 8.2.5).

8.3.5 Track-Hit Association for the DUT

In analogy to the analysis strategy for SPS data presented in Section 8.2.6, selection cuts for the track association of hits on the DUT are derived from the widths of the spatial and time correlations. They are shown in black in Figure 8.22 for all clusters on the DUT and all reference tracks penetrating the DUT. Even though it can already be seen that the timing behaviour differs between the samples with different substrate resistivities, a time cut of ± 200 ns is applied in all cases. From the spatial correlations it can be seen that most entries lie within a range of ± 300 µm in column direction and ± 150 µm in row direction.

The tails arise from uncorrelated tracks and clusters. They are more prominent in the column direction because of the elongated chip geometry with 25×400 pixels, leading to more uncorrelated hits from different rows for a given column.

In analogy to the SPS analysis, tracks with a time difference to the event boundaries smaller than the time association cut of 300 ns are rejected to avoid a possible drop of the measured efficiency as discussed in Section 8.2.6.

8.3.6 Track-based Alignment of the DUT

A track-based alignment was performed analogously as for the SPS data presented in Section 8.2.7.

8.3.7 Influence of Noisy Pixels

Like for the SPS analysis discussed in Section 8.2.9, the influence of noisy pixels is negligible.

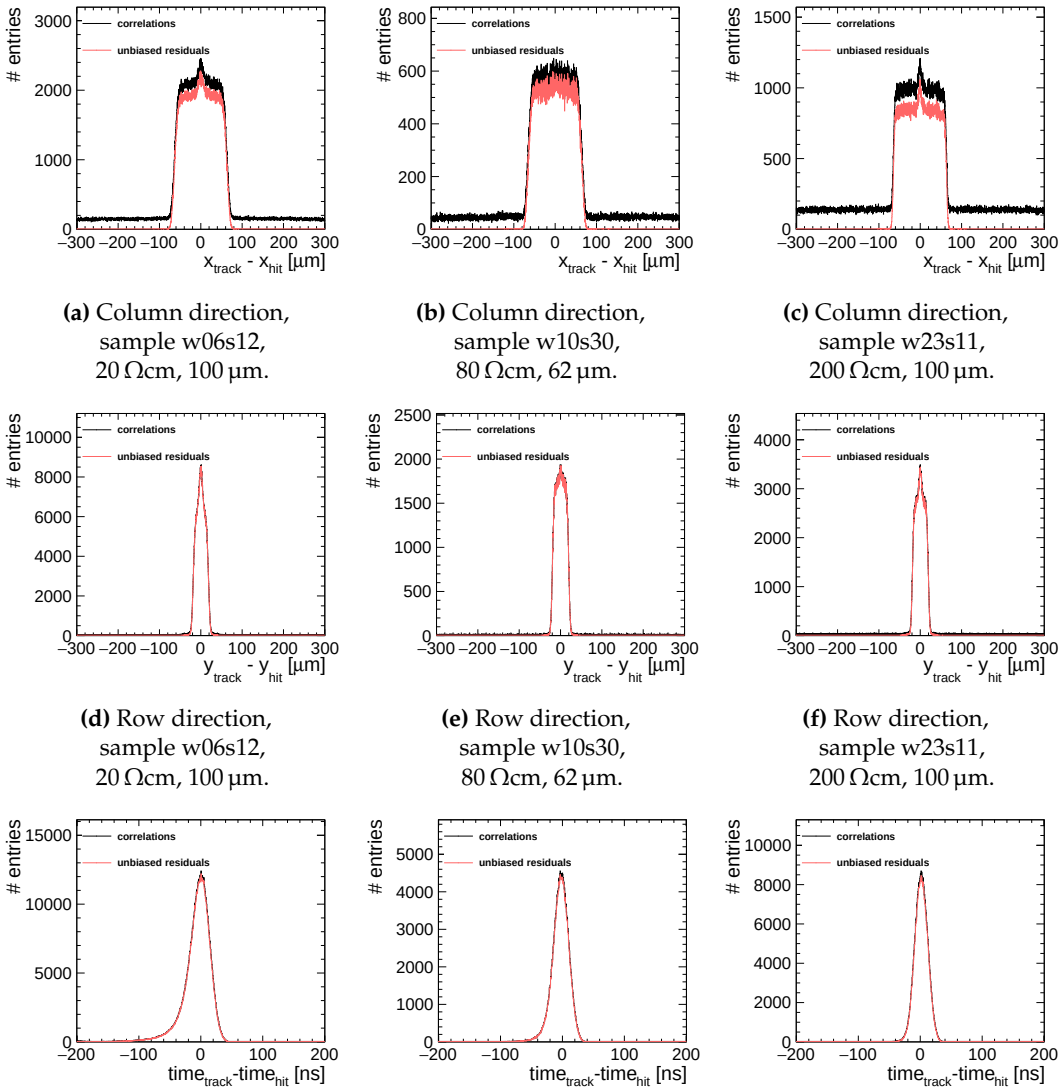

(a) Column direction, sample w06s12, 20 Ωcm, 100 µm.

(b) Column direction, sample w10s30, 80 Ωcm, 62 µm.

(c) Column direction, sample w23s11, 200 Ωcm, 100 µm.

(d) Row direction, sample w06s12, 20 Ωcm, 100 µm.

(e) Row direction, sample w10s30, 80 Ωcm, 62 µm.

(f) Row direction, sample w23s11, 200 Ωcm, 100 µm.

(g) Time, sample w06s12, 20 Ωcm, 100 µm.

(h) Time, sample w10s30, 80 Ωcm, 62 µm.

(i) Time, sample w23s11, 200 Ωcm, 100 µm.

Figure 8.22: Spatial correlations and unbiased residuals between reference tracks and clusters on the ATLASpix for the three samples with different substrate resistivities at a bias voltage of -50 V and a threshold of 820-850 e^- after a track-based alignment.

8.4 Estimation of Hit Detection Efficiency, Spatial and Time Resolution

In the following, the mathematical basis for the calculation of the efficiency as well as the determination of the spatial and time resolution is discussed.

8.4.1 Hit Detection Efficiency

The hit detection efficiency ϵ corresponds to the probability of detecting a particle passing through the sensor. It can be determined as

$$\epsilon = \frac{k}{N}, \tag{8.6}$$

where k is the number of tracks with an associated DUT cluster and N is the total number of tracks. If the spatial resolution of the reference telescope is smaller than the pixel size of the DUT, the efficiency can be studied as a function of the track position within the pixel. This allows for an investigation of possible efficiency losses towards the edges and corners of the pixel as expected from sub-threshold effects due to charge sharing.

The efficiency measurement can be treated using binomial statistics as it can be interpreted as repeated Bernoulli experiments. Accordingly, the likelihood function is a binomial distribution [46]

$$L(\epsilon|k,N) = \binom{N}{k}\epsilon^k(1-\epsilon)^{N-k}. \tag{8.7}$$

The uncertainty on the efficiency can be quantified as the boundaries of the frequentist Clopper-Pearson confidence interval of $\pm 1\sigma$ [153]. In analogy to the standard deviation of a Gaussian normal distribution, it corresponds to the central 68.3 % of the binomial distribution, but takes the lower limit of 0 and the upper limit of 1 into account correctly yielding asymmetric error bars. It corresponds to the recommended method by the Particle Data Group [46] and is implemented as the default method of the `TEfficiency` class [154, 155] in the *ROOT* framework.

The measured efficiency can be distorted by noise hits, which may cause a higher efficiency value. If $\epsilon_t < 1$ is the true efficiency, then the influence of noise on the measured efficiency ϵ_m is given by [156]

$$\epsilon_{\text{measured}} = \epsilon_{\text{true}} + (1 - \epsilon_{\text{true}}) \cdot \epsilon_{\text{noise}}, \tag{8.8}$$

where ϵ_{noise} is the probability of matching a track to a noise hit, which in turn can be obtained using

$$\epsilon_{\text{noise}} = \frac{\pi \cdot x_{\text{cut}} \cdot y_{\text{cut}}}{A_{\text{pixel}}} \cdot \overline{n_{\text{pixel}}} \cdot t_{\text{cut}}, \tag{8.9}$$

where $\overline{n_{\text{pixel}}}$ is the average noise rate per pixel, A_{pixel} the pixel area, and x_{cut}, y_{cut} and t_{cut} are the track association cuts in space and time as described in Section 8.2.6. For typical association cuts of 300 µm in x, 150 µm in y, and 200 ns in time this results in

$$\epsilon_{\text{noise}} = 5.4 \times 10^{-6}\,/\text{Hz} \cdot \overline{n_{\text{pixel}}}. \tag{8.10}$$

8.4.2 Spatial Resolution

In order to determine the spatial resolution of the DUT, the positional difference between the track intercept with the DUT and the associated cluster are calculated as[1]

$$x_{\text{unbiased residual}} = x_{\text{track intercept}} - x_{\text{associated cluster}}, \tag{8.11}$$

as illustrated in Figure 8.23. These are called *unbiased residuals* because the associated cluster is not part of the track, i.e. it does not bias the track.

The measured resolution deduced from the width of the unbiased residuals contains the combined resolutions of both the reference telescope and the DUT. In case of a Gaussian distribution, the telescope resolution can be subtracted quadratically:

$$\sigma_{\text{DUT}} = \sqrt{\sigma^2_{\text{measured}} - \sigma^2_{\text{telescope}}} \tag{8.12}$$

If the telescope resolution is much smaller (better) than the DUT resolution, it can be neglected in the calculation:

$$\sigma_{\text{DUT}} \approx \sigma_{\text{measured}} \tag{8.13}$$

Binary Resolution

The achievable spatial resolution of a pixel detector is directly linked to its clustering behaviour. A simple calculation (see Appendix E.1 of [43]) shows, that the so-called *binary resolution* is reached for a binary detector response, i.e. exclusively single-pixel

[1] For simplicity, the equations in this section are only labelled with x, as they are identical for y.

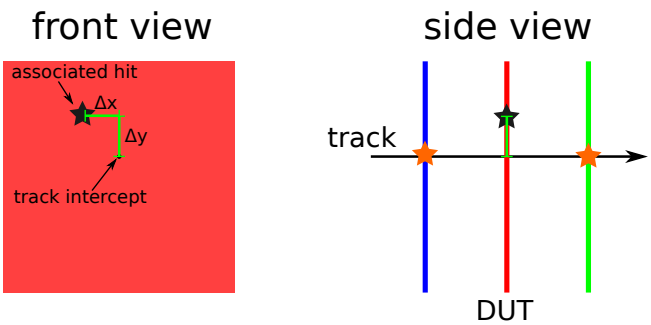

Figure 8.23: Illustration of the **unbiased spatial residual** between the incidence point of the reference track and the position of the associated cluster on the DUT.

clusters:

$$\sigma_{\text{binary}} = \frac{\text{pixel pitch}}{\sqrt{12}} \tag{8.14}$$

Assuming an infinitely precise track pointing resolution, the unbiased residuals would result in a box-shaped distribution with a width corresponding to the pixel pitch.

The limited track-pointing resolution of a real telescope leads to a smearing of the box edges. If the telescope resolution can be quantified by a Gaussian normal distribution, a convolution of a box function with a Gaussian could be used to describe the width of the unbiased residuals.

The occurrence of multi-pixel clusters can further affect the shape of the residuals. The arithmetic mean (see Equation 8.3) or the charge-weighted mean (see Equation 8.1) can be calculated to yield an estimation of the track incident point, which deviates from the binary resolution. In addition, if multi-pixel clusters occur only around the corners and edges of a pixel, this results in a bias towards small residuals for these clusters. This is further complicated by a possible non-linearity of the charge sharing arising from both the geometry of the electric field lines and sub-threshold effects.

Moreover, the occurrence of delta electrons can lead to a deterioration of the measured resolution. As discussed in Section 3.1.2, they can create large clusters due to a long lateral path within the silicon, and can thus extend from the track incident point by multiple pixel pitches. In these cases, the calculated cluster centre does not represent a good estimate of the track incident point resulting in tails of the residual distribution.

If the width of the unbiased residuals cannot be quantified by a fit function, the root mean square (RMS) of the distribution can be employed:

$$RMS_x = \sqrt{\frac{1}{N} \sum_{i=1}^{\text{entries}} (x_i - x_{\text{mean}})^2} \tag{8.15}$$

In case of a normal distribution, the RMS is identical to the standard deviation of the Gaussian.

8.4.3 Time Resolution

In analogy to the spatial resolution, the time resolution can be determined from the width of the unbiased time residuals between the reference track and the associated cluster on the DUT:

$$t_{\text{unbiased residual}} = t_{\text{track intercept}} - t_{\text{associated cluster}} \tag{8.16}$$

Generally, a large signal size and/or a low detection threshold is expected to yield better time resolutions because of a steeper threshold crossing. This leads to an reduced sensitivity to jitter of the comparator, i.e. time fluctuations caused by noise fluctuations on the signal, which are an irreducible contribution to the time resolution.

The time residual may show a non-Gaussian tail arising from timewalk as discussed in Section 4.1. If a sensor provides a measurement of the signal size, such as the time-over-threshold, a timewalk correction can be applied offline in the analysis.

Chapter 9

Characterisation of the Reference Telescopes

In order to achieve a reliable estimation of the performance of the DUT, a detailed understanding of the reference telescope is essential.

The precision of the reference telescope depends on the performance of the individual detector layers as well as the capability of the readout system. In addition, the track pointing resolution at the position of the DUT depends on the geometrical spacing and orientation of the individual reference planes as well as their material budgets. Whereas a straight-line tracking algorithm is sufficient for data from the SPS due to its high beam momentum, at DESY it is crucial to take the beam momentum and material budget of all devices along the particle trajectory into account because of the large impact of multiple scattering on the particle trajectory through the telescope.

The track pointing resolution can be estimated using the *GBL Track Resolution Calculator v2.0* [157], which makes use of the General-Broken-Line (GBL) formalism [151] and takes scattering in both the material budget of each detector plane as well as the surrounding air into account. The uncertainty on the track pointing resolution is estimated by repeating the calculation 10^4 times and applying a Gaussian smearing on the input parameters according to the assumed uncertainties.

9.1 Timepix3 telescope at the SPS

The Timepix3 telescope at the SPS was introduced in Section 7.2.

9.1.1 Track pointing resolution

In order to perform a calculation of the track resolution, the spacing and material budget of each detector plane including the DUT needs to be known. The material budget of the Timepix3 planes is $(4.0 \pm 0.5)\,\%X_0$ and the intrinsic resolution of each plane is (2.7 ± 0.2) µm in both column and row direction for the central 95.5 % [123].

For the ATLASpix on its carrier board, the material budget is 0.99-1.03 % X_0 depending on sensor thickness as shown in Section 6.2. A conservative uncertainty of $\pm 0.5\,\%X_0$ is assumed.

Table 9.1 lists the input parameters provided to the track resolution calculator. An error of 1 mm is assumed based on the read-off accuracy of the measuring tape used for the determination of the z-positions. For the uncertainties of the intrinsic resolution, values of and ± 200 nm are used [123, 145]. As a result, a track pointing resolution of (1.26 ± 0.05) µm is obtained. It should be noted that the most downstream telescope plane (Timepix3_6) is excluded for the further analysis. It does not improve the track pointing resolution significantly as seen in Table 9.1 but has shown to reduce the tracking performance. It is assumed that it was not configured correctly during the data taking leading to a degradation in its performance.

Table 9.1: Input parameters to the track resolution calculator representing the setup used for the test-beam campaigns in November 2018 and the resulting track pointing resolution σ_{TP} at the position of the DUT.

Detector plane	**z-position** [mm]	$\mathbf{X/X_0}$ [%]	**Intrinsic spatial resolution** [µm]
Timepix3_0 (D04)	0.0 ± 1	4.0 ± 0.5	2.7 ± 0.2
Timepix3_1 (E04)	21.5 ± 1	4.0 ± 0.5	2.7 ± 0.2
Timepix3_2 (G02)	43.5 ± 1	4.0 ± 0.5	2.7 ± 0.2
ATLASpix_0 (DUT)	105.0 ± 1	1.0 ± 0.5	-
Timepix3_3 (G03)	186.5 ± 1	4.0 ± 0.5	2.7 ± 0.2
Timepix3_4 (J05)	208.0 ± 1	4.0 ± 0.5	2.7 ± 0.2
Timepix3_5 (L09)	231.5 ± 1	4.0 ± 0.5	2.7 ± 0.2
Timepix3_6 (F09)	336.5 ± 1	4.0 ± 0.5	2.7 ± 0.2
Excluding Timepix3_6:			
σ_{TP} [µm]			1.26 ± 0.05
Including all Timepix3 planes:			
σ_{TP} [µm]			1.26 ± 0.05

9.1.2 Track time resolution

For a precise timing characterisation of the ATLASpix, the precision of the track timestamping needs to be known.

The track timestamp is calculated as the average timestamp of all telescope clusters forming the track:

$$t_{\text{track}} = \frac{1}{n} \sum_{i=0}^{n} t_i \tag{9.1}$$

where t_i are the individual cluster timestamps and n is the number of planes used for the track. Assuming that all Timepix3 planes of the telescope have an identical time resolution σ_{Timepix3} and the measurements are uncorrelated, the precision of the track timestamp is given by:

$$\sigma_{\text{track}} = \frac{\sigma_{\text{Timepix3}}}{\sqrt{n}} \tag{9.2}$$

As illustrated in Figure 9.1, the single-plane resolution σ_{Timepix3} can be determined by excluding one of the telescope planes from the tracking and instead treating it as the device-under-test. The actual DUT, the ATLASpix, acts as passive material for this analysis. This way, from the width of the unbiased track-hit time residual on the DUT (see Section 8.4.3), the single-plane resolution can be determined:

$$\sigma_{\text{track}-\text{DUT}} = \sqrt{\sigma^2_{\text{track}} + \sigma^2_{\text{DUT}}} \tag{9.3}$$

$$= \sqrt{\frac{\sigma^2_{\text{Timepix3}}}{n} + \sigma^2_{\text{Timepix3}}} \tag{9.4}$$

$$= \sqrt{\left(1 + \frac{1}{n}\right)}\, \sigma_{\text{Timepix3}} \tag{9.5}$$

$$\Rightarrow \sigma_{\text{Timepix3}} = \frac{\sigma_{\text{track}-\text{DUT}}}{\sqrt{1 + \frac{1}{n}}} \tag{9.6}$$

Figure 9.2 shows the track-hit time residual for plane Timepix3_3 as the DUT. To determine the width of the distribution, a Gaussian fit is applied. A small non-gaussian tail is observed on the left side of the distribution. Figure 9.3a shows the seed pixel ToT dependence of the time residual and Figure 9.3b shows the projection of the time residual for a seed pixel ToT value of 90. As can be seen, no significant

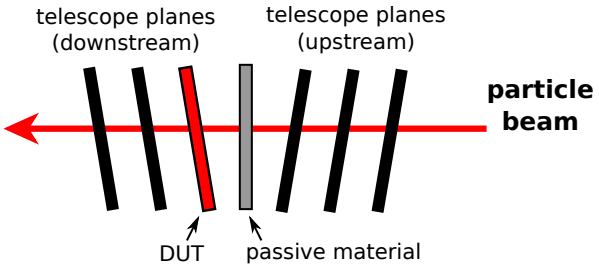

Figure 9.1: Schematic drawing of the Timepix3 telescope setup at the SPS (CERN) with one of the telescope planes used as the DUT and the actual DUT as passive material.

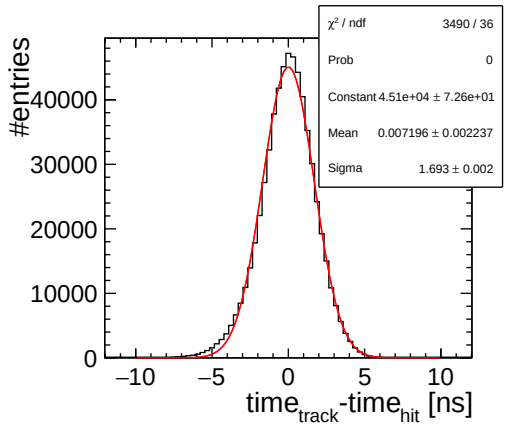

Figure 9.2: Track-hit time residual for plane Timepix3_3 with a Gaussian fit. The time residuals for all other planes are similar.

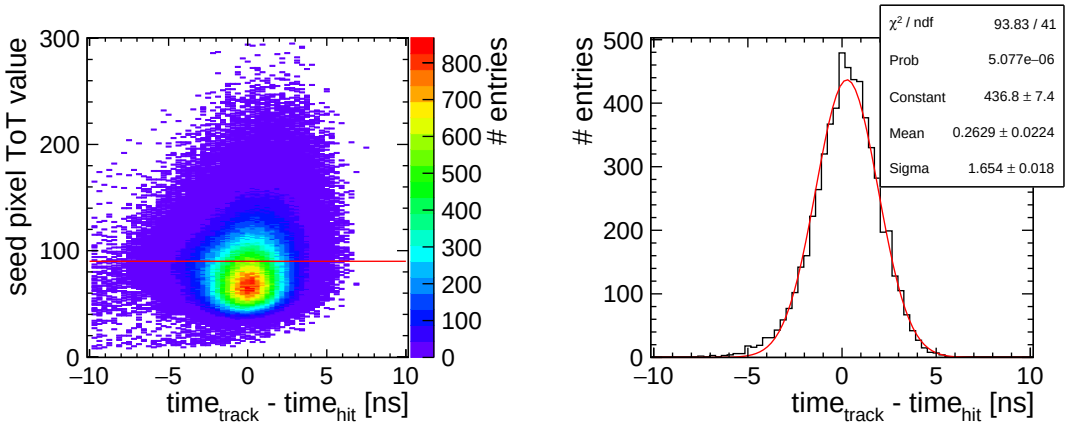

(a) Seed pixel ToT dependence.

(b) Seed pixel ToT value = 90.

Figure 9.3: Track-hit time residual for Timepix3_3. The red line in Figure 9.3a marks a ToT value of 70 for which the projection is shown in Figure 9.3b.

timewalk is present and the left tail is also present for a constant ToT value, i.e. for a constant signal size within the precision of the ToT measurement. Hence, it can be concluded that applying a ToT-based timewalk correction would not remove the tail. Similarly, no column or row dependence was found.

In order to estimate the systematic uncertainties arising from the tail, the difference between the RMS of the distribution and the standard deviation of the Gaussian fit is considered.

To verify the consistency of this measurement, the analysis is repeated six times such that each telescope plane is treated as the DUT iteratively. The resulting time resolution of the Timepix3 is shown Figure 9.4. They are consistent within the measurement uncertainties. Averaging over all measurements results in

$$\sigma_{\text{Timepix3}} = (1.4 \pm 0.1)\,\text{ns}. \tag{9.7}$$

Since the measurements are not independent from each other, the mean error is quoted instead of the error on the mean. Applying Equation 9.2 for six planes as used for the analysis of the ATLASpix, the track timestamp reaches a precision of

$$\sigma_{\text{track (6 planes)}} = (560 \pm 50)\,\text{ps}. \tag{9.8}$$

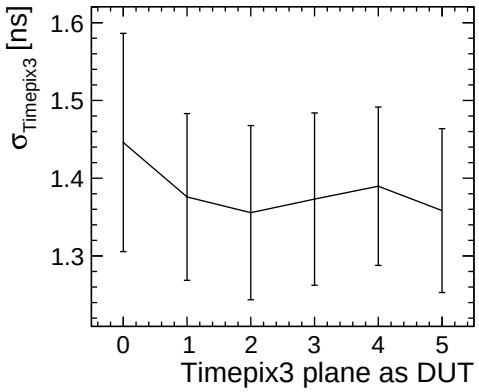

Figure 9.4: Average Timepix3 time resolution as obtained by Equation 9.3 for each plane used as the DUT.

9.2 EUDET telescopes at DESY

The EUDET-type telescopes at DESY were introduced in Section 7.4.

9.2.1 Track pointing resolution

The track pointing resolution at the position of the DUT depends on the geometrical spacing of the telescope planes as well as the selected beam momentum and the material budget of the all components along the beam. For all presented measurements, a beam momentum of 5.4 GeV/c was selected with a relative uncertainty of 2 % [129].

The Mimosa26 planes have a material budget of 0.075 %X_0 and an intrinsic spatial resolution of (3.2 ± 0.1) µm at a threshold $6\times$ above the pixel noise [130]. The Timepix3 has an intrinsic resolution of (12.75 ± 0.01) µm [123]. This value differs from the 4 µm quoted previously for the telescope at the SPS (see Section 9.1) because at DESY a different sensor with a smaller thickness of 100 µm instead of 300 µm was used. In addition, it was not rotated, resulting in less charge-sharing compared the sensors mounted in the SPS telescope. The smaller sensor thickness also leads to a slighty smaller material budget of 3.8 %X_0. However, this does not change the track pointing resolution in this case because the Timepix3 is the most downstream plane.

All relevant numbers are summarised in Table 9.2 and the different z-positions used at the various test-beam campaigns are shown in Table 9.3 with the resulting track pointing resolutions. In test-beams performed in June and July 2019, a track pointing resolution of ∼2.5 µm was achieved. In the test-beam in August 2020, the central planes of both the upstream and the downstream arm of the EUDET telescope were moved towards the DUT. By this a slight improvement in the track pointing resolution was achieved resulting in ∼2.4 µm.

Table 9.2: Input parameters to the track resolution calculator representing the EUDET telescope setup used for the test-beam campaigns at DESY.

Detector plane	$\mathbf{X/X_0}$ [%]	**Intrinsic spatial resolution** [µm]
Mimosa26_0	0.075 ± 0.01	3.2 ± 0.1
Mimosa26_1	0.075 ± 0.01	3.2 ± 0.1
Mimosa26_2	0.075 ± 0.01	3.2 ± 0.1
ATLASpix_0	1.0 ± 0.5	-
Mimosa26_3	0.075 ± 0.01	3.2 ± 0.1
Mimosa26_4	0.075 ± 0.01	3.2 ± 0.1
Mimosa26_5	0.075 ± 0.01	3.2 ± 0.1
Timepix3_0	3.8 ± 0.01	12.8 ± 1.0

Table 9.3: Z-positions of the detector planes representing the *DATURA* telescope setup used for the test-beam campaigns at DESY for the ATLASpix characterisation and the resulting track pointing resolution σ_{TP} at the DUT position. On all z-positions an uncertainty of ± 1 mm is assumed.

Detector plane	**z-position** [mm]				
	June 2019	July 2019	August 2020		
	narrow	*narrow*	*narrow*	*wide (1)*	*wide (2)*
Mimosa26_0	0	0	0	0	0
Mimosa26_1	153	153	278	278	278
Mimosa26_2	305	305	305	305	305
ATLASpix_0	333	331	340	365	377
Mimosa26_3	344	345	354	436	481
Mimosa26_4	456	455	381	462	507
Mimosa26_5	576	565	627	709	754
Timepix3_0	666	629	672	754	799
σ_{TP} [µm]	2.5 ± 0.1	2.5 ± 0.1	2.4 ± 0.1	4.3 ± 0.2	5.4 ± 0.3

For the rotation studies presented in Section 11.7, the telescope arms needed to be moved out from the DUT to allow for a rotation of the DUT including the chip board and the required cabling. For both rotation directions, the respective minimal spacing was chosen, which allowed for a maximal rotation of the DUT.

During a rotation scan, the spacing was kept constant for a better comparability. This deteriorates the track pointing resolution to 4.3 µm and 5.4 µm for the two rotation angles, respectively. For the calculation, a non-rotated DUT at the quoted z-position was assumed. It can also be seen that the uncertainty on the track pointing resolution is significantly larger for the wide telescope spacing. The usage of the Timepix3 plane does not have a significant impact on the track pointing resolution. Its purpose is to improve the precision of the track timestamp as discussed below.

9.2.2 Track time resolution

In order to perform a precise timing characterisation of the ATLASpix, an accurate and unambiguous track timestamp is required. While the scintillators used to trigger the readout of the Mimosa26 telescope planes yield precise timestamps, these cannot be assigned to a reconstructed track unambiguously if multiple tracks are reconstructed within one readout cycle issued by one trigger. Hence, a Timepix3 timing plane was installed at the downstream end of the telescope as discussed in Section 7.4. Even though the Timepix3 was characterised in detail elsewhere [136, 137], its performance needs to be verified because of its integration and operation in a different DAQ framework.

Improvement of Trigger Timestamp Reconstruction

The timing precision of the AIDA TLU together with the connected scintillators and SiPMs was investigated and characterised to serve as a reference. In this context, a significant improvement of the timing resolution was achieved by updating both the firmware of the AIDA TLU and the reconstruction software. The precise trigger timestamp can be reconstructed from a "coarse" and multiple "fine" timestamps. The "coarse" timestamp with a binning of 25 ns (derived from a 40 MHz clock) marks the detection of a coincidence. The "fine" timestamps have a binning of 781.25 ps (derived from a 1.28 GHz clock) but their range is limited to 8 bit corresponding to 200 ns before overflowing.

Previously, only the "coarse" timestamp was used, resulting in a resolution of $25\,\text{ns}/\sqrt{12} \sim 7\,\text{ns}$. Now, the "fine" timestamps are combined with the "coarse" timestamp while taking a possible counter overflow into account and correcting for it. The resulting time resolution is discussed below.

As decribed in Section 7.4, the TLU can be provided with up to six trigger signals. The required pattern for the detection of a coincidence can be configured to any desired logic combination. Within the scope of this thesis, two or three scintillators read out by photomultiplier tubes (PMTs) were used with a trigger pattern configured as

- 2 out of 2,
- 3 out of 3.

The PMTs were powered with 900 mV, 900 mV and 850 mV, respectively, and the detection threshold was set to -40 mV to achieve a high efficiency and a low noise rate [158]. The TLU registers a coincidence if all input signals as required by the trigger pattern are active within a coincidence window of 6.25 ns.[1] When a coincidence is detected, the "coarse" timestamp with a binning of 25 ns is recorded and stored

[1] The length of the coincidence window can be set to multiples of 6.25 ns. For all measurements presented in this thesis, it was kept at the minimum.

together with a unique trigger ID, which is incremented with each recorded coincidence. In addition, "fine" timestamps with a binning of 781.25 ps are stored for each individual trigger input. The principle is depicted in Figure 9.5. These "fine" timestamps have a range of 8 bits (0-200 ns) such that the full timestamp of each trigger input needs to be reconstructed by combining the "coarse" and the "fine" timestamps.

Special care needs to be taken to correctly handle cases in which one of the "fine" timestamp overflows. This is especially important when combining multiple trigger timestamps into one precise coincidence timestamp, if one "fine" timestamp overflows and another did not yet. The correct "coarse" timestamp needs to be found in this case to avoid an offset of one bit corresponding to 25 ns. Previously, the "fine" timestamps were implemented with range 5 bit (0-25 ns) instead of 8 bit such that the overflow detection discussed above was not possible in a robust way.

Time Resolution of the TLU Trigger Timestamps

The following analysis was performed on data recorded in a measurement campaign in July 2020 using the *AZALEA* telescope setup located in beamline TB24 of the DESY II test-beam facility. It should be noted that the performance of the PMT assemblies depends strongly on the bias voltage and threshold. In additions, variations between the assemblies used in the different beamlines cannot be excluded such that the presented results on the timing resolution of the scintillators and PMTs are only valid for the setup and settings used in TB24. However, the same Timepix3 sample was used throughout all test-beam periods with identical settings, such that the deduced performance of the Timepix3 is comparable between all beam periods.

Figure 9.6 shows the time correlations between triggers 0, 1 and 2. The offset of the peaks from zero correspond to the average delay between two timestamps. It can be observed that the delay between trigger 0 and 1 is much smaller compared to the delay between trigger 0 and 2 or trigger 1 and 2, which reflects the difference in time-of-flight, since both triggers 0 and 1 are placed upstream of the telescope, whereas trigger 2 is located on the downstream side of the telescope.

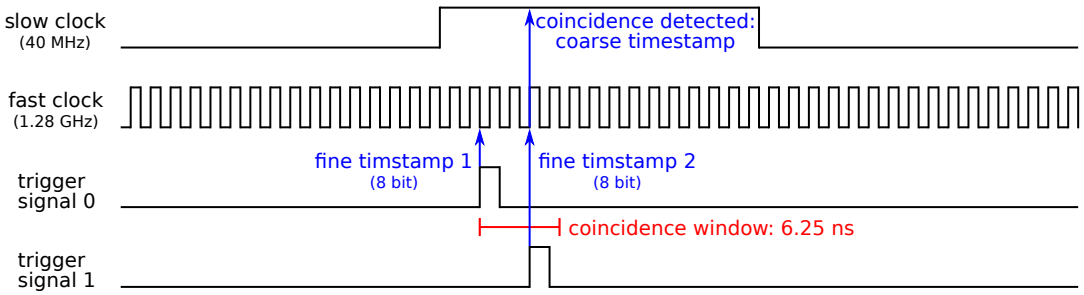

Figure 9.5: Exemplary illustration of the trigger timestamp generation in the AIDA TLU for two trigger input signals.

The performance of the individual scintillators with PMTs can be determined by extracting the width of all correlation plots between trigger i and trigger j as

$$\sigma_{ij} = \sqrt{\sigma_i^2 + \sigma_j^2} \tag{9.9}$$

and solving the system of equations:

$$\begin{aligned} \sigma_{01} &= \sqrt{\sigma_0^2 + \sigma_1^2} = (1.23 \pm 0.05)\,\text{ns} \\ \sigma_{02} &= \sqrt{\sigma_0^2 + \sigma_2^2} = (0.83 \pm 0.03)\,\text{ns} \\ \sigma_{12} &= \sqrt{\sigma_1^2 + \sigma_2^2} = (1.22 \pm 0.03)\,\text{ns} \end{aligned} \tag{9.10}$$

The values of σ_{ij} are obtained by Gaussian fits to the histograms shown in Figure 9.6. To exclude the tails due to uncorrelated timestamps from different particles and noise, the fitting is performed in two consecutive steps: First, a Gaussian is fitted on a range of ± 2 ns around the peak position. Then a second Gaussian is fitted on a range of ± 3 standard deviations around the mean of the first fit. In order to estimate the systematic errors due to deviations of the distributions from a Gaussian shape, the fit range is varied from two to four standard deviations. The above set of quadratic equations is solved yielding time resolutions of

$$\begin{aligned} \sigma_0 &= (0.60 \pm 0.05)\,\text{ns} \\ \sigma_1 &= (1.08 \pm 0.03)\,\text{ns} \\ \sigma_2 &= (0.57 \pm 0.05)\,\text{ns} \end{aligned} \tag{9.11}$$

for the individual scintillators with PMTs. The uncertainties are estimated by solving the quadratic equation in 10^5 iterations and applying a Gaussian smearing with the uncertainties specified in Equations 9.10 on the input parameters σ_{ij}. As shown in Figure 9.7, the resulting σ_i are histogrammed and Gaussian fits are applied to extract the mean and the standard deviation corresponding to the time resolutions and their uncertainties as shown in Equation 9.11. While σ_1 has the largest value, it has a

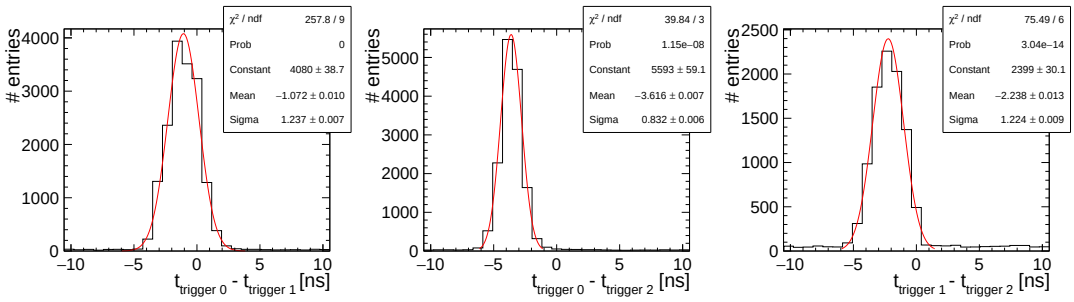

(a) Trigger 0 vs. trigger 1. **(b)** Trigger 0 vs. trigger 2. **(c)** Trigger 1 vs. trigger 2.

Figure 9.6: Time correlations between trigger timestamps from the scintillators and PMTs fed into the TLU. Gaussian fits are applied to extract the widths of the correlations σ_{ij} (see Equation 9.10) as the standard deviation and the uncertainty on the standard deviation.

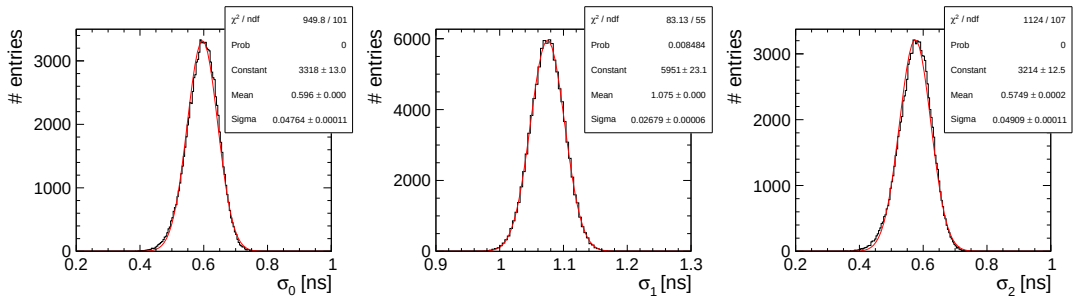

(a) Trigger 0. **(b)** Trigger 1. **(c)** Trigger 2.

Figure 9.7: Results for the trigger time resolutions σ_0, σ_1 and σ_2 obtained when solving the system of quadratic equations 9.10 in 10^5 iterations with a Gaussian smearing of the input parameters σ_{ij}. Gaussian fits are applied to extract the mean and the standard deviation corresponding to the time resolutions and their uncertainties.

smaller uncertainty compared to σ_0 and σ_2 because it is better constrained in Equations 9.10 since $\sigma_0 \approx \sigma_2$. The precision of the TLU trigger timestamp is then given by

$$\sigma_{\text{TLU}} = \frac{1}{n}\sqrt{\sum_{i=0}^{n}\sigma_i^2} \tag{9.12}$$

for n trigger inputs and the uncertainties are obtained by Gaussian error propagation:

$$\Delta\sigma_{\text{TLU}} = \frac{1}{n^2}\sqrt{\sum_{i=0}^{n}\left(\frac{\sigma_i \cdot \Delta\sigma_i}{\sigma_{\text{TLU}}^2}\right)} \tag{9.13}$$

This results in

- $\sigma_{\text{TLU}} = (620 \pm 20)$ ps when using trigger 0 and 1,
- $\sigma_{\text{TLU}} = (450 \pm 10)$ ps when using trigger 0, 1 and 2.

Time Resolution Timepix3 Timing Plane

Figure 9.8 shows the time correlations between the Timepix3 cluster timestamps and the combined precise TLU timestamp using two and three scintillators, respectively. The distributions can be described by a Gaussian fit to obtain $\sigma_{\text{TLU - Timepix3}}$ as the standard deviation and its uncertainty of the fit. The timing performance of the Timepix3 is then obtained by

$$\sigma_{\text{Timepix3}} = \sqrt{\sigma_{\text{TLU-Timepix3}}^2 - \sigma_{\text{TLU}}^2}. \tag{9.14}$$

Applying Equation 9.14 results in

- $\sigma_{\text{Timepix3}} = (1.09 \pm 0.02)$ ns when using triggers 0 and 1, and
- $\sigma_{\text{Timepix3}} = (1.10 \pm 0.01)$ ns when using triggers 0,1 and 2.

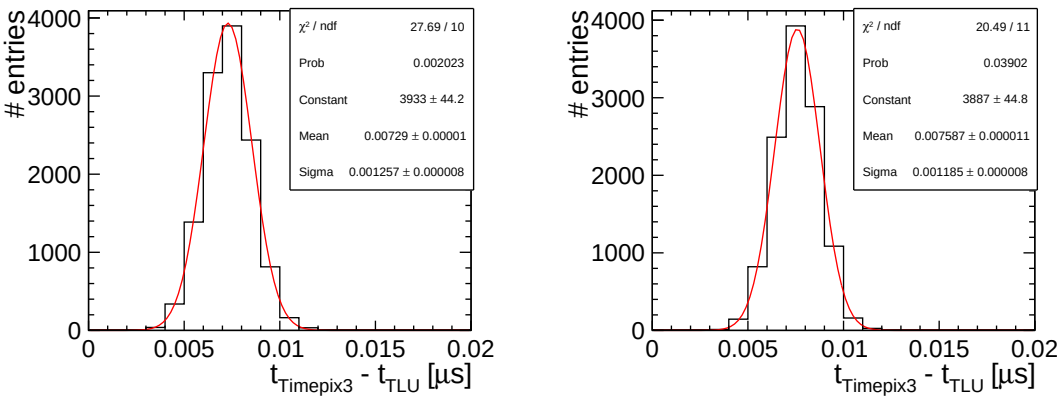

(a) Using two scintillators.

(b) Using three scintillators.

Figure 9.8: Time correlations between Timepix3 and the combined TLU trigger timestamp with a Gaussian fit.

The uncertainties are obtained by Gaussian error propagation. For a validation of these results and to cross-check the correctness of the implementation of the time-walk correction of the Timepix3, a data set recorded at the CERN SPS in 2015, which was used in [136, 137], was re-analysed. It yields consistent results as summarised in Table 9.4.

Table 9.4: Summary and comparision of different Timepix3 timing performance measurements.

Analysis	**Timing resolution** [ns]	
Re-analysis of SPS data (2015)	1.13 ± 0.01	
Analysis of DESY data (2020)	1.09 ± 0.02	using two scintillators
	1.10 ± 0.01	using three scintillators

In conclusion, the Timepix3 timing plane is used for the performance analysis the ATLASpix presented in Chapter 11 to provide unambiguous track timestamps for the data recorded at DESY with a precision of (1.09 ± 0.02) ns.

Part III

Performance Characterisation of the ATLASpix_Simple

Chapter 10

Laboratory Measurements

This chapter contains a presentation of all performed laboratory-based measurements for the characterisation of the ATLASpix. These comprise studies of the current-voltage characteristics and the breakdown behaviour as well as the noise rate. Furthermore, charge calibration measurements involving X-rays are presented. Unless otherwise stated, all measurements were performed at room temperature without cooling. In these conditions, the sensor reaches a stable temperature of $\sim$32 °C. The values for the detection threshold quoted in millivolts refer to the externally applied voltage. The baseline was set externally to 800 mV for all presented measurements. In Section 10.4, a conversion from voltage into equivalent charge is presented, which is applied throughout the whole chapter such that threshold values are quoted in electrons for a better comparability with other sensors.

During temperature dependent measurements, the temperature of the ATLASpix was stabilised using a fan and a heatgut as described in Section 6.4. The temperature of the ATLASpix was measured using the IR camera with the calibration presented in Section 6.3. Since the temperature was controlled via an air flow directed onto the backside of the chip board, it could only be controlled up to an accuracy of a few degrees Celsius.

10.1 IV Characteristics & Breakdown Voltage

As described in Chapter 4, the fundamental building block of a silicon pixel sensor is a pn-junction operated in reverse bias. Consequently, it is expected to show the current-voltage characteristic of a diode.

A larger depletion voltage is expected to be beneficial for the performance of the sensor. It generates a larger depleted volume such that a traversing ionising particle creates more electron/hole pairs within the depleted volume. Hence, the collected charge and therefore the induced signal is larger. However, it is important to stay below the breakdown voltage of the sensor to avoid an excessive leakage current causing a thermal runaway and therefore possible damage to the diode structure or the sensor as a whole.

The reverse bias current-voltage behaviour of the ATLASpix was measured using the laboratory setup introduced in Section 6.4.

10.1.1 IV Characteristics

Reverse bias IV curves were recorded at different temperatures for samples of all substrate resistivities. All IV measurements were performed on a fully powered and configured sensor to obtain results that represent the real operating conditions of the detector. Because the top layer of the ATLASpix is metallised, it is largely insensitive to light in the visual spectrum. Ambient light was found to increase the leakage current by $\mathcal{O}(\text{few } 10\,\text{nA})$. Consequently, no ambient light shielding was used for the presented measurements.

A high detection threshold of 950 mV $\approx 1630\,e^-$ was chosen to ensure an equally noise-free operation for all samples. For a correct determination of the leakage current and breakdown voltage, it needs to be taken into account that a 100 kΩ resistor is placed in series with the sensor in the high voltage net on the chip board. To obtain an IV curve that represents the effective bias voltage applied to the sensor, a correction needs to be made according to Ohm's law:

$$V_{\text{sensor}} = V_{\text{source}} - I_{\text{source}} \cdot R_{\text{series}} \tag{10.1}$$

where V_{sensor} represents the effective bias voltage applied to the sensor, V_{source} and I_{source} are the voltage and current applied and measured by the SourceMeter, respectively, and $R_{\text{series}} = 100\,\text{k}\Omega$ is the resistor on the chip board. Gaussian error propagation yields

$$\Delta V_{\text{sensor}} = \sqrt{(\Delta V_{\text{source}})^2 + \left(\frac{R_{\text{series}}}{I_{\text{source}}} \cdot \Delta I_{\text{source}}\right)^2 + \left(\frac{I_{\text{source}}}{R_{\text{series}}} \cdot \Delta R_{\text{series}}\right)^2} \tag{10.2}$$

$$\approx \sqrt{\left(\frac{R_{\text{series}}}{I_{\text{source}}} \cdot \Delta I_{\text{source}}\right)^2 + (I_{\text{source}} \cdot 0.02\,\%)^2} \tag{10.3}$$

where the error on ΔV_{source} is neglected due to the precision of the Keithley SourceMeter and a relative error of 0.02 % for R_{series} [159]. The uncertainty on the leakage currents is estimated by the standard deviation of 20 subsequent measurements for all presented measurements.

The importance of the correction becomes apparent in Figure 10.1, where the measured IV characteristics is compared with and without the applied correction for sample w23s11 at a temperature of ∼32 °C. At small leakage currents, the effect is negligible. For example, a current of 1 µA leads to a voltage drop of 100 mV, which is insignificant for bias voltages of $\mathcal{O}$(few 10 V). Typical currents at operating conditions are $\mathcal{O}$(few 10 nA), such that the effect is even smaller. However, for larger currents, which occur when approaching the breakdown voltage, the effect is more significant, e.g. 1 V for a current of 10 µA.

In Figure 10.2, a comparison of the IV characteristics is shown for samples with different substrate resistivities ρ. A clear difference in the IV characteristics can be

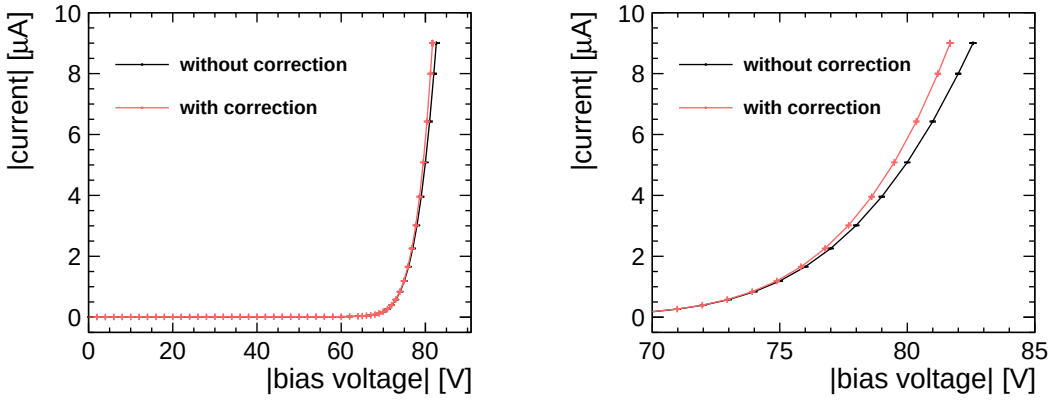

(a) Full range. **(b)** Zoom into the range from −70 V to −85 V.

Figure 10.1: Comparison of the IV characteristics without and with the ohmic correction (see Equation 10.1) for sample w23s11 at a temperature of ∼32 °C.

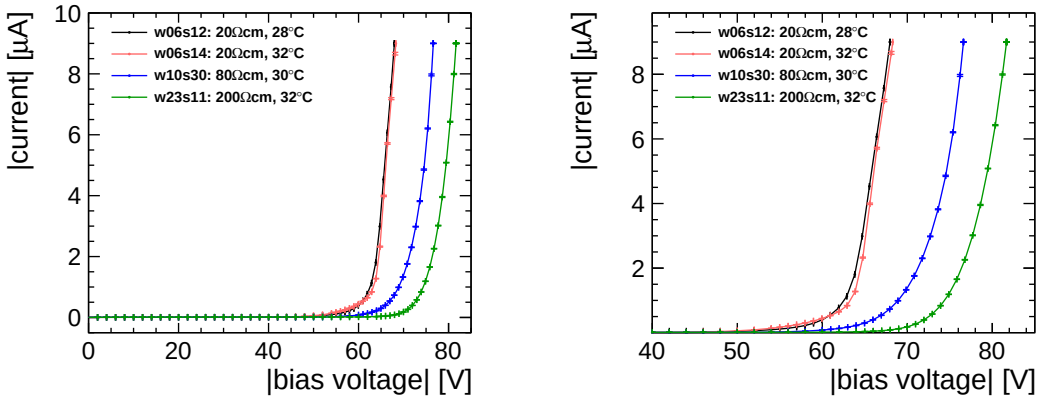

(a) Full range. **(b)** Zoom into the range from −40 V to −85 V.

Figure 10.2: Comparison of the IV characteristics samples with different substrate resistivities at a temperature of ∼30 °C.

observed at high bias voltages for the samples with different ρ. The variation between the two 20 Ωcm samples is much smaller compared to the deviation between the different substrate resistivities even though the measurements for w06s12 and w06s14 were performed with an approximate temperature difference of 4 °C. This implies that the observed differences between the samples with different resistivities do not stem from the temperature variations but are instead related to the different substrate resistivities. As can be seen, a later breakdown is observed for larger ρ. The extraction of the breakdown voltage from these measurements is discussed in more detail in Section 10.1.2.

In Figure 10.3, the IV characteristics are compared for samples of all substrate resistivities and different temperatures. In all cases, a clear trend can be seen that the leakage current increases with temperature. For a better comparison, the leakage current at a bias voltage of −40 V is extracted and plotted in Figure 10.4. A voltage

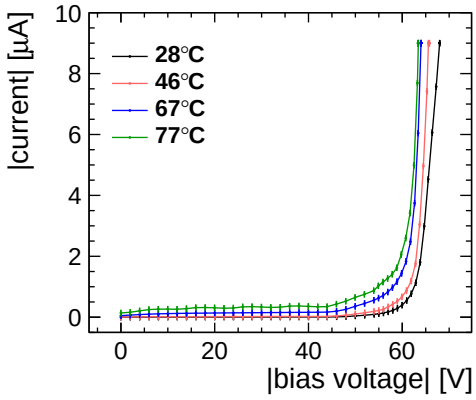

(a) Sample w06s12: 20 Ωcm.

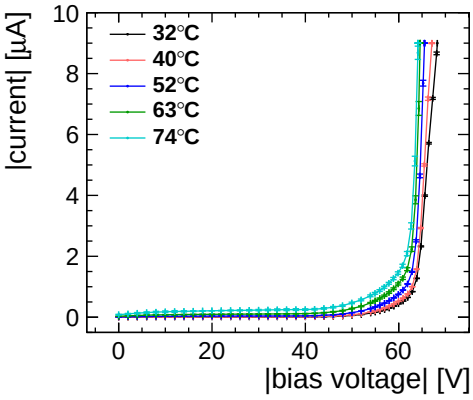

(b) Sample w06s14: 20 Ωcm.

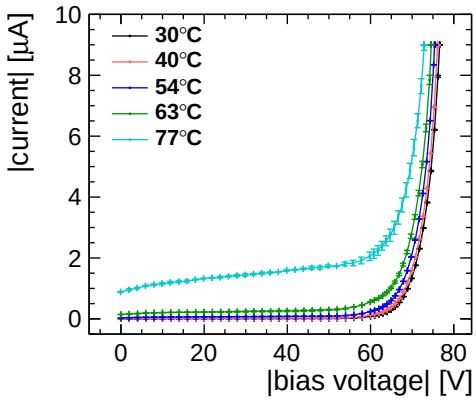

(c) Sample w10s30: 80 Ωcm.

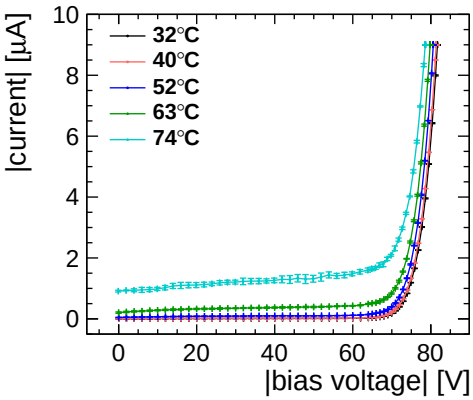

(d) Sample w23s11: 200 Ωcm.

Figure 10.3: IV characteristics of samples with all substrate resistivities at different temperatures.

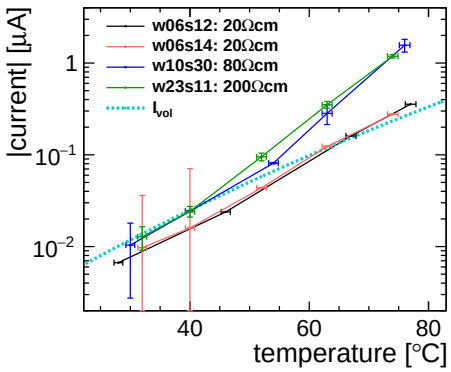

Figure 10.4: Leakage current at a bias voltage of −40 V for different samples. The trend line shows Equation 3.19.

of −40 V was chosen for this comparison to ensure staying well below the breakdown voltage for all samples. In all cases, an approximately exponential relation with temperature is observed. The cyan-coloured trend line shown in Figure 10.4 corresponds to Equation 3.19, which describes the volume contribution to the leakage current arising from thermally generated electron-hole pairs in the depletion

region. This shows that the total leakage current is dominated by the volume contribution as discussed in Section 3.2.2.

10.1.2 Determination of the Breakdown Voltage

The breakdown voltage is determined following the approach first introduced in [160] and applied in [161]. It is based on the k-value, which is calculated iteratively for each step of the IV measurement:

$$k(I,V) = \frac{\Delta I}{\Delta V} \cdot \frac{V}{I} \tag{10.4}$$

An ideal ohmic behaviour results in $k = 1$. Thus it can be understood as the slope of the current-voltage characteristic normalised to an ideal ohmic resistor. The breakdown voltage V_{bd} is extracted when $k \geq 4$, meaning that the ohmic behaviour is strongly exceeded. It is motivated by the fact that defects in wafers used for detector fabrication lead to a smooth and continuous increase of the current instead of an abrupt breakdown [160, 161, 52]. The value of 4 is chosen empirically because it yields consistent results for all temperatures and all samples studied within the scope of this thesis. It was also used in [161].

Figure 10.5 shows an exemplary plot in which the IV characteristics are overlaid with the iterative k-values calculated using Equation 10.4. The blue cross marks the voltage step at which $k \geq 4$ is reached, which is the breakdown voltage V_{bd}. The extracted breakdown voltages for all samples and all temperatures are summarised in Figure 10.6. The uncertainties on V_{bd} are assumed to be ± 1 V [161], whereas the error bars on the temperature measurements have been propagated using Equation 6.4.

The breakdown voltages of the two 20 Ωcm samples are compatible within the error bars, such that it can be concluded that the differences observed between the

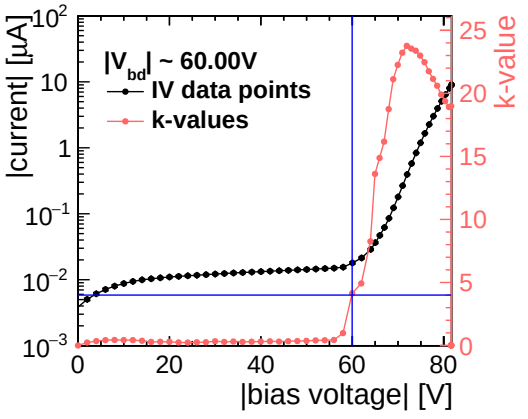

Figure 10.5: Exemplary plot showing the determination of the breakdown voltage at $k \geq 4$ for sample w23s11 at $T = 32\,^{\circ}\mathrm{C}$. The blue cross marks the point when $k = 4$.

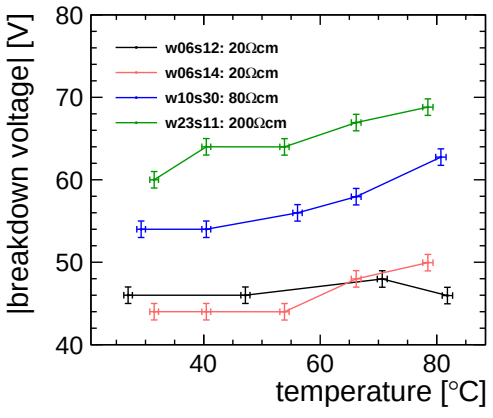

Figure 10.6: Breakdown voltage as a function of temperature for all samples, extracted using the k-value method.

other samples stem from the different substrate resistivities rather than sample-to-sample variations. It is observed that a larger substrate resistivity leads to a later breakdown. This corresponds to the expectation because a larger substrate resistivity leads to a smaller maximum electric field at a given bias voltage according to Equation 3.16.

Furthermore, the breakdown shifts to higher voltages with higher temperatures for the 80 Ωcm and 200 Ωcm samples. It can be explained as follows: The electron mobility decreases with increasing temperature between 250 K and 500 K for doping concentrations smaller than $1 \times 10^{18}\,\mathrm{cm}^{-3}$, i.e. $\rho > 0.04\,\Omega\mathrm{cm}$ [53], due to an increasing probability of electron-electron scattering [162]. As a consequence, the resistivity rises according to Equation 3.14, resulting in a higher breakdown voltage. For the 20 Ωcm samples, this trend cannot clearly be seen within the measurement uncertainties.

It should be noted that the sensors can also be operated at higher bias voltages than the determined breakdown. This is related to the fact that the breakdown occurs in a smooth and continuous way instead of an abrupt avalanche breakdown. The ATLASpix was shown to be functional for leakage current up to ∼100 µA. Higher values were not explored to avoid damage to the sensor. On the other hand, a relation between the leakage current and an increased noise rate is observed as discussed in detail in Section 10.3 below.

As described in Section 5.1, the production process is specified to bias voltages down to −120 V. The observed breakdown already occurs for significantly smaller voltages. The exact mechanism is still under investigation using Technology Computer Aided Design (TCAD) simulations within the scope of a PhD thesis [163].

10.2 Power Consumption

The power consumption is an important quantity as it impacts the design of the cooling system in a detector. For a monolithic pixel sensor, the power consumption comprises multiple contributions, which scale differently when increasing the sensor size. While the contribution from the active matrix scales linearly with its size, the digital periphery including the clocking circuitry and the readout state machine give a contribution, which remains approximately constant when scaling up the size of a sensor unless multiple readout links are implemented in parallel.

For the ATLASpix, four external voltages are applied as described in Section 5.3: VSSA (1.2 V) provides the power to the in-pixel charge-sensitive amplifiers, VDDA (1.85 V) powers the in-pixel logic. Accordingly, both scale with the size of the active matrix. VDDD (1.85 V) is used in the periphery and provides power to the pixel readout cells as well the clocking circuitry and the readout state machine. VDDHigh

(1.85 V) is the power provided to custom-designed periphery blocks using a differential current mode logic (DCL) instead of CMOS logic. The different contributions to VDDD can be retrieved by switching off individual blocks of the periphery via the relevant DAC values. The power consumption was determined by measuring the currents of the individual voltages using the setup presented in Section 6.4. The results are summarised in Table 10.1, where the stated uncertainties correspond to the statistical uncertainties after averaging over measurements with 3 different ATLASpix samples.

Table 10.1: Contributions to the total power consumption from different chip components. (*Below measurement sensitivity.)

Chip compontent	$P_{\mathbf{VDDA}}$ [mW]	$P_{\mathbf{VSSA}}$ [mW]	$P_{\mathbf{VDDD}}$ [mW]	$P_{\mathbf{VDDHigh}}$ [mW]	$P_{\mathbf{total}}$ [mW]
Active matrix	74.7 ± 4.3	42.4 ± 0.7	-	-	117.1 ± 5.1
Pixel readout cells (in periphery)	-		0*	-	0*
State machine	-	-	26.7 ± 0.4	-	26.7 ± 0.4
PLL and DCL	-	-	8.3 ± 0.3	32.3 ± 1.7	40.6 ± 1.7
Pre-emphasis + LVDS link	-	-	8.9 ± 0.3	-	8.9 ± 0.3
				$P_{\mathbf{ATLASpix}}$[mW]:	193 ± 6.7

The total power consumption adds up to 193 mW using the default configurations listed in Appendix A. It contains a contribution of $\sim$ 117 mW from the active matrix. The values for the pixel readout cells in the periphery lies below the measurement sensitivity of $\mathcal{O}(1\,\text{mA})$ in consistency with previous results [75]. Furthermore, the contributions from the reference voltages VMinusPix and VGatePix, as well as the bias voltage are negligible. At bias voltages $\leq$ 100 V and leakage currents well below 100 µA in the operating range, it leads to a power dissipation below 1 mW.

The relevant number for the use case in a tracking detector is the power consumption normalised to the active area. In this calculation, the power consumption of the periphery needs to be included because it has a significant impact on the required cooling capacity while not increasing the sensitive area. For the ATLASpix with an active area of 0.52 cm^2 (see Chapter 5), this corresponds to $\sim$370 mW/cm^2 normalised to the active area including the power consumption of the periphery. This values exceeds the maximum design value of the cooling system for the CLIC Tracker of 150 mW/cm^2 (see Table 2.1 in Section 2.4.3).

The scalable per-pixel power consumption of the ATLASpix is 12 µW. The blocks of the digital periphery, which are implemented only once per chip contribute with

$\sim$ 76 mW. This means that a reduction of the power consumption per area can be achieved by increasing the size of the active matrix by using a larger number of pixels while keeping the pixel size constant, as the contributions from the blocks in the digital periphery remain approximately constant. If additional readout links are needed for a higher bandwidth, their contribution needs to be scaled as well.

It should be noted that the power consumption is highly dependent on the particular chip settings. In other works a total power consumption of 160-200 mW was reported [51, 75]. It shows that the optimisation of chip settings can lead to a significant reduction of the power consumption. On the other hand, it may lead to a degraded performance, e.g. in terms of the time resolution, such that it needs to be carefully balanced with other requirements.

In the context of CLIC, a further reduction of the average power consumption would be possible through the implementation of a power pulsing scheme, i.e. a periodic switching between normal operation and a low-power idle mode [164]. Due to the low duty-cycle of < 0.001 % (see Section 2.4), the detectors do not need to be kept in an active mode continuously. It was demonstrated for other pixel detectors with power pulsing features, that this can lead to a significant reduction of the average power consumption by a factor of $\sim$ 80 [165, 166]. The feasibility of power pulsing with the ATLASpix was not investigated in this thesis.

10.3 Noise Rate

As discussed in Section 4.2, fake hits can arise from fluctuations of the amplifier output, caused by shot noise of the sensor leakage current as well as thermal and 1/f noise affecting the input transistor of the amplifier. In addition, the comparator threshold and baseline underlie fluctuations.

The noise rate was determined using the laboratory setup introduced in Section 6.4. For each step, data was acquired for 180 s with the default chip configuration and at normal operating conditions, i.e. at room temperature without additional cooling and without ambient light shielding. In these conditions, the sensor reaches a stable temperature of $\sim$32 °C. Ambient light does not show a measurable impact on the noise rate because the top layer of the sensor is covered with metal.

The average noise rate on the full chip is determined as

$$\overline{n_{\text{chip}}} = \frac{N_{\text{hits}}}{t_{\text{DAQ}}} \tag{10.5}$$

where N_{hits} is the number of hits during the data taking time t_{DAQ}. The error on the average noise rate is determined following Poisson statistics:

$$\Delta\overline{n_{\text{chip}}} = \frac{\sqrt{N_{\text{hits}}}}{t_{\text{DAQ}}} \tag{10.6}$$

where the uncertainty on the data acquisition time is neglected. In the following, the dependence on both bias voltage and detection threshold are investigated.

10.3.1 Threshold Dependence

In Figure 10.7a, the dependence of the noise on the detection threshold of the sensor is plotted for samples with different substrate resistivities at a bias voltage of $-50\,\mathrm{V}$. It can be seen that all samples reach a plateau well below 1 Hz for thresholds above $1200\,\mathrm{e}^-$. For thresholds above $3000\,\mathrm{e}^-$, no hits were detected during the data acquisition time of 180 s. At decreasing thresholds, the noise rate starts to increase strongly. The comparison of samples w06s12 and w06s14 shows that sample-to-sample variations are more significant than a possible impact of the different substrate resistivities.

Overall, the observed behaviour corresponds to the expectation because for a larger detection threshold the probability of a signal to be large enough to exceed the threshold decreases.

Comparing Figure 10.7a and 10.7b, it is seen that the total noise rate increases for threshold values below $1200\,\mathrm{e}^-$, whereas the number of firing pixels only starts to increase below a threshold of $800\,\mathrm{e}^-$. This means that with lower detection thresholds, the noise rate does not increase homogeneously across the whole sensor but is predominantly caused by a smaller number of noisy pixels.

Figure 10.8 shows an exemplary comparison of the noise hitmaps at a bias voltage of $-50\,\mathrm{V}$ and a threshold of $\sim 2000\,\mathrm{e}^-$ for the two $20\,\Omega\mathrm{cm}$ samples. It underlines that the noise rate at large thresholds is dominated by very few firing pixels and that the sensors can be operated nearly noise-free for thresholds larger than $1200\,\mathrm{e}^-$.

Generally, noisy pixels could be masked ("switched off") to reduce the noise rate and the occupancy of the readout system. As discussed in Section 5.3, this features

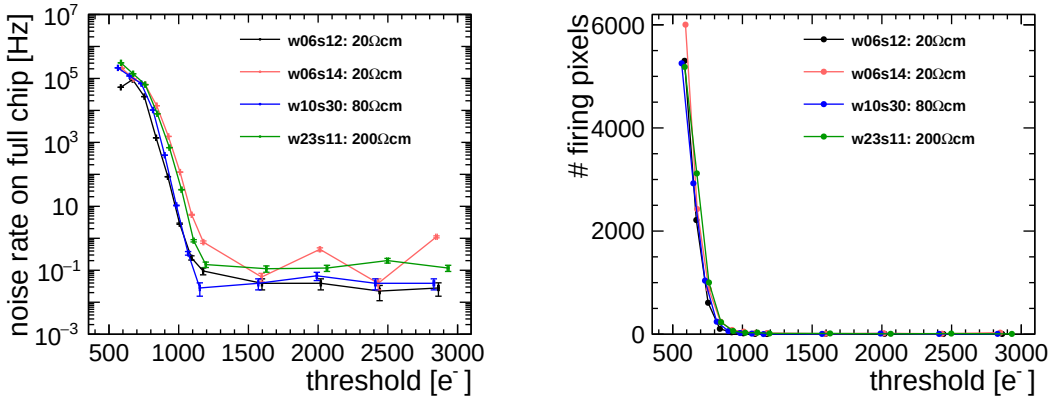

(a) Noise rate on the full chip.

(b) Number of firing pixels.

Figure 10.7: Threshold dependence of the noise rate at a bias voltage of $-50\,\mathrm{V}$ for samples with different substrate resistivities.

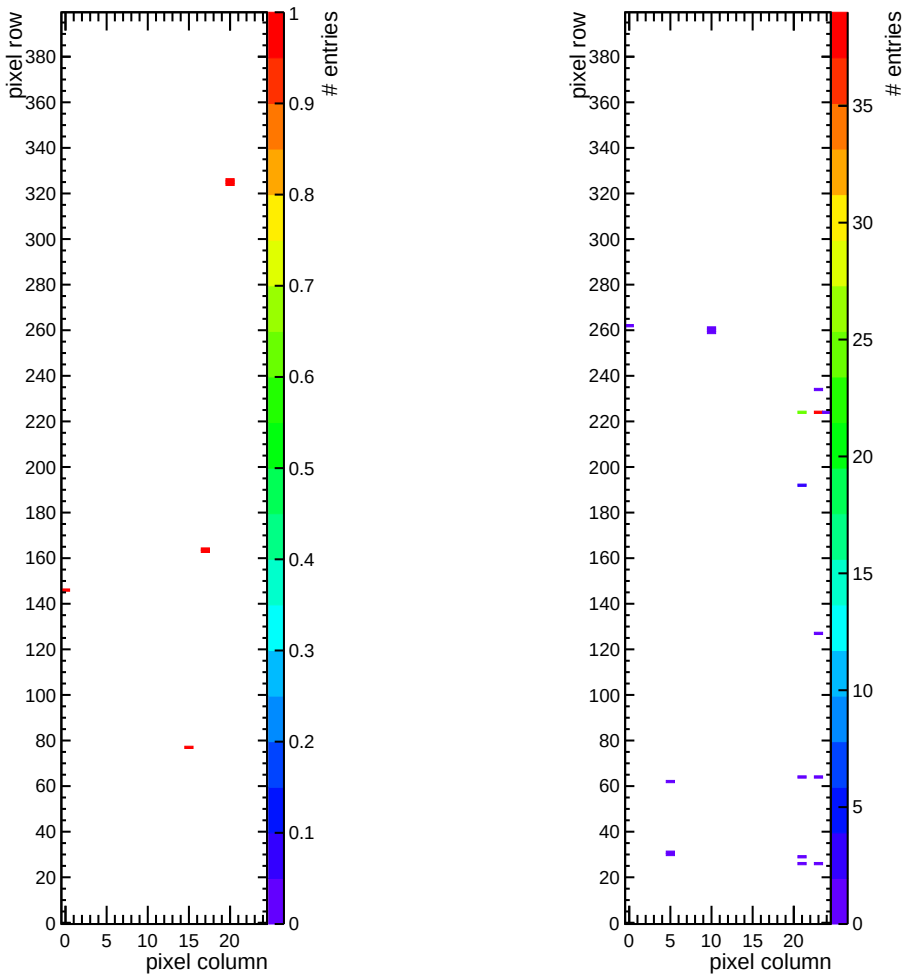

(a) Sample w06s12.

(b) Sample w06s14.

Figure 10.8: Noise hitmaps of the 20 Ωcm samples at a bias voltage of −50 V and a threshold of ∼2000 e^-.

does not work properly in the ATLASpix and was thus not used within the scope of this thesis.

The steepness of the increase of noise at low thresholds is related to the threshold dispersion, i.e. the variations in threshold from pixel to pixel across the matrix. It will be investigated in Section 10.4.1 in more detail using monoenergetic X-rays. The threshold dispersion also justifies the assumption that a few noisy pixels dominate the noise rate. These correspond to pixels with a threshold below average.

10.3.2 Bias Voltage Dependence

In Figure 10.9, the bias voltage dependence of the noise of samples with different substrate resistivities are compared at a threshold of ∼850 e^-. It is observed for all samples that the noise rate drops when increasing the bias voltage up to a certain point. After that it strongly increases.

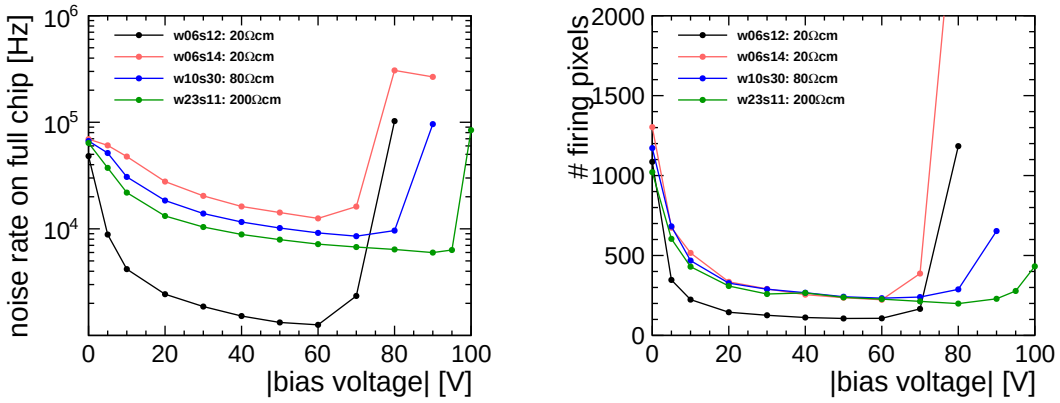

(a) Noise rate on the full chip.

(b) Number of noisy pixels.

Figure 10.9: Bias dependence of the noise rate at a threshold of 860 mV $\approx$ 850 e^- for samples with different substrate resistivities.

The decreasing noise with increasing bias voltages corresponds to the expectation. According to Equation 3.17, the sensor capacitance decreases with a larger bias voltage. This leads to a reduction of the signal size induced by thermal noise [43].

The comparison of w06s12 and w06s14 shows that sample-to-sample variations are more significant than the substrate resistivity at bias voltages between 0 V and −60 V. This is underlined by the fact that in this regime the noise rate is dominated by $\mathcal{O}(100)$ very noisy pixels. Consequently, a single pixel can already have a strong impact on the total noise rate. However, the point of strong increase is comparable for these two samples and lies at lower bias voltages as compared to the samples with larger substrate resistivities. The flattening of the noise rate at a bias voltage exceeding −80 V for sample w06s14, can be explained by the emerging saturation of the readout that occurs at large occupancies. An exemplary hitmap is displayed in Figure 10.10. Due to the architecture of the column drain readout (see Section 5.2.2), not all pixels can be read out at large occupancies causing a biased hitmap towards those pixels with readout priority. As a consequence, the measured number of hits per time is reduced with respect to the real number of noise hits. Consequently, the absolute value of the noise rate must be considered unreliable in this case.

It is seen that the upper and the lower half of the matrix show a similar noise pattern with a high number of hits in the rows above 0 and 200. This corresponds to the double-column drain scheme of the readout as described in Section 5.2.2. Rows 0 and 200 are read out with the highest priority, followed by rows 1 and 201, etc. Rows 199 and 399 have the lowest priority.

The noise rates of all samples are overlaid with the current-voltage characteristics and an indication of the breakdown voltage in Figure 10.11. It can be seen that a relation exists between the breakdown and the point of strongly increasing noise. The samples with larger substrate resistivities show a later breakdown and a later increase in noise. However, it is also apparent that the noise rate starts to increase

strongly only when exceeding V_{bd} by about 15-20 V because the current does not rise abruptly but in continuous way as discussed in Section 10.1.2. The correlation of the increasing noise with V_{bd} corresponds to the expectation: Beyond the breakdown, the leakage current rises strongly. This enhances the probability to trigger a fake hit because the in-pixel amplifiers are affected by the increasing shot noise of the sensor leakage current [167, 146].

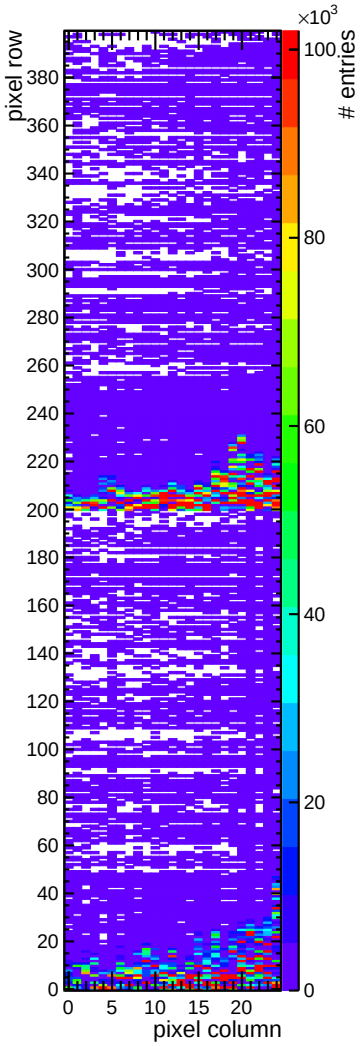

Figure 10.10: Noise hitmap at a bias voltage of $-90\,\text{V}$ and a threshold of $860\,\text{mV} \approx 850\,\text{e}^-$ for sample w06s14.

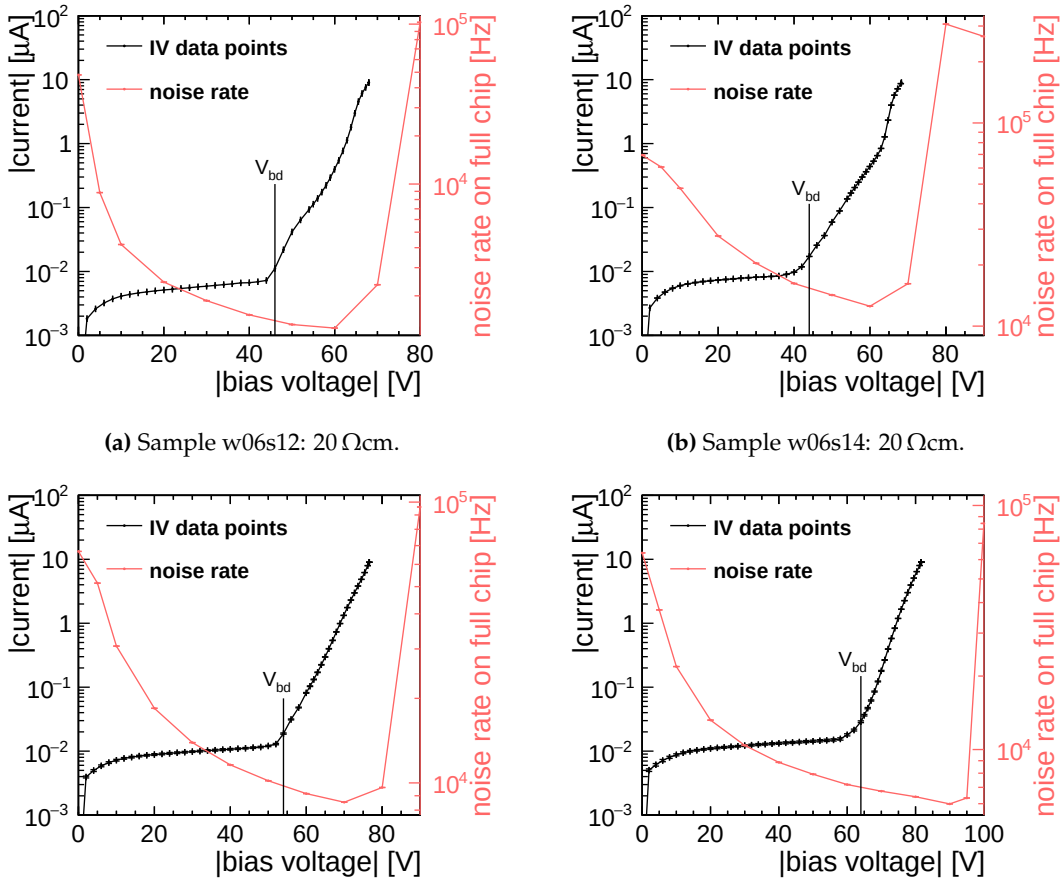

(a) Sample w06s12: 20 Ωcm.

(b) Sample w06s14: 20 Ωcm.

(c) Sample w10s30: 80 Ωcm.

(d) Sample w23s11: 200 Ωcm.

Figure 10.11: IV characteristics of samples with all substrate resistivities overlaid with the noise rate at a threshold of 860 mV $\approx$ 850 e^-. The vertical line indicates the breakdown voltage.

10.3.3 Time-over-Threshold Spectrum of Noise

Figure 10.12a shows the ToT spectrum of noise hits recorded for sample w23s11 at nominal conditions, i.e. a bias voltage of -50 V and a threshold of $\sim$850 e^-, and a ToT binning of 64 ns/bin. The distribution has a mean of $\sim$ 3 with a sharp drop-off towards ToT values < 2 and a slower decrease towards larger ToT values. Naively, the distribution would be expected to peak at 0 to 1 as noise hits arise from fluctuations of the baseline or threshold, or thermally generated electron-hole pairs corresponding to small signals. The observed spectrum can be explained by the occurrence of hysteresis in the comparator [82], which leads to a certain minimal measured delay between the times when the signal exceeds and then falls below the threshold.

Changing the clock divider `ckdivend2` from 7 to 15 leads to a ToT binning of 128 ns instead of 64 ns (see Section 5.2.1). According to the expectation, the mean of the noise ToT spectrum shifts to $\sim$ 1.5 and the ToT spectrum appears compressed by a factor of 2 as shown in Figure 10.12b

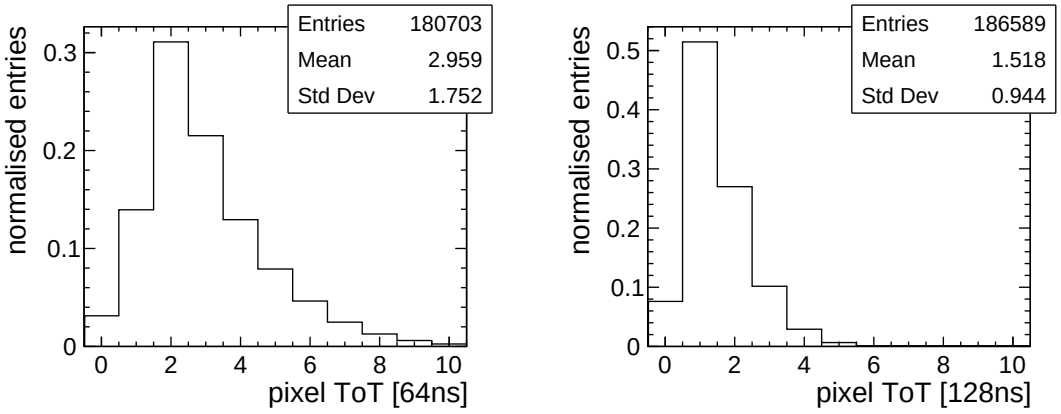

(a) `ckdivend2` $= 7$. **(b)** `ckdivend2` $= 15$.

Figure 10.12: Time-over-threshold spectrum for noise hits on sample w23s11 at a bias voltage of -50 V and a threshold of $\sim$850 e^- for two different ToT binnings.

10.4 Charge Calibration Measurements with Monoenergetic X-rays

A selection of the following results have been published in [168] and parts of this section use the exact same wording.

The detection threshold applied to the ATLASpix is a voltage level. A calibration is required to translate it into the number of electron-hole pairs equivalent to the deposited energy to allow for a physical interpretation and compare it to other devices. Likewise, the time-over-threshold is measured in clock counts as a difference between two timestamps and needs to be related to an energy scale in order to interpret the measured signal sizes.

For the results presented in this section, measurements have been performed with fluorescent X-rays of different materials as introduced in Section 6.5. An additional data point was obtained with an iron-55 radioactive source using the lab setup presented in Section 6.4. The data taking conditions as well as the analysis method were identical in both cases.

The intensity of the X-ray machine was regulated for each target to avoid an over-saturation of the readout and runs were taken with a length of 20 s or 40 s per threshold step. Both the threshold and the baseline voltages were applied externally and the baseline was set to 800 mV.

10.4.1 Analysis Method

The analysis is carried out as follows: For each pixel of the matrix, the number of pixel hits per run is plotted against the threshold. This yields a distribution as shown in Figure 10.13, which is an example for pixel (10,10) of sample w23s11 at a bias

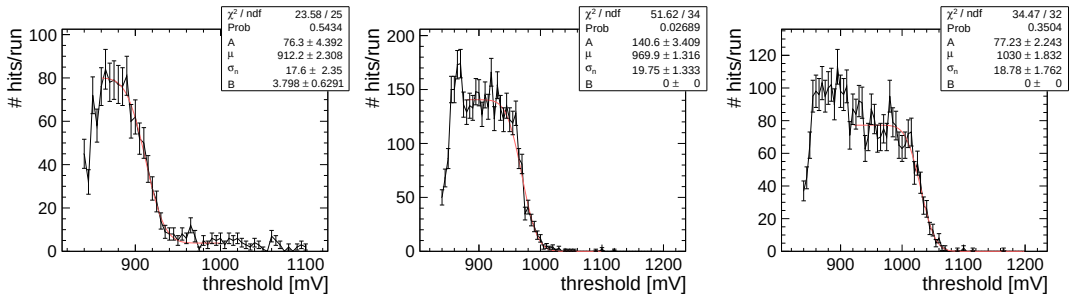

(a) Ti, $E_\gamma = 4.51\,\text{keV}$. **(b)** Fe, $E_\gamma = 6.40\,\text{keV}$ **(c)** Cu, $E_\gamma = 8.09\,\text{keV}$

Figure 10.13: Exemplary s-curve fit for pixel (10,10) of sample w23s11 with fluorescent X-rays from different targets at a bias voltage of $-50\,\text{V}$.

voltage of $-50\,\text{V}$. A so-called s-curve $f_s(x)$ can be used to describe the data:

$$f_s(x) = \frac{A}{2}\left(1 - \text{erf}\left(-\frac{x-\mu}{\sqrt{2}\sigma_n}\right)\right) + B \tag{10.7}$$

where A is a normalisation constant, μ is the threshold value corresponding to the mean signal of the X-ray, and σ_n represents the noise level of the pixel. $\text{erf}(x)$ is the error function defined as [169]

$$\text{erf}(x) = \frac{2}{\sqrt{\pi}}\int_0^x e^{-t^2}\text{d}t. \tag{10.8}$$

B is an offset to account for a high-energy contribution of the measured spectrum from primary X-rays Compton-scattered from the secondary target, which are observed for the low energy X-rays from titanium. As seen in Figure 10.13a, these higher-energy X-rays lead to a superimposed s-curve with a much lower plateau and a turn-off point at a higher threshold corresponding to the X-ray energy of the primary copper target. Thus, B can be interpreted as the plateau of the higher-energy X-rays, which is valid for the shown fit range $< 1000\,\text{mV}$. For all targets except titanium, B is set to zero. For the iron and copper targets, the intensity of the X-ray machine was reduced by a factor of $\sim 2-4$ to avoid the occurrence of a readout saturation before reaching the plateau. Hence, the contribution of scattered primary X-rays in the measured spectrum is reduced accordingly. For very low thresholds, the hit count drops in contrast to the expectation. This observation is explained by the readout saturation as discussed in Section 10.3. Consequently, this region is excluded from the fit of the s-curve.

The resulting fit parameters μ and σ_n are histogrammed as shown in Figure 10.14. The histograms show normal distributions, which are fitted with a Gaussian to obtain the mean and the standard deviation of each distribution: $\overline{\mu} \pm \overline{\sigma_\mu}$ and $\overline{\sigma_n} \pm \overline{\sigma_{\sigma_n}}$. The non-Gaussian tails visible in the left of Figure 10.14a and the right of Figure 10.14b originate from noisy pixels and line cross-talk, which will become apparent below.

To avoid a bias of the extracted peak positions by the non-Gaussian tails in the

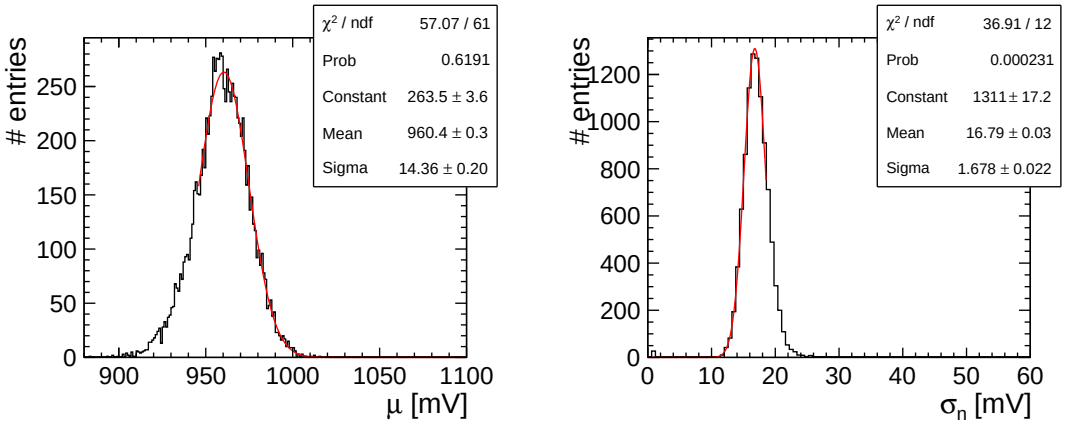

(a) Distribution of the threshold μ for all pixels with a Gaussian fit.

(b) Distribution of the noise σ_n for all pixels with a Gaussian fit.

Figure 10.14: Fit results obtained from s-curve fits for each pixel of sample w23s11 with fluorescent X-rays from an iron target at a bias voltage of $-50\,\mathrm{V}$.

further analysis, the fit procedure is performed in two steps: The resulting parameters from a first Gaussian fit are used to constrain the range for a second fit. For μ, the left tail is excluded by applying a fit interval of $[\overline{\mu} - \sigma_\mu, +\infty]$. For σ, the right tail is excluded by using an interval of $[-\infty, \overline{\sigma_n} + \sigma_{\sigma_n}]$.

From the Gaussian fits, the threshold $\overline{\mu}$ and threshold dispersion $\overline{\sigma_\mu}$ as well as the average pixel noise $\overline{\sigma_n}$ are extracted as the mean and the standard deviation of the fits to the distributions of thresholds and noise, respectively. In the following, the threshold values extracted for the different X-ray energies are used for a charge calibration of the threshold. Subsequently, the threshold dispersion and noise are discussed after the calibration into equivalent charge.

10.4.2 Gain and Baseline

The amount of deposited energy E deposited by an X-ray can be converted into the signal charge Q corresponding to the number of created electron-hole pairs (see Table 6.2 in Section 6.5). Figure 10.15 shows the values of $\overline{\mu}$ obtained in the previous section for the different X-ray energies. A first order polynomial is fitted for all samples:

$$\overline{\mu} = g\,[\mathrm{mV/keV}] \cdot E + b \tag{10.9}$$

$$= g\,[\mathrm{mV/1000e}] \cdot Q + b \tag{10.10}$$

where b denotes the extrapolated baseline, i.e. the y-intercept of the polynomial. The slope g of the fit function can be interpreted as the signal gain, which is summarised in Figure 10.16a for all presented samples.

No clear trend of the gain with the substrate resistivity can be seen. This implies that the observed differences stem from sample-to-sample variations and are dominated by a varying gain of in-pixel amplifier circuit.

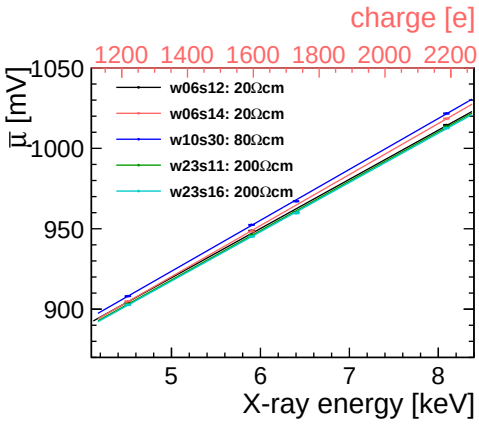

Figure 10.15: Signal size for different X-ray energies at a bias voltage of $-50\,\mathrm{V}$ for various samples. The second x-axis shows the conversion from X-ray energy into deposited charge as described in Section 6.5.

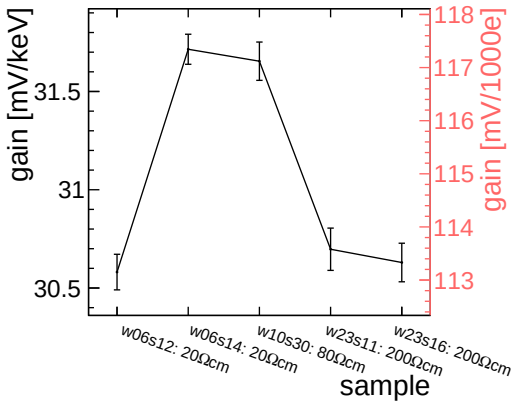

(a) Gain in [mV/keV] and in [mV/1000e].

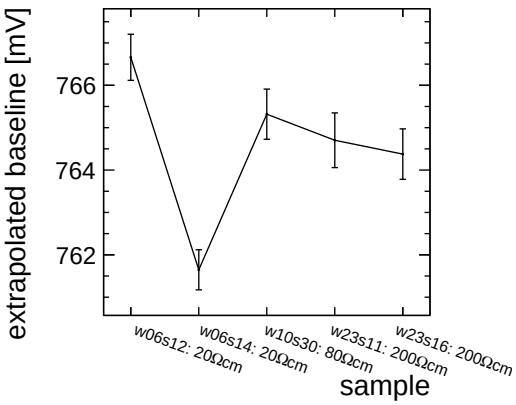

(b) Extrapolated baseline, i.e. x-intercept of the linear fit function.

Figure 10.16: Gain and extrapolated baseline extracted from the linear fits shown in Figure 10.15 for different samples at a bias voltage of $-50\,\mathrm{V}$. For sample w23s16 an additional measurement is shown for a bias voltage of $-95\,\mathrm{V}$.

Figure 10.16b summarises the extrapolated baseline, i.e. the y-intercept of the linear fit functions for all samples. It is observed that it differs notably from the externally applied baseline of 800 mV. This observation is consistent with a possible voltage offset within the in-pixel comparator, which can be $\mathcal{O}(\text{few } 10\,\mathrm{mV})$ [84]. As before, the deviations between the different samples are assumed to be caused by sample-to-sample variations.

The inversion of Equation 10.9 is used in the following to determine the signal charge for a given threshold:

$$Q = \frac{\overline{\mu} - b}{g} \tag{10.11}$$

with the uncertainty given by Gaussian error propagation:

$$\Delta Q = \sqrt{\left(\frac{1}{g}\Delta\overline{\mu}\right)^2 + \left(\frac{1}{g}\Delta b\right)^2 + \left(\frac{\overline{\mu} - b}{g^2}\Delta g\right)^2} \tag{10.12}$$

Averaging over all samples, a gain of $\overline{g} = (114.9 \pm 1.9)\,\mathrm{mV}/1000\mathrm{e}^-$ and an extrapolated baseline of $\overline{b} = (764.5 \pm 1.7)\,\mathrm{mV}$ are measured. The fact that the effective baseline is ∼35 mV below the external baseline has a significant impact on the threshold in electrons. Without taking the offset into account, the threshold would be underestimated by $35\,\mathrm{mV}/\overline{g} \approx 300\,\mathrm{e}^-$. It also shows that an energy calibration with only one data point (e.g. Fe-55) leads to an overestimation of the gain, if the gain is extracted from a linear fit between the external baseline of 800 mV and the signal.

It is important to note that the gain strongly depends on the chip configuration, in particular the value chosen for `VPPix` and `VNPix`, which regulate the current of the charge-sensitive amplifier in the pixel (see Chapter 5). Hence, the presented results are only valid for the used settings (see Appendix A). This needs to be taken into account when comparing these findings with other results. The effect of changing the chip settings was not investigated as part of this thesis.

10.4.3 Correlation Between Signal and Pixel Noise

Figure 10.17 shows the correlation between μ and σ_n for sample w23s11 with fluorescence X-rays from an iron target at a bias voltage of −50 V. As expected, a higher signal μ correlates with a higher pixel noise σ_n. A higher μ, meaning a higher signal for a given externally applied threshold, implies a lower local threshold of this particular pixel or a larger gain of its charge-sensitive amplifier. In turn, a lower local pixel threshold or a larger gain result in a larger probability to detect a fake hit.

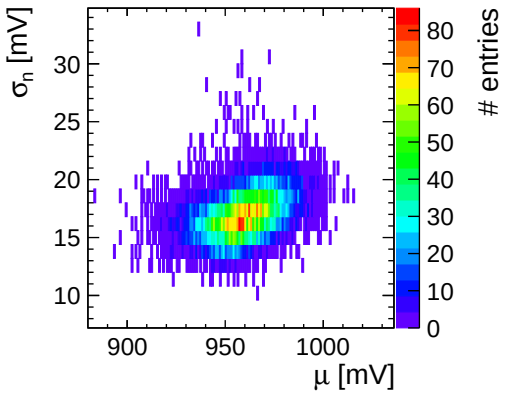

Figure 10.17: Correlation between μ and σ_n for samples w23s11 with fluorescence X-rays from an iron target at a bias voltage of −50 V.

10.4.4 Threshold Dispersion and Pixel Noise

Using the gain as a conversion factor, the threshold dispersion $\overline{\sigma_\mu}$ as well as the pixel noise $\overline{\sigma_n}$ determined previously can be translated into an equivalent charge as shown in Figure 10.18.

Threshold Dispersion

The threshold dispersion σ_μ for different X-ray energies is shown in Figure 10.18a. It varies between ∼10 mV and ∼17 mV corresponding to 85-150 e^- in the investigated energy range and a linear increase is observed with the energy. The threshold dispersion corresponds to the local variation of the amplifier gain and the detection threshold of the comparator. The experimental method involves a change of the threshold and therefore a shift of the working point of the in-pixel comparators. It cannot be excluded that these show a non-linear behaviour when changing the externally applied threshold, which may lead to a threshold dependence of the threshold dispersion [84]. In addition, the amplifier gain is expected to show a dispersion, which increases with larger signal sizes [84].

Pixel Noise

The average noise $\overline{\sigma_n}$ vs. the X-ray energy is plotted in Figure 10.18b. It also shows an increasing trend with rising X-ray energy and lies within a range of 12-21 mV corresponding to approximately 110-190 e^-. An intrinsic energy dependence on the fluctuations of the deposited charge is given by Fano noise (see Section 4.2). Table 10.2 summarises the expected contribution from Fano noise to the measured pixel noise at the relevant energies. Equation 4.4 yields the relative resolution of a signal, which needs to be multiplied by the deposited charge to obtain absolute numbers.

It is seen that the values obtained for the Fano noise are about 10× smaller than the measured noise. As it contributes to the total noise in a quadratic sum, it can be

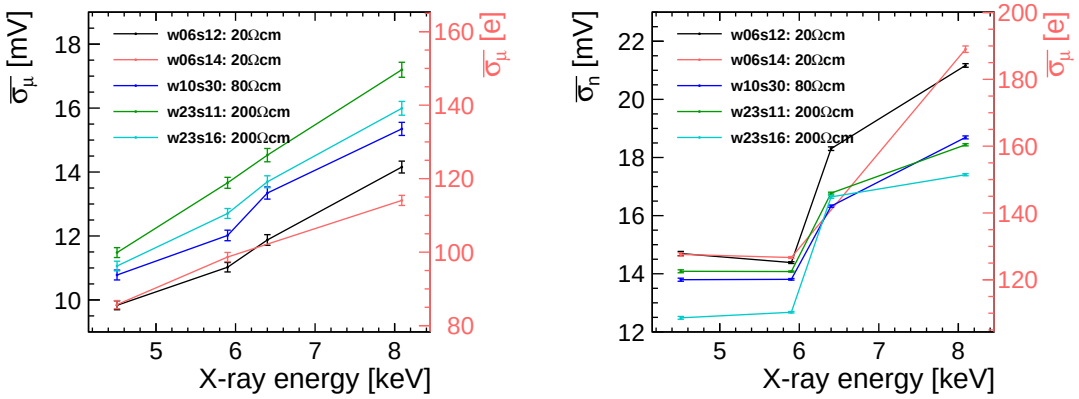

(a) Threshold dispersion σ_μ.

(b) Pixel noise $\overline{\sigma_n}$.

Figure 10.18: Charge-calibrated threshold dispersion and noise for different X-rays energies at a bias voltage of −50 V for various samples.

Table 10.2: Expected values for Fano noise as obtained using Equation 4.4 with a Fano factor of $F = 0.115$ [64] and an energy per electron-hole pair of $w = 3.7\,\text{eV}$ [115].

Target/Source	Energy of Kα [keV]	Deposited charge [e^-]	Fano noise [e^-]
Ti	4.51	1219	11.8
Fe-55 (source)	5.9	1595	13.6
Fe	6.4	1730	14.1
Cu	8.09	2186	18.0

inferred that it is negligible within the precision of the measurement. This implies that the measured pixel noise is dominated by the in-pixel electronics. The noise from the in-pixel electronics has contributions from the charge-sensitive amplifier and the comparator. Similarly as for the threshold dispersion, a shift of the operating point of the in-pixel comparator could be a possible cause for the observed behaviour.

Furthermore, contributions of contaminant X-rays with different energies in the spectrum impinging on the sensor may lead to systematic effects. A more detailed analysis would require the determination of the exact spectrum obtained with the X-ray tube using different target materials. Complementary studies with test-pulses injected into the amplifier could be performed to investigate whether the observed behaviour is related to the characteristics of the front-end electronics or the measurement procedure with X-rays.

10.4.5 Row Dependence of the Signal and Noise

Figure 10.19 shows the row dependence of the fit results for μ and σ_n. A clear row dependence is seen for the signal μ. For rows larger than 100-200, the signal rises with increasing row number.

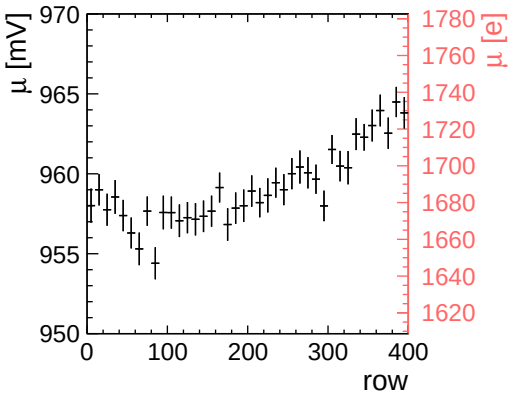

(a) Threshold μ. Averaged over 10 rows per bin.

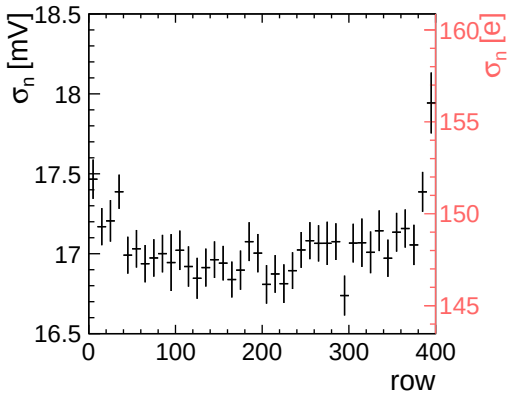

(b) Noise σ_n. Averaged over 10 rows per bin.

Figure 10.19: Row dependence of the fit results obtained from s-curve fits for each pixel of sample w23s11 with fluorescent X-rays from an iron target at a bias voltage of $-50\,\text{V}$.

The row dependence of the signal implies that either the local threshold has a gradient across the matrix, or alternatively, the gain of the in-pixel amplifiers may show a row dependence. A similar finding was presented in [75], where a row dependence of the analogue output of the charge-sensitive amplifier is observed. It is suspected that it may be related to a non-uniform distribution of VSSA, i.e. the power provided to the charge-sensitive amplifiers, which could result in a row dependence of the amplifier gain. VSSA is provided to the chip via pads placed on the top side of the matrix, i.e. above row 399. If a voltage drop occurs with larger distances to the pixels, the effective voltage level of VSSA in lower rows could be reduced resulting in a smaller gain. The row dependence will be discussed in more detail in the context of the hit detection efficiency (see Section 11.2) as well as the cluster size and ToT (see Section 11.3), where a similar trend is observed.

Assuming that a row dependence of the gain is responsible for row dependence of μ, a similar behaviour would be expected for the pixel noise because a higher gain would result in a larger probability to detect noise as shown in Figure 10.17. The statistical uncertainties of the pixel noise do not allow to infer a similar row dependence as seen for the threshold. At row 390-400, the pixel noise rises strongly. This coincides with an increased cross-talk probability as will be discussed in Section 8.2.2. This effect also explains the non-Gaussian tails seen in Figure 10.14: A pixel can be affected by cross-talk from a neighbouring pixel cell independent of its own threshold because it is caused by line cross-talk between the transmission lines connecting the pixel cell and periphery and hence occurs after the in-pixel comparator. This way, cross-talk hits can smear out the measured s-curve for a given pixel and thus cause a decreased measured pixel threshold and an increase of the measured pixel noise.

10.4.6 Signal-to-Noise Ratio

The same data used for the charge calibration of the threshold in the previous section can be exploited to calculate the signal-to-noise ratio (SNR) for the ATLASpix. It can be determined as

$$\overline{\mathrm{SNR}} = \frac{\overline{\mu} - b}{\overline{\sigma_n}} \tag{10.13}$$

where b denotes the effective baseline as extracted above. The statistical uncertainty is obtained by Gaussian error propagation:

$$\Delta\overline{\mathrm{SNR}} = \sqrt{\left(\frac{\Delta\overline{\mu}}{\overline{\sigma_n}}\right)^2 + \left(\frac{\Delta b}{\overline{\sigma_n}}\right)^2 + \left(\frac{\overline{\mu} - b}{\overline{\sigma_n}^2}\Delta\overline{\sigma_n}\right)^2}. \tag{10.14}$$

Figure 10.20 shows the SNR as calculated based on Equation 10.13 and using the mean thresholds $\overline{\mu}$ and mean pixel noise $\overline{\sigma_n}$ values extracted from the Gaussian fits of the μ-distributions for all samples and X-ray energies. For the uncertainty on the

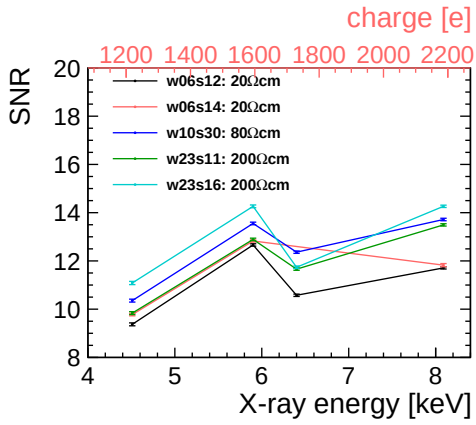

Figure 10.20: Signal-to-noise ratio for different X-ray energies and various samples at a bias voltage of $-50\,\mathrm{V}$.

SNR, the errors on the fit parameters are propagated using Equation 10.14. According to Equation 10.13, a linear relation would be expected for a larger signal assuming a constant pixel noise. However, as a threshold dependence on the noise was observed as seen in Figure 10.18b, the linear trend is distorted. It can furthermore be seen that sample-to-sample variations are more significant than a possible influence of the substrate resistivity. In the investigated energy range, the SNR varies between 9 and 14 depending on the signal size and the sample. For X-rays from the Fe-55 source at an energy of 5.9 keV, a SNR above 12 is reached with all samples.

10.4.7 Charge Calibration of the Time-over-Threshold Measurement

In order to perform a charge calibration of the time-over-threshold measurement, the same data as previously analysed for the energy calibration of the threshold is exploited. Hence, the calibration is restricted to the four available X-ray energies.

Monoenergetic X-rays in the used energy range always deposit their full energy when they are absorbed. Consequently, a Gaussian energy spectrum is expected to be measured due to the limited energy resolution of the device and the occurrence of Fano noise (see Table 10.2). Sub-threshold effects like small amounts of charge sharing into neighbouring cells, which remain below the detection threshold may distort the shape. Generally, charge sharing leading to multi-pixel clusters needs to be taken into account such that the ToT calibration is performed on cluster level. Clustering is performed allowing only adjacent pixels (including corners) within a time window of 300 ns to be grouped into a cluster. The cut of 300 ns is justified a posteriori through the test-beam results presented in Chapter 11. The cluster ToT corresponds to the sum of ToTs from all pixel within the cluster (see Equation 8.2).

Figure 10.21a shows an exemplary ToT spectrum both at pixel level and after clustering for sample w23s11 at a threshold of $\sim 850\,\mathrm{e}^-$ and a bias voltage of $-50\,\mathrm{V}$ for X-rays of the Fe-55 source. It can be observed that the ToT spectrum on pixel level resembles a Gaussian distribution with an additional bump at low ToT values. This

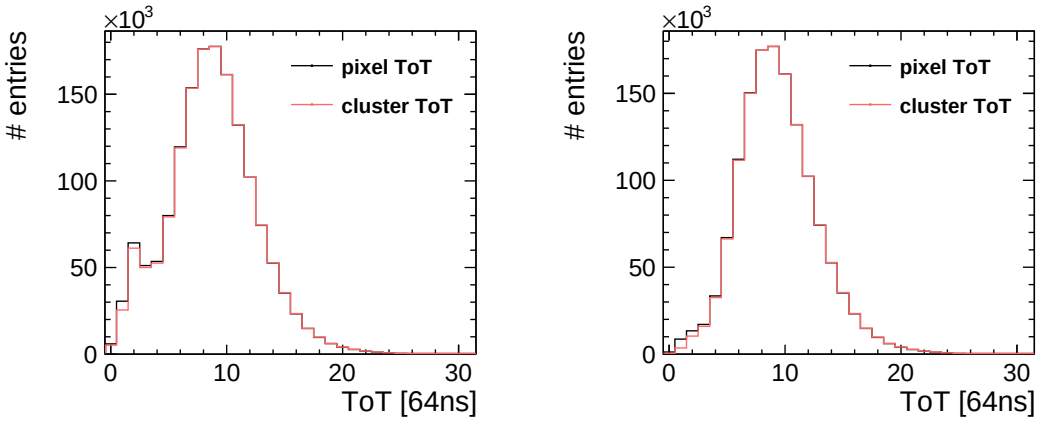

(a) No mask.

(b) Masking the 15 most noisy pixels.

Figure 10.21: ToT spectra on pixel level and after clustering for sample w23s11 at a threshold of 860 mV $\approx$ 850 e^- and a bias voltage of -50 V for X-rays from the Fe-55 radioactive source with an energy of 5.9 keV.

bump is expected to contain both fake hits, which have a low ToT value peaking at $\sim 2-3$ as discussed in Section 10.3.3, as well as pixels with a small ToT value due to charge sharing. However, the spectra on pixel level and after clustering are very similar meaning that only few entries in the low ToT bump on pixel level stem from charge sharing and the majority of them arise from fake hits. This is supported by Figure 10.21b, which shows the same spectrum when the 15 most noisy pixels are masked, i.e. excluded from the analysis.[1] It shows that the bump at low ToTs disappears and only a small difference between the spectrum on pixel-level and after clustering is seen. This indicates that the amount of charge sharing is very limited in the ATLASpix and the occurrence of single-pixel clusters is predominant. This observation is confirmed by the test-beam results presented in Section 11.3.2. The following analysis steps are performed on cluster level.

To extract the most-probable value (MPV) of the ToT for a given X-ray energy at a particular threshold and bias voltage, a Gaussian is fitted to the peak of the ToT distribution. The range is restricted to exclude the low-ToT bump caused by noise, which becomes more prominent with lower thresholds (see Figure 10.22a). Furthermore, it can be seen that the ToT spectrum develops a non-Gaussian shape with higher thresholds (see Figure 10.22c). This corresponds to the previous observation that ToT values below 2 are disfavoured due to the hysteresis of the comparator as discussed in Section 10.3.3. In consequence, the fit range is adjusted individually for each run to ensure a proper fit of the peak position representing the MPV. While the impact of noise disappears with higher thresholds, the obtained MPV of the ToT for larger thresholds is biased to be ≥ 2 by the comparator hysteresis and the MPV cannot be determined reliably. On the other hand, the charge calibration of the ToT

[1] Noisy pixels are identified in the hitmap as pixel with excessive number of entries compared to the average on the matrix. For all further results, no masking is applied.

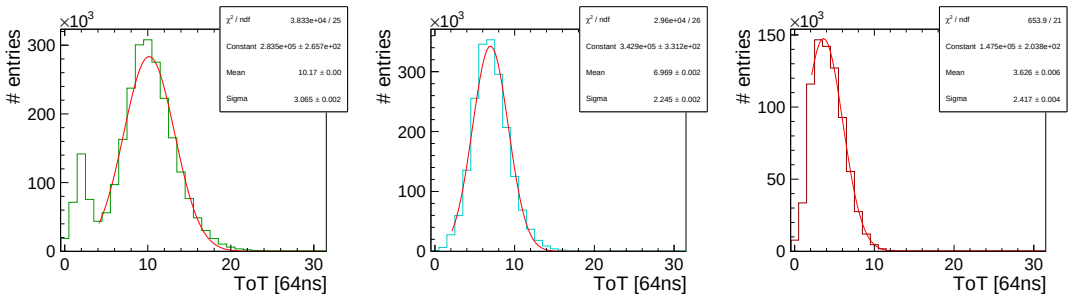

(a) Threshold of 845 mV ≈ 720 e^-.

(b) Threshold of 900 mV ≈ 1200 e^-.

(c) Threshold of 950 mV ≈ 1640 e^-.

Figure 10.22: Examples of the ToT spectrum for sample w23s16 at a bias voltage of −50 V for X-rays from the Fe-55 source with an energy of 5.9 keV at different thresholds.

spectrum is most relevant around the operating threshold to allow for a calibration of the ToT peak obtained with MIPs.

Figure 10.23 shows the dependence of the MPV on the detection threshold, as well as the number of hits per run for each threshold. The vertical orange line indicates the signal size as determined by the mean of the s-curve fits in Section 10.4.2. It can be observed that the MPV of the ToT follows a decreasing trend in the threshold range of ∼700-1700 e^-. In this range, the MPV can be determined unambiguously because of a low noise rate and a high number of hits. This behaviour corresponds to the expectation, since a higher detection threshold results in a shorter time-over-threshold for a given signal size. At very low thresholds, the signal peak becomes indistinguishable from the noise peak and the MPV cannot be determined in a reliable way. At thresholds larger than the cut-off of the signal given by the mean of the s-curve discussed above, the number of entries drops significantly as expected and the MPV of the ToT cannot be determined because the applied threshold exceeds the signal.

For an ideal triangular signal shape and an ideal response of the front-end electronics, a perfect linear dependence would be expected between the MPV of the ToT and the threshold. The observed slight non-linearity arises due to the following reasons: The signal fed from the amplifier into the comparator deviates from a perfect triangular shape as shown in Figure 10.24, where an oscilloscope measurement of the amplifier output signal is presented. In addition, especially at lower thresholds, noisy pixels can lead to a distortion of the spectrum. As seen in Section 10.3.3, fake hits mostly lead to a ToT of $\sim 2-3$, but significantly larger ToTs can occur. Furthermore, the comparator shows a hysteresis and thus behaves in a non-linear way at small ToTs.

In Figure 10.25, the dependence of the MPV of the ToT on the deposited charge is shown for different samples at a fixed threshold of 860 mV ≈ 840 e^-. In principle, these results can be used to determine the amount of charge deposited by a

minimum ionising particle. However, the non-linear behaviour and the restriction of the measurement to four data points does not allow for an extrapolation to higher charge depositions without large systematic uncertainties.

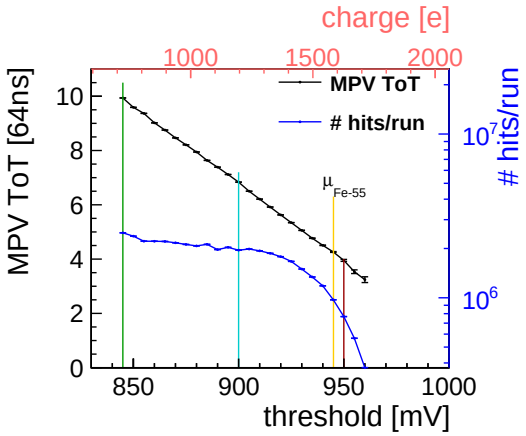

Figure 10.23: Threshold dependence of the MVP of the ToT spectrum for sample w23s16 at a bias voltage of −50 V for X-rays from the Fe-55 source with an energy of 5.9 keV. The orange line marks the cut-off threshold of the signal and the green, cyan and brown lines indicate the thresholds for which the ToT spectra are shown in Figure 10.22.

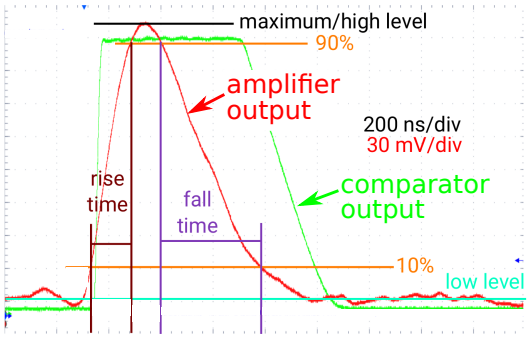

Figure 10.24: Example signal shape of the analogue output from the in-pixel amplifier shown in red and the comparator output shown in green measured with an oscilloscope. From [75] (modified).

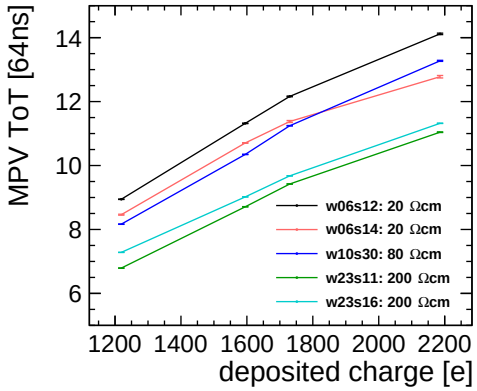

Figure 10.25: Dependence of the MPV of the ToT on the deposited charge for all samples at a bias voltage of −50 V and a threshold of 860 mV ≈ 840 e^-.

Chapter 11

Test-beam Measurements

In this chapter measurements and analysis results based on test-beam are presented. The data was recorded at the CERN SPS in 2018 and at DESY between 2019-2020 due to the Long Shutdown 2 (LS2) of accelerator complex at CERN. The test-beam facilities and the used experimental setups are introduced in Chapter 7. The reconstruction and analysis chain is presented in Chapter 8, and the performance of the reference telescopes is evaluated and discussed in Chapter 9.

A full characterisation is performed with a 200 Ωcm sample. The results are shown in Sections 11.1 to 11.5 based on data recorded at the SPS. The studies comprise the hit detection efficiency, cluster formation as well as the spatial and time resolution.

In Section 11.6, the influence of different substrate resistivities on the performance is investigated. The corresponding data was recorded at DESY. It is motivated by the fact that higher substrate resistivities are expected to improve the sensor performance: A larger ρ leads to a larger depletion region for a given bias voltage, which leads to a smaller sensor capacitance and a larger amount of charge deposited within the depletion region by a traversing ionising particle. On the other hand, the standard resistivity of the AMS aH180 technology is 20 Ωcm as described in Section 5. These studies help to answer the question if it is beneficial to deviate from the nominal process to gain performance.

The chapter ends with a determination of the active depth of a 200 Ωcm ATLASpix based on studies with inclined tracks shown in Section 11.7. The corresponding data was also taken at DESY.

11.1 Analysis Strategy for SPS Data

In order to avoid a bias by noisy pixels on the analysis results, only clusters associated to a reference track are investigated. Unless otherwise stated, all presented results were obtained with data recorded at the SPS with the 200 Ωcm sample w23s15 at a bias voltage of -75 V and a detection threshold of 845 mV corresponding to approximately 720 e^-. Because this sample was not available for laboratory measurements, the average calibration of the other 200 Ωcm samples w23s11 and w23s16 was applied (see Section 10.4.2).

As discussed in Section 7.2.1, the area of the DUT exceeds to acceptance of the reference telescope. Consequently, two different sets of runs are combined, for which the beam was focussed on the upper and the lower section of the pixel matrix, respectively. In both cases, the telescope and DUT alignment is performed using one selected run and the resulting alignment was used for all runs with the same geometry. Figure 11.1 shows the two-dimensional distribution of track-associated clusters for two exemplary runs. The histograms are filled at the cluster position if the associated track intercepts the pixel matrix. It can clearly be seen which sections of the matrix lie within the telescope acceptance. The number of entries gives an indication of the position of the beam spot.

As discussed in Section 10.4, a row dependence of the signal gain is observed. To avoid a bias of the results arising from an inhomogeneous illumination of the rows, the analysis results for the upper and the lower matrix sections are combined and

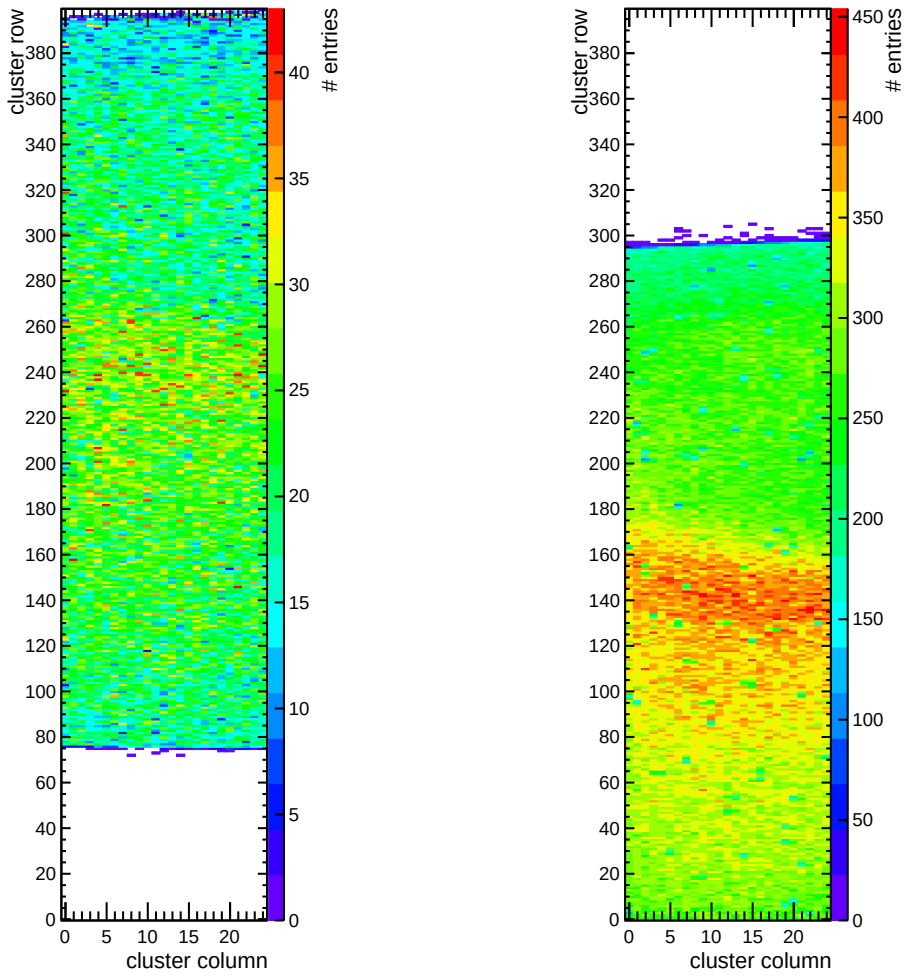

(a) Upper section of the matrix.

(b) Lower section of the matrix.

Figure 11.1: Two-dimensional distribution of track-associated clusters across the matrix for two runs covering the upper and the lower area of the matrix at a bias voltage of $-75\,\mathrm{V}$ and a threshold of $845\,\mathrm{mW} \approx 720\,\mathrm{e}^-$.

rescaled such that each row contributes with the same weight. For the studies of the threshold dependence for the various parameters, data is only available for the configuration focussing on the upper section of the matrix, i.e. rows above 76.

Region-of-Interest

Unless explicitly stated, the entire matrix is used as the region-of-interest. Only the outermost pixels of the matrix are excluded to avoid edge effects, when a physical track penetrating the sensor just outside of the active area but is reconstructed within the active area due to the limited resolution of the telescope.

11.2 Hit Detection Efficiency

The hit detection efficiency corresponds to the probability of detecting a traversing ionising particle and is determined as described in Section 8.4.1.

11.2.1 Threshold and Bias Dependence

Figures 11.2 and 11.3 show the hit detection efficiency as a function of the detection threshold and the bias voltage, respectively. In both cases, the total noise rate on the sensor is plotted as well. Because the beam structure at the CERN SPS consisting of spills with a duration of $\mathcal{O}(5\,\mathrm{s})$ and a duty cycle of $\approx 10\,\%$, it is possible to determine the noise rate in situ by extracting the hit rate on the sensor from periods between the beam spills. This way, it is ensured that the operating conditions are identical for both the efficiency and the noise measurements.

Threshold Dependence

As can be seen in Figure 11.2, the efficiency is above 99.9 % for thresholds between $670\,\mathrm{e}^-$ and $850\,\mathrm{e}^-$. With an increasing detection threshold it drops significantly. This corresponds to the expected behaviour as for an increasing threshold the fraction of signals large enough to exceed the threshold is reduced. The same behaviour is observed for the noise rate, which is below 1 Hz on the full sensor for threshold larger than $670\,\mathrm{e}^-$ and drops even further for higher thresholds. On the contrary, at a very low threshold below $670\,\mathrm{e}^-$, the noise rate increases strongly. At an even lower threshold of $585\,\mathrm{e}^-$ the efficiency drops. This observation is consistent with the laboratory measurements of the noise rate presented in Section 10.3.1. At very low thresholds, an excessive noise rate causes the readout to saturate. Consequently, not all hits originating from particles can be read out and the measured hit detection efficiency is reduced.

The highest measured efficiency is $\epsilon_{\mathrm{max}} = (99.9945^{+0.0009}_{-0.0010})\,\%$, which is reached at a bias voltage of $-75\,\mathrm{V}$ with a detection threshold of $\sim 670\,\mathrm{e}^-$ (see Figure 11.2b). As discussed in Section 8.4.1, the accidental matching of noise hits can lead to an

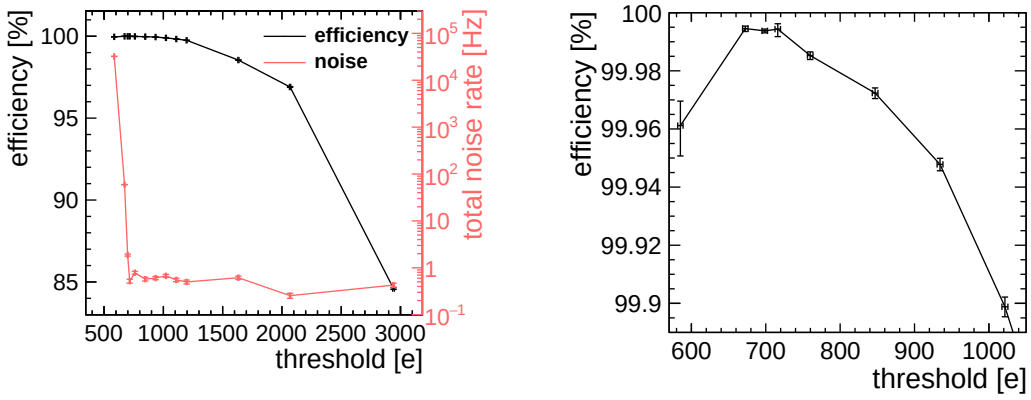

(a) Efficiency and noise rate.

(b) Efficiency (zoom).

Figure 11.2: Hit detection efficiency and total noise rate on the sensor in dependence on the detection threshold for runs focussing on the upper section of the matrix (rows above 76) at a bias voltage of $-75\,\mathrm{V}$.

increased measured efficiency. At this point, a total noise rate of $(59.4 \pm 0.5)\,\mathrm{Hz}$ is measured on the full sensor. With Equation 8.9, this leads to contribution of $\epsilon_{\mathrm{noise}} \sim 3.2 \times 10^{-6}\,\%$ to the measured efficiency and is therefore negligible compared to the statistical uncertainty on the measurement.

The measured inefficiency is $(100\,\% - \epsilon_{\mathrm{max}}) \approx 0.0055\,\%$. The following reasons lead to an efficiency smaller than 100 %:

- A small fraction of particles deposits only a small amount of energy as described by the Landau statistics. In particular in the pixel corners, this leads to sub-threshold losses as discussed below in Section 11.2.2.
- Each pixel has a dead time: If a pixel is traversed by a second particle before its corresponding readout cell was read out, the second hit cannot be detected. The dead time cannot easily be quantified. It depends on the position of the pixel in the matrix (determining the readout priority) as well as the chip occupancy as discussed in Section 5.2.2.
- A small probability exists that a track is reconstructed incorrectly but still passes the strict selection cuts. In this case, no associated cluster can be found for this "fake track".

It should be noted that the performance of a threshold equalisation was not possible with the ATLASpix (see Section 5.3). It can be expected that this would allow to lower the threshold even further and therefore recover part of the inefficiency while avoiding a saturation of the readout by noise hits.

Bias Dependence

Figure 11.3 shows the dependence of the efficiency and the noise on the bias voltage. The efficiency rises with increasing bias voltages and stays above 99.9 % for bias

voltages larger than −40 V. This is expected because a larger bias voltage creates a larger depleted volume and thus a larger signal because more energy is deposited within the depleted region by a traversing ionising particle. Notably, already at a bias voltage of −5 V, the sensor reaches an efficiency above 97 %. The noise rate decreases slightly with larger bias voltages, which is consistent with a decrease of the sensor capacitance as discussed in Section 10.3.2.

11.2.2 In-Pixel Efficiency

Figures 11.4 and 11.5 show the in-pixel efficiency distributions for different thresholds and bias voltages. For larger thresholds or lower bias voltages, where the total efficiency is significantly reduced, the efficiency remains highest within the pixel centre and falls off towards the pixel corners and edges. This corresponds to the expectation since more charge sharing can occur close to the pixel corners and edges leading to larger clusters, while the induced signal in one pixel is reduced and more likely to remain below threshold.

At the lowest threshold (Figure 11.4a) and the largest bias voltage (Figure 11.5d), the efficiency is homogeneous across large parts of the pixel area. Nonetheless, even under these conditions a small efficiency loss is observed in the pixel corners. To quantify the efficiency losses at the pixel edges and corners, an in-pixel ROI is defined as illustrated by the blue box in Figure 11.4a. From each pixel edge, a distance of 10 µm is excluded. The efficiency within this in-pixel ROI reaches a value of $\epsilon_{\text{max}} = (99.9972^{+0.0007}_{-0.0010})\%$.

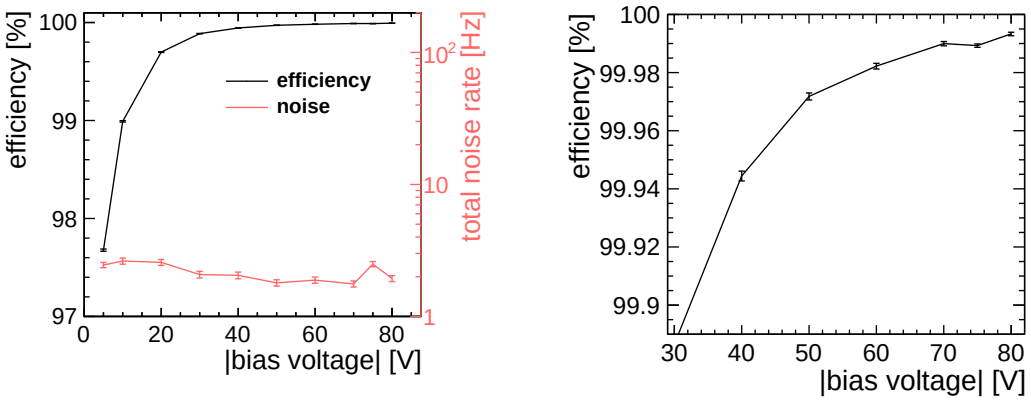

(a) Efficiency and noise rate.

(b) Efficiency (zoom).

Figure 11.3: Hit detection efficiency and total noise rate on the full sensor in dependence on the bias voltage at a threshold of 845 mV ≈ 720 e^-.

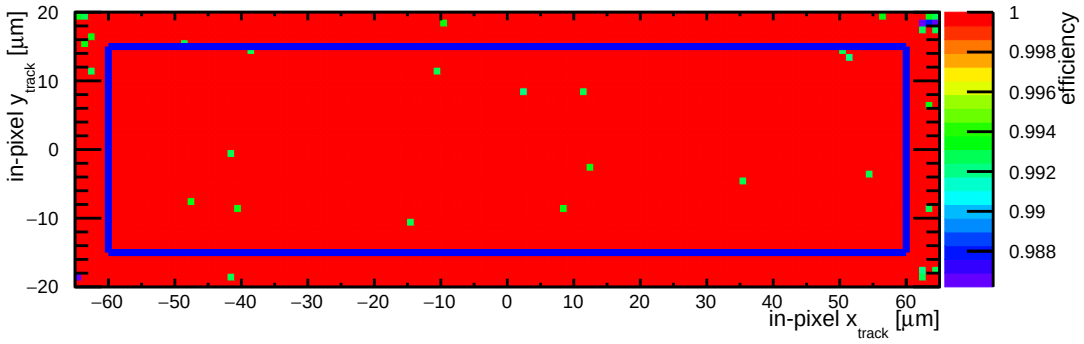

(a) Threshold = 840 mV ≈ 670 e^-, total efficiency = $(99.9945^{+0.0009}_{-0.0011})\%$. The blue box marks the in-pixel region-of-interest, in which an efficiency of $(99.9972^{+0.0007}_{-0.0010})\%$ is measured.

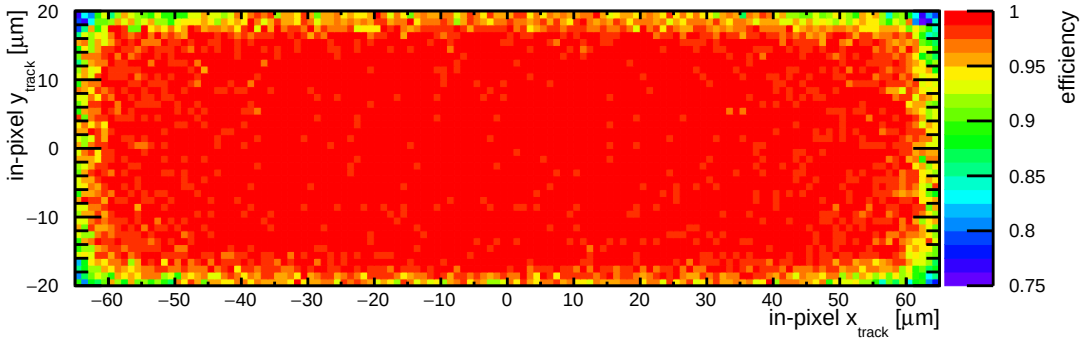

(b) Threshold = 950 mV ≈ 1630 e^-, total efficiency = $(98.545^{+0.014}_{-0.014})\%$.

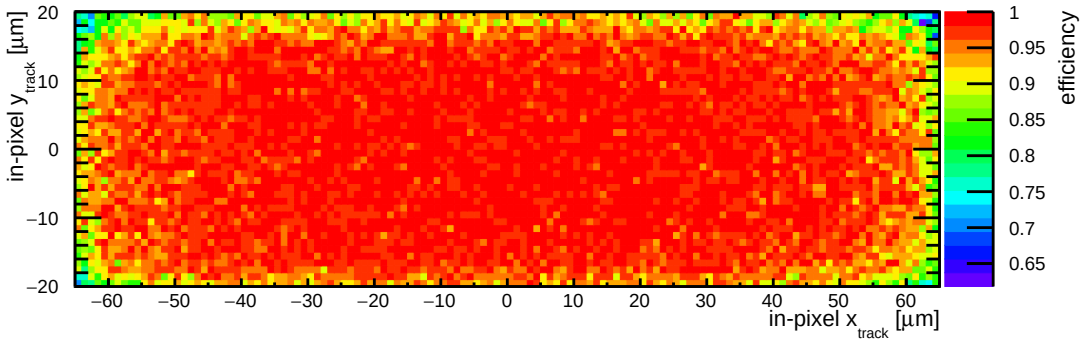

(c) Threshold = 1000 mV ≈ 2060 e^-, total efficiency = $(96.90^{+0.03}_{-0.03})\%$.

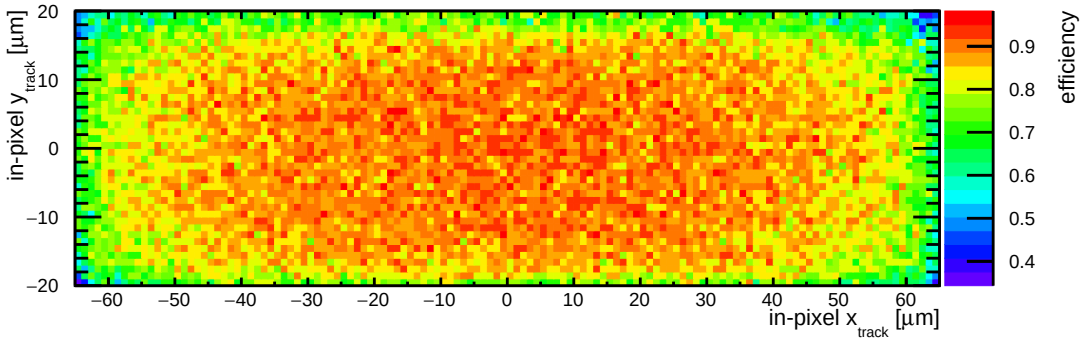

(d) Threshold = 1100 mV ≈ 2930 e^-, total efficiency = $(84.60^{+0.05}_{-0.05})\%$.

Figure 11.4: In-pixel plots of the hit detection efficiency for different thresholds at a bias voltage of −75 V. Different z-ranges are chosen for a better visibility of the efficiency losses in the corners for low thresholds.

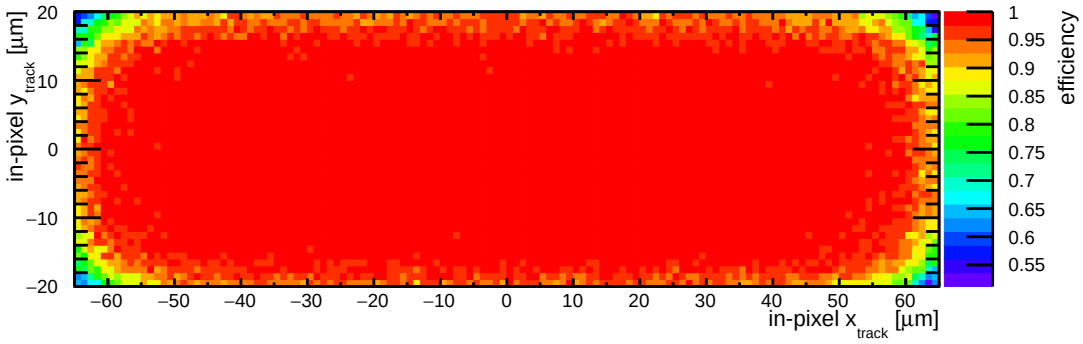

(a) Bias voltage = $-5\,\mathrm{V}$, total efficiency = $(97.68^{+0.01}_{-0.01})\%$.

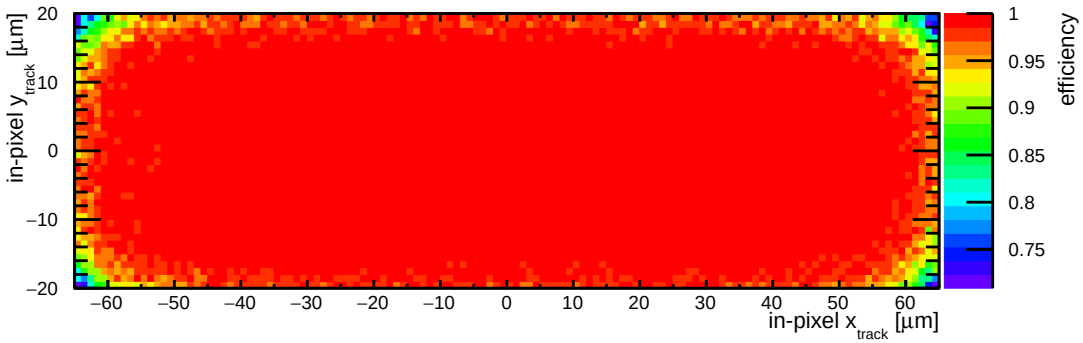

(b) Bias voltage = $-10\,\mathrm{V}$, total efficiency = $(98.991^{+0.007}_{-0.007})\%$.

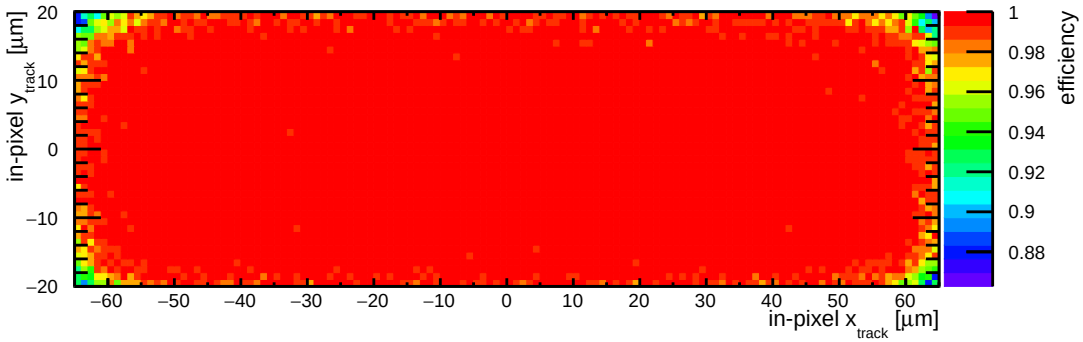

(c) Bias voltage = $-20\,\mathrm{V}$, total efficiency = $(99.698^{+0.004}_{-0.004})\%$.

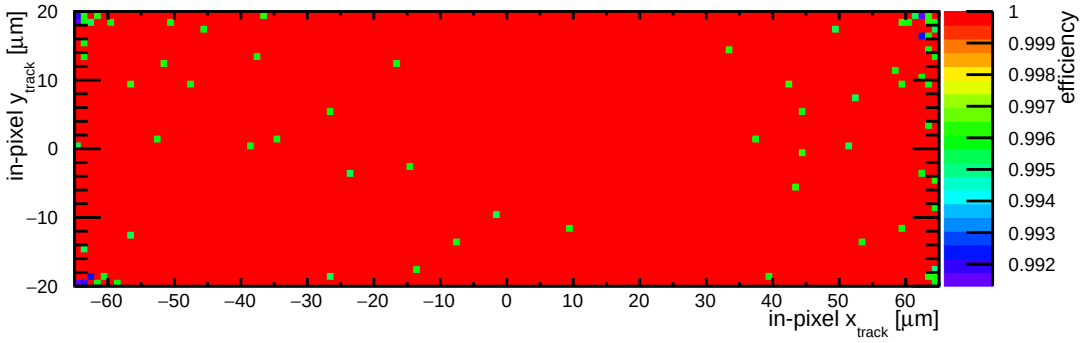

(d) Bias voltage = $-80\,\mathrm{V}$, total efficiency = $(99.9933^{+0.0006}_{-0.0006})\%$.

Figure 11.5: In-pixel plots of the hit detection efficiency for different bias voltages at a threshold of 845 mV $\approx 720\,\mathrm{e}^-$. Different z-ranges are chosen for a better visibility of the efficiency losses in the corners for low thresholds.

11.2.3 Efficiency Across the Matrix and Row Dependence

In Figure 11.6 the hit detection efficiency is plotted across the pixel matrix for different thresholds. As before, not the entire chip lies within the telescope acceptance. It can be seen that for a low threshold of 840 mV $\approx$ 673 e^- the efficiency is uniformly high across the entire sensor (Figure 11.6a). At larger thresholds, for which the efficiency is reduced as discussed above, a clear gradient is observed across the sensor: The efficiency is higher for larger row numbers and drops for smaller row numbers.

Figure 11.7 shows the efficiency plotted across the sensor for different bias voltages combining runs focussing on the upper and the lower section of the matrix. Similarly to the previous observation, it is seen that the efficiency is uniformly high for large bias voltages (Figure 11.7c). At smaller bias voltages, a clear inhomogeneity is observed across the pixel matrix.

This effect becomes more apparent in Figure 11.8, where the row dependence of the efficiency is shown for different thresholds (see Figure 11.8a) and different

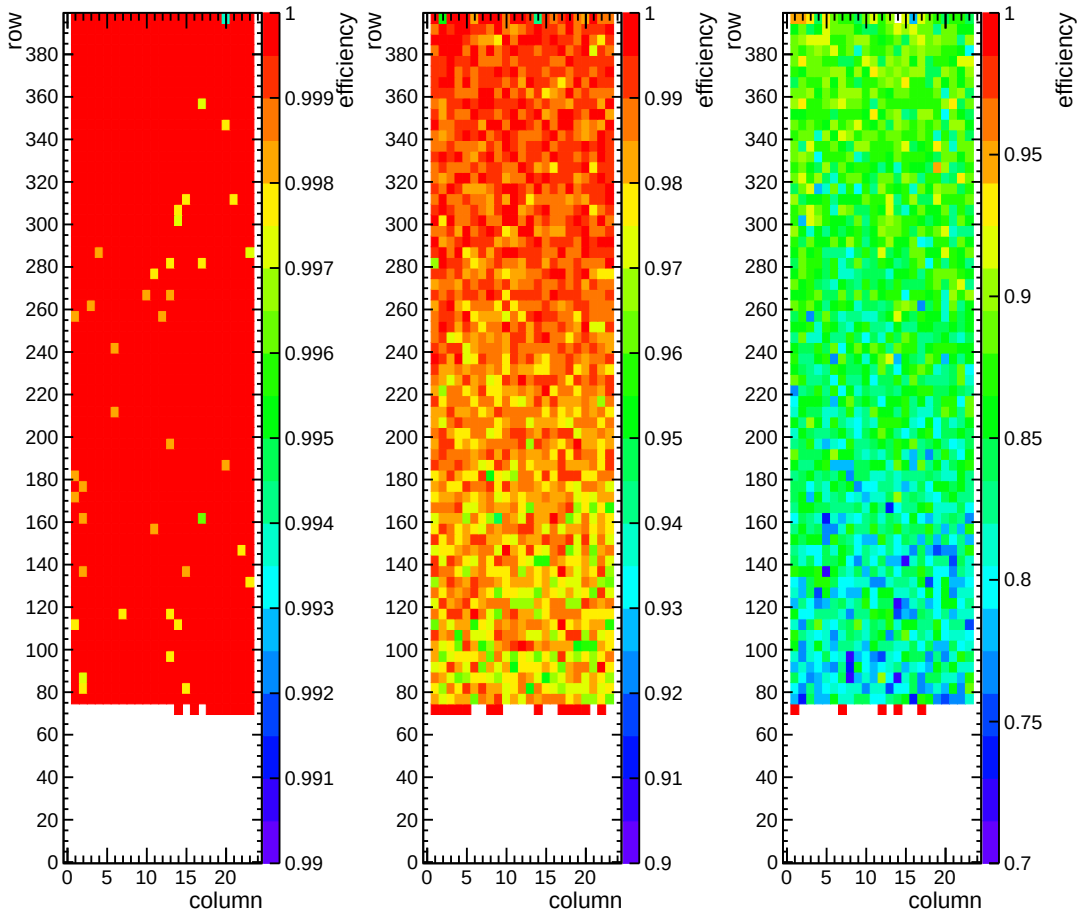

(a) Threshold = 840 mV $\approx$ 673 e^-, total efficiency $= (99.9945^{+0.0009}_{-0.0011})\%$.

(b) Threshold = 950 mV $\approx$ 1629 e^-, total efficiency $= (98.545^{+0.014}_{-0.014})\%$.

(c) Threshold = 1100 mV $\approx$ 2932 e^-, total efficiency $= (84.60^{+0.05}_{-0.05})\%$.

Figure 11.6: Hit detection efficiency across the pixel matrix for different thresholds plotted across the pixel matrix for the upper matrix area. Averaged over 5 rows per bin.

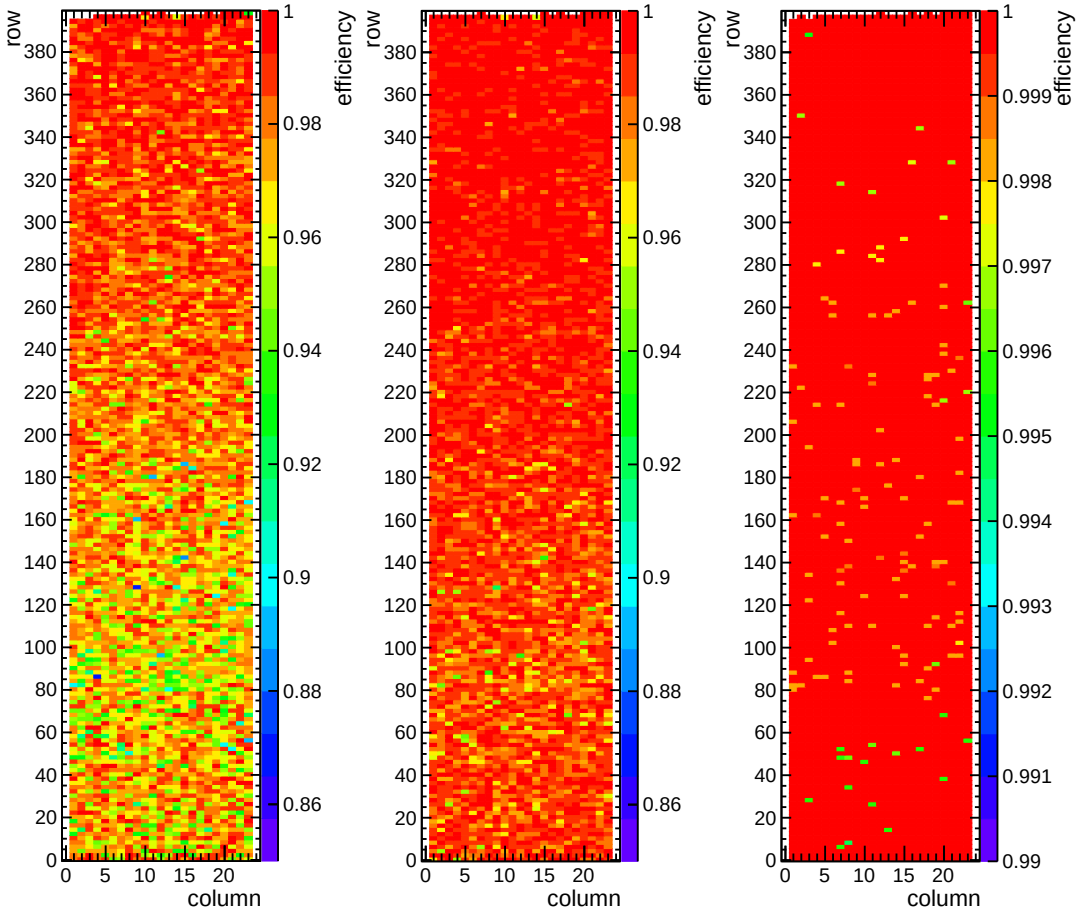

(a) Bias voltage = $-5\,\mathrm{V}$, total efficiency = $(97.68^{+0.01}_{-0.01})\%$.

(b) Bias voltage = $-10\,\mathrm{V}$, total efficiency = $(98.991^{+0.007}_{-0.007})\%$.

(c) Bias voltage = $-80\,\mathrm{V}$, total efficiency = $(99.9933^{+0.0006}_{-0.0006})\%$.

Figure 11.7: Hit detection efficiency for different bias voltages plotted across the pixel matrix combining runs focussing on the upper and lower matrix area a threshold of $845\,\mathrm{mV} \approx 720\,\mathrm{e}^-$. Averaged over 5 rows per bin.

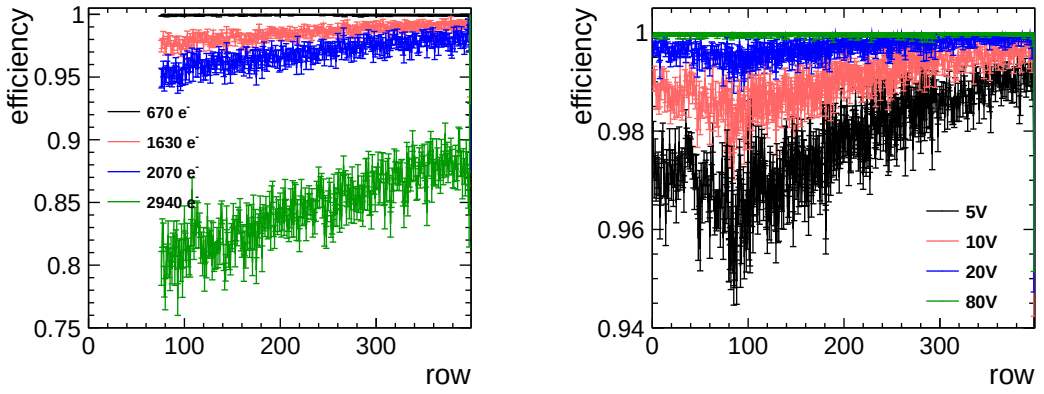

(a) Different thresholds at a bias voltage of $-75\,\mathrm{V}$.

(b) Different bias voltages at a threshold of $845\,\mathrm{mV} \approx 720\,\mathrm{e}^-$.

Figure 11.8: Row dependence of the hit detection efficiency for different thresholds and bias voltages.

bias voltages (see Figure 11.8b). The largest efficiency is measured for high row numbers. With decreasing row numbers, the efficiency drops before it reaches a minimum around the rows 75 to 100. For even lower row numbers, the efficiency rises again. A comparable trend is also observed for the row dependence of the signal size discussed in Section 10.4.5, where it was suspected that a power non-uniform power distribution to the in-pixel amplifiers could cause a row dependence in the signal gain. This hypothesis would also explain the observed efficiency: A lower efficiency is reached in a row with a lower gain at a given detection threshold.

11.3 Cluster Formation

The investigation of the cluster formation allows to draw conclusions about the amount of charge sharing, which is a direct consequence of the electric field configuration within the device and influences the achievable spatial resolution of the sensor.

As discussed in Section 4.1, charge deposited in one pixel can be collected in the neighbouring pixel due to lateral diffusion. If a particle deposits its energy close to the edge or corner of a pixel, charge sharing can lead to clusters with a size up to four. In addition, delta rays can lead to increased cluster sizes. The row dependence of the amplifier gain discussed in Sections 10.4.2 and 11.2.3 is expected to affect the cluster size as well: If the gain is larger for higher row numbers, it reduces sub-threshold losses from small amounts of charge shared into neighbouring pixels and thus results in a row dependence of the cluster size.

On the other hand, also cross-talk can lead to an increased cluster size: As described in Section 5.2.1, each pixel in the active matrix of the ATLASpix is connected to its corresponding readout cell in the digital periphery via a signal transmission line. Because these are routed densely in the ATLASpix[1], cross-talk can occur between adjacent lines due to capacitive coupling [146]. If the induced signal on a neighbouring line is large enough, this may lead to the detection of a fake hit. The routing scheme allows for an occurrence of double-pixel or three-pixel clusters within one column as illustrated in Figure 11.9. Cross-talk between columns is not possible. The cross-talk probability depends on the capacitance between adjacent transmission lines, which increases with their lengths such that more cross-talk is expected for higher row numbers. It also depends on the presence of near metal layers for power or ground distribution. It is important to note that the probability for cross-talk is independent of the incidence point of a particle within one pixel. This fact is used in the following to distinguish it from charge sharing.

[1]The exact value of the minimal line spacing underlies a non-disclosure agreement as part of the AMS aH18 process.

Figure 11.10a shows the normalised distribution of cluster sizes for all clusters. Single-pixel clusters make up the largest fraction with ∼92.4 %. In ∼6.4 % of all cases two-pixel clusters occur and for ∼1.2 % the cluster size is ≥ 3.

In Figure 11.10b, the cluster widths are shown in column and row direction. The cluster width in row direction is significantly larger than in column direction as expected from the elongated pixel geometry. From simple geometric considerations, in the row direction, i.e. the shorter direction, a track is much more likely to penetrate the sensor close to the pixel edge leading to a higher probability of charge sharing compared to the other direction. In addition, a delta electron crosses more pixels for a given distance within the silicon.

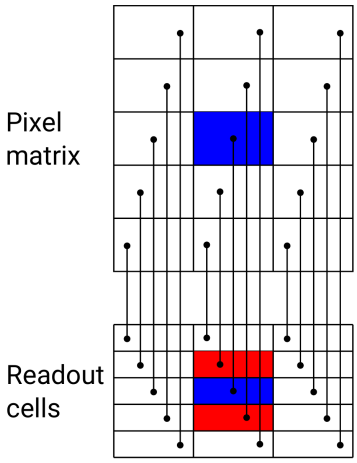

Figure 11.9: Illustration of an exemplary three-hit cluster arising from cross-talk due to the dense routing between the pixel matrix and the readout cells in the periphery. If the pixel marked in blue detects a hit caused by a traversing particle, fake hits may be detected in the pixel cells shown in red. From [51].

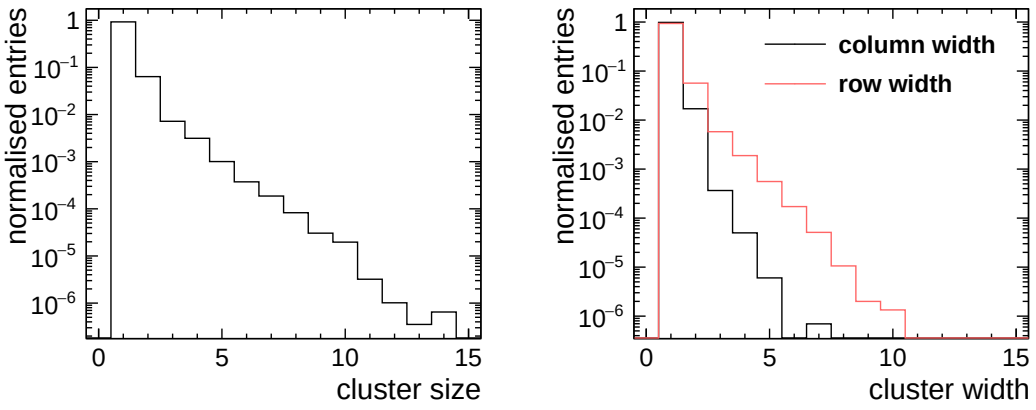

(a) Cluster sizes.

(b) Cluster widths in column and row direction.

Figure 11.10: Normalised distributions of cluster sizes and cluster widths in column and row direction at a bias voltage of −75 V and a threshold of 845 mW ≈ 720 e^-.

11.3.1 In-Pixel Cluster Size Distribution

Figure 11.11 show the track position on the DUT mapped onto the area of one pixel for the mean cluster size and for different cluster sizes from 1 to 4. It shows that single-pixel clusters occur mostly within the centre of the sensor, whereas larger clusters are more likely to occur along the edges and in the corners.

This corresponds to the expectation: If a particle penetrates a pixel close to its centre, the signal charge is collected by one pixel. If a pixel is hit close to its edge, charge sharing into the neighbouring pixel can occur, leading to a two-pixel cluster. In the corners, charge sharing into three or four adjacent pixels is possible.

As stated above, both cross-talk and the non-uniformity of the gain are expected result in a row dependence of the cluster size. The fact that the occurrence of cross-talk is independent of the track incidence point is used in the following to disentangle it from charge sharing by exploiting the excellent track pointing resolution of the telescope of $\sim$1.3 µm (see Section 9.1.1). An in-pixel region-of-interest is defined as illustrated in Figure 11.11a to exclude tracks penetrating the sensor closer than 10 µm to a pixel edge. The tracks within the in-pixel ROI are unlikely to cause a cluster size larger than one due to charge sharing. On the other hand, their probability of inducing cross-talk is unchanged. Also delta rays can cause a cluster size larger than one if a pixel was hit in the centre.

11.3.2 Row Dependence of the Cluster Size

Figures 11.12a, shows the mean cluster size plotted against the row number. The much larger error bars for rows above 300 are explained by a shorter data acquisition time for the run focussing on the upper matrix section resulting in much lower statistics. A general trend of an increasing mean cluster size towards larger row numbers is observed. It stems from an increase of the mean cluster row width, while the column width remains constant within the measurement uncertainties as seen in Figure 11.12b. In addition, a peak is observed in row 301 and a strong increase in the cluster row width occurs for rows above 390. The observed behaviour arises from a combination of line cross-talk and charge sharing as discussed in the following.

Figure 11.12c shows the row dependence of all clusters associated to tracks and those restricted to the in-pixel ROI shown in Figure 11.11a. It is seen that the mean size of clusters associated to tracks penetrating the central area of a pixel is smaller than the mean of all clusters as expected from the definition of the ROI. However, it is larger than one as explained by the occurrence of delta rays. Furthermore, it does not follow the previously mentioned row dependence, while the peak at row 301 and the strong rise above row 390 are comparable. This means that the general increase in the cluster size with larger row number cannot be caused by cross-talk and is instead explained by the row dependence of the gain.

On the other hand, the peak at 301 and the increase above 390 are comparable in both cases and can thus be related to cross-talk. The transmission lines for pixels

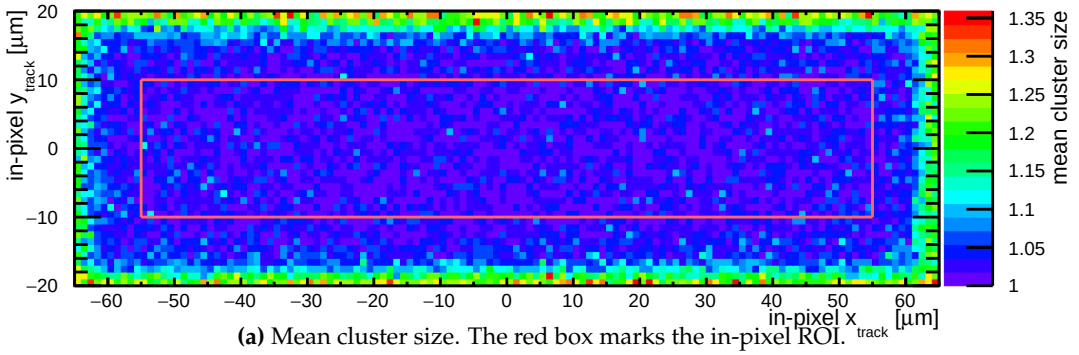

(a) Mean cluster size. The red box marks the in-pixel ROI.

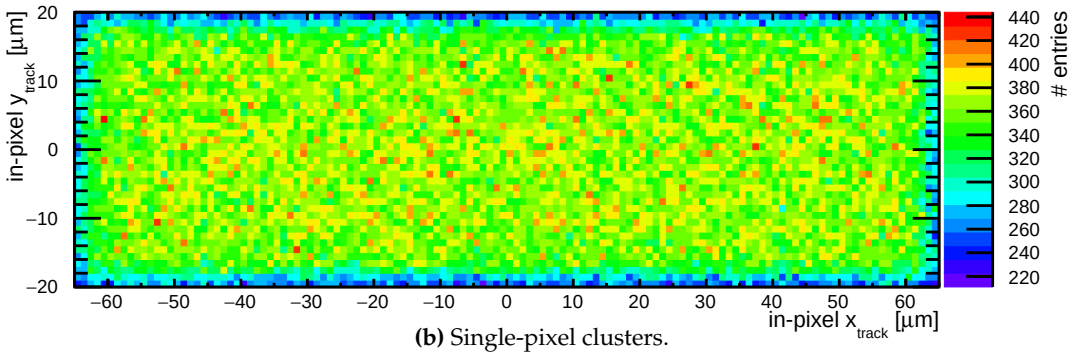

(b) Single-pixel clusters.

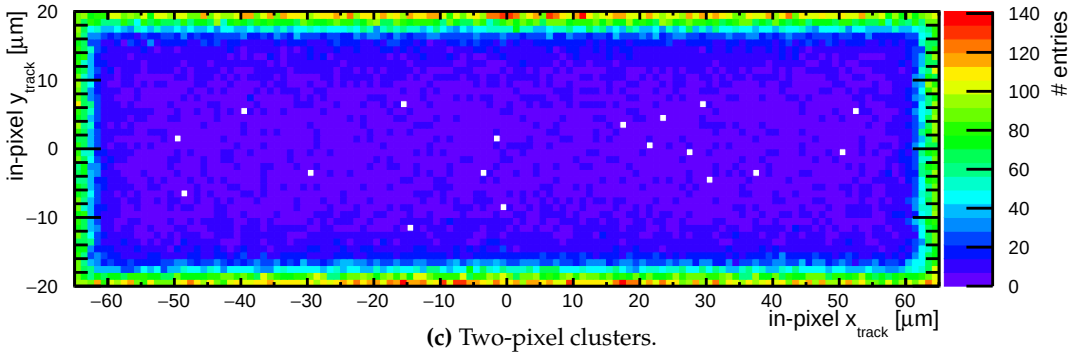

(c) Two-pixel clusters.

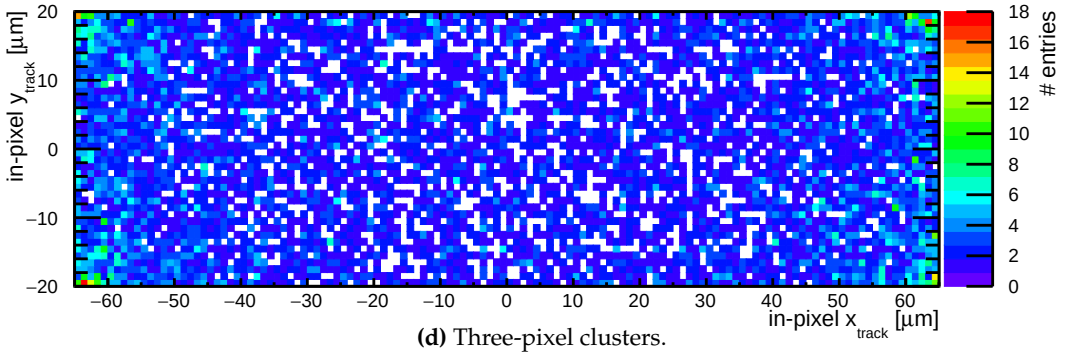

(d) Three-pixel clusters.

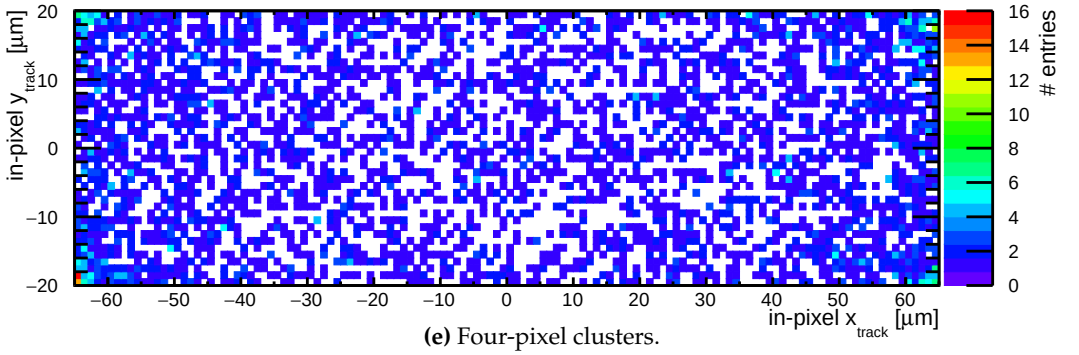

(e) Four-pixel clusters.

Figure 11.11: In-pixel distributions for different cluster sizes, filled at the track incident position at a bias voltage of $-75\,\mathrm{V}$ and a threshold of $845\,\mathrm{mW} \approx 720\,\mathrm{e}^-$.

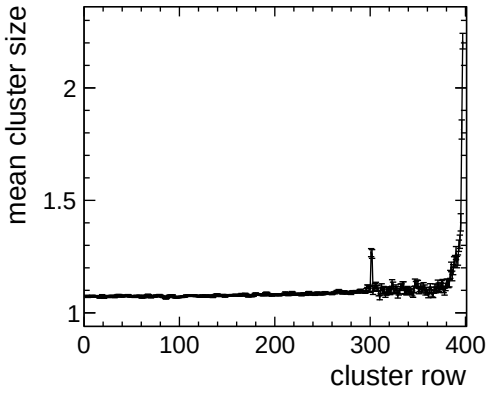

(a) Mean cluster size.

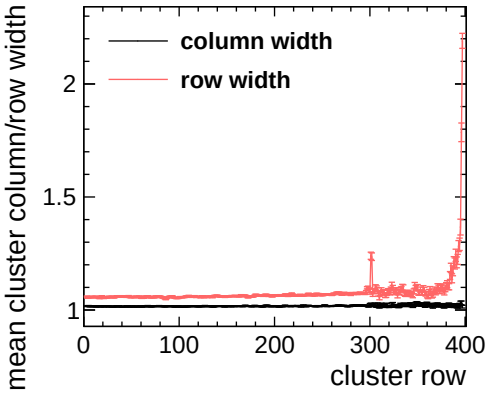

(b) Mean cluster column/row width.

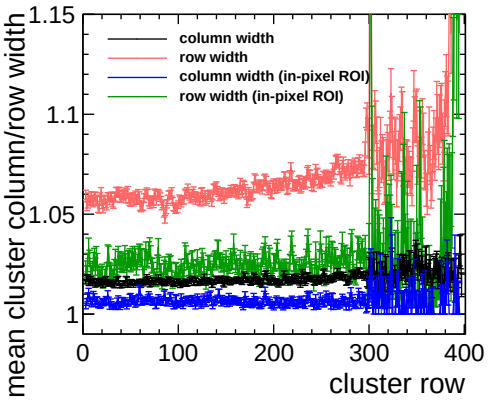

(c) Mean cluster size for all tracks and tracks within the in-pixel ROI.

Figure 11.12: Mean cluster size in dependence of the row number of associated clusters for two runs covering the upper and the lower section of the matrix at a bias voltage of $-75\,\mathrm{V}$ and a threshold of $845\,\mathrm{mW} \approx 720\,\mathrm{e}^-$.

in row 301 have one adjacent transmission line with the minimal line spacing, leading to an increased capacitive coupling, whereas all others have a larger spacing.[2] For rows larger than 390, the probability for cross-talk increases significantly as the length of the transmission lines and thus their capacitive coupling reaches a critical limit [51].

As stated above, no cross-talk is seen between row 0 and 300. Consequently, for all further conclusions about the cluster formation, the region-of-interest is restricted to row numbers between 74 and 299 for runs focussing on the upper matrix section as illustrated by the red box in Figure 11.13a and rows below 294 for runs focussing on the lower matrix section as drawn in Figure 11.13b. This way, regions with an increased cross-talk probability are excluded. In addition, the outermost pixels of

[2] Minimal line spacings also occur at row 101 and 199. In [51], the cross-talk probability was found to depend on the voltage level of VMinusPix, which is the ground level of the line driver in the active pixel. A voltage of 650 mV is used for the results presented in this thesis. It is shown in [51] that for different values of VMinusPix, cross-talk can also be observed in rows 101 and 199.

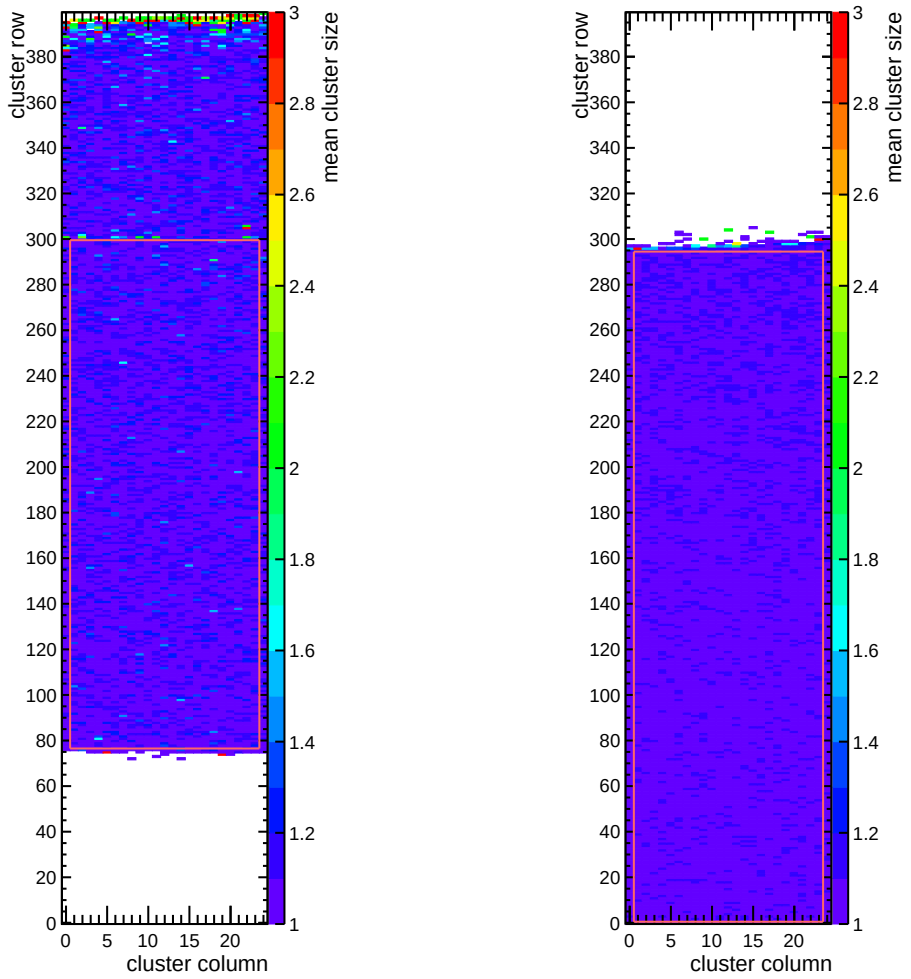

(a) Upper section of the matrix.

(b) Lower section of the matrix.

Figure 11.13: Two-dimensional distribution of cluster sizes across the matrix for two runs covering the upper and the lower section of the matrix at a bias voltage of $-75\,\mathrm{V}$ and a threshold of $845\,\mathrm{mW} \approx 720\,\mathrm{e}^-$. The red boxes mark the selected regions-of-interest to avoid regions with a high cross-talk probability.

the matrix are excluded to avoid a bias of the results from tracks penetrating the chip close to its edges, which may lead to smaller clusters if a fraction of the charge diffused outside of the active area of the sensor.

11.3.3 Threshold Dependence

In Figure 11.14, the threshold dependence of the mean cluster size is plotted. In addition, the mean column width and row width are displayed. For this analysis, data is only available for the upper matrix section (see Figure 11.13a). As expected, it can be seen that the cluster size is dominated by the row width whereas the column width remains very close to 1. Furthermore, it is observed that the cluster size decreases with increasing threshold until a minimum at a threshold of about $2000\,\mathrm{e}^-$ is reached. For even larger thresholds, the cluster size increases again. The decrease of the cluster size up to a threshold of $2000\,\mathrm{e}^-$ follows the expectation: For a given

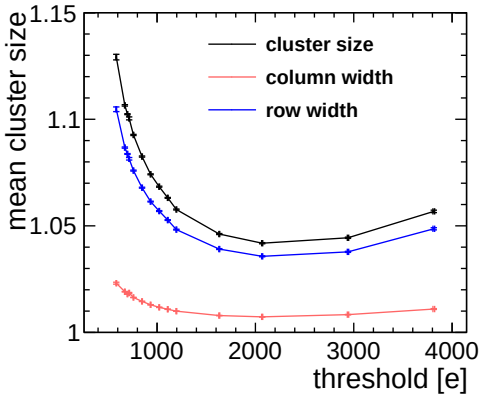

Figure 11.14: Threshold dependence of the mean cluster size and column/row width of associated clusters at a bias voltage of $-75\,\mathrm{V}$.

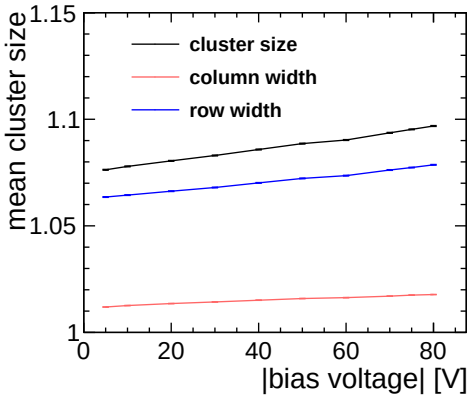

Figure 11.15: Bias voltage dependence of the mean cluster size and column/row width of associated clusters at a threshold of $845\,\mathrm{mW} \approx 720\,\mathrm{e}^-$.

amount of charge sharing, the probability of the signal crossing the threshold decreases for a larger threshold. A possible explanation for the increase at thresholds larger than $2000\,\mathrm{e}^-$ could be a bias towards large energy depositions from the high-energy tail of the Landau distribution including delta rays. The effect is more pronounced in the row direction due to the smaller pixel pitch. This hypothesis could be tested by supplementary simulations, which were not performed within the scope of this thesis.

11.3.4 Bias Dependence

Figure 11.15 shows the bias voltage dependence of the cluster size. A trend of increasing cluster sizes with larger bias voltages is observed. It can be explained as follows: A larger bias voltage leads to a larger depleted volume and hence to a larger signal. Consequently, for a given track penetrating the sensor close to the pixel edges, a larger amount of charge is shared to the neighbouring pixel, which increases the probability to exceed the threshold.

11.3.5 Cluster ToT and Seed Pixel ToT

Figure 11.16 shows the cluster ToT and seed pixel ToT for all clusters on the ATLASpix within the ROI marked in Figure 11.13b. Both distributions peak at a ToT value around 10 and overlap in large parts. This is expected due to the fact that the vast majority of clusters contain only one single pixel, for which the cluster ToT and the seed pixel ToT are identical. The seed pixel ToT spectrum is restricted to a range of 0-63 corresponding to the limitation of *TS2* to 6 bit (see Section 5.2.1). The cluster ToT, which is the sum of all individual pixel ToTs within a cluster, can reach larger values for clusters containing multiple pixels. This becomes apparent in Figure 11.16b, which shows the same distribution as in Figure 11.16a on a logarithmic y-axis. Furthermore, a peak at 60-63 can be observed. It is related to a bug of the

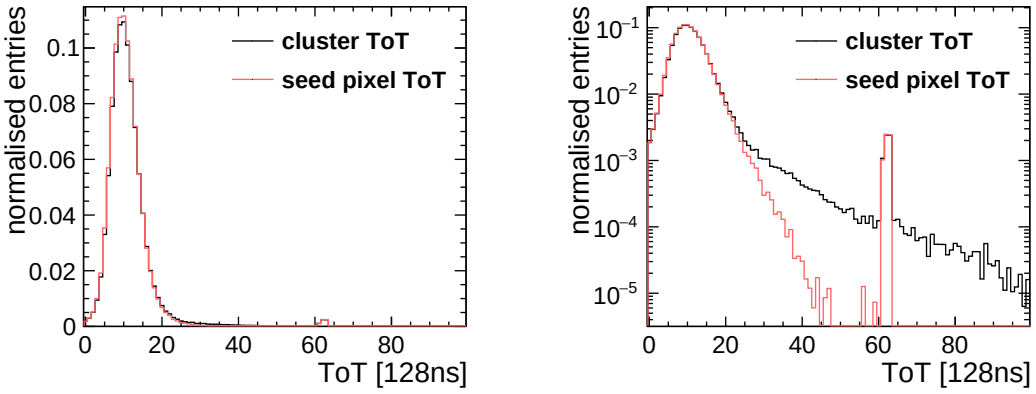

(a) Linear y-axis.

(b) Logarithmic y-axis.

Figure 11.16: Comparison of the total cluster ToT and seed pixel ToT distributions at a bias voltage of $-75\,\mathrm{V}$ and a threshold of $845\,\mathrm{mW} \approx 720\,\mathrm{e}^-$.

FPGA timestamping of the Caribou system and does not represent a feature of the ATLASpix internal timestamping.

In-Pixel Distributions

Figure 11.17 shows the two-dimensional in-pixel distributions of the cluster ToT and the seed pixel ToT filled at the track incident point within a pixel and all pixels mapped into one. It can clearly be seen that the mean seed pixel ToT (see Figure 11.17a) is larger if a particle penetrates a pixel close to its centre, whereas it drops towards the edges and corners of a pixel. This is explained by the fact that in the pixel centre, the majority of the deposited charge is collected by one single pixel such that the measured signal is the largest. Towards the edges and corners, the seed signal becomes smaller because part of the charge is collected in the neighbouring pixels.

The mean cluster charge behaves differently as seen in Figure 11.17b. It is smaller towards the pixel edges in column direction due to an increased probability for the charge shared into the neighbouring pixels to remain below the detection threshold. In the row dimension, the cluster charge is increased when approaching the pixel edges.

This observation can be explained by a combination of two mechanisms: It was discussed in Section 10.3.3 that small ToT values below 1-2 (for `ckdivend2` $= 15$) are disfavoured due to a hysteresis of the comparator resulting in a minimal measured time-over-threshold. If a small fraction of charge is collected by a neighbouring pixel, and it is sufficient to exceed the detection threshold, its ToT is likely to be ≥ 1. This means that the cluster ToT behaves non-linearly at low thresholds: For a given amount of deposited charge, the sum of two pixels, of which one has a small ToT, can be larger than the ToT measured for one pixel if it collects the entire charge. This introduces a bias towards a slightly larger cluster ToT for multi-pixel clusters.

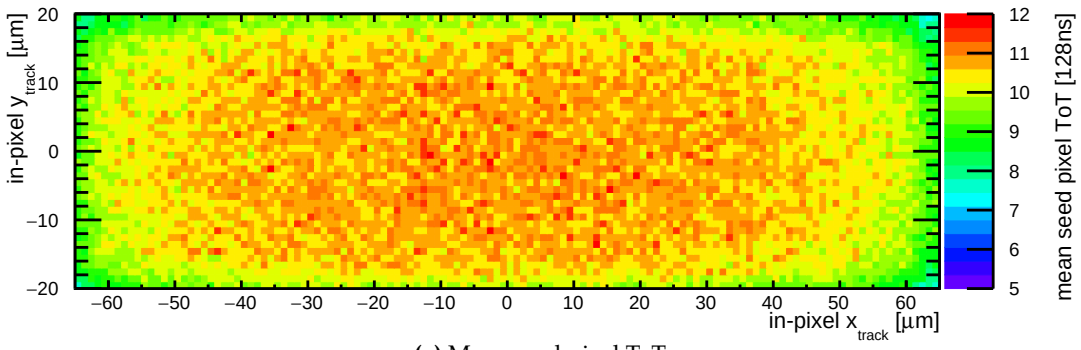

(a) Mean seed pixel ToT.

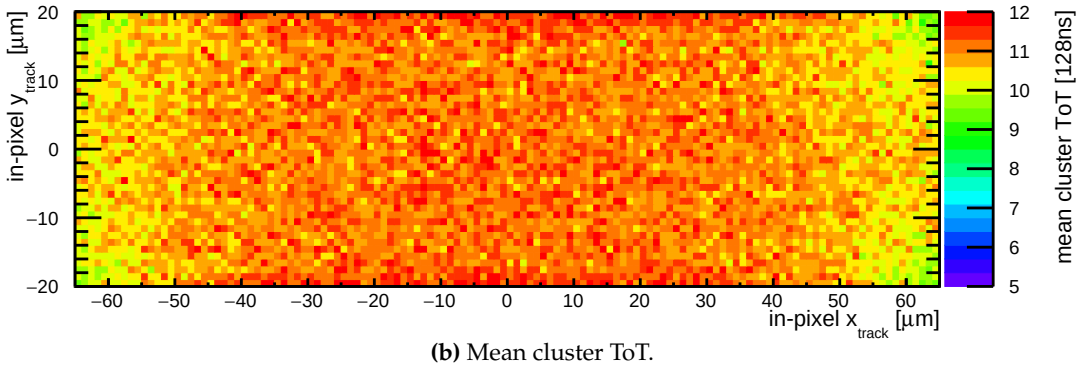

(b) Mean cluster ToT.

Figure 11.17: In-pixel distribution of the mean seed pixel ToT and the mean cluster ToT at a bias voltage of $-75\,\mathrm{V}$ and a threshold of $845\,\mathrm{mV} \approx 720\,\mathrm{e}^-$.

In addition, for high bias voltages, the depth of the depletion region can be slightly larger between the pixels compared to under the deep N-wells, which form the sensor diode because between the pixels it can extend to the front-side. In this case, the deposited energy within the depletion region would be slightly larger between pixels resulting in a larger measured cluster ToT. This hypothesis is supported by preliminary TCAD studies on the depth and shape of the depletion region, which are carried out at the time of writing within the scope of a PhD thesis [163]. The effect is suppressed along the short pixel edges because there, charge has a higher probability to be shared into more than two pixels and thus stay below the detection threshold.

The described behaviour is only observed at low thresholds and high bias voltages. At higher thresholds (see Figure 11.18) or lower bias voltages (see Figure 11.19), the in-pixel distribution of the in-pixel mean cluster ToT resembles the one of the seed pixel ToT. This is consistent with the mechanism described above. At higher thresholds or lower bias voltages, the charge shared into neighbouring pixels is more likely to remain below threshold such that the described effects cannot occur.

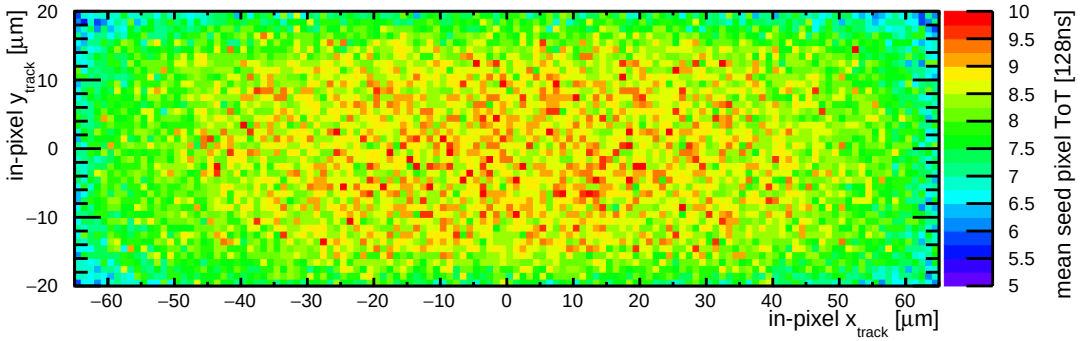

(a) Mean seed pixel ToT.

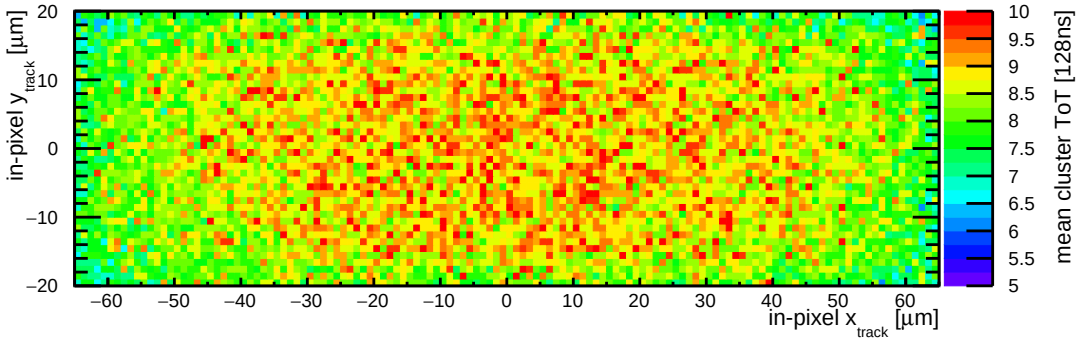

(b) Mean cluster ToT.

Figure 11.18: In-pixel distribution of the mean seed pixel ToT and the mean cluster ToT at a bias voltage of $-75\,\mathrm{V}$ and a high threshold of $950\,\mathrm{mV} \approx 1630\,\mathrm{e}^-$.

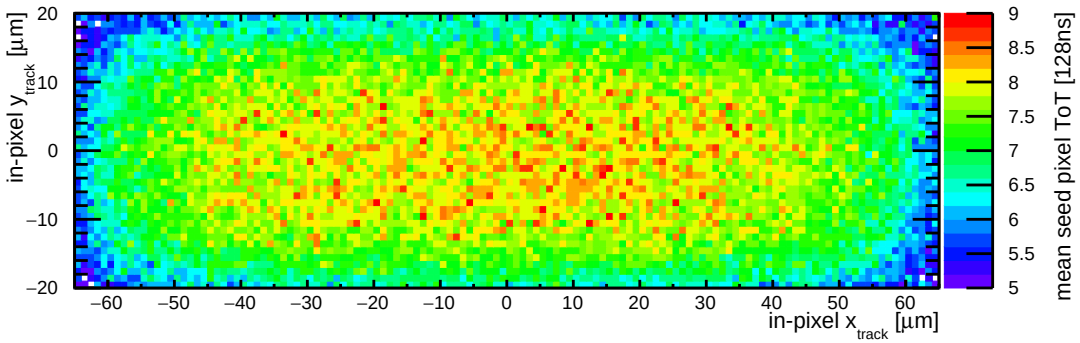

(a) Mean seed pixel ToT.

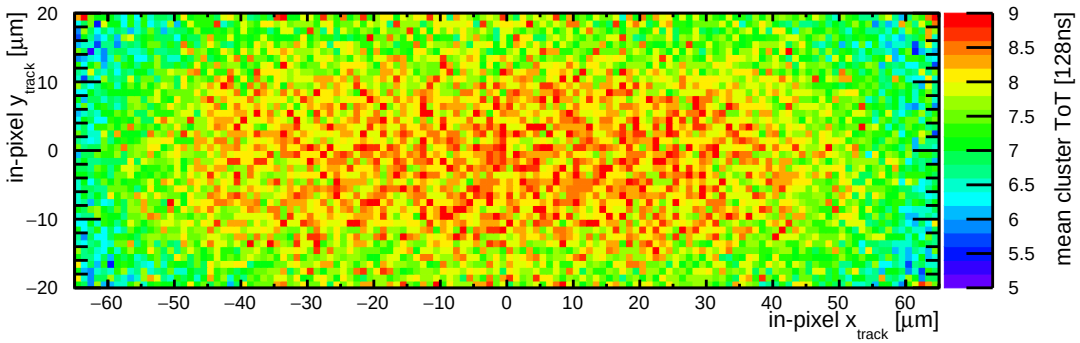

(b) Mean cluster ToT.

Figure 11.19: In-pixel distribution of the mean seed pixel ToT and the mean cluster ToT at a low bias voltage of $-5\,\mathrm{V}$ and a high threshold of $845\,\mathrm{mV} \approx 720\,\mathrm{e}^-$.

Landau-Gauss Fit of the ToT Spectrum and Row Dependence

As discussed in Section 3.1, the energy deposition of minimum ionising particles (MIPs) is expected to follow a Landau distribution due to rare events in which a large amount of energy is deposited. Consequently, the measured ToT spectrum can be approximated by a convolution of a Landau distribution with a Gaussian reflecting the limited energy resolution of the device. Figure 11.20a shows an exemplary fit, from which the most probable value of the distribution can be extracted as a fit parameter. While the convolution of a Landau with a Gaussian roughly describes the spectrum, it is observed that a high $\chi^2/ndof \approx 4200/50$ is obtained.

It is explained as follows: The row dependence of the gain discussed in Section 10.4.5 is not only expected to affect the efficiency (see Section 11.2.3) and the cluster size (see Section 11.3.2) but also the ToT measurement because a smaller gain leads to a shorter time-over-threshold for a given deposited charge. Figure 11.20b shows the row dependence of the MPV of the cluster ToT and the seed pixel ToT. Between row 0 and row 100, the MPV remains constant within the measurement uncertainties. For larger row numbers, the MPV follows an increasing trend.

Thus, it shows a comparable behaviour as was observed both in the signal size during the X-ray measurements (see Section 10.4.2), the hit detection efficiency (see Section 11.2.3), and the mean cluster size (see Section 11.3.2).

Charge Calibration

In principle, the charge calibration of the ToT as determined in Section 10.4.7 allows for a conversion of the measured ToT into the corresponding deposited charge. The significant row dependence of the ToT measurement needs to be taken into account either by applying the calibration row by row, or alternatively, by a rescaling of the

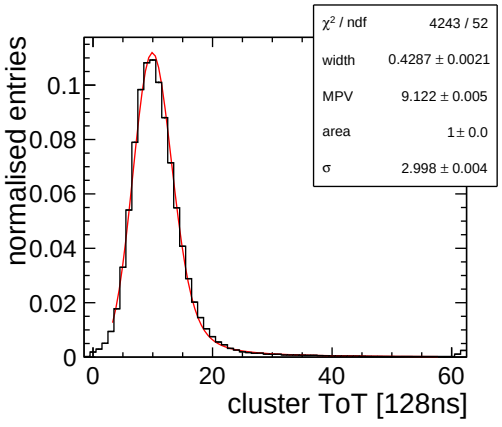

(a) Cluster ToT spectrum fitted with a convolution of a Landau with a Gaussian.

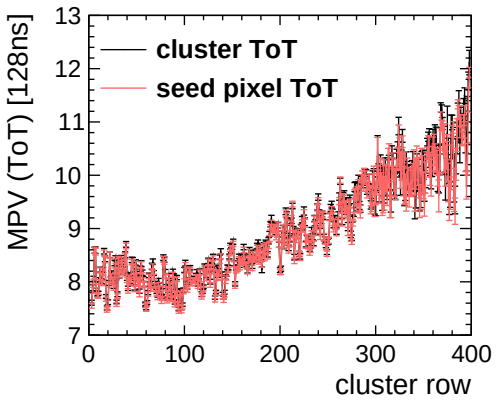

(b) Row dependence of the MPV of the cluster and seed pixel ToT distributions.

Figure 11.20: Fitted cluster ToT spectrum and row dependence of the cluster and seed pixel ToT MPV at a bias voltage of $-75\,\mathrm{V}$ and a threshold of $845\,\mathrm{mW} \approx 720\,\mathrm{e}^-$.

row-dependent spectrum, such that each row contributes with the same weight to avoid a bias of the spectrum by a varying number of entries per row.

The ToT calibration in Section 10.4.7 was performed with a clock divider `ckdivend2` $= 7$ corresponding to a time binning of 64 ns. As seen in Figure 11.20a, the MPV of the cluster ToT at nominal conditions is $\sim$ 9.1, recorded with `ckdivend2` $= 15$ resulting in a time binning of 128 ns. This corresponds to a value of $\sim$ 18.2.

In Figure 10.25, it is seen that with the X-ray calibration, a maximal ToT value of $\sim$ 10 is reached for the 200 Ωcm samples at a bias voltage of -50 V and a threshold of 840 e^-. Thus, an extrapolation of the MPV from 10 to approximately 18 would be required for a charge calibration of the MIP peak obtained from the fit shown in Figure 11.20a. However, the calibration shows a non-linear behaviour such that an extrapolation would result in large systematic uncertainties, which cannot be quantified properly.

Threshold and Bias Dependence

Figure 11.21 shows the threshold dependence (Figure 11.21a) and the bias voltage dependence (Figure 11.21b) of the MPV obtained from a fit of the cluster ToT distribution with a Landau-Gauss convolution. For the threshold dependence, it is observed that the MPV of the ToT spectrum decreases for larger thresholds. This corresponds to the expectation since a higher threshold leads to a reduced time-over-threshold (ToT) for a given signal size.

In Figure 11.21b, it can be seen that the MPV of the ToT increases with larger bias voltages. Also this behaviour is expected since a higher bias voltage corresponds to a larger depleted volume and hence for a larger signal. This leads to a longer time-over-threshold at a given threshold.

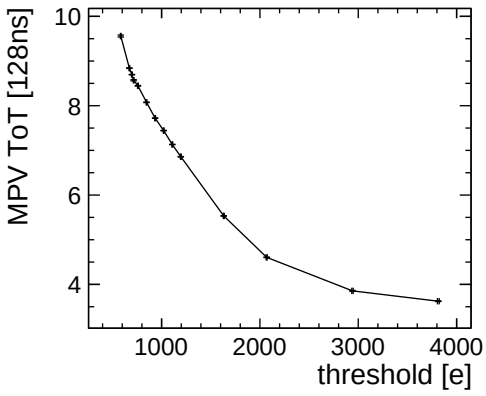

(a) Threshold dependence at a bias voltage of -75 V.

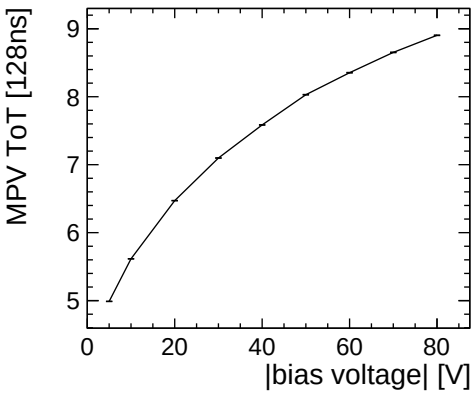

(b) Bias voltage dependence at a threshold of 845 mV $\approx$ 720 e^-.

Figure 11.21: Threshold and bias voltage dependence of the MPV of the cluster and seed pixel ToT distributions.

11.3.6 In-Cluster Timing

The in-cluster timing, i.e. the time difference between individuals pixels within a cluster, is investigated to determine a time cut for the clustering as described in Section 8.2.2.

Figure 11.22 shows the in-cluster timing distribution for different bias voltages and detection thresholds. For this, the time difference between all pixels within a cluster and the seed pixel, i.e. the pixel with the largest ToT within the cluster, is plotted versus the pixel ToT. The seed pixel is excluded as it would lead to a time difference of zero by definition. It can be seen that most pixels of a cluster lie within a time window of less than 300 ns. Furthermore, the effect of timewalk can be clearly observed as pixels with a small ToT show a larger time difference to the pixel with the largest ToT.

The comparison of different bias voltages in Figures 11.22d to 11.22f, shows that for a smaller bias voltage, the in-clustering timing distribution becomes wider even though the total cluster size is slightly smaller as discussed before. This is consistent with the expectation since a smaller depleted volume leads to a smaller signal such that the effect of timewalk is more pronounced. The number of entries increases with rising bias voltage, which is consistent with the increasing efficiency and the trend towards larger cluster sizes.

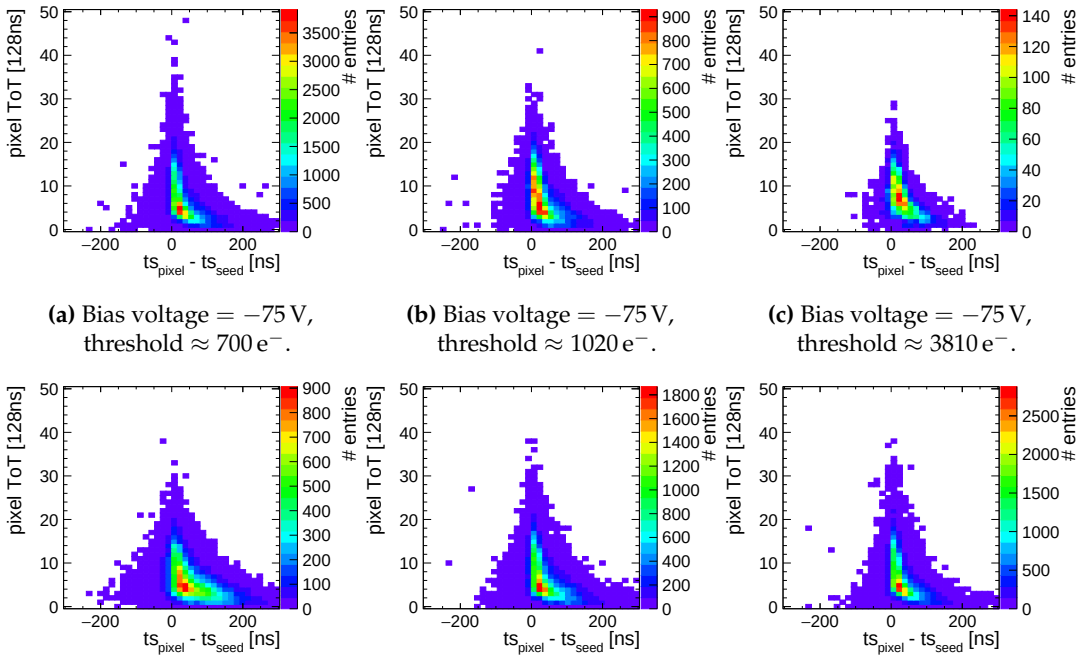

(a) Bias voltage $= -75\,\mathrm{V}$, threshold $\approx 700\,\mathrm{e}^-$.

(b) Bias voltage $= -75\,\mathrm{V}$, threshold $\approx 1020\,\mathrm{e}^-$.

(c) Bias voltage $= -75\,\mathrm{V}$, threshold $\approx 3810\,\mathrm{e}^-$.

(d) Bias voltage $= -5\,\mathrm{V}$, threshold $\approx 720\,\mathrm{e}^-$.

(e) Bias voltage $= -40\,\mathrm{V}$, threshold $\approx 720\,\mathrm{e}^-$.

(f) Bias voltage $= -80\,\mathrm{V}$, threshold $\approx 720\,\mathrm{e}^-$.

Figure 11.22: Time difference between secondary pixels within a cluster (all pixels excluding the seed pixel) and the seed pixel timestamp for different detection thresholds and bias voltages.

The comparison of the different threshold voltages is shown in Figures 11.22a to 11.22c. It is seen that the widths of the distributions, i.e. the amount of time-walk does not differ significantly. An increasing amount of timewalk arising from a larger threshold affects all pixels including the seed pixel. In addition, the fraction of multi-pixel clusters is reduced and only those with a large secondary pixel ToT are detected.

In conclusion, Figure 11.22 motivates the time cut of $\pm 300\,\mathrm{ns}$ applied for the clustering as described in Section 8.2.2.

11.4 Spatial Resolution

As discussed in Section 8.4, the spatial resolution can be quantified as the width of the unbiased spatial residuals, i.e. the difference between the interpolated track intercept on the DUT sensor and its measured position. Figure 11.23 shows the spatial residuals in column and row direction at a threshold of $845\,\mathrm{mV} \approx 720\,\mathrm{e}^-$ and a bias

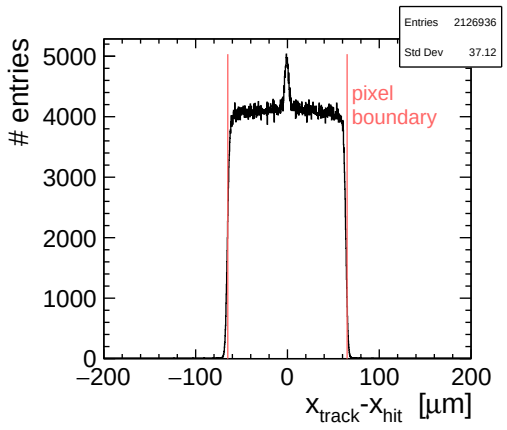

(a) Column direction.

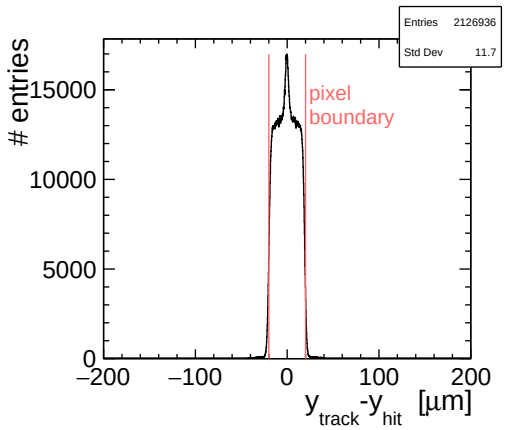

(b) Row direction.

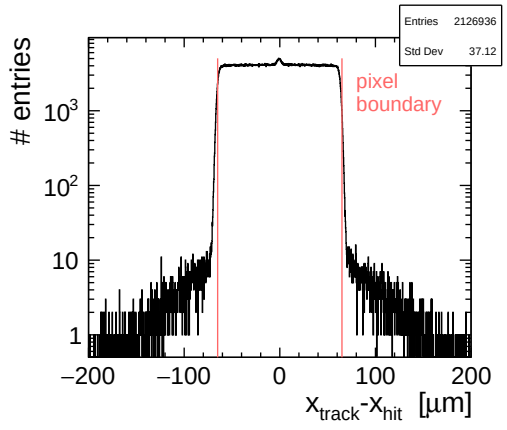

(c) Column direction, logarithmic y-axis.

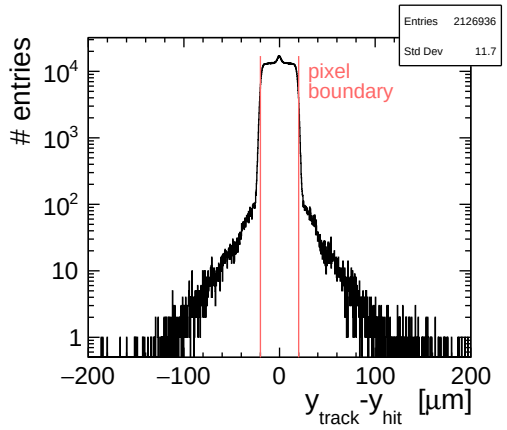

(d) Row direction, logarithmic y-axis.

Figure 11.23: Unbiased spatial residuals in column and row direction at a threshold of $845\,\mathrm{mV} \approx 720\,\mathrm{e}^-$ and a bias voltage of $-75\,\mathrm{V}$. The red vertical lines indicate the pixel pitch. The cluster position is calculated as the arithmetic mean of all pixels within a cluster according to Equation 8.3.

voltage of −75 V. The cluster positions are calculated as the arithmetic mean of all pixels within a cluster according to Equation 8.3.

It is seen that the residuals in both direction (column and row) are dominated by a box-shaped distribution. A clear difference in the width of the distributions is observed between the column and row direction in Figure 11.23, which reflects the asymmetric pixel dimensions. It can also be noted that tails expand to the left and the right of the main distribution. These represent events with a large residual, i.e. a large difference between the extrapolated track incident point and the associated cluster. Furthermore, a sharp peak is superimposed on the box-shaped distribution, which is more pronounced in the row direction.

11.4.1 Contributions from Different Cluster Sizes

The above behaviour can be understood through Figure 11.24, which shows the spatial residuals separately for different cluster sizes. Due to the low number of multi-pixel clusters compared to single-pixel clusters, the numbers of entries are rescaled

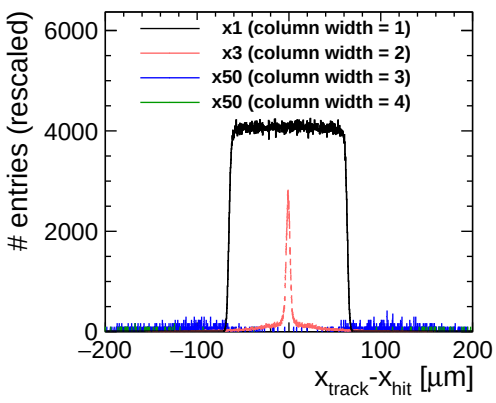

(a) Column direction.

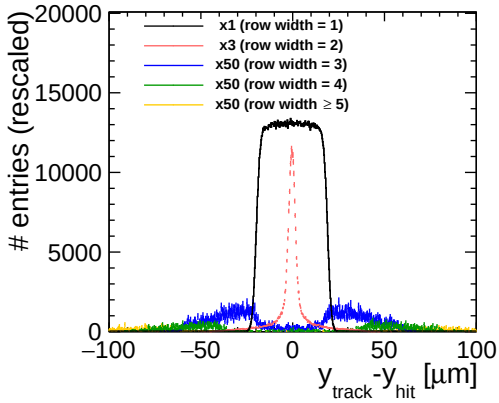

(b) Row direction.

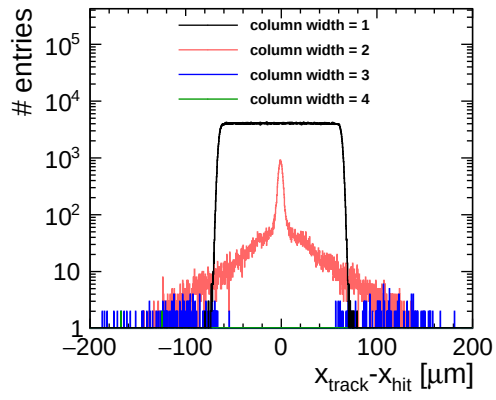

(c) Column direction, logarithmic y-axis.

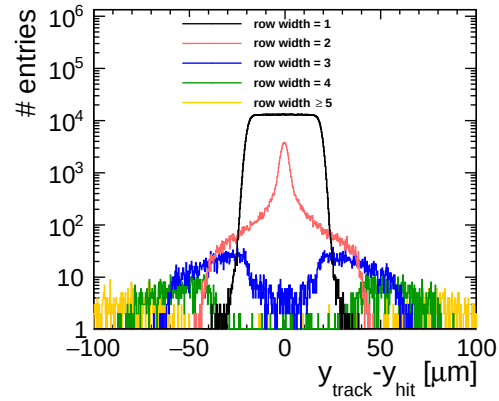

(d) Row direction, logarithmic y-axis.

Figure 11.24: Unbiased spatial residuals for different cluster widths in the respective directions at a threshold of 845 mV ≈ 720 e^- and a bias voltage of −75 V. The entries for the larger cluster sizes are rescaled for a better visibility. The cluster position is calculated as the arithmetic mean of all pixels within a cluster according to Equation 8.3

in Figure 11.24a and 11.24b for a better visibility.

Single-pixel clusters are responsible for the above mentioned box shape, which dominates the residual distribution. This corresponds to the expectation as the prediction of the track intercept point is limited by the pixel pitch and single-pixel clusters make up the largest fraction of clusters.

On the other hand, two-pixel clusters form the sharp peak in the centre of the distribution. As seen in the Section 11.3.2, two-pixel clusters predominantly occur very close to the pixel edges and corners. Hence, the arithmetic mean yields a precise approximation of the track incident point. In addition, part of the two-pixel clusters are responsible for the left and right tails, which can stem partially from delta electrons or cross-talk.

Larger clusters predominantly occur in the tails. In the column direction (Figure 11.24c), clusters with a column width of 3 are responsible for the tails and almost no larger clusters occur, whereas also larger cluster sizes contribute to the tails in the row direction (Figure 11.24c).

Notably clusters with a row width of 3 pixels occur with residuals centered around $\approx \pm 40\,\mu m$, while those with a width of 4 and 5 lead to residuals of $\approx \pm 60\,\mu m$ and $\approx \pm 80\,\mu m$, respectively. This corresponds to an offset of 1, 1.5 and 2 pixel pitches in this dimension.

In addition, a small probability exists that a track is reconstructed incorrectly but still passes the strict selection cuts. This can also lead to an outlier in the residuals.

Delta Electrons

It was discussed in Section 11.3 that clusters with an extent of ≥ 3 pixels in one dimension are not expected to originate from lateral diffusion. However, they can arise either from line-crosstalk (only in row direction) or from delta rays (in both directions). Cross-talk can cause one or two "fake" hits in adjacent pixels to a real hit within one column due to capacitive coupling of the transmission lines.

As illustrated in Figure 11.25, the arithmetic mean of the cluster is still expected to lie within the central pixel of a 3-pixel cluster originating from cross-talk. It therefore has a distance of less than one pixel pitch from the track incidence point. Conversely, if a delta ray is the origin of a three-pixel cluster as shown on the right of Figure 11.25, it is more likely that the track incidence point and the arithmetic cluster centre will have a distance of approximately one pixel pitch. As expected from geometrical considerations, this effect is more prominent in the row direction due to the smaller pixel dimension. Analogously, clusters with an extent of 4 or 5 pixels in one dimension caused by a delta ray are expected to have an average offset of 1.5 and 2 pixel pitches, respectively. This suggests that delta rays are mainly responsible for the periodic outliers in the residual distributions shown above.

Also the tails in the column direction are consistent with delta rays, where the 3-pixel cluster accumulate around residual values of $\approx \pm 130\,\mu m$. Due to the larger pixel dimension, the effect is less pronounced here. Furthermore, no line cross-talk is

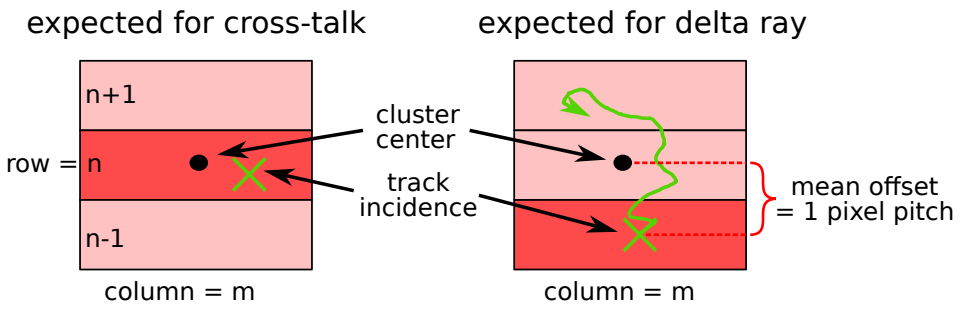

Figure 11.25: Illustration for the origin of three-pixel clusters from line cross-talk and delta rays.

possible in the column direction and in accordance, no clusters with a column width of 3 show a residual close to zero.

11.4.2 Comparison with the Binary Resolution

Due to the complex composition of contributions from the different cluster sizes, the spatial residuals cannot easily be described by a fit function. Thus, the width of the spatial residuals is determined as the root mean square (RMS) of the unbiased residuals according to Equation 8.15.

Table 11.1 shows a comparison of the binary resolutions in column and row direction quantified as the RMS of the spatial residuals on a range of $\pm 200\,\mu m$ as shown in Figure 11.23 and compared to the binary resolution obtained with Equation 8.14. The quoted uncertainties correspond to the uncertainties, when varying the histogram ranges by $\pm 100\,\mu m$. It is seen that the ATLASpix reaches a spatial resolution close to the binary resolution. The RMS includes a contribution from the track-pointing resolution of $(1.26 \pm 0.05)\,\mu m$ (see Section 9.1). It is negligible when subtracting it quadratically according to Equation 8.12. In conclusion, the achieved resolution is very close to the binary resolution limited by the pixel pitch. Possible improvement strategies are discussed at the end of this section.

Table 11.1: Comparison of the theoretical binary resolution with the measured RMS at a threshold of $845\,mV \approx 720\,e^-$ and a bias voltage of $-75\,V$.

Direction	Binary Resolution	$RMS_{ATLASpix}$
column	$130\,\mu m/\sqrt{12} \approx 37.5\,\mu m$	$(37.1 \pm 0.1)\,\mu m$
row	$40\,\mu m/\sqrt{12} \approx 11.6\,\mu m$	$(11.7 \pm 0.1)\,\mu m$

Threshold Dependence

Figure 11.26 shows the threshold dependence of the spatial resolution for the ATLASpix. As above it is quantified as the RMS of the unbiased spatial residuals. It can be seen that in both column and row direction, the RMS rises with an increasing threshold before reaching a maximum at a threshold around $1200\,e^-$. It falls off

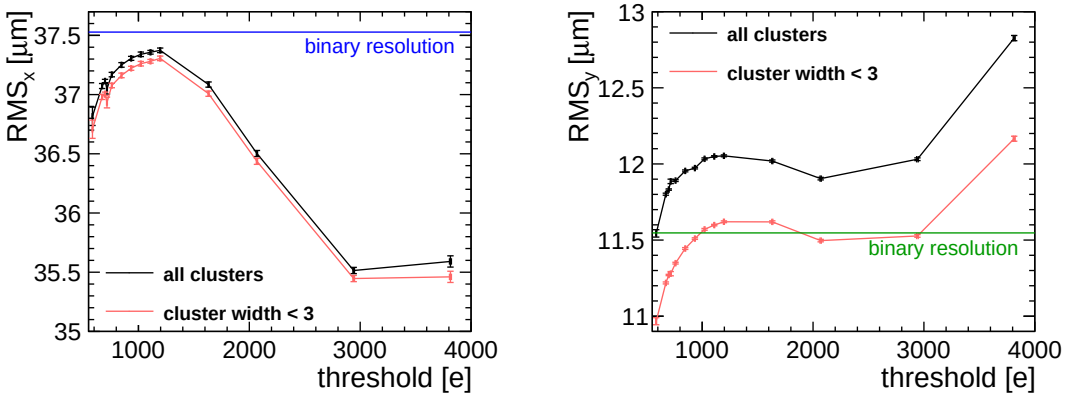

(a) Column direction.

(b) Row direction.

Figure 11.26: Threshold dependence of the RMS of the spatial residuals for runs focussing on the upper section (rows 76-399) of the matrix at a bias voltage of $-75\,\mathrm{V}$.

again for even larger thresholds. This behaviour is expected because with an increasing threshold the number of multi-pixel cluster is reduced. However, two-pixel cluster yield a better estimate for the track intercept point than single-pixel clusters as seen above. The observation that the RMS reaches a maximum at a threshold of $1200\,\mathrm{e}^-$ and then decreases again is related to the decreasing hit detection efficiency: For large thresholds, the efficiency drops first along the pixel edges and corners. This creates a bias of the detected pixel hits towards the pixel centre, which remains more efficient at higher thresholds. For large thresholds above $3000\,\mathrm{e}^-$ in the column direction and $2000\,\mathrm{e}^-$ in row direction the RMS rises again. This observation is consistent with the increase of the mean cluster sizes (see Figure 11.14). As stated in Section 11.3.3, it is likely related to a bias towards large energy depositions from the right tail of the Landau distribution including delta rays leading to larger clusters.

Bias Dependence

In Figure 11.27, the dependence of the RMS on the bias voltage is shown in both column and row direction. As above it is quantified as the RMS of the unbiased spatial residuals. It is seen that with an increasing bias voltage, the RMS grows both in column and row direction. After reaching a maximum at a bias voltage of $-30\,\mathrm{V}$ it slowly decreases again for even larger bias voltages. This behaviour is explained as follows: At very low bias voltages, the sensor is not fully efficient as discussed in Section 11.2 (see Figure 11.5). In particular, the inefficiencies occur close to the pixel edges and corners. Hence, the fraction of multi-pixel clusters is reduced (see Figure 11.15) and also single-pixel clusters are detected more efficiently towards the pixel centre. Consequently, the detected hit positions are biased towards the pixel centre. At a bias voltage of around $-30\,\mathrm{V}$, the sensor becomes fully efficient (see Figure 11.3a) such that the above-mentioned bias towards the pixel centre is minimised. For larger bias voltages, the efficiency remains high. However, a larger bias voltage leads to a larger depleted volume and thus to a larger signal for a given deposited

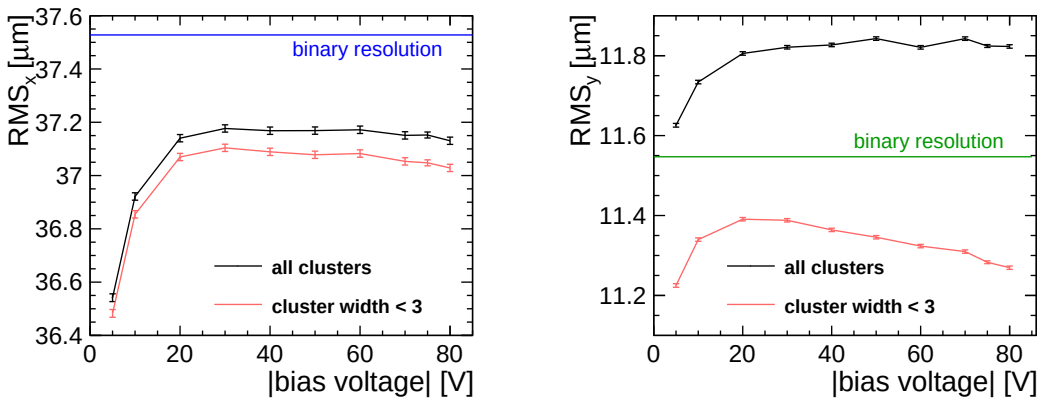

(a) Column direction.

(b) Row direction.

Figure 11.27: Bias voltage dependence of the RMS of the spatial residuals for combined runs focussing on the upper and the lower section of the matrix at a threshold of 845 mV $\approx$ 720 e^-.

energy. Hence, the cluster size increases as previously shown in Section 11.3 (see Figure 11.15). The larger cluster sizes slightly improve the measured spatial resolution. This becomes particularly evident when focussing on the RMS for clusters with a width smaller than three, shown in red.

Comparison of Arithmetic and ToT-Weighted Mean

For the previous results, the cluster centre is determined as the arithmetic mean of the pixels within the cluster using Equation 8.3. In contrast, Figure 11.28 shows the unbiased residuals for different cluster sizes if the cluster position is determined as the ToT-weighted mean according to Equation 8.1. The comparison shows that a determination of the cluster position as the ToT-weighted mean leads to a worse prediction of the track intercept, in particular for two-pixel clusters.

Because two-pixel clusters predominantly occur close to the pixel edges, the arithmetic mean yields a precise estimation of the track intercept. On the other hand, charge sharing is highly non-linear in the ATLASpix, such that the seed pixel creates a strong pull on the cluster centre. Overall, an RMS of (37.2 ± 0.1) µm and (11.8 ± 0.1) µm is measured in column and row direction, respectively. This is consistent with the values shown in Table 11.1 within the uncertainties and shows that the overall difference is insignificant due to the large abundance of single-pixel clusters.

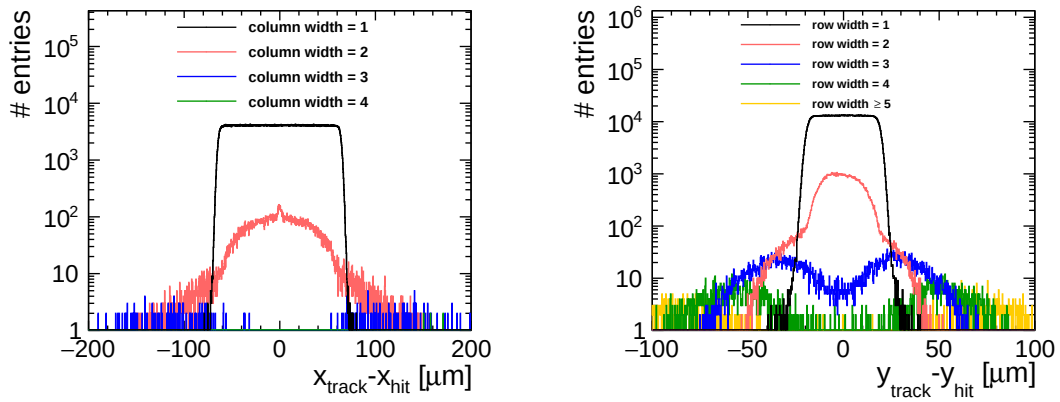

(a) Column direction, logarithmic y-axis.

(b) Row direction, logarithmic y-axis.

Figure 11.28: Unbiased spatial residuals for different cluster widths in the respective directions at a threshold of 845 mV $\approx$ 720 e^- and a bias voltage of -75 V. The cluster position is calculated as the ToT-weighted mean according to Equation 8.1.

11.4.3 Limitations & Possible Improvements

In summary, the spatial resolution of the ATLASpix is very close to the binary resolution because of the predominance of single-pixel clusters. The arithmetic mean of two-pixel clusters yields a precise estimate of the track incidence point due to their occurrence close to the pixel edges. On the other hand, delta rays cause outliers in the residuals, which lead to a degradation of the spatial resolution. This effect is more pronounced in the row direction due to the smaller pixel pitch.

Furthermore, it was found that a determination of the cluster position as the ToT-weighted mean leads to a slightly worse spatial resolution. Because two-pixel clusters predominantly occur close to the pixel edges, the arithmetic mean is a precise estimation of the track intercept. On the other hand, charge sharing is highly non-linear in the ATLASpix, such that the seed pixel creates a strong pull on the cluster centre.

The pitch in column direction suffices to meet the requirement of the maximal longitudinal granularity of 1-10 mm for the CLIC tracking detector (see Table 2.1 in Section 2.4.3). On the other hand, the requirement for the spatial resolution in transversal direction of 7 µm is not fulfilled.

Due to the abundance of single-pixel clusters, only small improvements on the spatial resolution may be achieved by an optimisation of the sensor settings for a suppression of cross-talk, or the implementation of an algorithm to detect and suppress delta rays [170].

For a significant improvement of the spatial resolution, a smaller pixel pitch of approximately 25 µm would be required in the row direction. To this end, a modified pixel detector based on the design of the ATLASpix was produced with a pixel pitch of 165 $\times$ 25 µm [171]. Its characterisation is ongoing at the time of writing.

11.5 Time Resolution

Analogously to the spatial resolution, the time resolution can be determined as the width of time residuals, i.e. the time difference between a track and the timestamp of an associated cluster on the DUT, as discussed in Section 8.4.

11.5.1 Row Dependence

Figure 11.29 shows the time residuals for two combined runs covering the full matrix at nominal conditions. A prominent non-Gaussian right tail is visible.

The reason for this is revealed in Figures 11.30a, which show the time residuals plotted against the row number of the earliest pixel within a cluster, which is the pixel defining the cluster timestamp. It is seen that the peak of the time residuals shifts towards smaller values for larger row numbers. As the residuals are calculated as $t_{\text{track}} - t_{\text{hit}}$, it either means that smaller ("earlier") track timestamps or larger ("later") cluster timestamps on the ATLASpix are measured with larger row numbers.

Figure 11.30b shows the peak position of the time residuals as a function of the row number overlayed for two runs covering rows 0 to 298 and rows 76 to 400, respectively. They overlap precisely. Hence, it can be excluded that the reference track timing varies across the matrix because the two runs were taken with the reference telescope covering different areas of the sensor. In particular, the small dips and peaks such as seen in row 200 occur at the exact same row numbers in both cases. It can be inferred that these do not originate from statistical fluctuations but represent features of the ATLASpix matrix, and are explained as follows: Each pixel has its own signal transmission line connecting the pixel cell with the periphery. Due to an increasing length of the transmission lines for larger row numbers as well as a non-uniform routing scheme involving multiple metal layers, the line capacitance varies, which affects the signal shape and consequently the timing behaviour [51].

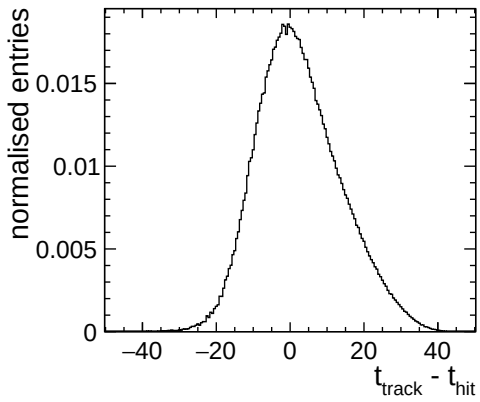

Figure 11.29: Track-hit time residuals for two combined runs covering the full matrix. Bias voltage $-75\,\text{V}$, threshold $845\,\text{mV} \approx 720\,\text{e}^-$.

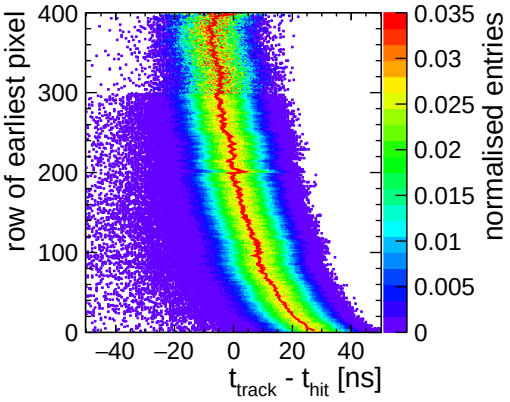

(a) Time residuals vs. row number of earliest pixel. The red lines mark the peak positions for each row.

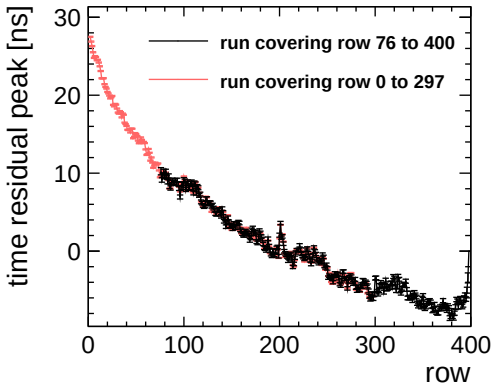

(b) Peak positions of the time residuals for each row.

Figure 11.30: Row dependence of the track-hit time residuals. Bias voltage −75 V, threshold 845 mV ≈ 720 e⁻.

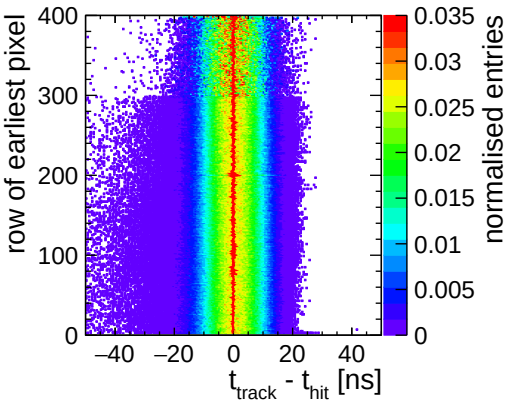

Figure 11.31: Row dependence of the track-hit time residuals after applying the row-dependent delay correction. The red line marks the peak positions for each row. Bias voltage −75 V, threshold 845 mV ≈ 720 e⁻.

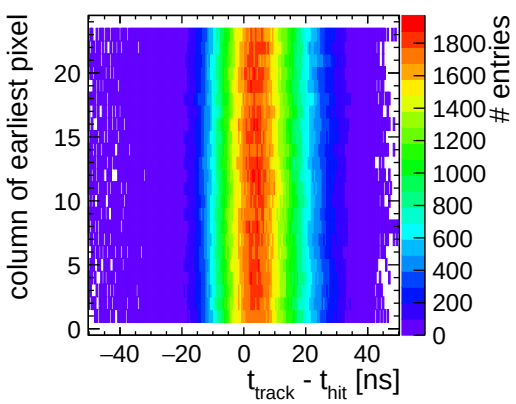

Figure 11.32: Column dependence of the track-hit time residuals before applying any corrections. Bias voltage −75 V, threshold 845 mV ≈ 720 e⁻.

A row-dependent delay correction can be applied offline to the data, for which the timestamp of each hit cluster on the ATLASpix is shifted by the peak value of the time residual for each row as shown in Figure 11.30b. The resulting two-dimensional distribution is displayed in Figure 11.31, where it can be seen that the peak positions of the residuals are now constant with the row number.

A column dependence of the timing behaviour is not expected. As shown in Figure 11.32, no column dependence is observed.

11.5.2 Timewalk

As discussed in Section 4.1, timewalk describes the effect that varying signal sizes lead to different delays of the threshold crossing. Because the ATLASpix provides

ToT information as a measure of the signal size, the effect of timewalk can be investigated and corrected.

Figure 11.33a shows the time residuals as a function of the ToT of the earliest pixel within the cluster, which is the one that defines the cluster timestamp, after the row-dependent delay correction is applied.

As expected from timewalk, a ToT dependence of the peak position of the time residuals is observed: Hit clusters with a small earliest pixel ToT tend to have a larger ("later") timestamp. Analogously to the row-dependent delay correction, a timewalk correction is applied to the data offline, for which the timestamp of each hit cluster is shifted by the peak value of the time residual for a given earliest pixel ToT. The resulting time residuals are shown in Figure 11.33b, where no further ToT dependence of the peak position is observed.

In Figure 11.34a, the time residuals are compared directly before any correction, after applying the row correction, and after applying both the row and the timewalk correction. Because the residuals do not follow a normal distribution before applying the corrections, they cannot be described by a Gaussian fit. Instead, the RMS on a range of $\pm 100\,\text{ns}$ is used to quantify the time resolution in analogy to the spatial residuals discussed in Section 11.4 (see Equation 8.15). To estimate the uncertainties, the range is varied between $\pm 80\,\text{ns}$ and $\pm 120\,\text{ns}$. After applying both corrections, the standard deviation of a Gaussian normal distribution is determined in addition from a fit as shown in Figure 11.34b. To estimate the systematic uncertainties due to deviations from an ideal Gaussian shape, the difference between the standard deviation and the RMS is considered. The results are summarised in Table 11.2. All measured time residuals contain a contribution of $\sim 560\,\text{ps}$ from the time resolution of the reference track timestamp as discussed in Section 9.1.2, which is negligible within the measurement uncertainties.

The discrepancy between the RMS and the σ arise from outliers deviating from

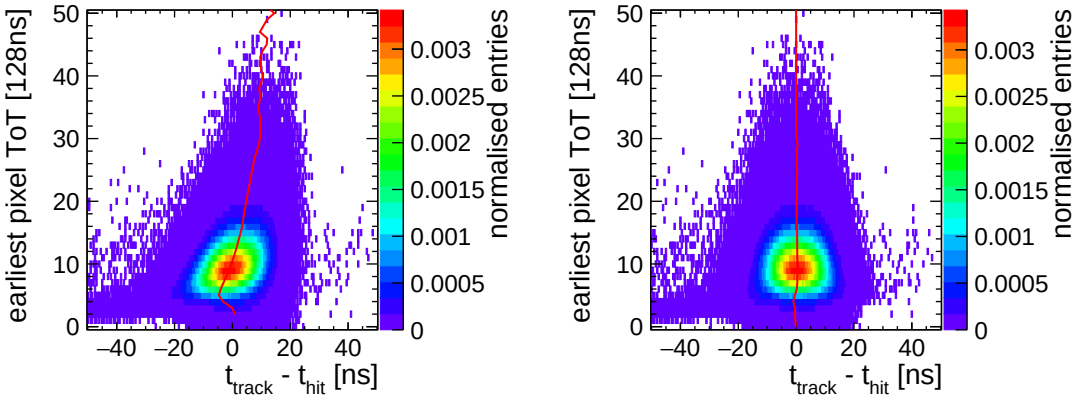

(a) After row correction.

(b) After row and timewalk correction.

Figure 11.33: ToT dependence of the track-hit time residuals after applying the row-dependent correction and after both the row and timewalk correction. The red line marks the peak positions for each ToT bin. Bias voltage $-75\,\text{V}$, threshold $845\,\text{mV} \approx 720\,\text{e}^-$.

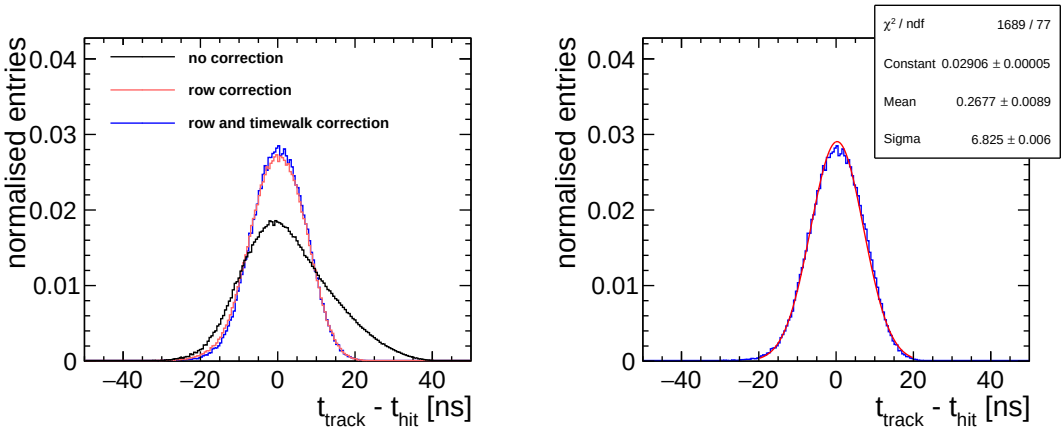

(a) Before and after corrections.

(b) After all correction with a Gaussian fit.

Figure 11.34: Track-hit time residuals before and after corrections. Bias voltage −75 V, threshold 845 mV ≈ 720 e^-.

Table 11.2: Comparison of the time resolutions for the ATLASpix quantified as the RMS of the time residuals before and after corrections, and as the standard deviation of a Gaussian fit.

Correction	$\mathbf{RMS_{meas}}$ [ns]	$\sigma_{\mathbf{meas}}$ [ns]
before	11.41 ± 0.03	
row	7.46 ± 0.04	
row + timewalk	7.17 ± 0.03	6.82 ± 0.35

the normal distributions as can be seen in Figure 11.34b. They can occur because the of the limited precision of the timewalk correction. The precision of the ToT measurement is restricted to a range of 0-63 , such that a certain amount of timewalk is irreducible when two signals with different sizes are measured within the same ToT bin. This effect becomes more pronounced with a larger binning of the ToT measurement. For the measurements presented in this chapter the maximal ToT binning of 128 ns was chosen by setting the clock divider `ckdivend2` to its maximal value of 15.

11.5.3 Threshold Dependence

The threshold dependence of the ATLASpix time resolution is shown in Figure 11.35 for a data set covering rows 76 to 399. As before it is quantified as the RMS on a range of ±100 ns. Generally, it is seen that the time resolution deteriorates with higher thresholds. Furthermore, it can be observed that the row correction yields a large improvement at low thresholds, whereas it becomes negligible compared to the strongly increasing timewalk towards higher thresholds. The application of a timewalk correction at high thresholds results in a significant improvement of the time resolution, whereas it becomes less important at lower thresholds. This corresponds to the expectation as the amount of timewalk is expected to increase with higher thresholds for a given signal size as discussed in Section 4.1.

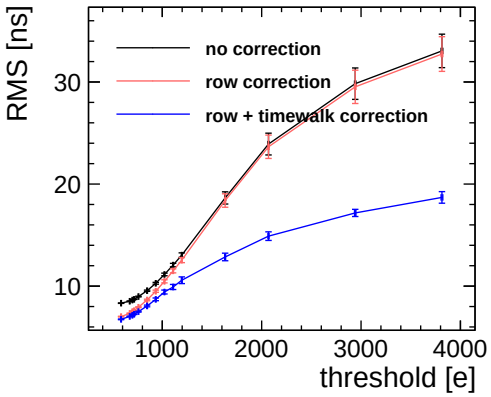

Figure 11.35: Threshold dependence of the time resolution quantified as the RMS of the track-hit time residuals at a bias voltage of $-75\,\mathrm{V}$ for a data set covering the upper section of the matrix (rows 76-399).

Even after the application of the timewalk correction, the time resolution deteriorates with larger thresholds. This has multiple reasons: At higher thresholds, the threshold crossing is less steep as seen in Figure 10.24. This leads to an increased sensitivity to jitter of the comparator, i.e. time fluctuations caused by noise fluctuations on the signal. These are an irreducible contribution to the time resolution. In addition, for a larger threshold smaller ToT values are measured for a given signal size. As a consequence, a smaller fraction of the dynamic range of the ToT is exploited, meaning that the measured ToT spectrum spreads across a smaller number of ToT bins. Hence, the effectivity of the timewalk correction is reduced due to the limited resolution of the ToT measurement.

11.5.4 Bias Dependence

The bias voltage dependence of the time resolution is shown in Figure 11.36 for combined data sets covering the full matrix. It is seen that the time resolution improves with an increasing bias voltage. The row correction has a larger influence at higher bias voltages, where the time resolution is generally smaller.

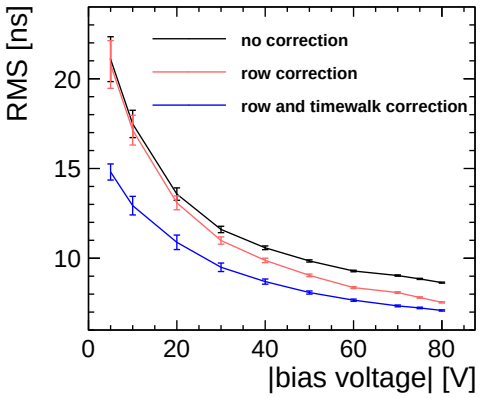

Figure 11.36: Bias dependence of the ATLASpix time resolution quantified as the RMS of the track-hit time residuals at a threshold of $845\,\mathrm{mV} \approx 720\,\mathrm{e}^-$.

The timewalk correction yields a stronger improvement at lower bias voltages and becomes less important at higher bias voltages. This behaviour is expected because a larger bias voltage results in a larger depleted volume and thus larger signals. Larger signals due to a higher bias voltage at a given threshold are comparable to a lower threshold at a given bias voltage as discussed above.

11.5.5 Best Result, Limitions & Possible Improvements

The overall best results are obtained for the lowest threshold and the highest investigated bias voltages. They are summarised in Table 11.3.

Table 11.3: Summary of the time resolutions for the ATLASpix obtained at the **lowest thresholds** and **highest bias voltages** after both row-dependent delay and timewalk correction.

Threshold	**Bias voltage [V]**	**RMS$_{\text{meas}}$ [ns]**	**σ_{meas} [ns]**
830 mV $\approx$ 590 e$^-$	-75	6.82 ± 0.04	6.7 ± 0.1
845 mV $\approx$ 720 e$^-$	**-80**	7.04 ± 0.03	6.80 ± 0.3

As before, Gaussian fits are performed to determine the time resolution as the standard deviation σ_{meas} of the fit function and the difference to the RMS is considered as the uncertainty. The contribution of $\sim$560 ps from the time resolution of the reference track timestamp as discussed in Section 9.1.2 is negligible within the measurement uncertainties.

While the optimisation of chip settings is not part of this thesis, in [51] an improvement of the time resolution down to (5.9 ± 0.3) ns is achieved after row and timewalk correction.

The largest limitation of the time resolution is the timestamp binning of 16 ns, which contributes with $16\,\text{ns}/\sqrt{12} \approx 4.6\,\text{ns}$. A faster timestamp counter with a binning of 8 ns would result in reduction of the time resolution to

$$\sqrt{(6.7\,\text{ns})^2 - \frac{(16\,\text{ns})^2}{12} + \frac{(8\,\text{ns})^2}{12}} \approx 5.4\,\text{ns} \tag{11.1}$$

based on the time resolution measured with the chip settings used in this thesis and $\sim$4.3 ns with the settings used in [51].

A faster timestamp binning of 8 ns is implemented in the next sensor generation, the *ATLASpix3* [172] together with an optimisation of the routing scheme, resulting in a reduction of the row dependence [173], leading to a time resolution of 3.7 ns after timewalk correction [174]. Further results can be found in [174, 175].

11.6 Studies with Different Substrate Resitivities

A selection of the following measurements have been published in [176] and parts of this section use the exact same wording.

Previously, the performance of the ATLASpix was investigated for a substrate resistivity of 200 Ωcm. In the following, the focus lies on the comparison of samples with different substrate resistivities.

The data was recorded at DESY during several test-beam campaigns. Table 11.4 gives an overview of the samples used for the studies with different substrate resistivities. Unless otherwise stated, all of the following results are obtained at a bias voltage of −50 V and a detection threshold of 860 mV corresponding to 820-850 e^-, depending on the sample. The exact values for each sample are shown in Table 11.4.

Table 11.4: Overview of the ATLASpix samples used for the studies with different substrate resistivities at DESY.

Sample	Thickness [µm]	Resistivity [Ωcm]	Nominal Bias Voltage [V]	Nominal Threshold
w06s12	100	20	-50	860 mV ≈ 840 e^-
w10s30	62	80 (50-100)	-50	860 mV ≈ 820 e^-
w23s11	100	200 (100-400)	-50	860 mV ≈ 850 e^-

The nominal thresholds in electrons deviate slightly. Consequently, direct comparisons at the nominal threshold value need to be done with caution. The nominal threshold was chosen as a compromise to ensure that all samples are operated under the same conditions without an excessive noise rate.

Sample w10s30 has a thickness of 62 µm compared to 100 µm. It was used because no sample with a thickness of 100 µm was available. This needs to be kept in mind when interpreting the performance characteristics of the samples with different substrate resistivities presented below.

11.6.1 Analysis Strategy with DESY Data

It was shown previously that the ATLASpix has a clear row dependence in many performance parameters, such as the cluster size or the hit detection efficiency. When comparing the performance of samples with different substrate resistivities, it is crucial to minimise the bias from the row dependence due to a different DUT coverage by the reference telescope stemming from a different alignment of the DUT with respect to the reference telescope. Else, observed differences cannot clearly be related to the substrate resistivity. Hence, a region-of-interest (ROI) is derived from the common overlap of all samples. Figure 11.37 shows the two-dimensional distributions

of clusters on the three investigated samples. As previously, the outermost columns are excluded to avoid possible edge effects from tracks impinging close to the sensor boundaries. In additions, rows above 299 are excluded due to a possible occurrence of cross-talk as discussed in Section 11.3.2. Therefore, the ROI is ranges from column 1 to 23 and from row 52 to 299.

Furthermore, the bias of the results arising from an inhomogeneous illumination of the rows is minimised by a rescaling of the numbers of entries per row such that each row contributes with the same weight.

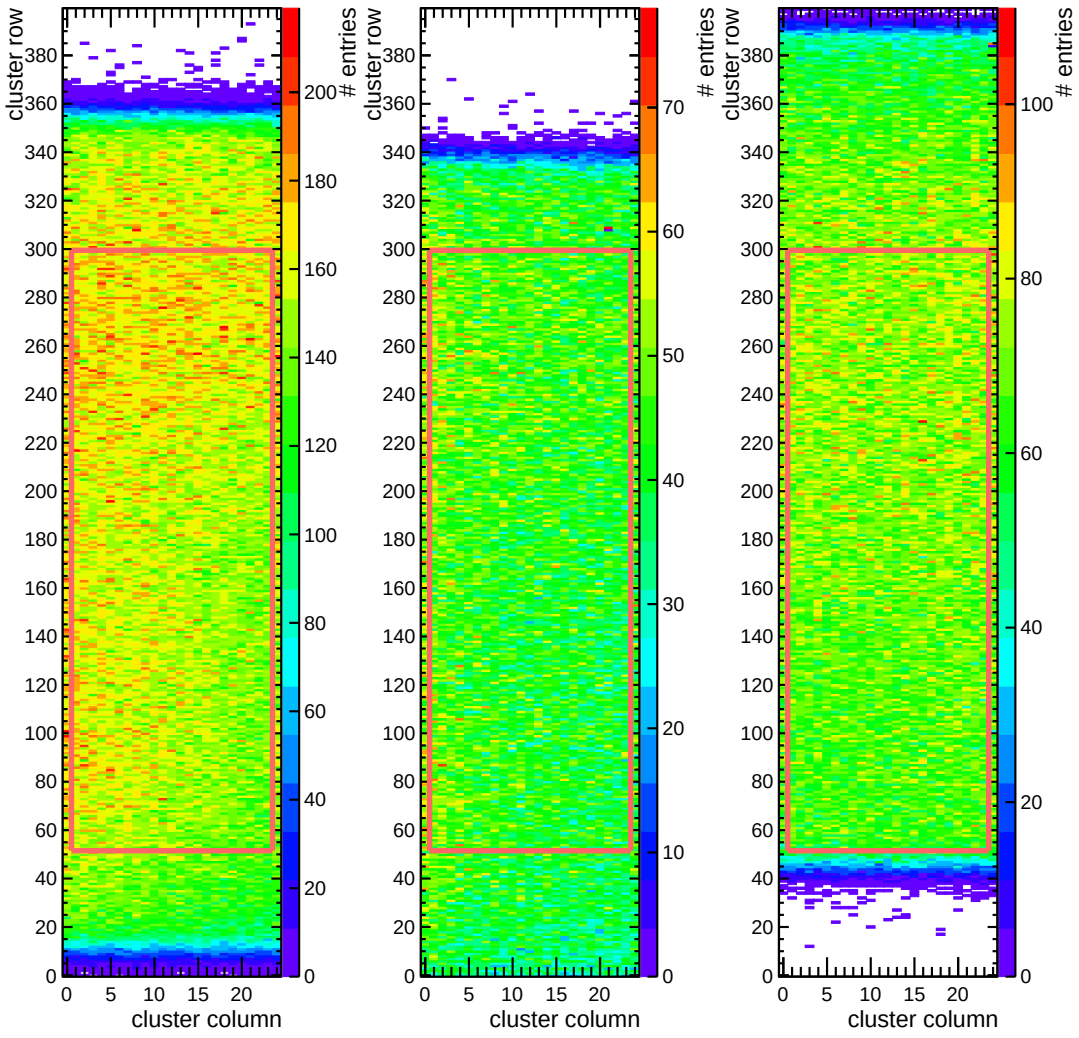

(a) Sample w06s12, 20 Ωcm, 100 µm.

(b) Sample w10s30, 80 Ωcm, 62 µm.

(c) Sample w23s11, 200 Ωcm, 100 µm.

Figure 11.37: Two-dimensional distribution of the track-associated clusters across the matrix for samples with different substrate resistivities at nominal conditions. The red box marks the selected region-of-interest corresponding to the area covered by the telescope acceptance in all cases and excluding rows above 299, which are affected by cross-talk.

11.6.2 Hit Detection Efficiency

Since the substrate resistivity has a significant impact on the depth and shape of the depletion region and the configuration of the electric field, it is also expected to influence the hit detection efficiency. Consequently, the hit detection efficiency and its dependence on the detection threshold as well as the bias voltage have been studied. The results are shown in Figure 11.38 and Figure 11.39. They are overlayed with the total noise rate of each sample.

For the SPS analysis presented in Section 11.2, the noise rate could be extracted in-situ from the number of hits between the distinct beam spills received from the SPS. This is not possible for the data recorded at DESY due to the different beam structure, which has a periodicity of 0.976 µs [129] and is therefore quasi-continuous in view of the event length of 230.4 µs. Hence, the noise rates presented as part of the laboratory measurements discussed in Chapter 10 are used.

Threshold Dependence

As can be seen in Figure 11.38, the efficiency drops with an increasing detection threshold. Comparing the different substrate resistivities, it drops significantly slower for the 200 Ωcm sample than for the lower substrate resistivities. As a consequence, the 200 Ωcm sample can be operated for a much larger range of the threshold while maintaining a high detection efficiency.

This behaviour is expected because a higher substrate resistivity leads to a larger depleted volume for a given bias voltage. Consequently, the signal induced by the generated charge carriers of an incident particle is larger so that it can exceed the detection threshold for higher thresholds before becoming inefficient. At very low thresholds, the efficiency drops significantly for all samples. This coincides with a strong increase in the noise rate. It is consistent with the measurements from the SPS test-beam campaigns presented in Section 11.2 and the laboratory measurements

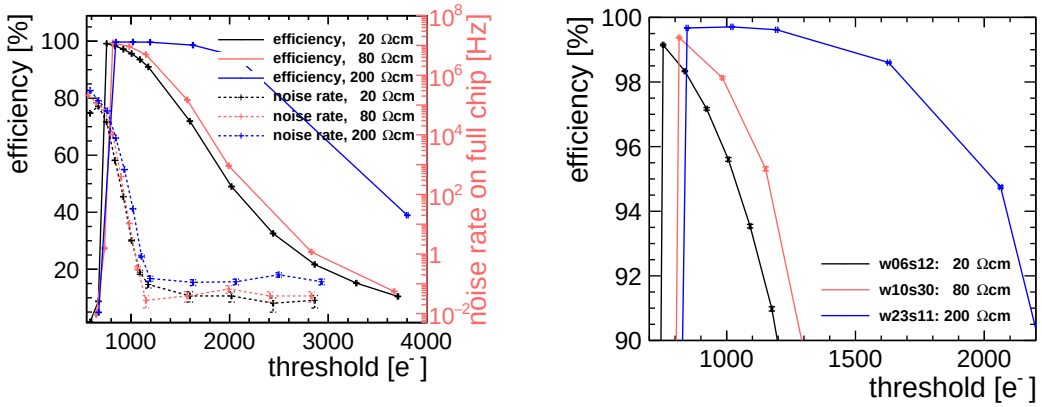

(a) Efficiency and noise rate.

(b) Efficiency (zoom).

Figure 11.38: Threshold dependence of the hit detection efficiency and noise rate comparing samples with different substrate resistivities at a bias voltage of −50 V.

presented in Section 10.3.1. At very low thresholds, an excessive noise rate causes a saturation of the readout. In consequence, not all hits generated by traversing particles can be read out correctly and the measured efficiency is reduced. Figure 11.38b shows a zoomed view of Figure 11.38a. It reveals that the efficiency keeps rising for the 20 Ωcm and 80 Ωcm samples until the point when it collapses due to the readout saturation. This observation supports the assumption that the efficiency of the lower resistivity samples would likely increase further if smaller operating thresholds were possible by masking noisy pixels online and applying a threshold equalisation.

Notably, the 80 Ωcm sample is only slightly more efficient than the 20 Ωcm even though for a given bias voltage, the depletion depth should be twice as large according to Equation 3.15. This observation indicates that for the 20 Ωcm a significant amount of charge is collected from the non-depleted volume via diffusion into the depletion zone, while this contribution could be reduced for the 80 Ωcm sample due to the reduced thickness of 62 µm. In addition, the resistivity may deviate from the nominal 80 Ωcm within a range of 50-100 Ωcm as specified by the manufacturer due to deviations from the standard process (see Section 5.4). If the actual resistivity is closer to 50 Ωcm, this would also lead to a reduction of the depleted volume for a given bias voltage and thus to a smaller performance difference compared to the 20 Ωcm sample.

Bias Dependence

Figure 11.39a shows how the hit detection efficiency changes with the applied bias voltage. It can be observed that the efficiency rises with increasing bias voltage for the lower substrate resistivities. For the 200 Ωcm sample no data is available below −30 V as the data was found to be corrupted. However, it is seen in Section 11.2 that it reaches an efficiency of 90 % even at −5 V. For the lower resistivities, the efficiency saturates only slowly whereas it already reaches a stable plateau at a bias voltage around −30 V for the 200 Ωcm. This means that the 200 Ωcm sample can be operated at a high efficiency at a much lower bias voltage.

Also this observation meets the expectation since a higher substrate resistivity leads to a larger depleted volume for a given bias voltage.

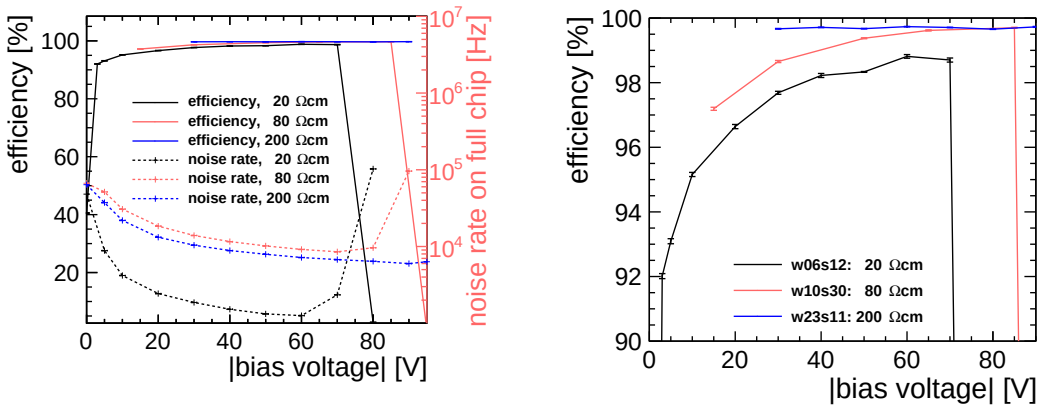

(a) Efficiency and noise rate.

(b) Efficiency (zoom).

Figure 11.39: Bias voltage dependence of the hit detection efficiency and noise rate comparing samples with different substrate resistivities at the nominal threshold of 860 mV $\approx$ 820 $-$ 850 e^-.

In-Pixel Efficiency

In Figures 11.40 and 11.41 , the in-pixel efficiencies are plotted for the three investigated samples at the lowest operation thresholds and the highest bias voltages before the efficiency drops as discussed above. It can be seen that the 200 Ωcm sample is highly efficient across the entire pixel area.[3]

In contrast, the lower resistivity samples show significant inefficiencies for tracks penetrating the sensor close to the pixel corners. This corresponds to the expectation as the signal size is expected to be smaller for the lower resistivities at a given bias voltage. In consequence, a reduction of the signal size per pixel by charge sharing into the neighbouring pixels leads to a decreased number of cases in which the signal can exceed the detection threshold. It also shows that an even lower detection threshold could potentially help to recover part of the inefficiency. This would require the ability to perform an online masking of noisy pixels to avoid a saturation of the readout. On the other hand, a higher bias voltage is not applicable for the 20 Ωcm and 80 Ωcm, for which the noise rates already increase significantly for the highest bias voltages shown in Figure 11.39a due to the large leakage currents occurring above the determined breakdown voltages (see Section 10.1.2).

[3] In Figure 11.4a (see Section 11.2.2), small inefficiencies are observed in the pixel corners even at the lowest achievable threshold. It is assumed that this effect is not visible in the data presented here due to the lower available statistics and the slightly worse track pointing resolution of ∼2.5 µm of the EUDET telescope used at DESY (see Section 9.2.1) compared to ∼1.3 µm for the Timepix3 telescope at the SPS (see Section 9.1.1).

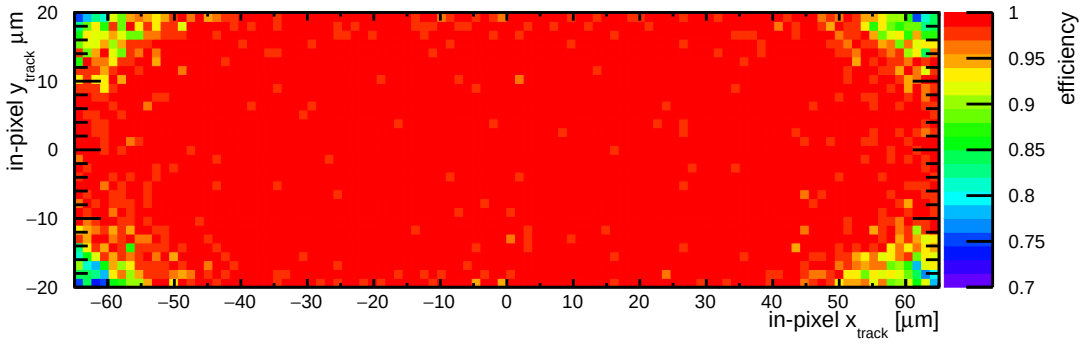

(a) Sample w06s12 (20 Ωcm, 100 µm). Threshold ≈ 750 e^-, mean efficiency = $(99.1489^{+0.024}_{-0.025})\%$.

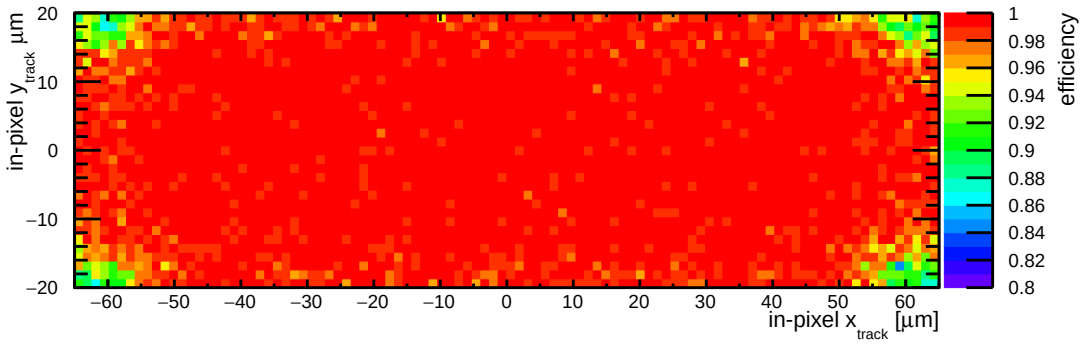

(b) Sample w10s30 (80 Ωcm, 62 µm). Threshold ≈ 820 e^-, mean efficiency = $(99.376^{+0.014}_{-0.015})\%$.

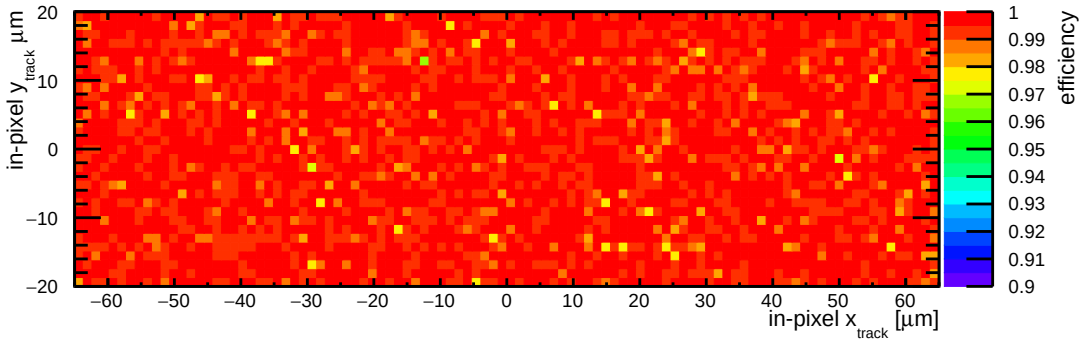

(c) Sample w23s11 (200 Ωcm, 100 µm). Threshold ≈ 850 e^-, mean efficiency = $(99.672^{+0.009}_{-0.009})\%$.

Figure 11.40: In-pixel efficiency for samples with different substrate resistivities at a bias voltage of −50 V and the lowest threshold before the efficiency drop observed in Figure 11.38.

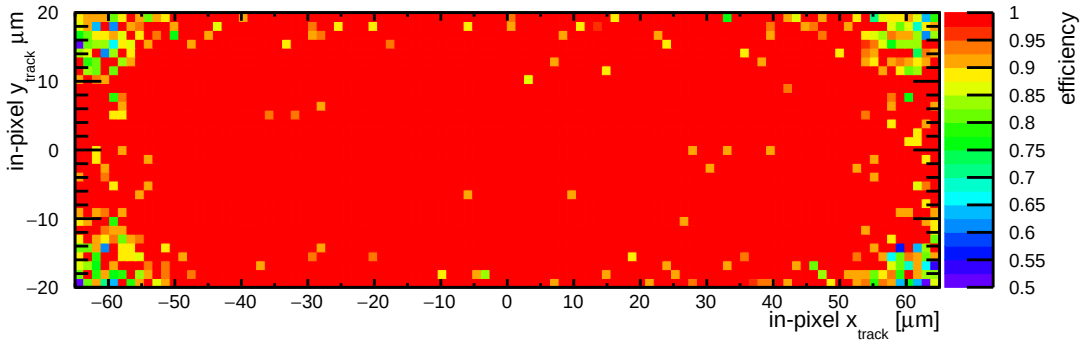

(a) Sample w06s12 (20 Ωcm, 100 µm). Bias voltage = −70 V, mean efficiency = $(98.701^{+0.062}_{-0.065})\%$.

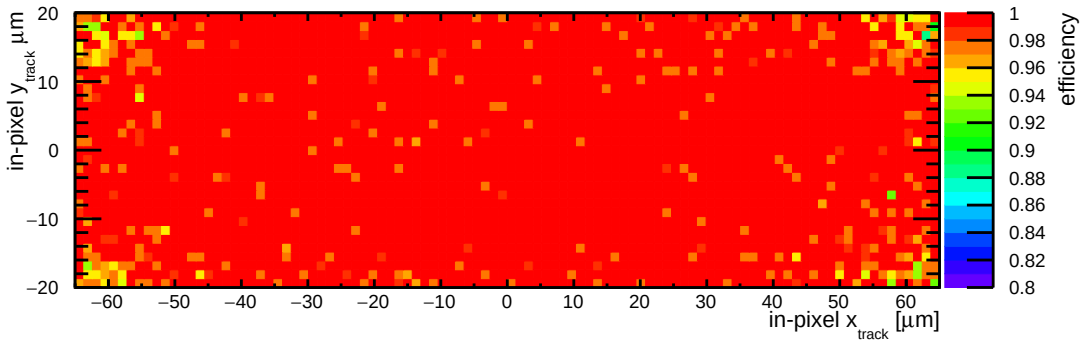

(b) Sample w10s30 (80 Ωcm, 62 µm). Bias voltage = −85 V, mean efficiency = $(99.670^{+0.015}_{-0.016})\%$.

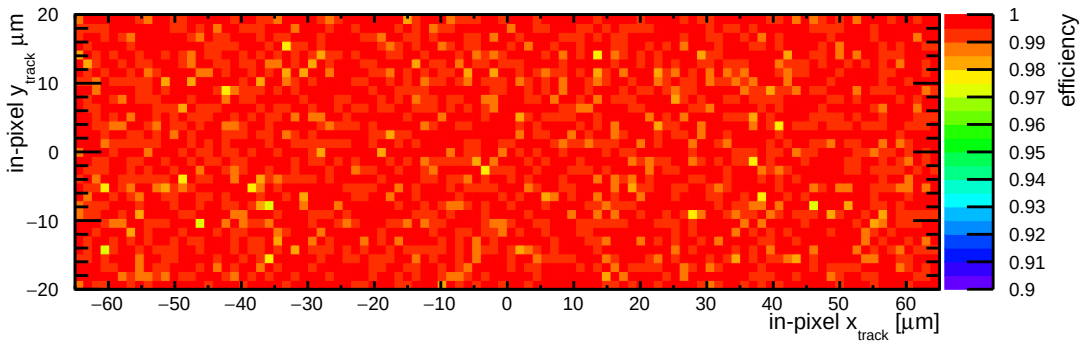

(c) Sample w23s11 (200 Ωcm, 100 µm). Bias voltage = −80 V, mean efficiency = $(99.657^{+0.008}_{-0.009})\%$.

Figure 11.41: In-pixel efficiency for samples with different substrate resistivities at their nominal thresholds and the highest bias voltage before the efficiency drop observed in Figure 11.39.

11.6.3 Time Resolution

Also the timing performance for the different substrate resistivities of the ATLASpix is compared based on the data set obtained in measurement campaigns at the DESY II test-beam facility. It is expected that a larger substrate resistivity leads to a better timing resolution for the following reason: A higher substrate resistivity leads to a larger depleted volume for a given bias voltage, which results in a larger energy is deposited in the depletion region. In consequence, the crossing of the detection threshold is expected to be steeper and the amount of timewalk should be reduced at a given threshold.

Figure 11.42 shows two-dimensional histograms of the seed pixel ToT of clusters on the ATLASpix plotted against the time residual of the reference track and the associated cluster on the ATLASpix. It is seen that the amount of timewalk is reduced significantly for larger substrate resistivities. The dependence on the substrate resistivity follows the expectation.

A correction for a row-dependent signal delay as well as a timewalk correction of the cluster timestamp are applied offline following the same strategy as discussed within the context of the SPS analysis presented in Section 11.5. The time residuals before and after applying the correction are shown in Figure 11.43.

Because the residuals do not follow a normal distribution before applying the corrections, they cannot be described by a Gaussian fit. Instead, the RMS on a range of ± 100 ns is used to quantify the time resolution in analogy to the SPS analysis presented in Section 11.5. After applying both corrections, the standard deviation of a Gaussian normal distribution is determined in addition from a fit as shown in Figure 11.44. The results are summarised in Table 11.5. The uncertainties on the RMS are estimated by varying the range between ± 80 ns and ± 120 ns. The systematic uncertainties on σ_{meas} are estimated as the difference between the σ_{meas} and the RMS to account for the deviation of the distribution from a Gaussian shape.

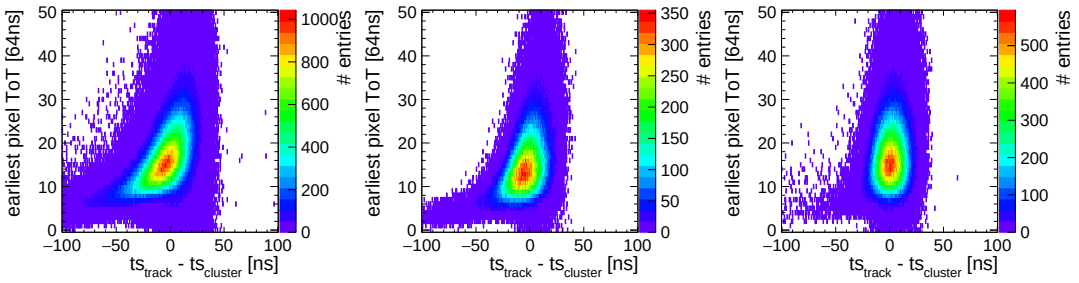

(a) Sample w06s12, 20 Ωcm, 100 µm.

(b) Sample w10s30, 20 Ωcm, 62 µm.

(c) Sample w23s11, 200 Ωcm, 100 µm.

Figure 11.42: Time residuals vs. the earliest pixel ToT of the ATLASpix for different substrate resistivities at nominal detection threshold and bias voltage before applying any correction.

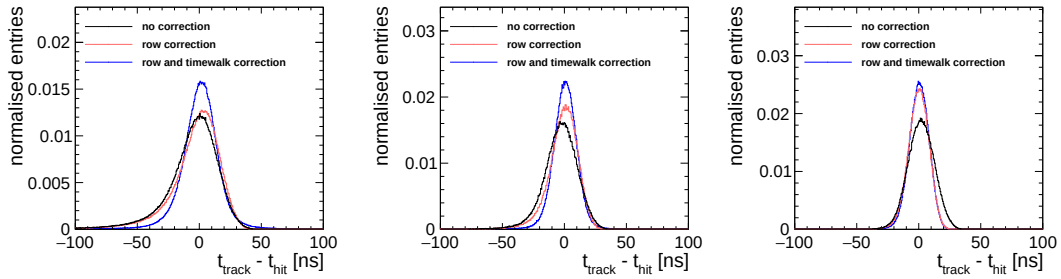

(a) Sample w06s12, 20 Ωcm, 100 µm.

(b) Sample w10s30, 80 Ωcm, 62 µm.

(c) Sample w23s11, 200 Ωcm, 100 µm.

Figure 11.43: Comparison of the time residuals before any correction, after applying the row-dependent delay correction, and after applying both the row and the timewalk correction for samples with different substrate resistivities at the nominal conditions.

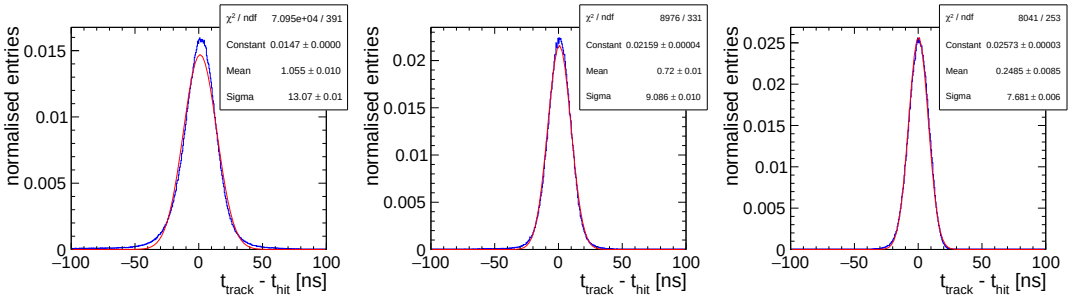

(a) Sample w06s12, 20 Ωcm, 100 µm.

(b) Sample w10s30, 80 Ωcm, 62 µm.

(c) Sample w23s11, 200 Ωcm, 100 µm.

Figure 11.44: Comparison of the time residuals for samples with different substrate resistivities at nominal conditions after applying the row and timewalk correction with Gaussian fits to extract the time resolution.

All measured time residuals contain a contribution of ∼1.1 ns from the time resolution of the reference track timestamp as discussed in Section 9.2.2, which is subtracted quadratically from σ_{meas}.

The comparison confirms the expectation that a higher substrate resistivity leads to a significant improvement of the time resolution. In particular, before applying any offline corrections, the lower resistivities show a very pronounced timewalk, which leads to a significant degradation of the time resolution. After corrections, the highest substrate resistivity still yield the best resolution. Due to a larger depleted volume, the signals are larger, which leads to a steeper threshold crossing. It is therefore less affected by jitter, which represents an irreducible contribution to the time resolution. In addition, the timewalk correction only has a limited precision due to the binning of the ToT measurement.

Table 11.5: Comparison of the time resolutions for ATLASpix samples with different substrate resistivities quantified as the RMS of the time residuals before and after corrections and by a Gaussian fit. The track time resolution of ∼1.1 ns is subtracted quadratically from σ_{meas}. The uncertainties on the RMS are estimated by varying the range and the systematic uncertainties on σ_{meas} are obtained as the difference between the σ_{meas} and the RMS.

Correction	Sample	RMS_{meas} [ns]	σ_{meas} [ns]	σ_{ATLASpix} [ns]
before	20 Ωcm, 100 µm	20.3 ± 1.1		
	80 Ωcm, 62 µm	14.0 ± 0.2		
	200 Ωcm, 100 µm	10.7 ± 0.1		
row	20 Ωcm, 100 µm	20.0 ± 1.1		
	80 Ωcm, 62 µm	12.8 ± 0.2		
	200 Ωcm, 100 µm	8.7 ± 0.1		
row + timewalk	20 Ωcm, 100 µm	16.5 ± 0.9	13.1 ± 3.4	13.0 ± 3.4
	80 Ωcm, 62 µm	10.7 ± 0.2	9.1 ± 1.6	9.0 ± 1.6
	200 Ωcm, 100 µm	8.2 ± 0.1	7.7 ± 0.6	7.6 ± 0.6

11.7 Determination of the Active Depth

Some of the following results have been published in [168] and parts of this section use the exact same wording.

All results presented previously are based on particles impinging on the detector at normal incidence, i.e. with an incidence angle of approximately 90° with respect to the sensor surface. Inclined tracks are expected to lead to increased cluster sizes because a particle penetrates several adjacent pixels while passing through the detector material. As illustrated in Figure 11.45, this depends on the incidence angle α as well as the pixel pitch and the active depth d_{active}. Hereby, the active depth refers to the depletion depth and a possible layer below the depletion depth from which charge may be collected via diffusion into the depleted volume.

In this simple geometrical model, the average cluster width in column/row direction is given by

$$\text{cluster width}_{\text{column/row}} = \frac{d_{\text{active}}}{\text{pitch}_{\text{column/row}}} \cdot \tan(\alpha). \tag{11.2}$$

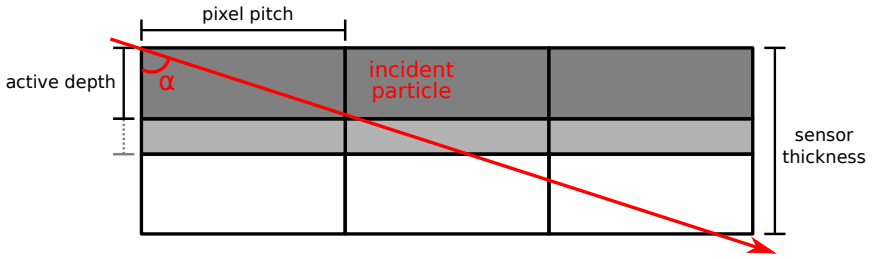

Figure 11.45: Schematic drawing of the track incidence angle α dependence on the expected cluster size.

In turn, a measurement of the angle dependence of the cluster size can be used to obtain an estimation of the active depth. While the active depth is expected to be approximately constant across the sensor, it can be determined independently by investigating angle dependence of the cluster sizes in column and row direction for different rotation orientations. This represents a simplified model, which neglects possible sub-threshold losses as well as lateral diffusion. While lateral diffusion can increase the mean cluster size, sub-threshold losses may lead to a reduction of the measured cluster size. As shown in Section 11.3.2, the cluster size is strongly dominated by single-pixel clusters, implying that lateral diffusion plays a minor role for the 200 Ωcm sample.

For the results presented in this section, sample w23s22 with a substrate resistivity of 200 Ωcm and a thickness of 100 µm was operated at a bias voltage of -90 V and a detection threshold of 850 mV $\approx 760\,e^-$.

The rotation directions are displayed in Figure 11.46. In order to have enough clearance for a rotation of the DUT including its chip board within the telescope, the spacing of the telescope planes needed to be widened up. In consequence, the track pointing resolution is reduced to (4.32 ± 0.25) µm and (5.38 ± 0.32) µm for rotation in column and row direction, respectively, as determined in Section 9.2 (see Table 9.3).

Region-of-Interest

As discussed in Section 8.2.2, line cross-talk can lead to increased cluster sizes in the row direction. In order to avoid a bias on the analysis results in this section, a region-of-interest is defined to exclude rows above 300.

On the other hand, a bias towards smaller cluster sizes is possible, if a particle does not penetrate the full active depth of the sensor as illustrated in Figure 11.47. For this to occur, the maximal distance from the sensor edge for a given angle and active depth is given by $d_{\text{active}} \cdot \tan(\alpha_{\text{max}})$. Measurements were performed at rotation

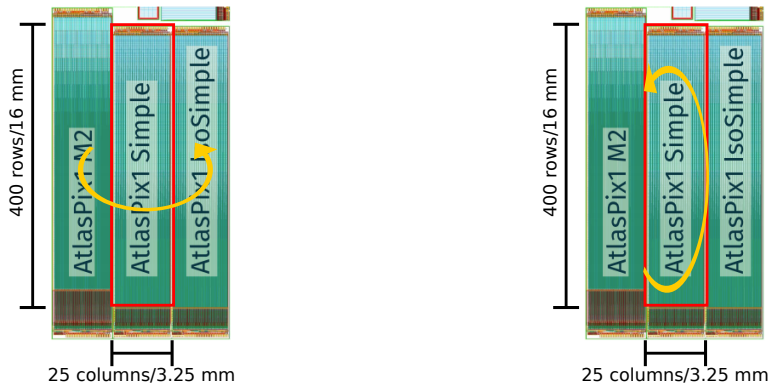

(a) Rotation parallel to the local y-axis, in "column direction".

(b) Rotation parallel to the local x-axis, in "row direction".

Figure 11.46: Schematic drawing of the rotation orientations. From [73] (modified).

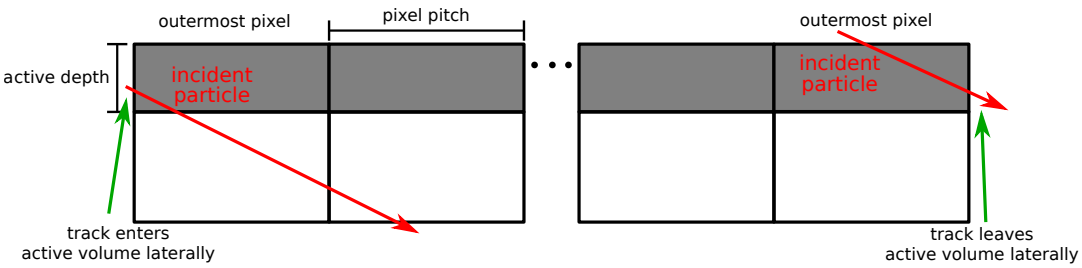

Figure 11.47: Illustration of a bias towards smaller measured cluster sizes for particles penetrating the sensor close to its edge and not traversing the total depth of the sensitive volume.

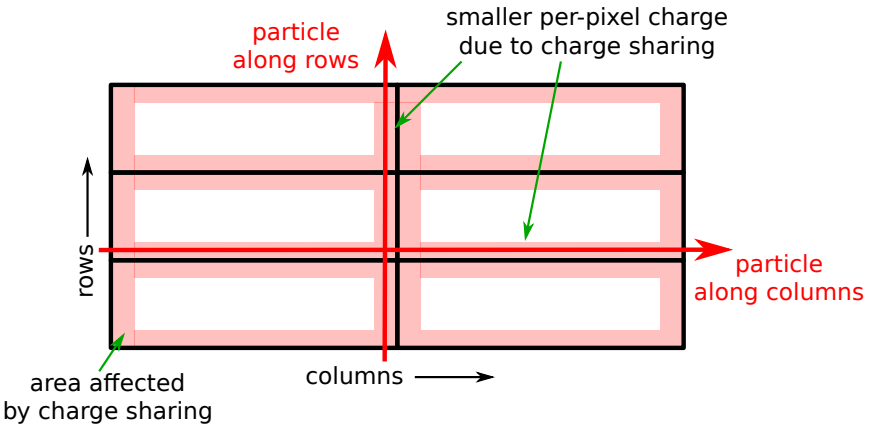

Figure 11.48: Illustration of a possible bias towards smaller measured cluster sizes due sub-threshold losses from charge sharing. In the row direction, this effect is more pronounced because less charge is deposited per pixel at shallow incidence angles due to the smaller pixel dimension.

angles $\leq 80^\circ$ and an upper limit on the active depth is given by the silicon substrate thickness of $\sim$85 µm.[4] Consequently, a distance to the sensor edge of $85\,\mu\text{m} \cdot \tan(80^\circ)$ corresponding to $\lesssim 4$ columns and $\lesssim 13$ rows is excluded from either edge of the sensor. This results in a ROI spanning column 4 to 20 and row 13 to 286.[5]

In addition, if a particle traverses the sensor close to a pixel edge, the per-pixel charge can be reduced by charge sharing as illustrated in Figure 11.48. From geometrical considerations, this effect is expected to impact the cluster width in the row direction stronger than in the column direction because less charge is deposited per pixel, which increases sub-threshold losses. To minimise this effect, an in-pixel region-of-interest is defined to exclude tracks from the analysis, which are reconstructed close to the pixel edges. In the column direction, tracks with an intercept point closer than 5 µm towards the row edges are excluded. In the row direction, a cut of 30 µm towards the column edges is applied. A larger cut is chosen because the row direction is expected to be affected stronger by sub-threshold losses.

[4] From the total chip thickness of 100 µm, approximately $\sim$15 µm need to be subtracted for the metal stack (see Section 6.2).

[5] To avoid a track entering the area sensitive to cross-talk, rows above $(299 - 13) = 286$ are excluded.

11.7.1 Extracted Active Depth from Mean Cluster Size

Figure 11.49 shows the mean cluster widths in column and row direction, respectively, plotted against the tangent of the rotation angle. As expected, the mean cluster width increases with larger rotation angle. Generally, larger cluster widths are observed in the row direction as expected from the smaller pixel pitch.

A saturation of the mean cluster size as observed for large angles in the row direction (see Figure 11.49b) arises from a limited rate capability of the column drain readout scheme (see Section 5.2.2). This limitation does not exist in the column direction.

Using equation 11.2, the active depth can be retrieved from the slope of a linear fit by dividing it by the pixel pitch in the respective dimension. At a bias voltage of $-90\,\mathrm{V}$, this yields an estimation for the active depth of $(60.8 \pm 1.9)\,\mu\mathrm{m}$ in the column direction and $(55.2 \pm 1.3)\,\mu\mathrm{m}$ in the row direction. The quoted uncertainties are the statistical errors on the fit. Systematic uncertainties are discussed below.

Systematic Uncertainties

The *Physikalische Instrumente M-060* precision rotation stage used in the experimental setup has a precision well below 0.001° [177]. Thus, it can be assumed that the difference between two rotational alignments is very precise. On the other hand, the analysis is sensitive to a global offset on the angle. E.g. adding an offset of $\pm 0.5°$ to each angle results in a change of the extracted depletion depth by $\sim \pm 2.5\,\mu\mathrm{m}$ in the column direction and $\sim \pm 1.3\,\mu\mathrm{m}$ in the row direction. During the rotation of the DUT with respect to the beam, a certain amount of mechanical stress on the cables and connectors of the Caribou system could not be avoid. This caused a slight deformation of the chip board supporting the ATLASpix, which may have led to a small non-uniformity of the incidence angle across the area of the ATLASpix and could

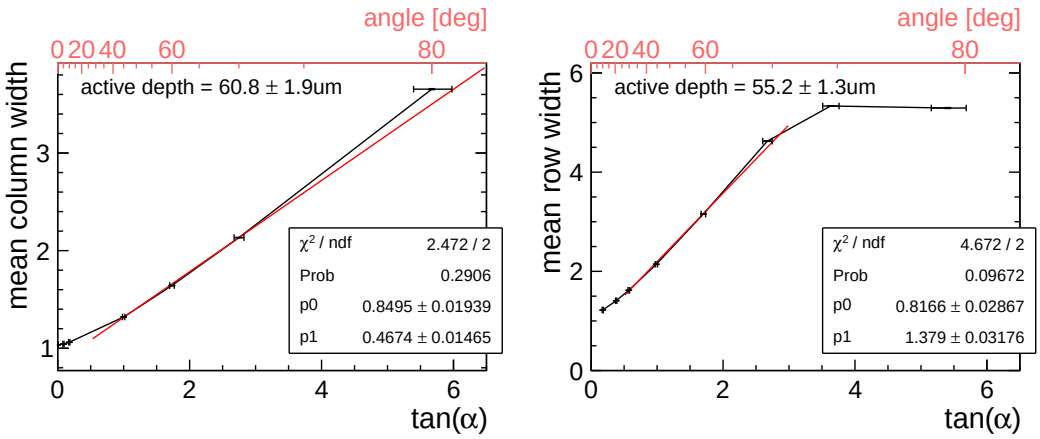

(a) Rotation in column direction.

(b) Rotation in row direction.

Figure 11.49: Angle dependence of the mean cluster size in column and row direction with a linear fit to extract the depletion depth using Equation 3.12.

affect the measurement in the row direction more due to the larger dimension of the chip board as well as the pixel matrix in this direction.

Taking the systematic effects into accout, the measurements in column and row direction are consistent within the uncertainties and lead to an estimated depletion depth of $(58 \pm 1.6_{\text{stat.}} \pm 1.9_{\text{syst.}})\mu\text{m}$.

11.7.2 Estimation of the Substrate Resistivity

The depletion depth for an ideal pn-junction at a given bias voltage can be calculated using Equation 3.15. Figure 11.50 shows the expected depletion depth for different bias voltages and substrate resistivities as obtained with Equation 3.15. Table 11.6 summarises the values obtained for different substrate resistivities at a bias voltage of $-90\,\text{V}$.

Table 11.6: Calculation of the depletion depth for different substrate resistivities at a bias voltage of $-90\,\text{V}$ using Equation 3.15. The hole mobility in the shown resistivity range is $424\,\text{cm}^2/\text{Vs}$ [53].

Substrate Resistivity [Ωcm]	Depletion Depth [µm]
200	40
300	49
400	57

Under the assumption that charge collection via diffusion is negligible at high bias voltages, the comparison with the active depth of 55-61 µm extracted from the analysis of inclined tracks suggests that the substrate resistivity lies around 400 Ωcm compared to the nominal value of 200 Ωcm. A possible range of 100-400 Ωcm is stated by the manufacturer due to deviations of the production parameters from the standard process [73].

It should be noted that the electric field configuration and the development of the depletion region is more complex than in this model for an ideal pn-junction.

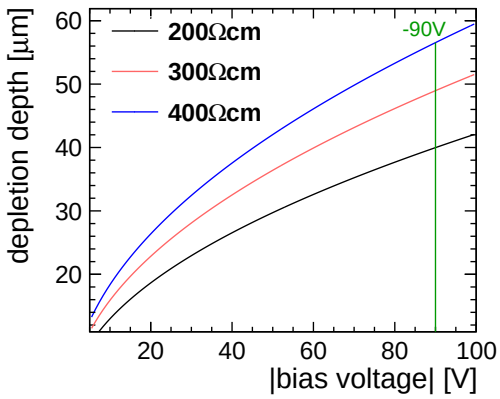

Figure 11.50: Calculation of the depletion depth for different bias voltages and substrate resistivities using Equation 3.15. The hole mobility in the shown resistivity range is $424\,\text{cm}^2/\text{Vs}$ [53].

However, preliminary TCAD simulations suggest a good agreement with this simplified model due to the large collection electrode of the ATLASpix and a uniform development of the depletion region for sensors with backside biasing [163].

11.7.3 Comparison with the Charge Calibration of the ToT

The previous measurement does not involve a calibration of the threshold or the ToT measurement. Hence, the depletion depth can be determined in an independent way via the charge calibration of the ToT measurement. Equation 3.3 (see Section 3.1.2) yields the most probable charge deposition by a traversing ionising particle in silicon with certain thickness. Therefore, its inverse function yields an estimation on the depletion depth for a given MPV under the assumption that charge collection via diffusion is negligible at high bias voltages.

For sample w23s22, which is used for the determination of the depletion depth based on the row dependence of the cluster size presented above, no laboratory measurements are available. In addition, large sample-to-sample variations are observed during the charge calibration with monoenergetic X-rays as discussed in Section 10.4. Furthermore, the previous results are obtained at a bias voltage of $-90\,\mathrm{V}$ while the charge calibration was performed at $-50\,\mathrm{V}$. This would result in systematic uncertainties, which cannot easily be quantified.

Instead, sample w23s11 is used in the following, for which data recorded at DESY and X-ray calibration measurements are available at the same operating conditions of $860\,\mathrm{mV} \approx 850\,\mathrm{e}^-$ and a bias voltage of $-50\,\mathrm{V}$.

Figure 11.51 shows the measured ToT spectrum within the region-of-interest defined in Section 11.6.1 and rescaled such that each row contributes with the same weight. A convolution of a Landau with a Gaussian is fitted to the spectrum to obtain an estimation on the MPV. As discussed in Section 11.3.5, the row dependence of the ToT leads to a deviation from the Landau-Gaussian shape. In order to estimate

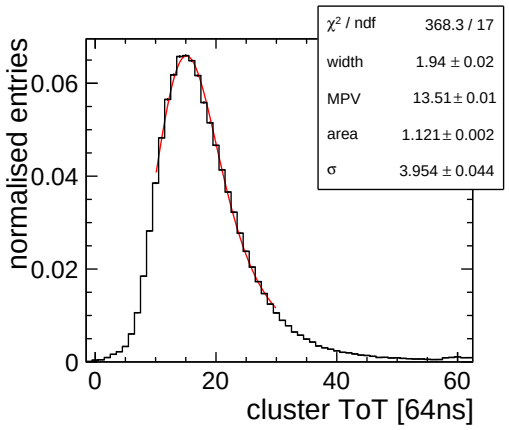

Figure 11.51: Cluster ToT spectrum for sample w23s11 obtained at DESY at a threshold of $860\,\mathrm{mV} \approx 850\,\mathrm{e}^-$ and a bias voltage of $-50\,\mathrm{V}$ within the ROI defined in Section 11.6.1. The spectrum is fitted with a convolution of a Landau with a Gaussian.

the systematic uncertainties, the fit range is varied by ±5 ToT values. An MPV of 13.5 ± 0.1 is obtained.

For the calibration of the ToT it is important to apply the same ROI and rescaling to the data used for the calibration. Figure 11.52 shows the MPV of the cluster ToT obtained with the monoenergetic X-ray measurements presented in Section 10.4 within the aforementioned ROI. It is seen that an MPV of ~ 13.5 lies above the range covered by the calibration. A straight line (shown in red) is fitted to extrapolate the calibration to a ToT value of 13.5. In order to estimate the systematic uncertainties arising from the non-linear behaviour, two further straight lines are fitted to the lower two and the upper two data points as shown in blue and green, respectively. This results in an estimated deposited charge of $(2700 \pm 140)\,\mathrm{e}^-$. Applying the inverse of Equation 3.3 yields an approximate depletion depth of $(42 \pm 2)\,\mu\mathrm{m}$ at a bias voltage of $-50\,\mathrm{V}$.

In order to compare this with the result obtained from the angle dependence of the cluster size in Section 11.7.1, it can be rescaled to $-90\,\mathrm{V}$ using Equation 3.15:

$$W(-90\,\mathrm{V}) \approx \sqrt{\frac{90\,\mathrm{V}}{50\,\mathrm{V}}} \cdot W(-50\,\mathrm{V}) \approx (57 \pm 2)\,\mu\mathrm{m}. \tag{11.3}$$

The two results stemming from independent measurements are consistent within the estimated uncertainties, which supports the conclusion that the actual substrate resistivity lies around 400 Ωcm compared to the nominal 200 Ωcm.

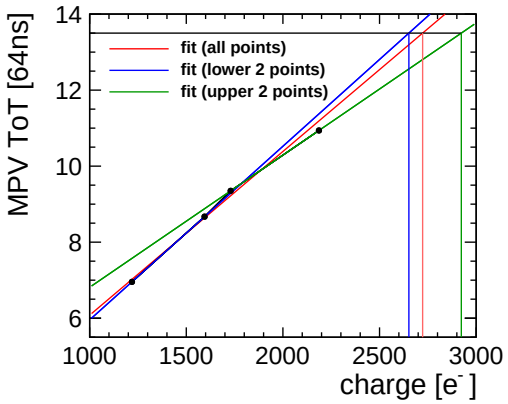

Figure 11.52: MPV of the cluster ToT spectrum obtained with monoenergetic X-rays as discussed in Section 10.4 for sample w23s11 at a threshold of $860\,\mathrm{mV} \approx 850\,\mathrm{e}^-$ and a bias voltage of $-50\,\mathrm{V}$ within the ROI defined in Section 11.6.1. Three linear fit functions are used to estimate the deposited charge needed for an MPV of the ToT of ~ 13.5 as obtained from the fit in Figure 11.51.

Chapter 12

Conclusions

The search for physics beyond the Standard Model is one of the biggest challenges of today's particle physics. It motivates future particle accelerator-based high-precision experiments at the energy frontier.

The Compact Linear Collider (CLIC) is a proposed high-energy high-luminosity e^+e^- collider allowing for precision measurements of Standard Model physics and providing unique sensitivity for new physics scenarios. The foreseen physics goals and operating conditions pose challenging demands on the performance of all detector subsystems. An all-silicon tracking detector meeting these requirements is under development.

The ATLASpix high-voltage monolithic active pixel sensor (HV-MAPS) prototype was designed to demonstrate the suitability of the technology for the ATLAS Inner Tracker Upgrade and the CLIC tracking detector. The chip features a pixel pitch of $130 \times 40\,\mu m^2$ and an active area of $3.25 \times 16.0\,mm^2$. Within the scope of this thesis, the performance of the ATLASpix_Simple was characterised in order to contribute to the understanding of the benefits and limitations of the sensor and evaluate it with respect to the requirements of the CLIC tracking detector.

The detailed characterisation of a pixel sensor prototype requires a precise understanding of the reference measurement. Hence, the performance of the reference telescopes used during test-beam measurements at the SPS and at DESY was characterised and the track time resolution was determined. It was shown that the CLICdp Timepix3 telescope at the SPS reaches a track time resolution of $\sim$560 ps. For the EUDET-type telescopes at DESY, the precision of the recorded trigger timestamp from the AIDA TLU was improved from $\sim$7 ns to $\sim$500 ps. With the usage of a Timepix3 timing reference plane in the telescope, an unambiguous track time resolution of $\sim$1.1 ns is achieved. In addition, the reconstruction and analysis framework Corryvreckan was significantly extended and adapted to the needs of the analysis.

The characterisation of the ATLASpix_Simple comprised extensive laboratory and test-beam measurements: in laboratory measurements, sensor performance parameters were studied for ATLASpix_Simple samples with different substrate resistivities of 20 Ωcm, 80 Ωcm and 200 Ωcm. The temperature dependence of the reverse bias leakage current was measured and the breakdown behaviour was investigated

as a function of the temperature. It was found that instead of showing an abrupt avalanche breakdown, the leakage current increases in a smooth and continuous way. The leakage current remains below 0.1 µA up to −60 V for a 200 Ωcm sample at room temperature, while lower substrate resistivities show an earlier increase. The 200 Ωcm samples can be operated up to −90 V until the leakage current causes a strong increase in the noise rate.

A power consumption of ∼190 mW corresponding to ∼370 mW/cm^2 was measured with the used chip settings. The noise rate on the sensor is dominated by a few noisy pixels and large variations occur between sensors. At an average noise rate on the full chip of 3×10^5 Hz, a saturation of the readout is observed, which is a consequence of the architecture of the column drain readout scheme. Pixel masking or a threshold equalisation was not possible with the ATLASpix_Simple due to unintended design features.

The signal gain was determined to be ∼115 mV/1000e$^-$ using X-rays with multiple energies. Sensor-to-sensor fluctuations were found to be larger than a possible influence of the sensor capacitance due to different substrate resistivities. It was seen that the effective baseline lies around 35 mV below the externally applied baseline due to a voltage offset in the comparator. This corresponds to ∼300 e$^-$. In addition, a row dependence in the signal gain was observed during X-ray calibration measurements. A threshold dispersion of 100 e$^-$, a pixel noise of ∼120 e$^-$ and a signal-to-noise ratio of ≥ 12 were measured at the energy of an Fe-55 signal source. Furthermore, a charge calibration of the time-over-threshold measurement was performed.

Extensive test-beam studies were carried out with data recorded in several measurement campaigns at the SPS and DESY test-beam facilities. The cluster formation was studied and it was seen that single-pixel clusters occur predominantly, while multi-pixel clusters due to charge sharing only occur close to the pixel edges and corners. In addition, cross-talk between the transmission lines connecting the pixels in the active matrix with the readout cells in the periphery leads to increased cluster sizes at row 301 and for rows larger than 390.

Due to abundance of single-pixel clusters, the achieved spatial resolution of approximately 37.1 µm and 11.7 µm in column and row direction is close to the binary resolution limited by the pixel pitch.

A hit detection efficiency above 99.99 % was measured at a threshold of ∼670 e$^-$ and a bias voltage of −75 V for a 200 Ωcm sample. At low thresholds, a significantly increasing noise rate causes a saturation of the readout leading to a reduced measured efficiency. At the lowest thresholds small inefficiencies occur in the pixel corners due to sub-threshold losses. These become more pronounced at high thresholds and/or low bias voltages. While the efficiency increases with higher bias voltages due to a reduction of the losses in the pixel corners, even at −5 V, an efficiency above 97 % was measured for the 200 Ωcm sample. Lower substrate resistivities lead to a

smaller efficiency due to a smaller depleted region and thus a smaller signal at a given bias voltage. In addition, it was observed that the non-uniformity of the signal gain leads to a row dependence of the mean cluster size and the hit detection efficiency.

The time resolution was investigated and it was shown that it is affected strongly by a row-dependent delay arising from an increasing capacitance of the signal transmission lines between the active pixels and the periphery. Before corrections, a time resolution of $\sim$11.4 ns was determined. A row-dependent delay and a timewalk correction based on the time-over-threshold measurements of the ATLASpix_Simple lead to a significant improvement such that 6.8 ns was achieved for a 200 Ωcm. The time resolution of the lower substrate resistivities is significantly worse and timewalk is much more pronounced.

The active depth of the ATLASpix_Simple was determined using inclined tracks and a charge calibration of the time-over-threshold measurement. At a bias voltage of -90 V, it amounts to 55-61 µm for a substrate resistivity of 200 Ωcm. The comparison with the expected depletion depth for a pn-junction with the respective doping concentrations suggests that the substrate resistivity lies around 400 Ωcm compared to the nominal 200 Ωcm, which is consistent with the possible range specified by the manufacturer. This finding is in agreement with preliminary TCAD simulations [163].

Table 12.1 summarises the obtained ATLASpix_Simple performance parameters and compares them with the requirements for the CLIC tracking detector. It shows that most requirements are fulfilled. In order to meet the required spatial resolution of

Table 12.1: Comparison of the ATLASpix_Simple performance with the requirements for CLIC tracking detector.

	CLIC Tracker Requirements	**ATLASpix _Simple Performance**
Spatial resolution (transversal)	7 µm (pitch if binary: 25 µm)	$\sim$11.7 µm (pitch: 40 µm)
Granularity (longitudinal)	1-10 mm (pixel size)	130 µm
Time resolution	5 ns	$\sim$6.7 ns
Hit detection efficiency	$99.7 - 99.9$ %	>99.99 %
Material budget per layer	$1 - 2$ % X_0 (incl. mechanical support)	$\sim$1 % X_0 (incl. PCB)
Power Consumption	< 150 mW/cm^2	370 mW/cm^2 (without power pulsing)
Radiation hardness NIEL TID	 <1×10^{11} n_{eq}/cm^2/year <300 Gy/year	 >1×10^{15} n_{eq}/cm^2 [51] >4.8×10^5 Gy [51]

the CLIC tracking detector, a modified pixel geometry with a pitch of $\leq$25 µm in row direction is required. The power consumption exceeds the design limit of the cooling system for the CLIC tracking detector. The comparison with other studies using the same sensor [51, 75] suggests that an optimisation of chip settings can lead to a significant reduction by ∼25 %, while similar sensors with a larger active matrix show a reduced power consumption by ∼50 % [175]. In the context of CLIC, a further reduction of the average power consumption could be achieved by power pulsing. With a finer binning of the hit timestamp of 8 ns instead of 16 ns, a resolution of 5 ns could be achieved. While the radiation tolerance of the ATLASpix_Simple was not investigated within the scope of this thesis, other studies have shown that it suffices the requirements of the CLIC tracking detector [51].

The successful operation and promising results obtained with the ATLASpix_ Simple has led to the design and manufacturing of several further HV-MAPS prototypes for different applications:

The ATLASpix2 [76, 178] and ATLASpix3 [172] were designed to target specifically to the ATLAS Inner Tracker Phase II Upgrade [179]. The ATLASpix3 was investigated in [173, 174, 175]. With the ATLASpix3, it was demonstrated that an optimisation of the routing and a per-pixel delay tuning significantly reduces the row dependent delay [173]. It reaches a time resolution of ∼3.7 ns and an efficiency above 99.7 % [174].

In an engineering run called *Run2020* [171], a variety of new HV-MAPS sensors was produced based on the design of the ATLASpix_Simple and the ATLASpix3. They feature different amplifier and comparator implementations for a direct performance comparison, and have pixel sizes between 165 × 25 µm^2 to 165 × 100 µm^2. They are investigated at the time of writing with respect to their suitability for an upgrade of the tracking system of the LHCb experiment [163, 180], and the use in future test-beam telescopes [181, 182]. The smallest pixel size is also targeting the requirements of the CLIC tracking detector. With a modified pixel geometry of 165 × 25 µm compared to 130 × 40 µm of the ATLASpix_Simple, it is expected to yield the required spatial resolution of ∼7 µm. The enlargement of the pixel size in the other direction is still in line with the requirements of the CLIC tracker, which only requires pixels with a length $<$1 mm. With a timestamp binning of 8 ns in combination with an improved routing scheme, this sensor is expected to meet all of requirements of the CLIC tracking detector.

The work presented in this thesis has contributed to a more detailed understanding of the benefits and limitations of an HV-MAPS prototype, and the presented findings have helped to optimise the design of new prototypes. The comparison of the different substrate resistivities has shown a significant performance gain for the 200 Ωcm sample. In future submissions a potential performance gain with even higher substrate resistivities could be explored. The column drain readout scheme

runs into limitations for larger occupancies. While a threshold equalisation and pixel masking allow for a reduction of the readout occupancy caused by noise hits, further studies are needed to investigate the possible limitation if large clusters occur due to tracks with shallow incidence angles or at higher particle rates. The observed row dependence of the timing caused by the line capacitances can be mitigated by an optimised routing scheme and a per-pixel delay tuning as demonstrated with the ATLASpix3 [173]. The row dependence of the signal gain arising from a non-uniform power distribution across the matrix is expected to become more severe for larger sensor areas. It shows the relevance of studying the uniformity of performance parameters across the pixel matrix. Simulation-based design verifications would help to identify and avoid similar issues during the design phase of new prototypes.

Furthermore, the achieved improvement of reference time measurement with the EUDET-type telescopes at DESY will allow investigating new prototypes with faster time resolutions. The Corryvreckan reconstruction and analysis framework was extended and improved significantly, and has a growing number of users. It is used for the test-beam characterisation of the aforementioned new prototypes.

In conclusion, it was shown that high-voltage monolithic active pixel sensors represent an attractive technology for many applications in future HEP experiments and beyond. They combine a high efficiency, good time resolution and high radiation tolerance with a low material budget due to the monolithic architecture. Multiple new prototypes based on the design of the ATLASpix_Simple were developed for a variety of applications ranging from the tracking detectors of the upgraded LHCb experiment and CLIC to the development of new test-beam telescopes. They are being investigated at the time of writing, and the following generation of HV-MAPS is in preparation.

Appendix A

Default Sensor Configurations

The following settings have been used for all measurements presented in this thesis unless otherwise stated.

Table A.1: Default configuration settings.

DAC Name/ Configuration bit	Value [dec]
BLResPix	40
ThResPix	0
VNPix	40
VNFBPix	20
VNFollPix	30
VNRegCasc	20
VDel	63
VPComp	20
VPDAC	10
VNPix2	0
BLResDig	63
VNBiasPix	0
VPLoadPix	5
VNOutPix	5
VPVCO	15
VNVCO	5
VPDelDclMux	30
VNDelDclMux	30
VPDelDcl	30
VNDelDcl	30
VPDelPreEmp	30
VNDelPreEmp	30
VPDcl	50
VNDcl	20
VNLVDS	63
VNLVDSDel	10
VPPump	5

DAC Name/ Configuration bit	Value [dec]
RO_res_n	1
Ser_res_n	1
Aur_res_n	1
sendcnt	0
resetckdivend	0
maxcycend	63
slowdownend	0
timerend	9
ckdivend2	7/15
ckdivend	0
VPRegCasc	20
VPRamp	10
VNcompPix	15
VPFoll	10
VNDACPix	0
VPBiasRec	63
VNBiasRec	2
Invert	0
SelEx	1
SelSlow	0
EnPLL	1
TriggerDelay	0
Reset	0
ConnRes	1
SelTest	0
SelTestOut	0

Appendix B

Corryvreckan Configurations

The following configurations have been used for all measurements presented in this thesis unless otherwise stated.

B.1 SPS Test-beam Analysis

```
[Corryvreckan]
log_level = INFO

detectors_file = "geometries/Alignment_November2018.geo"
histogram_file = "output.root"

[Metronome]
event_length = 20us

[EventLoaderTimepix3]
input_directory = "/path/to/data"

[EventLoaderATLASpix]
input_directory = "/path/to/data/atlaspix_data"
clock_cycle = 8ns
clkdivend2 = 15

[Clustering4D]
time_cut_abs = 300ns
use_earliest_pixel = true

[Clustering4D]
type = "ATLASpix"
time_cut_abs = 200ns
charge_weighting = false
use_earliest_pixel = true

[Correlations]
make_correlations=true
time_cut_abs = 20us
time_binning = 1.5625ns
```

```
[Tracking4D]
min_hits_on_track = 6
time_cut_abs = 10ns
spatial_cut_abs = 200um, 200um
exclude_dut = true
get_correlations = true
unique_cluster_usage = true

[DUTAssociation]
time_cut_abs = 200ns
spatial_cut_abs = 300um, 150um

[AnalysisDUT]
time_cut_frameedge = 200ns
n_time_bins = 1600
time_binning = 0.5ns
correlations = true

[AnalysisEfficiency]
time_cut_frameedge = 200ns
inpixel_bin_size = 1.0um
inpixel_cut_edge = 10um,10um

[AnalysisTimingATLASpix]
n_time_bins = 1600
time_binning = 0.5ns
time_cut_frameedge = 200ns
calc_corrections = true
use_earliest_pixel = true
correction_file_row = /path/to/correction_file.root
correction_graph_row = "graph_row_correction"
correction_file_timewalk = /path/to/correction_file.root
correction_graph_timewalk = "graph_timewalk_correction"
```

B.2 DESY Test-beam Analysis

```
[Corryvreckan]
log_level = "WARNING"
log_format = "DEFAULT"

output_directory = "output"
detectors_file = "geometries/Alignment_July2019_w23s11.geo"
histogram_file = "output.root"

[EventDefinitionM26]
detector_event_time = "TLU"
detector_event_duration = "MIMOSA26"
file_timestamp = "/path/to/data_tlu"
file_duration = "/path/to/data_m26"
shift_triggers = 1

[EventLoaderEUDAQ2]
name = "TLU_0"
file_name = "path/to/data_tlu"

[EventLoaderEUDAQ2]
type = "MIMOSA26"
file_name = "/path/to/data_m26"
shift_triggers = 1

[EventLoaderATLASpix]
input_directory = "/path/to/data_atlaspix"
clock_cycle = 8ns
clkdivend2 = 7

[EventLoaderEUDAQ2]
name = "Timepix3_0"
buffer_depth = 1000
file_name = "/path/to/data_timepix3"
calibration_path_tot = "/path/to/calibration/W0005_E02_cal_tot.txt"
calibration_path_toa = "path/to/calibration/W0005_E02_cal_toa.txt
eudaq_loglevel = INFO

[ClusteringSpatial]
type = "Mimosa26"
use_trigger_timestamp = true

[Clustering4D]
type = "Timepix3"
time_cut_abs = 100ns
use_earliest_pixel = false
charge_weighting = true
```

```
[Clustering4D]
type = "ATLASpix"
time_cut_abs = 300ns
use_earliest_pixel = true
charge_weighting = false

[Correlations]
do_time_cut = true
time_cut_abs = 234.4us

[Tracking4D]
track_model = "gbl"
momentum = 5.4GeV
spatial_cut_abs = 200um, 200um
time_cut_abs = 230.4us
min_hits_on_track = 7
exclude_dut = true
require_detectors = "Timepix3_0"
timestamp_from = "Timepix3_0"

[DUTAssociation]
time_cut_abs = 300ns
spatial_cut_abs = 300um, 150um

[AnalysisDUT]
chi2ndof_cut = 3.
time_cut_frameedge = 300ns
n_time_bins = 1200
time_binning = 0.5ns
correlations = true

[AnalysisEfficiency]
chi2ndof_cut = 3.
time_cut_frameedge = 300ns
inpixel_bin_size = 1.0um, 1.0um

[AnalysisTimingATLASpix]
time_cut_abs = 300ns
chi2ndof_cut = 3.
calc_corrections = false
tot_bin_example = 20
inpixel_bin_size = 5.2um,1.6um
correction_file_row = "/path/to/correction_file"
correction_graph_row = "graph_row_correction"
correction_file_timewalk = "/path/to/correction_file"
correction_graph_timewalk = "graph_timewalk_correction"
```

Appendix C

Analysis of the CLICdp Timepix3 Telescope at the SPS

In this chapter, the origin of the two distinct populations observed in the in-cluster timing distribution shown in Figure 8.3 presented in Section 8.2.2 is investigated in more detail to validate the provided explanation for the occurrence of two distinct populations arising from different charge carrier drift times.

For the following analysis, one of the telescope planes is defined as the DUT in analogy to the analysis of the telescope timing performance presented in Section 9.1.2 (see Figure 9.1). The actual ATLASpix DUT is treated as a passive scatterer within the telescope. The results in this chapter are shown for Timepix3_1, i.e. the central plane of the upstream arm of the telescope (see Figure 7.2). The consistency of the results was tested by iteratively assigning each of the telescope planes as the DUT and repeating the analysis.

Rotation of the Telescope Planes

As described in Section 7.2, the telescope planes are rotated around the local x- and y-axes (column and row direction) by $\pm 9^\circ$ in order to increase the amount of charge sharing and thus improve the achievable spatial resolution [124]. Figure C.1 shows a schematic drawing of the layer stack of a Timepix3 assembly. It is seen that the frontside of the sensor, i.e. the side on which holes are collected for the signal generation faces the Timepix3 readout ASIC, which is mounted on a PCB.

Figure C.2 shows an illustration of the telescope planes indicating the orientation and rotation of each plane. All sensor planes are oriented with their sensor backside towards the DUT, meaning that the upstream planes are penetrated by the beam from the frontside towards the backside, and the downstream planes from the

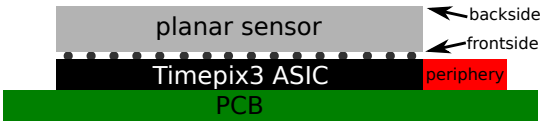

Figure C.1: Schematic illustration of the layer stack of a Timepix3 assembly (not to scale). The Timepix3 ASIC is glued to a PCB and bump-bonded to a planar p-in-n sensor. Holes are collected on the sensor frontside.

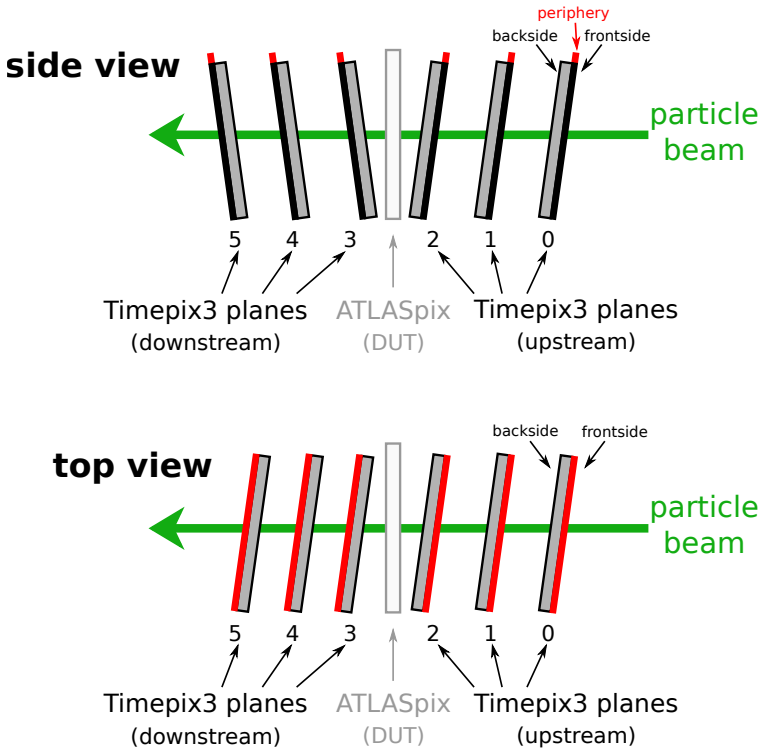

Figure C.2: Simplified schematic illustrating the rotation and orientation of the planes of the CLICdp Timepix3 telescope at the CERN SPS. Upstream planes are mounted such that the beam penetrates them from the backside. Downstream planes vice versa. All planes are mounted upside down, i.e. with the periphery towards the top.

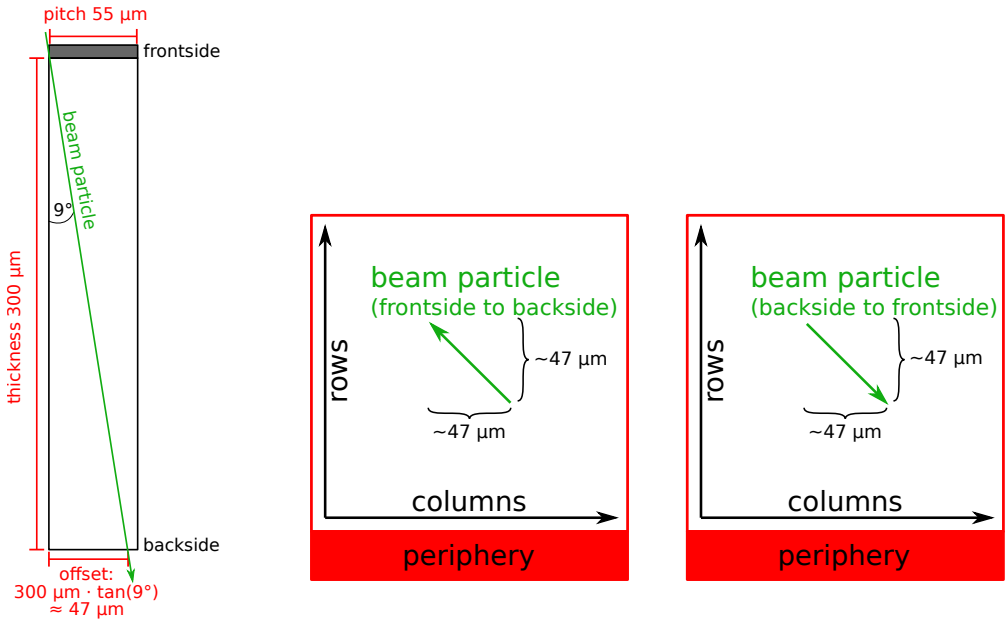

(a) Particles penetrate the sensor under an angle of ∼9°.

(b) Upstream planes are penetrated from the frontside to the backside (not to scale).

(c) Downstream planes are penetrated from the backside to the frontside (not to scale).

Figure C.3: Illustration of a particle traversing the telescope parallel to the beam axis. The rotation of the planes by ±9° around the local x- and y-axes leads to lateral components of the particle trajectory of ∼47 µm in x and y within the sensor planes.

backside towards the frontside. Due to mechanical constraints of the cabling, the sensors are mounted upside down such that the periphery (below row 0) is pointing upwards.

Due to the rotation of the planes, a particle traversing the telescope parallel to the beam axis travels a lateral distance of $300\,\mu\text{m} \cdot \tan(9^\circ) \approx 47\,\mu\text{m}$ within the sensor plane in both the local x- and y-direction as illustrated in Figure C.3. This fact is needed for the understanding of the results presented below.

In-pixel Cluster Size Distributions

Figure C.4 shows the in-pixel cluster size distributions for different cluster sizes. The plots are filled at the reconstructed incidence point of the track with the sensor projected into one pixel cell.

It can be seen that single-pixel clusters occur mostly when the track penetrates a pixel close to its centre. Two-pixel clusters occur predominantly when a particle penetrates a pixel close to the symmetry axes of the pixel in both column and row direction. Larger clusters occur along diagonal bands.

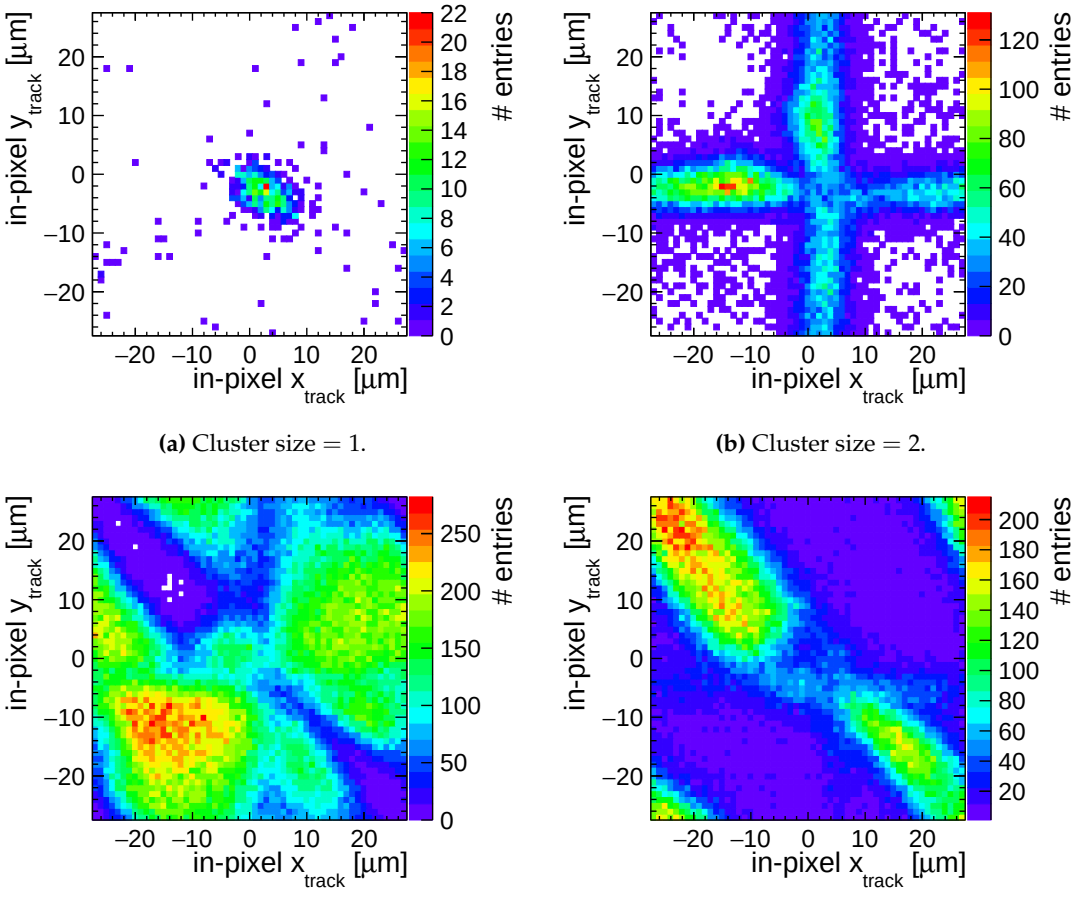

(a) Cluster size = 1.

(b) Cluster size = 2.

(c) Cluster size = 3.

(d) Cluster size = 4.

Figure C.4: In-pixel distribution for different cluster sizes on the Timepix3_2. The plots are filled at the track incidence point within a pixel cell.

These distributions can be understood through the illustrations shown in Figure C.5. For the different cluster sizes, they show the track incidence points and the projection of the particle trajectory through the sensor into the lateral plane. It is important to note that the reconstructed track incidence point is calculated at $1/2$ of the sensor thickness, not the frontside or the backside.

As seen above, single-pixel clusters only occur when a particle penetrates the sensor close to a pixel centre. For two-pixel clusters, four different cases are distinguished, in which particles penetrate two adjacent pixels in different configurations.

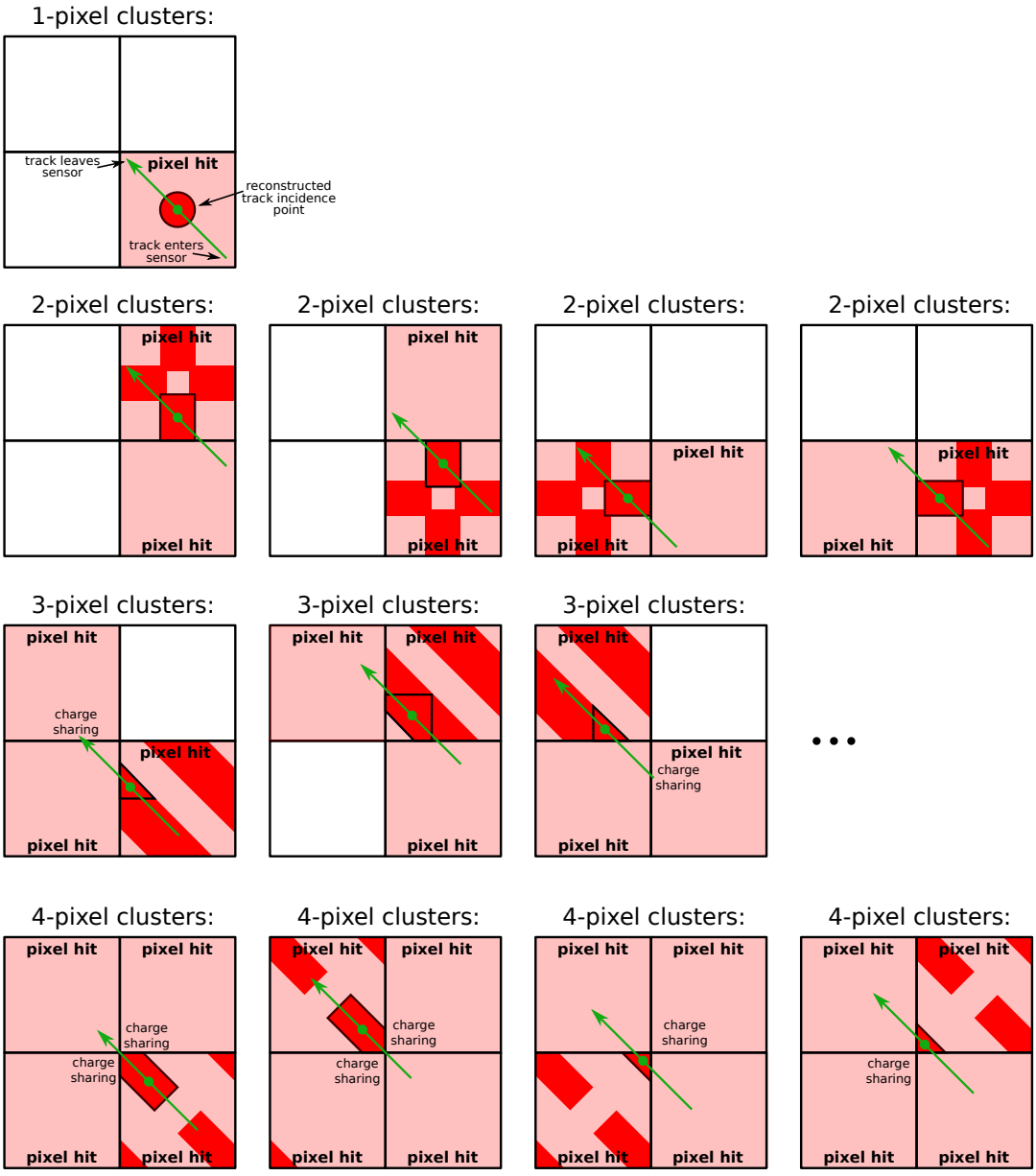

Figure C.5: Schematic drawing of a 4×4 pixel sub-matrix illustrating how different track incidence points within the pixel lead preferably to particular cluster sizes as seen in Figure C.4. The green arrow indicates the track penetrating a pixel at the round end and leaving the sensor at the pointy end.

Similarly, three-pixel clusters can occur when a particle traverses through three pixels directly, or through two adjacent pixels and one of the neighbouring pixel collects sufficient charge by diffusive charge sharing. Finally, four-pixel clusters can occur when a particle traverses multiple pixels and in addition, a sufficient amount of charge is shared into adjacent pixels by diffusion.

The distinct occurrence of two-pixel clusters along the symmetry axes of the pixel is used in the following to investigate the origin of the two populations within the in-cluster timing distribution discussed in Section 8.2.2 (see Figure 8.3).

In-Cluster Timing Distribution

In analogy to Figure 8.3 presented in Section 8.2.2, Figure C.6 shows the time difference between all secondary pixels within a cluster with respect to the seed pixel, i.e. the pixel with the largest ToT, plotted against the ToT value of the secondary pixels. The distributions are shown for all clusters (Figure C.6a) and separately for different cluster sizes (Figures C.6b, C.6c, C.6d). In all cases, the effect of timewalk is clearly seen in that pixels with a smaller ToT correlate with a larger ("later") timestamp with respect to the seed pixel. It can also be observed that the two distinct populations occur in all cases, whereas they are most clearly separated for two-pixel clusters (see Figure C.6b).

As stated previously, entries on the left side of the y-axis indicate that the secondary pixel has an earlier timestamp than the seed pixel, which shows that the pixel with the largest signal is not always the pixel with the earliest timestamp as would be expected from timewalk (see Section 4.1).

The reason for this becomes clear in Figure C.7. Figures C.7a, C.7d, C.7g, C.7j show the in-pixel distributions for two-pixel clusters with different arrangements of seed pixel and secondary pixel, i.e. the seed pixel above, below, left, and right of the secondary pixel. It is seen that the arrangement of seed with respect to the secondary pixel of the cluster correlates with different track incidence points within the pixel. The corresponding illustrations of the track incidence points in Figures C.7b, C.7e, C.7h and C.7k show in which cases the particle penetrates the seed pixel closer towards the frontside or the backside, respectively.

In Figures C.7c, C.7f, C.7i and C.7l, the corresponding in-cluster timing distributions are shown. It confirms the explanation that the left population corresponds to the case where charge is deposited towards the backside of the seed pixel and the frontside of the secondary pixel leading to a slower charge collection in the seed pixel despite the larger total charge deposition, and vice versa.

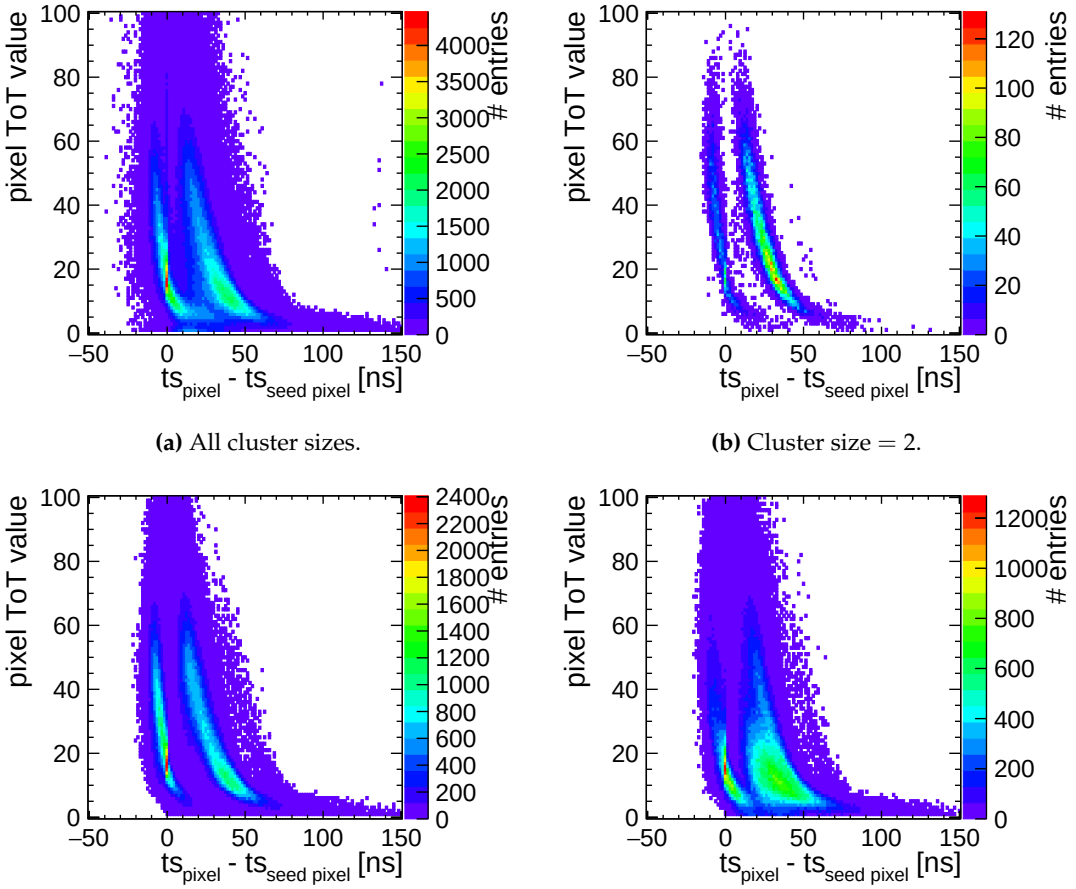

(a) All cluster sizes.

(b) Cluster size = 2.

(c) Cluster size = 3.

(d) Cluster size = 4.

Figure C.6: Time difference between seed pixel and other pixels within a cluster on the Timepix3_02 plane of the CLICdp Timepix3 telescope at the CERN SPS.

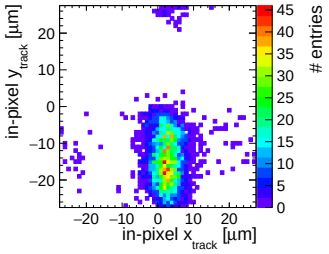

(a) In-pixel track incidence point if seed pixel above second pixel.

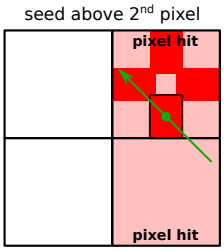

(b) Illustration of track incidence point, seed pixel above second pixel.

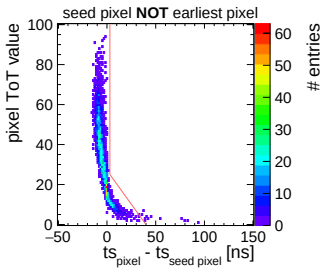

(c) In-cluster timing distribution, seed pixel above second pixel.

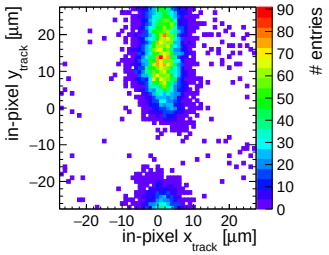

(d) In-pixel track incidence point if seed pixel below second pixel.

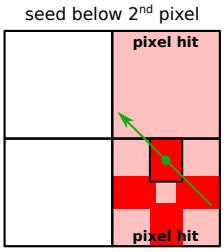

(e) Illustration of track incidence point, seed pixel below second pixel.

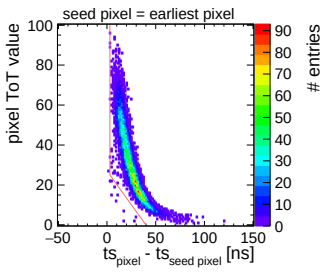

(f) In-cluster timing distribution, seed pixel below second pixel.

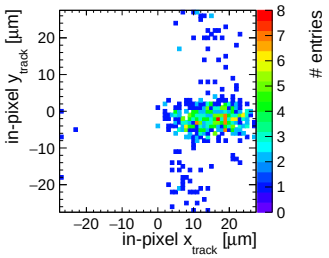

(g) In-pixel track incidence point if seed pixel left of second pixel.

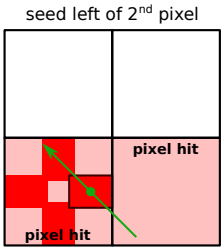

(h) Illustration of track incidence point, seed pixel left of second pixel.

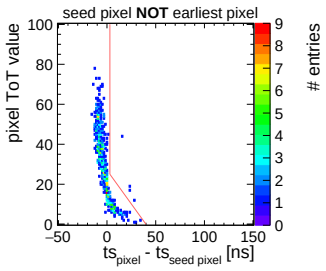

(i) In-cluster timing distribution, seed pixel left of second pixel.

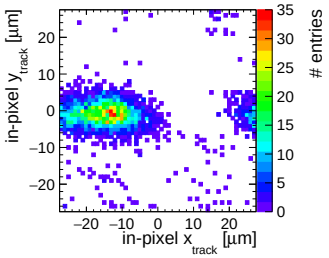

(j) In-pixel track incidence point if seed pixel right of second pixel.

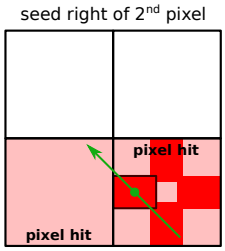

(k) Illustration of track incidence point, seed pixel right of second pixel.

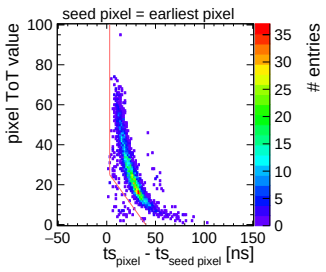

(l) In-cluster timing distribution, seed pixel right of second pixel.

Figure C.7: In-pixel track incidence point, illustration and in-cluster timing distributions for Timepix3_02 for cluster size = 2 for different configurations of seed pixel and secondary pixel. The red line in (c), (f) and (l) is identical in all cases and shows the clear distinction of the two populations.

List of Publications

Parts of the ideas and work presented in this thesis have appeared previously in the following list of journal articles and conference proceedings.

2021/06 **Performance Studies of the ATLASpix HV-MAPS Prototype for Different Substrate Resistivities**
J. Kröger (submitted to JPS Conf. Proc.), CLICdp-Conf-2021-004, https://cds.cern.ch/record/2773952
Main author

2021/05 **Test-beam characterisation of the CLICTD technology demonstrator - A small collection electrode high-resistivity CMOS pixel sensor with simultaneous time and energy measurement**
R. Ballabriga et al., Nucl. Instrum. Meth. A 1006, p. 165396
Co-author, contributions to data acquisition and analysis framework

2020/11 **Corryvreckan: A Modular 4D Track Reconstruction and Analysis Software for Test Beam Data**
D. Dannheim et al. 2021 JINST 16 P03008
Co-author, development, maintenance and documentation of software project

2020/11 **Efficient Analysis of Test-beam Data with the Corryvreckan Framework**
J. Kröger, L. Huth, Proceedings of the 29th International Workshop on Vertex Detectors (VERTEX2020), 10.7566/JPSCP.34.010024, arXiv:2011.09205 [phyics.ins-det]
Main author

2020/10 **Design and Characterization of the CLICTD Pixelated Monolithic Sensor Chip**
I. Kremastiotis et al., IEEE Transactions on Nuclear Science, vol. 67, no. 10, 2263–2272
Co-author, contributions to data acquisition and analysis framework

2020/05 **Silicon Pixel R&D for the CLIC Tracking Detector**
J. Kröger, JINST 15 C08005
Main author

2020/01 **MuPix and ATLASPix – Architectures and Results**
A. Schöning et al., PoS Vertex2019 024
Co-author, contributions to data acquisition and analysis

2019/12 **User Manual for the Corryvreckan Test Beam Data Reconstruction Framework, Version 1.0**
J. Kröger et al., arXiv:1912.00856 [physics.ins-det]
Co-author, major contributions to project documentation

2019/05 **Detector Technologies for CLIC**
D. Dannheim et al., eds., CERN Yellow Reports: Monograph 10.23731/CYRM-2019-001
Co-author, contributions to data acquisition and analysis

2018/10 **Irradiation study of a fully monolithic HV-CMOS pixel sensor design in AMS 180 nm**
H. Augustin et al., Nucl. Instrum. Meth. A905, 53–60
Co-author, contributions to data acquisition and analysis

2018/07 **MuPix8 – A large-area HV-MAPS chip**
H. Augustin et al., PoS Vertex2017 057
Co-author, contributions to data acquisition and analysis

Bibliography

[1] F. Dyson. *Imagined Worlds*. The Jerusalem-Harvard Lectures. Harvard University Press, 1998. URL: https://www.hup.harvard.edu/catalog.php?isbn=9780674539099.

[2] CERN. *The Large Electron-Positron Collider*. [Online; Last accessed Sunday 8th August, 2021]. URL: https://home.cern/science/accelerators/large-electron-positron-collider.

[3] G. Aad et al. "Observation of a new particle in the search for the Standard Model Higgs boson with the ATLAS detector at the LHC". In: *Physics Letters B* 716.1 (2012), pp. 1–29. ISSN: 0370-2693. DOI: 10.1016/j.physletb.2012.08.020.

[4] S. Chatrchyan et al. "Observation of a new boson at a mass of 125 GeV with the CMS experiment at the LHC". In: *Physics Letters B* 716.1 (2012), pp. 30–61. ISSN: 0370-2693. DOI: 10.1016/j.physletb.2012.08.021.

[5] CERN. *The Large Hadron Collider*. [Online; Last accessed Sunday 8th August, 2021]. URL: https://home.cern/science/accelerators/large-hadron-collider.

[6] Nobel Prize Outreach AB 2021. *The Nobel Prize in Physics 2013*. [Online; Last accessed Sunday 8th August, 2021]. URL: https://www.nobelprize.org/prizes/physics/2013/summary/.

[7] G. Apollinari, I. Béjar Alonso, O. Brüning, et al. *High-Luminosity Large Hadron Collider (HL-LHC): Technical Design Report V. 0.1*. CERN Yellow Reports: Monographs. 2017. DOI: 10.23731/CYRM-2017-004.

[8] P. N. Burrows, N. C. Lasheras, L. Linssen, et al., eds. *The Compact Linear Collider (CLIC) - 2018 Summary Report*. CERN Yellow Reports: Monographs. 2018. DOI: 10.23731/CYRM-2018-002.

[9] M. Prathapan et al. "Design of a HVCMOS pixel sensor ASIC with on-chip readout electronics for ATLAS ITk Upgrade". In: *PoS* TWEPP2018 (2019), p. 074. DOI: 10.22323/1.343.0074.

[10] D. Dannheim, K. Krüger, A. Levy, et al., eds. *Detector technologies for CLIC*. CERN Yellow Reports: Monographs. CERN, 2019. DOI: 10.23731/CYRM-2019-001.

[11] M. Thomson. *Modern particle physics*. New York: Cambridge University Press, 2013. ISBN: 978-1-107-03426-6.

[12] Y. Fukuda et al. "Evidence for Oscillation of Atmospheric Neutrinos". In: *Phys. Rev. Lett.* 81 (8 Aug. 1998), pp. 1562–1567. DOI: 10.1103/PhysRevLett.81.1562.

[13] K. Eguchi et al. "First Results from KamLAND: Evidence for Reactor Antineutrino Disappearance". In: *Phys. Rev. Lett.* 90 (2 Jan. 2003), p. 021802. DOI: 10.1103/PhysRevLett.90.021802.

[14] F. P. An et al. "Observation of Electron-Antineutrino Disappearance at Daya Bay". In: *Phys. Rev. Lett.* 108 (17 Apr. 2012), p. 171803. DOI: 10.1103/PhysRevLett.108.171803.

[15] L. Canetti and M. Shaposhnikov. "The νMSM and muon to electron conversion experiments". In: *Hyperfine Interactions* 214.1 (Mar. 2013), pp. 5–11. ISSN: 1572-9540. DOI: 10.1007/s10751-013-0796-7.

[16] Wikimedia Commons. *Standard Model of Elementary Particles*. [Online; Last accessed Sunday 8th August, 2021]. URL: https://commons.wikimedia.org/wiki/File:Standard_Model_of_Elementary_Particles.svg.

[17] A. D. Sakharov. "Violation of CP-invariance, C-asymmetry, and baryon asymmetry of the Universe". In: *In The Intermissions... Collected Works on Research into the Essentials of Theoretical Physics in Russian Federal Nuclear Center, Arzamas-16*. World Scientific, 1998, pp. 84–87.

[18] E. Corbelli and P. Salucci. "The extended rotation curve and the dark matter halo of M33". In: *Monthly Notices of the Royal Astronomical Society* 311.2 (Jan. 2000), pp. 441–447. ISSN: 0035-8711. DOI: 10.1046/j.1365-8711.2000.03075.x.

[19] R. Massey, T. Kitching, and J. Richard. "The dark matter of gravitational lensing". In: *Reports on Progress in Physics* 73.8 (July 2010), p. 086901. DOI: 10.1088/0034-4885/73/8/086901.

[20] P. J. E. Peebles and B. Ratra. "The cosmological constant and dark energy". In: *Rev. Mod. Phys.* 75 (2 Apr. 2003), pp. 559–606. DOI: 10.1103/RevModPhys.75.559.

[21] M. Mezzetto and F. Terranova. "Three-flavour oscillations with accelerator neutrino beams". In: *Universe* 6.2 (2020), p. 32. DOI: 10.3390/universe6020032.

[22] M. Ibe, A. Kusenko, and T. T. Yanagida. "Why three generations?" In: *Physics Letters B* 758 (2016), pp. 365–369. ISSN: 0370-2693. DOI: 10.1016/j.physletb.2016.05.025.

[23] M. Dine. *Supersymmetry and String Theory: Beyond the Standard Model*. Cambridge University Press, 2007. DOI: 10.1017/CBO9780511618482.

[24] CERN. *The ATLAS Experiment*. [Online; Last accessed Sunday 8th August, 2021]. URL: https://atlas.cern/.

[25] CERN. *The CMS Experiment*. [Online; Last accessed Sunday 8th August, 2021]. URL: https://cms.cern/.

[26] K. Arndt et al. *Technical design of the phase I Mu3e experiment*. 2021. arXiv: 2009.11690 [physics.ins-det].

[27] European Strategy for Particle Physics Preparatory Group. *Physics Briefing Book*. 2020. arXiv: 1910.11775 [hep-ex].

[28] T. K. Charles et al. "The Compact Linear Collider (CLIC) - 2018 Summary Report". In: 2/2018 (Dec. 2018). Ed. by P. N. Burrows et al. DOI: 10.23731/CYRM-2018-002.

[29] D. Schulte. "Beam-beam Effects in Linear Colliders". In: *CERN Yellow Rep. School Proc.* 3 (2017). Ed. by W. Herr, pp. 431–445. DOI: 10.23730/CYRSP-2017-003.431.

[30] D. Arominski et al. "Beam-induced backgrounds in CLICdet". In: (Dec. 2019). URL: https://cds.cern.ch/record/2704642.

[31] J. de Blas et al. *The CLIC potential for new physics*. Ed. by J. de Blas. CERN Yellow Reports: Monographs. Geneva: CERN, Dec. 2018. DOI: 10.23731/CYRM-2018-003.

[32] H. Abramowicz et al. "Higgs physics at the CLIC electron–positron linear collider". In: *Eur. Phys. J. C* 77.7 (2017), p. 475. DOI: 10.1140/epjc/s10052-017-4968-5.

[33] A. Zarnecki. *Top-quark physics at CLIC*. Tech. rep. Geneva: CERN, Nov. 2019. URL: https://cds.cern.ch/record/2699889.

[34] "The Compact Linear Collider (CLIC) - Project Implementation Plan". In: 4/2018 (Dec. 2018). Ed. by M. Aicheler et al. DOI: 10.23731/CYRM-2018-004.

[35] CERN Document Server. *CLIC accelerator schematic diagrams*. [Online; Last accessed Sunday 8th August, 2021]. URL: https://cds.cern.ch/record/2655160.

[36] N. Alipour Tehrani et al. "CLICdet: The post-CDR CLIC detector model". In: (Mar. 2017). URL: https://cds.cern.ch/record/2254048.

[37] M. A. Thomson. "Particle flow calorimetry and the PandoraPFA algorithm". In: *Nuclear Instruments and Methods in Physics Research Section A: Accelerators, Spectrometers, Detectors and Associated Equipment* 611.1 (2009), pp. 25–40. ISSN: 0168-9002. DOI: 10.1016/j.nima.2009.09.009.

[38] CERN. *A Large Ion Collider Experiment*. [Online; Last accessed Sunday 8th August, 2021]. URL: https://alice.cern/.

[39] CERN. *LHCb - Large Hadron Collider beauty experiment*. [Online; Last accessed Sunday 8th August, 2021]. URL: https://lhcb-public.web.cern.ch/.

[40] *The Mu3e Experiment*. [Online; Last accessed Sunday 8th August, 2021]. URL: https://www.physi.uni-heidelberg.de/Forschung/he/mu3e/.

[41] T. Gehrke et al. "Theoretical and experimental comparison of proton and helium-beam radiography using silicon pixel detectors". In: *Physics in Medicine and Biology* 63 (Jan. 2018). DOI: 10.1088/1361-6560/aaa60f.

[42] H. Spieler. *Semiconductor Detector Systems*. Series on Semiconductor Science and Technology. OUP Oxford, 2005. ISBN: 9780198527848.

[43] H. Kolanoski and N. Wermes. *Teilchendetektoren – Grundlagen und Anwendungen*. Springer, 2016. DOI: 10.1007/978-3-662-45350-6.

[44] A. H. Compton. "A Quantum Theory of the Scattering of X-rays by Light Elements". In: *Phys. Rev.* 21 (5 May 1923), pp. 483–502. DOI: 10.1103/PhysRev.21.483.

[45] J. Ashkin and H. A. Bethe. "Passage of radiation through matter". In: *Experimaltal Nuclear Physics* 1.2 (1953), p. 253.

[46] Particle Data Group, P. A. Zyla, et al. "Review of Particle Physics". In: *Progress of Theoretical and Experimental Physics* 2020.8 (Aug. 2020). 083C01. DOI: 10.1093/ptep/ptaa104.

[47] L. D. Landau. "On the energy loss of fast particles by ionization". In: *J. Phys.* 8 (1944), pp. 201–205. URL: https://cds.cern.ch/record/216256.

[48] P. V. Vavilov. "Ionization losses of high-energy heavy particles". In: *J. Exp. Theor. Phys.* 5 (1957), pp. 749–751.

[49] H. Bichsel. "Straggling in thin silicon detectors". In: *Rev. Mod. Phys.* 60 (3 July 1988), pp. 663–699. DOI: 10.1103/RevModPhys.60.663.

[50] K. Nakamura and. "Review of Particle Physics". In: *Journal of Physics G: Nuclear and Particle Physics* 37.7A (July 2010), p. 075021. DOI: 10.1088/0954-3899/37/7a/075021.

[51] A. Herkert. "Characterization of a Monolithic Pixel Sensor Prototype in HV-CMOS Technology for the High-Luminosity LHC". PhD thesis. Heidelberg University, 2019.

[52] L. Rossi et al. *Pixel detectors: from fundamentals to applications*. Particle acceleration and detection. Berlin: Springer, 2006. DOI: 10.1007/3-540-28333-1.

[53] G. Masetti, M. Severi, and S. Solmi. "Modeling of carrier mobility against carrier concentration in arsenic-, phosphorus-, and boron-doped silicon". In: *IEEE Transactions on Electron Devices* 30.7 (1983), pp. 764–769. DOI: 10.1109/T-ED.1983.21207.

[54] W. Shockley. "The theory of p-n junctions in semiconductors and p-n junction transistors". In: *The Bell System Technical Journal* 28.3 (1949), pp. 435–489. DOI: 10.1002/j.1538-7305.1949.tb03645.x.

[55] J. L. Hudgins. "Wide and narrow bandgap semiconductors for power electronics: A new valuation". In: *Journal of Electronic Materials* 32.6 (June 2003), pp. 471–477. ISSN: 1543-186X. DOI: 10.1007/s11664-003-0128-9.

[56] Wikimedia Commons. *MOSFET functioning*. [Online; Last accessed Sunday 8th August, 2021]. URL: https://commons.wikimedia.org/wiki/File:MOSFET_functioning.svg.

[57] Wikimedia Commons. *IvsV mosfet*. [Online; Last accessed Sunday 8th August, 2021]. URL: https://commons.wikimedia.org/wiki/File:IvsV_mosfet.svg.

[58] W. Shockley. "Currents to Conductors Induced by a Moving Point Charge". In: *Journal of Applied Physics* 9.10 (1938), pp. 635–636. DOI: 10.1063/1.1710367.

[59] S. Ramo. "Currents Induced by Electron Motion". In: *Proceedings of the IRE* 27.9 (1939), pp. 584–585. DOI: 10.1109/JRPROC.1939.228757.

[60] A. Velyka. "Concept and Development of Enhanced Lateral Drift (ELAD) Sensors". PhD thesis. Hamburg University, 2019. DOI: 10.3204/PUBDB-2020-02268.

[61] E. Belau et al. "Charge collection in silicon strip detectors". In: *Nuclear Instruments and Methods in Physics Research* 214.2 (1983), pp. 253–260. ISSN: 0167-5087. DOI: 10.1016/0167-5087(83)90591-4.

[62] U. Fano. "Ionization Yield of Radiations. II. The Fluctuations of the Number of Ions". In: *Phys. Rev.* 72 (1 July 1947), pp. 26–29. DOI: 10.1103/PhysRev.72.26.

[63] W. R. Leo. *Techniques for nuclear and particle physics experiments: a how-to approach; 2nd ed.* Berlin: Springer, 1994. DOI: 10.1007/978-3-642-57920-2.

[64] R. C. Alig, S. Bloom, and C. W. Struck. "Scattering by ionization and phonon emission in semiconductors". In: *Phys. Rev. B* 22 (12 Dec. 1980), pp. 5565–5582. DOI: 10.1103/PhysRevB.22.5565.

[65] I. Peric. "Design and Realisation of Integrated Circuits for the Readout of Pixel Sensors in High Energy Physics and Biomedical Imaging". PhD thesis. Bonn University, 2004.

[66] N. Razek et al. "A GaAs/Si X-Ray Pixel Detector Based on Low Temperature Covalent Wafer Bonding". In: *ECS Meeting Abstracts* MA2020-02.22 (Nov. 2020), pp. 1632–1632. DOI: 10.1149/ma2020-02221632mtgabs.

[67] I. Kremastiotis et al. "Design and standalone characterisation of a capacitively coupled HV-CMOS sensor chip for the CLIC vertex detector". In: *Journal of Instrumentation* 12.09 (Sept. 2017), P09012–P09012. DOI: 10.1088/1748-0221/12/09/p09012.

[68] M. Vicente. "Pixel detector hybridization and integration with Anisotropic Conductive Films". In: *TIPP2021 Conference* (May 2021). URL: https://indico.cern.ch/event/981823/contributions/4295330/.

[69] N. Wermes. "Pixel detectors for charged particles". In: *Nuclear Instruments and Methods in Physics Research Section A: Accelerators, Spectrometers, Detectors and Associated Equipment* 604.1 (2009). PSD8, pp. 370–379. ISSN: 0168-9002. DOI: 10.1016/j.nima.2009.01.098.

[70] I. Perić. "A novel monolithic pixelated particle detector implemented in high-voltage CMOS technology". In: *Nucl. Instrum. Meth.* A582 (2007), pp. 876–885. DOI: 10.1016/j.nima.2007.07.115.

[71] I. Kremastiotis, R. Ballabriga, and N. Egidos. "Design of a monolithic HR-CMOS sensor chip for the CLIC silicon tracker". In: *PoS* TWEPP2018 (2019), p. 072. DOI: 10.22323/1.343.0072.

[72] R. Ballabriga et al. "Test-beam characterisation of the CLICTD technology demonstrator - A small collection electrode high-resistivity CMOS pixel sensor with simultaneous time and energy measurement". In: *Nuclear Instruments and Methods in Physics Research Section A: Accelerators, Spectrometers, Detectors and Associated Equipment* 1006 (2021), p. 165396. DOI: 10.1016/j.nima.2021.165396.

[73] I. Perić et al. *Description of the ATLASPix Simple and ATLASPIX M2 Preliminary v2*. 2018.

[74] H. Augustin et al. "MuPix8 — Large area monolithic HVCMOS pixel detector for the Mu3e experiment". In: *Nucl. Instrum. Meth. A* 936 (2019). Ed. by G. Batignani et al., pp. 681–683. DOI: 10.1016/j.nima.2018.09.095.

[75] D. Immig. "Characterization of ATLASPix1, an HV-CMOS Demonstrator for the Phase-II Upgrade of the ATLAS Inner Tracker". MA thesis. Heidelberg University, 2019.

[76] D. M. S. Sultan et al. "Electrical characterization of AMS aH18 HV-CMOS after neutrons and protons irradiation". In: *Journal of Instrumentation* 14.05 (May 2019), pp. C05003–C05003. DOI: 10.1088/1748-0221/14/05/c05003.

[77] AMS. *AMS aH180 Process Parameters*.

[78] *AMS AG, Austria*. [Online; Last accessed Sunday 8th August, 2021]. URL: https://ams.com/process-technology/.

[79] A. X. Widmer and P. A. Franaszek. "A DC-Balanced, Partitioned-Block, 8B/10B Transmission Code". In: *IBM Journal of Research and Development* 27.5 (1983), pp. 440–451. DOI: 10.1147/rd.275.0440.

[80] L. Meng. "Development of CMOS Sensors for High-Luminosity ATLAS Detectors". PhD thesis. University of Geneva, 2018. URL: https://cds.cern.ch/record/2637873.

[81] M. D. Buckland. "Simulation and evaluation of HV-CMOS pixel sensors for the CLIC vertex detector". PhD thesis. Liverpool University, 2018. URL: https://cds.cern.ch/record/2633983.

[82] H. Augustin. *Private Communication*. 2021.

[83] M. Benoit. *Private Communication*. 2018.

[84] I. Perić. *Private Communication*. 2018-2021.

[85] D. M. S. Sultan et al. *ATLASpix wiki*. [Online; Last accessed Sunday 8th August, 2021]. URL: https://gitlab.cern.ch/ATLASPix/wiki.

[86] H. Liu et al. "Development of a modular test system for the silicon sensor R&D of the ATLAS Upgrade". In: *Journal of Instrumentation* 12.01 (Jan. 2017), P01008–P01008. DOI: 10.1088/1748-0221/12/01/p01008.

[87] A. Fiergolski. "A Multi-chip Data Acquisition System Based on a Heterogeneous System-on-Chip Platform". In: *Proceedings of International Conference on Technology and Instrumentation in Particle Physics 2017*. Ed. by Z.-A. Liu. Singapore: Springer Singapore, 2018, pp. 303–308.

[88] T. Vanat. "Caribou – A versatile data acquisition system". In: *PoS* TWEPP2019 (2020), p. 100. DOI: 10.22323/1.370.0100.

[89] *Caribou Project Repository*. [Online; Last accessed Sunday 8th August, 2021]. URL: https://gitlab.cern.ch/Caribou.

[90] *User Guide: ZC706 Evaluation Board for the Zynq-7000 XC7Z045 SoC v1.8*. 2019. URL: https://www.xilinx.com/support/documentation/boards_and_kits/zc706/.

[91] SAMTEC. *SEARAY® High-Density Open-Pin-Field Arrays*. [Online; Last accessed Sunday 8th August, 2021]. URL: https://www.samtec.com/connectors/high-speed-board-to-board/high-density-arrays/searay.

[92] *Data Sheet: Keithley 2450 SourceMeter SMU Instrument*. 2019. URL: https://www.tek.com/keithley-source-measure-units/keithley-smu-2400-series-sourcemeter.

[93] *The Yocto Project Website*. [Online; Last accessed Sunday 8th August, 2021]. URL: https://www.yoctoproject.org/.

[94] *The Open Embedded Website*. [Online; Last accessed Sunday 8th August, 2021]. URL: https://www.openembedded.org/.

[95] *Peary Software Repository*. [Online; Last accessed Sunday 8th August, 2021]. URL: https://gitlab.cern.ch/Caribou/peary.

[96] E. Santin, P. Valerio, and A. Fiergolski. "CLICpix2 User's Manual". In: (2017). URL: https://edms.cern.ch/document/1800546/1.

[97] I. Kremastiotis et al. "Design and standalone characterisation of a capacitively coupled HV-CMOS sensor chip for the CLIC vertex detector". In: *Journal of Instrumentation* 12.09 (Sept. 2017), P09012–P09012. DOI: 10.1088/1748-0221/12/09/p09012.

[98] L. Caminada et al. "ATLAS FE-I4 ASIC". In: *PoS* Vertex2012 (2013), p. 023. DOI: 10.22323/1.167.0023.

[99] B. Ristic. "Active Pixel Sensors in AMS H18/H35 HV-CMOS Technology for the ATLAS HL-LHC Upgrade". In: *Nucl. Instrum. Meth. A* 831 (2016). Ed. by Yoshinobu Unno et al., pp. 88–93. DOI: 10.1016/j.nima.2016.06.001.

[100] T. Kugathasan et al. "Monolithic CMOS sensors for sub-nanosecond timing". In: *Nucl. Instrum. Methods Phys. Res., A* 979 (2020), 164461. 12 p. DOI: 10.1016/j.nima.2020.164461.

[101] C. Zhang et al. "Development of RD50-MPW2: a high-speed monolithic HV-CMOS prototype chip within the CERN-RD50 collaboration". In: *PoS* TWEPP 2019 (2020), p. 045. DOI: 10.22323/1.370.0045.

[102] Physikinstrumente. *Data Sheet: CDCLVD1213*. 2020. URL: https://www.ti.com/product/CDCLVD1213.

[103] alpha advanced materials. *Data Sheet: STAYSTIK 571 – Silver Filled Electrically Conductive Film*. 2016.

[104] S. Ebnesajjad. "8 - Characteristics of Adhesive Materials". In: *Handbook of Adhesives and Surface Preparation*. Ed. by S. Ebnesajjad. Plastics Design Library. Oxford: William Andrew Publishing, 2011, pp. 137–183. ISBN: 978-1-4377-4461-3. DOI: 10.1016/B978-1-4377-4461-3.10008-2.

[105] PDG - Particle Data Group. *Atomic and Nuclear Properties of Materials*. [Online; Last accessed Sunday 8th August, 2021]. URL: https://pdg.lbl.gov/2015/AtomicNuclearProperties/.

[106] C. Adler. *Radiation length of the ALICE TRD*. 2006. URL: https://www-physics.lbl.gov/~gilg/PixelUpgradeMechanicsCooling/Material/Radiationlength.pdf.

[107] *Data Sheet: Peltier Module MCPE1-03108NC-S*. URL: https://www.farnell.com/datasheets/3178956.pdf.

[108] *Data Sheet: Platinum Temperature Sensor with slim dimensions, P1K0.308.7W.B.007*. URL: https://www.farnell.com/datasheets/1643993.pdf.

[109] *User's manual FLIR Exx series*. URL: https://www.flir.eu/support/products/e75/#Documents.

[110] *Service Manual: FLUKE 45 Dual Display Multimeter*. 1999. URL: https://www.seattleu.edu/media/college-of-science-and-engineering/files/departments/electricalandcomputerengineering/Fluke_45_ServiceManual3ec7.pdf.

[111] *Industrial platinum resistance thermometers and platinum temperature sensors (IEC 60751:2008); German version EN 60751:2008*. 2009.

[112] G. Audi et al. "The Nubase evaluation of nuclear and decay properties". In: *Nuclear Physics A* 729.1 (2003). The 2003 NUBASE and Atomic Mass Evaluations, pp. 3–128. ISSN: 0375-9474. DOI: 10.1016/j.nuclphysa.2003.11.001.

[113] Laboratoire National Henri Becquerel. *LNE-LNHB/CEA - Table de Radionucleides - Fe-55*. [Online; Last accessed Sunday 8th August, 2021]. URL: http://www.lnhb.fr/nuclides/Fe-55_tables.pdf.

[114] *X'Pert PRO System - User's Guide 040501*.

[115] G. W. Fraser et al. "The X-ray energy response of silicon Part A. Theory". In: *Nuclear Instruments and Methods in Physics Research Section A: Accelerators, Spectrometers, Detectors and Associated Equipment* 350.1 (1994), pp. 368–378. ISSN: 0168-9002. DOI: 10.1016/0168-9002(94)91185-1.

[116] *AXAF Project Science: Widths for Charactersitic X-Ray Lines*. [Online; Last accessed Sunday 8th August, 2021]. URL: https://wwwastro.msfc.nasa.gov/xraycal/linewidths.html.

[117] *X-Ray Mass Attenuation Coefficients for Silicon*. [Online; Last accessed Sunday 8th August, 2021]. URL: https://physics.nist.gov/PhysRefData/XrayMassCoef/ElemTab/z14.html.

[118] A. Thompson et al. *X-RAY DATA BOOKLET*. Center for X-Ray Optics and Advanced Light Source, Lawrence Berkeley National Laboratory, Oct. 2009. URL: https://cxro.lbl.gov/x-ray-data-booklet.

[119] *AXAF Project Science: Widths for Characteristic X-Ray Lines*. [Online; Last accessed Sunday 8th August, 2021]. URL: https://wwwastro.msfc.nasa.gov/xraycal/linewidths.html.

[120] F. Pitters et al. "Time and Energy Calibration of Timepix3 Assemblies with Thin Silicon Sensors". In: (Nov. 2018). URL: https://cds.cern.ch/record/2649493.

[121] F. Pitters. *Private Communication*. 2021.

[122] *CERN: The Super Proton Synchrotron*. [Online; Last accessed Sunday 8th August, 2021]. URL: https://home.cern/science/accelerators/super-proton-synchrotron.

[123] N. Alipour Tehrani. "Test-beam measurements and simulation studies of thin pixel sensors for the CLIC vertex detector". PhD thesis. ETH Zurich, 2017.

[124] E. Dall'Occo. "The Timepix3 Telescope and Sensor R&D for the LHCb VELO Upgrade". In: (Dec. 2018). URL: https://cds.cern.ch/record/2651308.

[125] T. Poikela et al. "Timepix3: a 65K channel hybrid pixel readout chip with simultaneous ToA/ToT and sparse readout". In: *JINST* 9.05 (2014), p. C05013. DOI: 10.1088/1748-0221/9/05/C05013.

[126] M. Campbell. *Private Communication*. 2021.

[127] "Charged particle tracking with the Timepix ASIC". In: *Nuclear Instruments and Methods in Physics Research Section A: Accelerators, Spectrometers, Detectors and Associated Equipment* 661.1 (2012), pp. 31–49. DOI: 10.1016/j.nima.2011.09.021.

[128] J. Visser et al. "SPIDR: a read-out system for Medipix3 and Timepix3". In: *Proceedings of IWORID 2015, Hamburg, Germany*. Vol. 10. 12. 2015, p. C12028. DOI: 10.1088/1748-0221/10/12/C12028.

[129] R. Diener et al. "The DESY II test beam facility". In: *Nucl. Instrum. Meth* A922 (2019), pp. 265–286. DOI: 10.1016/j.nima.2018.11.133.

[130] H. Jansen et al. "Performance of the EUDET-type beam telescopes". In: *EPJ Tech. Instrum.* 3.1 (2016), p. 7. DOI: 10.1140/epjti/s40485-016-0033-2.

[131] Y. Liu et al. "EUDAQ2—A flexible data acquisition software framework for common test beams". In: *JINST* 14.10 (2019), P10033. DOI: 10.1088/1748-0221/14/10/P10033. arXiv: 1907.10600 [physics.ins-det].

[132] P. Baesso, D. Cussans, and J. Goldstein. "The AIDA-2020 TLU: a flexible trigger logic unit for test beam facilities". In: *JINST* 14.09 (2019), P09019. DOI: 10.1088/1748-0221/14/09/P09019.

[133] T. Bisanz et al. "EUTelescope: A modular reconstruction framework for beam telescope data". In: *JINST* 15.09 (2020), P09020. DOI: 10.1088/1748-0221/15/09/P09020.

[134] J. Baudot et al. "First test results Of MIMOSA-26, a fast CMOS sensor with integrated zero suppression and digitized output". In: *2009 IEEE Nuclear Science Symposium Conference Record (NSS/MIC)*. 2009, pp. 1169–1173. DOI: 10.1109/NSSMIC.2009.5402399.

[135] C. Hu-Guo et al. "First reticule size MAPS with digital output and integrated zero suppression for the EUDET-JRA1 beam telescope". In: *Nuclear Instruments and Methods in Physics Research Section A: Accelerators, Spectrometers, Detectors and Associated Equipment* 623.1 (2010). 1st International Conference on Technology and Instrumentation in Particle Physics, pp. 480–482. ISSN: 0168-9002. DOI: 10.1016/j.nima.2010.03.043.

[136] F. Pitters. "Silicon Detector Technologies for Future Particle Collider Experiments". PhD thesis. Technical University of Vienna, 2019.

[137] F. Pitters et al. "Time resolution studies of Timepix3 assemblies with thin silicon pixel sensors". In: *JINST* 14.05 (2019), P05022. DOI: 10.1088/1748-0221/14/05/P05022.

[138] J. Kröger and L. Huth. "Efficient Analysis of Test-beam Data with the Corryvreckan Framework". In: *Proceedings of the 29th International Workshop on Vertex Detectors (VERTEX2020)*. Nov. 2020. DOI: 10.7566/JPSCP.34.010024.

[139] D. Dannheim et al. "Corryvreckan: A Modular 4D Track Reconstruction and Analysis Software for Test Beam Data". In: *JINST* 16.03 (2021), P03008. DOI: 10.1088/1748-0221/16/03/P03008.

[140] The Corryvreckan Authors. *Corryvreckan Project Website*. [Online; Last accessed Sunday 8th August, 2021]. URL: https://cern.ch/corryvreckan.

[141] The Corryvreckan Authors. *Corryvreckan Software Repository*. [Online; Last accessed Sunday 8th August, 2021]. URL: https://gitlab.cern.ch/corryvreckan/corryvreckan.

[142] *CLIC Detector & Physics Study*. [Online; Last accessed Sunday 8th August, 2021]. URL: https://clicdp.web.cern.ch/.

[143] J. Kröger, S. Spannagel, and M. Williams. "User Manual for the Corryvreckan Test Beam Data Reconstruction Framework, Version 1.0". In: (Dec. 2019). arXiv: 1912.00856 [physics.ins-det].

[144] J. Kröger, S. Spannagel, and M. Williams. *Corryvreckan User Manual, latest version*. [Online; Last accessed Sunday 8th August, 2021]. 2020. URL: http://cern.ch/go/db9Z.

[145] M. Williams. "Evaluation of Fine-Pitch Hybrid Silicon Pixel Detector Prototypes for the CLIC Vertex Detector in Laboratory and Test-Beam Measurements". PhD thesis. Glasgow University of Glasgow, 2020.

[146] L. Rossi et al. "The Front-End Electronics". In: *Pixel Detectors: From Fundamentals to Applications*. 2006. DOI: 10.1007/3-540-28333-1_3.

[147] W. Snoeys. *Private Communication*. 2021.

[148] K. Akiba et al. "LHCb VELO Timepix3 Telescope". In: *JINST* 14.05 (2019), P05026. DOI: 10.1088/1748-0221/14/05/P05026.

[149] F. James and M. Roos. "Minuit: A System for Function Minimization and Analysis of the Parameter Errors and Correlations". In: *Comput. Phys. Commun.* 10 (1975), pp. 343–367. DOI: 10.1016/0010-4655(75)90039-9.

[150] The ROOT Authors. *TVirtualFitter Class Reference*. [Online; Last accessed Sunday 8th August, 2021]. URL: https://root.cern.ch/doc/master/classTVirtualFitter.html.

[151] C. Kleinwort. "General broken lines as advanced track fitting method". In: *Nucl. Instr. Meth. Phys. A* 673 (2012), p. 107. ISSN: 0168-9002. DOI: 10.1016/j.nima.2012.01.024.

[152] V. Blobel, C. Kleinwort, and F. Meier. "Fast alignment of a complex tracking detector using advanced track models". In: *Computer Physics Communications* 182.9 (2011). Computer Physics Communications Special Edition for Conference on Computational Physics Trondheim, Norway, June 23-26, 2010, pp. 1760–1763. DOI: 10.1016/j.cpc.2011.03.017.

[153] C. J. Clopper and E. S. Pearson. "The Use of Confidence or Fiducial Limits Illustrated in the Case of the Binomial". In: *Biometrika* 26.4 (1934), pp. 404–413. URL: http://www.jstor.org/stable/2331986.

[154] The ROOT Authors. *TEfficiency Class Reference*. [Online; Last accessed Sunday 8th August, 2021]. URL: https://root.cern.ch/doc/master/classTEfficiency.html.

[155] The ROOT Authors. *TEfficiency Class Reference, Section Clopper Pearson*. [Online; Last accessed Sunday 8th August, 2021]. URL: https://root.cern.ch/doc/master/classTEfficiency.html#ae80c3189bac22b7ad15f57a1476ef75b .

[156] L. Huth. "A High Rate Testbeam Data Acquisition System and Characterisation of High Voltage Monolithic Acitve Pixel Sensors". PhD thesis. Heidelberg University, 2018.

[157] S. Spannagel and H. Jansen. *GBL Track Resolution Calculator v2.0*. Version v2.0. Apr. 2016. DOI: 10.5281/zenodo.48795.

[158] R. Hammann. *Optimisation of the Trigger System of the DESY II Test Beam Facility Pixel Beam Telescopes*. Tech. rep. DESY, Sept. 2019. URL: https://github.com/hammannr/DESYSummie2019/blob/master/RobertHammann.pdf.

[159] VISHAY. *Data Sheet: Precision Low TCR High Temperature Thin Film Resistor*. 2012. URL: https://www.farnell.com/datasheets/2049263.pdf.

[160] N. Bacchetta et al. "Improvement in breakdown characteristics with multiguard structures in microstrip silicon detectors for CMS". In: *Nuclear Instruments and Methods in Physics Research Section A: Accelerators, Spectrometers, Detectors and Associated Equipment* 461.1 (2001). 8th Pisa Meeting on Advanced Detectors, pp. 204–206. ISSN: 0168-9002. DOI: 10.1016/S0168-9002(00)01207-9.

[161] G.-F. Dalla Betta et al. "Investigation of leakage current and breakdown voltage in irradiated double-sided 3D silicon sensors". In: *Journal of Instrumentation* 11.09 (Sept. 2016), P09006–P09006. DOI: 10.1088/1748-0221/11/09/p09006.

[162] S. S. Li and W. R. Thurber. "The dopant density and temperature dependence of electron mobility and resistivity in n-type silicon". In: *Solid-State Electronics* 20.7 (1977), pp. 609–616. ISSN: 0038-1101. DOI: 10.1016/0038-1101(77)90100-9.

[163] A. Meneses González. PhD thesis. Heidelberg University, in preparation.

[164] G. Blanchot, D. Dannheim, and C. Fuentes. "Power-pulsing schemes for vertex detectors at CLIC". In: *Journal of Instrumentation* 9.01 (Jan. 2014), pp. C01005–C01005. DOI: 10.1088/1748-0221/9/01/c01005.

[165] S. Ruiz Daza. "Power pulsing with CLICpix2". In: (Sept. 2019). URL: https://cds.cern.ch/record/2690112.

[166] E. Perez Codina. "Timepix3 performance in power pulsing operation". In: *PoS* VERTEX2018 (Mar. 2019), p. 059. 6. DOI: 10.22323/1.348.0059.

[167] I. Perić et al. "High-Voltage CMOS Active Pixel Sensor". In: *IEEE Journal of Solid-State Circuits* (2021), pp. 1–1. DOI: 10.1109/JSSC.2021.3061760.

[168] J. Kroeger. *Performance Studies of the ATLASpix HV-MAPS Prototype for Different Substrate Resistivities*. Tech. rep. Geneva: CERN, June 2021. URL: https://cds.cern.ch/record/2773952.

[169] The ROOT Authors. *Computation of the error function erf(x)*. [Online; Last accessed Sunday 8th August, 2021]. URL: https://root.cern.ch/root/html524/TMath.html#TMath:Erf.

[170] *Measurement of delta-rays in ATLAS silicon sensors*. Tech. rep. Geneva: CERN, Jan. 2013. URL: https://cds.cern.ch/record/1509553.

[171] I. Perić. *TSI Engineering Run HVMAPS: LHCb/CLIC/Telepix Chip Descriptions Version 2*. 2020.

[172] I. Perić and others. *ATLASpix3 User Manual*. 2019.

[173] R. Schimassek et al. "Test results of ATLASPIX3 — A reticle size HVCMOS pixel sensor designed for construction of multi chip modules". In: *Nuclear Instruments and Methods in Physics Research Section A: Accelerators, Spectrometers, Detectors and Associated Equipment* 986 (2021), p. 164812. ISSN: 0168-9002. DOI: 10.1016/j.nima.2020.164812.

[174] D. Kim. "Timing Study and Optimization of ATLASpix3 a full-scale HV-MAPS Prototype". MA thesis. Heidelberg University, 2020.

[175] L. Mandok. "Analoge Charakterisierung und Optimierung des HV-MAPS Prototypen ATLASpix3". MA thesis. Heidelberg University, 2020.

[176] J. Kröger. "Silicon pixel sensor R&D for the CLIC tracking detector". In: *Journal of Instrumentation* 15.08 (Aug. 2020), pp. C08005–C08005. DOI: 10.1088/1748-0221/15/08/c08005.

[177] TI. *Datenblatt: Präzisionsdrehtisch M-060, M-061, M-062*. 2020. URL: https://www.physikinstrumente.de/fileadmin/user_upload/physik_instrumente/files/datasheets/M-060-Datenblatt.pdf.

[178] D. M. S. Sultan et al. "Electrical Characterization of 180 nm ATLASPix2 HV-CMOS Monolithic Prototypes for the High-Luminosity LHC". In: *JINST* 15.05 (2020), P05022. DOI: 10.1088/1748-0221/15/05/P05022.

[179] A. Macchiolo. "The Phase-2 ATLAS ITk pixel upgrade". In: *Nuclear Instruments and Methods in Physics Research Section A: Accelerators, Spectrometers, Detectors and Associated Equipment* 962 (2020), p. 162261. ISSN: 0168-9002. DOI: 10.1016/j.nima.2019.06.002.

[180] J. Hammerich. PhD thesis. University of Liverpool, in preparation.

[181] D. Immig. PhD thesis. Heidelberg University, in preparation.

[182] B. Weinläder. PhD thesis. Heidelberg University, in preparation.

Acknowledgements

The last page of this thesis is dedicated to say thank you to all those, who supported me throughout these adventurous and unforgettable 3.5 years.

First and foremost, I would like to say thank you to my Doktorvater André Schöning for his supervision and for giving me this unique opportunity to participate in the Wolfgang-Gentner Programme. Furthermore, I am thankful to Norbert Hermann for accepting to be the second referee of this thesis.

My special thanks are given to Dominik Dannheim for being an amazing supervisor, who was always available for feedback and advice, and for all the fruitful discussions.

I would also particularly like to thank Simon Spannagel for teaching me the art of coding, making me part of the Corryvreckan project, and for being an inspiring colleague.

My thanks goes the CLICdp Vertex and Tracker team for the memorable test-beam campaigns at DESY, and for the extensive and constructive discussions we had during our weekly meetings.

Furthermore, I would like to express my gratitude towards all members of the former EP-LCD (now EP-DT-TP) group under the leadership of Lucie Linssen for the wonderful team spirit and pleasant working environment.

I would also like to say thanks to Heiko Augustin, Adrian Herkert, Lennart Huth and David Immig, for supporting me with their knowledge of the HV-MAPS technology and their test-beam experience.

Despite the fact that I had the large office to myself for a significant amount of time given the circumstances, I would like to thank Dominik Arominski, Pedro Dias de Almeida and Thorben Quast for sharing it with me in a very focussed atmosphere. In addition, I would like to thank Anna Ahooma, Carmelo Scarcella and Alexander Zech for the great communal life and a very pleasant time during periods of teleworking and beyond.

In particular, I would like to express my deepest gratitude towards my parents, Heike and Wilfried Kröger, as well as my brother Lars for their continuous support throughout my entire education.

And finally, my greatest thanks goes to Nadine Heckler for sharing this adventurous time with me.

- **Wolfgang Gentner Fellowship:** This work has been sponsored by the Wolfgang Gentner Programme of the German Federal Ministry of Education and Research (grant no. 05E15CHA until 2021, 05E18CHA since 2021).
- **CERN/SPS:** The help from the staff operating the CERN SPS and the North Area test facilities is gratefully acknowledged.
- **DESY:** Part of the measurements leading to these results have been performed at the Test Beam Facility at DESY Hamburg (Germany), a member of the Helmholtz Association (HGF).
- **AIDA:** This project has received funding from the European Union's Horizon 2020 Research and Innovation programme under Grant Agreement no. 654168.
- **HighRR:** I acknowledge the support of the High Resolution and High Rate Detectors in Nuclear and Particle Physics (HighRR) Research Training Group [GRK 2058].